MODELING SHOCK WAVE PROPAGATION IN DISCRETE NI/AL POWDER MIXTURES

A Dissertation
Presented to
The Academic Faculty

By

Ryan A. Austin

In Partial Fulfillment
Of the Requirements for the Degree
Doctor of Philosophy in Mechanical Engineering

Georgia Institute of Technology

December, 2010

MODELING SHOCK WAVE PROPAGATION IN DISCRETE NI/AL POWDER MIXTURES

Approved by:

Dr. David L. McDowell, Advisor
G.W.W. School of Mechanical Engineering
Georgia Institute of Technology

Dr. Naresh N. Thadhani
School of Materials Science and Engineering
Georgia Institute of Technology

Dr. Yasuyuki Horie
AFRL/MNME, Munitions Directorate
Eglin Air Force Base

Dr. Min Zhou
G.W.W. School of Mechanical Engineering
Georgia Institute of Technology

Dr. Jianmin Qu
G.W.W. School of Mechanical Engineering
Georgia Institute of Technology

Date Approved: November 11, 2010

ACKNOWLEDGEMENTS

As I reflect on my time at Georgia Tech, I am reminded of the many people who contributed to this work. First of all, I would like to thank my advisor, Dr. David McDowell, for his role in my Ph.D. program and for helping to shape me as a researcher. I would also like to thank Dr. Yuki Horie and Dr. Naresh Thadhani for their mentorship in this field of study. I wish to gratefully acknowledge Dr. Jianmin Qu and Dr. Min Zhou for serving on the reading committee, and Dr. David Benson for allowing me to use his finite element code in this work.

Many wonderful colleagues and friends have contributed to a fulfilling and enjoyable experience at Georgia Tech. In particular, I wish to thank Jason Mayeur, Laurent Capolungo, and D.J. Luscher for their friendship, their intellectual curiosity, and for many interesting conversations during our daily trips to the coffee stand. They have undoubtedly had an impact on this work. I would also like to thank Jim Shepherd, Doug Spearot, Ambarish Kulkarni, Narasimhan Swaminathan, Dan Eakins, Lou Ferranti, Honggang Zhou, Rajesh Prasanna, Nima Salajegheh, Craig Przybyla, Garritt Tucker, and Sam Britt for many useful discussions and interactions.

I am indebted to my entire family for their extraordinary support over these past years. In particular, I would like to thank Bud Austin and Sandy Carter for their hospitality in Atlanta, and my sister, Lindsey, for many enjoyable visits. I am truly grateful to my parents, Ken and Trudy Austin, for being my first (and most demanding) teachers, and for their support as I completed this work. Finally, I wish to thank my girlfriend, Nam, for her patience and understanding, her encouragement in difficult times, her beautiful smile, and her beautiful personality.

TABLE OF CONTENTS

LIST OF TABLES

LIST OF FIGURES

SUMMARY

The focus of this work is on the modeling and simulation of shock wave propagation in reactive metal powder mixtures. Reactive metal systems are non-explosive, solid-state materials that release chemical energy when subjected to sufficiently strong stimuli. Shock loading experiments have demonstrated that ultra-fast chemical reactions can be achieved in certain micron-sized metal powder mixtures. However, the mechanisms of rapid mixing that drive these chemical reactions are currently unclear. The goal of this research is to gain an understanding of the shock-induced deformation that enables these ultra-fast reactions. The problem is approached using direct numerical simulation. In this work, a finite element (FE) model is developed to simulate shock wave propagation in discrete particle mixtures. This provides explicit particle-level resolution of the thermal and mechanical fields that develop in the shock wave. The Ni/Al powder system has been selected for study. To facilitate mesoscale FE simulation, a new dislocation-based constitutive model has been developed to address the viscoplastic deformation of fcc metals at very high strain rates ($>10^5$ s^{-1}). Six distinct initial configurations of the Ni/Al powder system have been simulated to quantify the effects of powder configuration (e.g., particle size, phase morphology, and constituent volume fractions) on deformation in the shock wave. Results relevant to the degree of shock-induced mixing in the Ni/Al powders are presented, including specific analysis of the thermodynamic state and microstructure of the Ni/Al interfaces that develop during wave propagation. Finally, it is shown that velocity fluctuations at the Ni/Al interfaces (which arise due to material heterogeneity) may serve to fragment the particles down to the nanoscale, and thus provide an explanation of ultra-fast chemical reactions in these material systems.

CHAPTER 1

INTRODUCTION

The focus of this research is on the modeling of shock wave propagation in reactive metal powder mixtures. Reactive metal systems are non-explosive solid-state mixtures that release chemical energy when subjected to sufficiently strong stimuli, e.g., shock waves. As such, these material systems have potential uses as energetic materials. The chemical reactions that occur in shock-compressed media have been classified according to their time scale (Thadhani, 1994). The so-called *shock-induced* chemical reactions occur in the shock front or shortly-behind it (in the stress pulse) during the time scale of mechanical equilibration (< 1 μs). *Shock-assisted* chemical reactions occur on the longer time scale of bulk temperature equilibration (> 10 μs) after the state of stress has been released. The mechanism of shock-assisted chemical reactions is temperature- and defect-enhanced mass diffusion, where, for example, one constituent melts and the other dissolves into it. On the other hand, the mechanisms of shock-induced chemical reactions are currently unclear. Shock-induced reactions result in nearly full conversion of reactant particles (~10 μm in size) to product phases in a sub-microsecond time span. However, the maximum length of mass diffusion in metals is only about 0.1 μm in the shock wave (Horie and Sawaoka, 1993). Therefore, a purely diffusive mechanism of mixing is orders of magnitude too slow to account for shock-induced reactions. A fundamental understanding of shock-induced (ultra-fast) reactions is highly desirable from a scientific standpoint, as well as the standpoints of technical applications that seek to make use of them. To achieve this fundamental understanding, the mechanisms of rapid mass mixing that support shock-induced reactions must be identified.

It is thought that the mesoscopic deformation of the particles has an important role in the shock-initiation of powder mixtures, but again, the precise mechanisms and threshold conditions (e.g., peak stress amplitude) of the shock-induced reactions are not generally understood. The mechanisms of heterogeneous inelastic deformation in the shock front demand resolution via physically-based models that account for microstructure evolution and dynamic effects. Accordingly, the objectives of this work are to:

- Develop physically-based models that resolve the deformation and mixing of metal particle mixtures during shock wave propagation,
- Gain understanding of the micromechanical aspects of initiating ultra-fast chemical reactions in shocked powder mixtures,
- Develop an improved predictive capability to support identification of powder mixtures that are likely to exhibit large scale chemical reaction in the shock wave, and
- Quantify the effect of initial powder configuration with respect to the shock-induced deformation and mixing of the constituents (reactants).

As mentioned above, the mechanically-driven mixing of powder constituents is the most important factor that determines whether or not large scale chemical reactions occur in the shock wave. Current experimental methods cannot resolve (in space and time) the shock-induced deformation of the particles. Therefore, it is attractive to approach this problem using direct numerical simulation. In this work, the finite element (FE) method is used to simulate shock wave propagation in discrete micron-sized powder mixtures. This approach has been selected because we believe there is much to be learned from simulation methods that provide direct access to the time and length scales of particle deformation in the shock wave.

The general simulation framework that is developed in this thesis may be used to study any reactive powder system. The Ni/Al powder system has been selected as the model system for study. This system has been selected because the Ni/Al intermetallic reactions are highly exothermic and a few distinct configurations of the Ni/Al powder system have been studied in shock compression experiments. The initial powder configuration can have a strong influence on whether or not large scale reactions are initiated in the shock wave. For example, it has been shown that shock-induced reactions can be achieved in flaky Ni + spherical Al powders, but not in certain spherical Ni+Al powders (Eakins and Thadhani, 2006; Eakins, 2007). Therefore, the effects of powder configuration (e.g., particle size, volumetric distribution, porosity, and phase arrangement) are investigated using the framework that is developed here.

At the outset of this work, a sufficiently general mechanistic model for the deviatoric stress-strain responses of metals was not available for the high strain rates that are encountered in the shock front. This

is an important problem to address because the shock front in a granular material is not a discontinuity at the mesoscale and the heterogeneity of deformation in the shock front is thought to play an important role in mixing and reaction initiation. As such, accurate modeling of shock-induced particle deformation should address the highly dynamic conditions that are encountered during pore collapse (e.g., local strain rates on the order of 10^7 s^{-1}). Existing constitutive models that are typically used in shock wave calculations are (i) empirically-based, (ii) rate-independent, or (iii) or based on thermally-activated dislocation glide kinetics, which are inappropriate for strain rates above ~10^4 s^{-1}. Accordingly, there is a general need for a mechanistic constitutive model that addresses the viscoplastic deformation of metals at very high strain rates.

To achieve the objectives of this work, a set of milestones were developed to guide the course of research in the Ni/Al powder system. The research milestones are as follows:

- Develop a physically-based constitutive model for the high-rate viscoplastic deformation of metal particles in the shock loading regime.
- Construct a finite element model that resolves shock wave propagation at the particle level (mesoscale).
- Define a set of Ni/Al powder mixtures that are of specific interest and simulate shock waves of varying intensity in these powder mixtures.
- Analyze the discrete particle simulation results, with emphasis on mechanisms that enable the ultra-fast mixing that is required to explain shock-induced reactions.

In Chapter 2, a dislocation-density based constitutive model is developed for the rate- and path-dependent deformation of fcc metals in the shock loading regime. In this model, the glide kinetics take into account the proper dynamic effects (e.g., phonon damping and an upper limit of dislocation speed) and microstructure evolution laws are constructed to distinguish the nucleation, multiplication, and trapping of dislocations. A new model of heterogeneous dislocation nucleation is developed to treat the emission of dislocation segments from sources (e.g., grain boundaries and particle surfaces) and microstructure-sensitive criteria are proposed for pinning down the shock stress ranges where heterogeneous and

homogeneous dislocation nucleation should dominate in planar shock waves. Thus, the model developed in this work addresses a critical need for a more predictive viscoplastic constitutive law at high strain rates. The development of the constitutive law is especially relevant to the discrete particle simulations because the deformation and mixing of the constituents in (and closely behind) the shock front determines whether or not shock-induced chemical reactions are initiated in a given powder.

The focus of Chapter 3 is the application and validation of the viscoplastic constitutive model of Chapter 2. Here, a framework is developed for simulating steady planar waves (of finite strain) in homogeneous slabs of material. The viscoplastic constitutive model is then applied to three fcc metals (Cu, Ni, and Al) and a precipitate-hardening Al alloy (6061-T6) and incorporated in the steady wave simulation framework. These calculations resolve the structure of the shock front, including all relevant field variables and dislocation density components. This allows the performance of the constitutive model to be assessed through comparison to experimental data.

In Chapter 4, the literature on the shock wave chemistry of metal powder systems is reviewed. Here, emphasis is placed on experimental work pertaining to the Ni/Al powder system. The time-resolved experiments that offer definitive proof of ultra-fast (shock-induced) chemical reactions in the Ni/Al system are cited. This is followed by a discussion of mechanisms that have been hypothesized for the ultra-fast mass mixing in shocked powder mixtures.

The numerical methods that are used to simulate shock wave propagation in the (multi-phase) discrete particle mixtures are outlined in Chapter 5. In this work, the shock waves are simulated in digital representations of the powder mixture using an arbitrary Lagrangian-Eulerian (ALE) finite element code. The viscoplastic constitutive model of Chapter 2 has been implemented in the finite element code as a user material subroutine. Thus, the mesoscale simulations that are performed in this work represent the first attempt to resolve the shock-induced deformation of metallic particles using a constitutive model that is specialized for the high rates of deformation that are encountered during the shock transition. The Ni/Al powder mixtures of interest (6 in total) are defined in Chapter 5 and a procedure is developed to generate digital instantiations of powder geometry. Finally, the boundary value problem for simulating wave propagation is defined and the constitutive models for the thermal and mechanical responses of all phases are specified.

In Chapter 6, the discrete particle simulation results are presented for the Ni/Al powder mixtures. As a first step, Hugoniot curves and shock rise times are computed and compared to available experimental data. Sets of deformation fields are then presented for the distinct powder mixtures to highlight flow morphology, dislocation density, and thermal response. Since chemical reactions originate at the surfaces where Ni and Al come into direct contact, the entire (disjointed) Ni/Al interface is tracked in the shock wave simulations. Rank orderings of the Ni/Al powder mixtures are established according to distinct metrics of reactant mixing. Finally, simulated responses in the reflected shock waves are analyzed because shock-induced chemical reactions have been detected here for certain Ni/Al powder mixtures (Bennett et al., 1992; Yang et al., 1997). In the reflected waves, the heterogeneity of the material velocity fields and the rate of deformation fields are quantified. The simulations indicate that reflected wave fronts introduce velocity gradients (or fluctuations) at the Ni/Al interfaces, which may serve as the driving forces of ultra-fast mesoscopic mixing processes and subsequent large scale chemical reaction in the shock wave.

Finally, it should be noted that the intrinsic shock sensitivities of reactive metal systems are typically low. Therefore, pre-densified reactive metal powder mixtures may serve in some capacity as structural-energetic materials. Structural-energetic materials are material systems that perform two functions simultaneously: they (i) support structural loads, and (ii) release energy via chemical reaction. In systems applications, structural components that are traditionally inert may be replaced structural-energetic materials. If this can be done, one increases the specific energy release of an article. For quite some time the approach to designing reactive powder mixtures has been to select (guess) mixture attributes that may be favorable for specific performance objectives (e.g., prescribed structural load-bearing capacity and/or large scale chemical reaction). According to these selections, powder mixtures are prepared and subjected to shock wave loading. The specimens are then probed (in real time or in the recovered state) to determine whether or not chemical reactions have occurred. This is a costly and time-intensive approach to materials design. The simulation framework developed here (and the repository of simulation data that has been collected for the Ni/Al system) can provide guidance to designers of these materials systems, thus accelerating the insertion of the appropriate powder mixtures into technical applications of interest.

CHAPTER 2

A CONSTITUTIVE MODEL FOR THE VISCOPLASTIC DEFORMATION OF FCC METALS IN SHOCK WAVES

The responses of metals subjected to high stresses and very high rates of deformation ($>10^5$ s^{-1}) is an area of active research. This is, in part, because a fundamental understanding of the dynamic responses of metals are critical to a number of technical applications, e.g., high-speed impact phenomena, metal cutting, shock-consolidation of powders, vehicular crash simulation, and the development of armor. The deviatoric stresses in materials subjected to shock wave loading are sometimes neglected due to the state of high pressure. This approximation is reasonable for materials subjected to strong shock waves (longitudinal stress amplitudes greater than say 50–100 GPa). For stress amplitudes less than a few tens of GPa (i.e., the so-called "weak" shock waves that display distinct elastic and plastic wave fronts), the deviatoric response of the material can be of significance (Davison and Graham, 1979; Swegle and Grady, 1985) and many applications of practical interest fall into this regime.

Homogeneous slabs of metal that are subjected to (weak) shock waves experience rates of deformation in the range of 10^4–10^8 s^{-1}. Currently, constitutive models that address this strain rate regime are not fully-satisfying, as many existing models are highly idealized or disconnected from the physics of shock-wave-induced deformation. Thus, there is a general need for a model of high-strain-rate metal viscoplasticity. This is especially important for our simulations of shock wave propagation in discrete Ni/Al particle mixtures because the particle-level mixing and deformation in (and closely behind) the shock front is of great importance, as this is where *shock-induced* chemical reactions must initiate.

The purpose of the work presented in this chapter is to develop a physically-based constitutive model for the viscoplastic response of polycrystalline fcc metals in the shock loading regime. A physically-based model is desirable because the macroscopic properties and responses of metals are intimately related to the underlying microstructure (i.e., crystal structure, defects, grain size, secondary phases, etc.). Therefore, we have focused on dislocation-based descriptions of viscoplastic flow and

structure evolution (material hardening). This approach is also motivated by a desire to quantify dislocation density in the shocked Ni/Al particle mixtures, as this may provide insight to the mechanism of ultra-fast mixing and chemical reaction. The proposed model provides a microstructure-sensitive description of the kinematics and kinetics of slip, and a framework for rate- and path-dependent microstructure evolution. Our focus is the development of a viscoplastic constitutive model for pure fcc metals. However, to facilitate comparison of the model to experiments performed on 6061-T6 Al alloy, modifications are introduced to extend the scope of the model to certain alloys. Although the model that is developed here is intended to address the shock loading regime, it may also be applied to "shockless" high-strain-rate phenomena (e.g., quasi-isentropic compression waves).

2.1. Background

The measurement of flow stress at very high rates of deformation is challenging from an experimental point of view. In this section, experiments that have been performed to measure the dynamic flow stress of polycrystalline fcc metals and fcc-based alloys are briefly reviewed. Pressure-shear plate impact experiments have been performed by Clifton and co-workers to measure the flow stress of Al (Li, 1981) and Cu (Huang and Clifton, 1985; Tong et al., 1992; Frutschy and Clifton, 1998) at strain rates in the range of 10^5–10^6 s^{-1}. Meyers et al. (2003) calculated the flow stress of Cu in a laser shock compression experiment wherein the elastic strain components in the shock front were inferred from x-ray diffraction data. The strain rate in this experiment was estimated to be ~10^7 s^{-1}. In the weak shock loading regime, Wallace (1980a) calculated profiles of the shear stress in the shock front for 6061-T6 based on experimentally-measured free-surface velocity profiles (Johnson and Barker, 1969); here, strain rates up to 10^7 s^{-1} were achieved. A concise review of techniques that have been used to measure material strength in the shocked state and quasi-isentropic ramp waves has been provided by Vogler and Chhabildas (2006). For example, Huang and Asay (2005; 2007) used a re-shock and release technique to (indirectly) measure the strength of Al and 6061 Al alloy on the Hugoniot. Millett et al. (2008) have also determined the yield strength of pure Ni, a binary Ni-Co alloy, and Ni_3Al in the shocked state using plate impact experiments where the longitudinal and transverse stresses were measured simultaneously, although well-founded

concerns have been raised regarding the preparation of specimens in these experiments (Winter and Harris, 2008).

A number of constitutive models can conceivably be utilized to address the viscoplastic response of metals in the high-strain-rate regime (10^2–10^4 s^{-1}). For example, single-parameter internal state variable (ISV) models based on the dislocation density (Klepaczko, 1975; Mecking and Kocks, 1981) and the mechanical threshold stress (Follansbee and Kocks, 1988) have been developed to describe the viscoplastic response of metals for strain rates in the range 10^{-4}–10^4 s^{-1}. Composite models that make use of two ISVs have also been introduced (Mughrabi, 1986) and developed (Nes, 1998) to distinguish the contributions of dislocation cell walls and cell interiors. The aforementioned models are based on glide kinetics that describe dislocations overcoming obstacles with the assistance of thermal fluctuations (i.e., thermally-activated dislocation depinning). This treatment is valid for applied stresses below the mechanical threshold, which translates to rates of deformation below ~10^5 s^{-1}. Above the mechanical threshold, the kinetics of viscoplastic deformation are controlled by different mechanisms. Specifically, in the case of crystallographic slip, it appears that the generation and continuous glide of dislocation line segments, which are subject to phonon damping and relativistic effects, should be taken into account (Kocks et al., 1975).

Constitutive models that are commonly used in shock wave calculations include the Zerilli-Armstrong model (1987), the Johnson-Cook model (1985), and the Steinberg-Guinan model (1980). The Zerilli-Armstrong model is based on thermally-activated dislocation glide kinetics, and therefore is not applicable during the shock transition. The Johnson-Cook model is an empirically-fit relation with little insight to the physical mechanisms of deformation and no account of history effects. The Steinberg-Guinan model has been successful in correlating material strength behind the shock front and warrants further discussion. In this model, the yield strength is framed as a first-order Taylor expansion in pressure and temperature about the ambient state. Here, it is assumed that all microstructural processes have saturated above a critical strain rate (~10^5 s^{-1}) and that the stress-strain response is not affected by the rate of deformation above this critical strain rate. While the Steinberg-Guinan model provides an acceptable description of material strength behind the shock front, the assumption of rate-independent plastic deformation in the shock front does not hold. Furthermore, when the Steinberg-Guinan model is used in simulations of Rayleigh-Taylor surface instabilities in thin metal foils that are subjected to isentropic

compression waves, the computed perturbation growth factors are larger than those measured in experiments (Remington et al., 2006). This indicates the flow stress of the material has been underestimated in the numerical simulations.

The Preston-Tonks-Wallace model (2003) addresses the rate-dependent flow stress of metals over a wide range of strain rates (10^{-3}–10^{12} s^{-1}) by merging a model of thermally-activated dislocation glide at lower deformation rates with a power-law relation that describes the flow response in strong (overdriven) shock waves. The power-law form for overdriven shocks (deformation rates in the range of 10^{9}–10^{12} s^{-1}) is suggested by the thermodynamic calculations of Wallace (1981). Since a constitutive model for the deviatoric response in the transition regime (10^{4}–10^{8} s^{-1}) was not available at that time, the models for thermally-activated dislocation glide and overdriven shocks were extrapolated into this regime. This is somewhat inadequate since a physical description of viscoplastic flow in this regime is lacking. Our goal is to provide a model that addresses this regime.

A model of shock-induced plasticity was recently proposed by Armstrong et al. (2007; 2009). Here, the kinetics of viscoplastic deformation are based on thermally-activated (homogeneous) nucleation of dislocation loops in the shock front. This is an attractive description of plasticity for shear stresses approaching the ideal strength of the lattice. Additionally, this model explains the increased strain rate sensitivity at high rates of deformation (>10^{4} s^{-1}) by virtue of a decrease of the activation volume associated with thermally-activated dislocation nucleation. However, in polycrystalline metals (and alloys) subjected to weak shock waves, homogeneous dislocation nucleation may not occur at all. Instead, dislocation generation may be driven by the heterogeneous nucleation of dislocations from sources that are operated at shear stresses significantly lower than those required for homogeneous nucleation. Furthermore, material strength in the wake of the shock front is not governed by the cohesive limit of the crystal, but rather the obstacles to glide on the slip planes. Therefore, we seek to develop a constitutive model that merges a description of heterogeneous dislocation nucleation at lower shock stresses with homogeneous dislocation nucleation at higher shock stresses.

2.2. Kinematics

In this section, multiaxial flow rules are presented for the finite deformation of isotropic bodies and single crystals. Viscoplastic flow occurs by crystallographic slip for shock stress amplitudes below the twinning threshold, which depends on the stacking fault energy and grain size (Murr et al., 1997; Meyers et al., 2003). For micron-scale grains, the slip-to-twinning transition shock stress is about 20 GPa for Cu, 30 GPa for Ni, and presumably higher for Al (Murr, 1988). The kinematic relation for a macroscopic model of plasticity will be presented first, followed by formulation for crystal plasticity. For stronger shock waves, i.e., stress amplitudes above the twinning threshold, a framework that addresses the kinematics of concurrent shock-induced phase transformations and crystallographic slip within transformed domains would be most useful (Barton et al., 2005).

2.2.1. Macroscopic plasticity

For the sake of simplicity under monotonic loading conditions, we utilize J_2 flow theory with pure isotropic hardening to describe the macroscopic (isotropic) response. Therefore, the plastic rate of deformation may be written as

$$\mathbf{D}^p = \frac{3\dot{\psi}}{2\bar{\sigma}}\mathbf{s} \tag{2.1}$$

where $\bar{\sigma}$ is the uniaxial equivalent stress, $\dot{\psi}$ is the equivalent rate of plastic deformation, and $\mathbf{s}$ is the deviatoric part of the Cauchy stress tensor, $\boldsymbol{\sigma}$. For rate-dependent plastic flow, an expression for $\dot{\psi}$ can be derived by considering the plastic rate of deformation in a simple tension test. It has been shown that $\dot{\psi} = (2/3)\Phi$, where Φ is the rate of change of the angle between two line segments in the current configuration (which are mutually-orthogonal and oriented 45 degrees relative to the loading direction) that is caused by isochoric plastic deformation (Clifton, 1970). This relation has an analogy in small-strain theory. From Mohr's circle, it may be seen that $\dot{\gamma}^p/2 = (\dot{\varepsilon}_1^p - \dot{\varepsilon}_3^p)/2 = (3/2)\dot{\varepsilon}_1^p$ for an isochoric plastic deformation, where $\dot{\gamma}^p$ is the maximum plastic shearing rate and $\dot{\varepsilon}_i^p$ are the principal values of the plastic strain rate tensor. Making the appropriate substitutions in Eq. (2.1), the macroscopic plasticity law may be written as

$$\mathbf{D}^p = \left(\Phi/\bar{\sigma}\right)\mathbf{s} \tag{2.2}$$

A dislocation-based description of the plastic shearing rate can be written using the generalized Orowan equation, i.e.,

$$\Phi = bN_m\bar{v} + b\dot{N}\bar{x} \tag{2.3}$$

Here, b is the magnitude of the Burgers vector, N_m is the mobile dislocation density, $\bar{v}$ is the mean dislocation velocity, $\dot{N}$ is the rate of dislocation generation, and $\bar{x}$ is the mean displacement of the generated segments. The first term in Eq. (2.3) describes the slip rate that is accommodated by gliding dislocation segments, while the second term accounts for the plastic shearing rate that is accommodated by the displacement of generated dislocation segments. The classical Orowan relation is recovered when the generation term is negligibly small (i.e., $\dot{N}\bar{x} \simeq 0$). In the case of nucleation-controlled plasticity (i.e., $\dot{N}\bar{x} >> N_m\bar{v}$), the kinematic relation that has been used by Armstrong et al. (2007) is recovered. The mean dislocation velocity and the dislocation generation rate are sensitive to the shear stress ($\tau = \bar{\sigma}/2$), where it is assumed that slip has highest preference on planes of maximum shear (Taylor, 1965; Davison and Graham, 1979).

2.2.2. Crystal plasticity

The kinematics of single crystals are formulated in terms of the crystallographic shearing rates of the slip systems. Based on a multiplicative decomposition of the deformation gradient, $\mathbf{F} = \mathbf{F}^e \cdot \mathbf{F}^p$, the plastic part of the velocity gradient in the intermediate configuration $\hat{\Omega}$ is written as

$$\hat{\mathbf{L}}^p = \sum_{\alpha} \dot{\gamma}^{\alpha}\, \hat{\mathbf{s}}^{\alpha} \otimes \hat{\mathbf{m}}^{\alpha} \tag{2.4}$$

where α denotes the slip system, $\dot{\gamma}^{\alpha}$ are the crystallographic shearing rates, and $\hat{\mathbf{s}}^{\alpha}$ and $\hat{\mathbf{m}}^{\alpha}$ are unit vectors in the slip and slip plane normal directions, respectively, in the intermediate configuration. The crystallographic shearing rate for the α^{th} slip system is written as

$$\dot{\gamma}^{\alpha} = bN_m^{\alpha}\bar{v}^{\alpha} + b\dot{N}^{\alpha}\bar{x}^{\alpha} \tag{2.5}$$

where all quantities are now resolved on the appropriate slip system. The mean dislocation velocities $\overline{v}^{\alpha}$ and the dislocation generation rates $\dot{N}^{\alpha}$ are now driven by the shear stress resolved on the α^{th} slip system, i.e.,

$$\tau^{\alpha} = \boldsymbol{\sigma} : \left(\mathbf{s}^{\alpha} \otimes \mathbf{m}^{\alpha} \right) \tag{2.6}$$

where $\mathbf{s}^{\alpha}$ and $\mathbf{m}^{\alpha}$ reside in the current configuration Ω.

2.2.3. Application to shock wave plasticity

The kinematic relation that should be used in shock wave calculations is dictated by the length scale that is to be resolved. Since the constitutive model presented here seeks to address the high rate of deformation that occurs during a shock transition, the width of the shock front (w) is a length scale of interest. When selecting the kinematic relation, one should consider the size of the shock front relative to other material length scales. For example, if the viscoplastic response of polycrystalline metal with grains of size d is of interest, the macroscopic model provides a suitable description of the kinematics if $w/d >> 1$. If $w/d < 1$, the single crystal plasticity model may be used to resolve slip within individual grains. In granular materials, the particle size is another material length scale that should be considered since the shock transition is spread over a few particle diameters for waves of moderate amplitude. Since one of our long-term goals is to develop a continuum framework to simulate the shock-induced responses of granular media (i.e., discrete particle mixtures composed of hundreds of particles; each particle containing hundreds of grains), we focus on developing a macroscopic model for which the description of slip has been coarsened.

2.3. Glide kinetics

2.3.1. Dislocation mobility

In this section, kinetic relations are derived for a model of macroscopic plasticity. The mean velocity of glide dislocations depends on the magnitude of the shear stress τ relative to the glide resistance of the material. The mechanical threshold stress τ_0 is defined as the shear stress required to propagate

dislocations on their respective slip planes at the temperature θ = 0 K (Kocks et al., 1975). In this work, it is assumed that the mechanical threshold stress is determined by a combination of microstructure attributes that provide long-range and short-range glide resistance. This constitutive assumption was introduced originally by Seeger (1954; 1956). Hence, the mechanical threshold stress may be written as

$$\tau_0 = \tau_{\mu 0} + \tau_0^* \tag{2.7}$$

where $\tau_{\mu 0}$ and τ_0^* are the long-range and short-range resistances at 0 K, respectively. For θ > 0 K, thermal fluctuations can provide the energy necessary to assist dislocations in overcoming short-range obstacles. Long-range barriers cannot be readily overcome with the aid of thermal fluctuations. Therefore, the long-range resistance τ_μ at a given finite temperature serves as an athermal threshold below which there is no slip. The only temperature dependence of the athermal threshold is that introduced by the shear modulus, i.e., $\tau_\mu = (\mu/\mu_0)\tau_{\mu 0}$, where μ_0 is the shear modulus at 0 K. This scaling is introduced because long-range stress fields are transmitted through the lattice. For stresses in the range $\tau_\mu < \tau < \tau_0$, glide dislocations wait at obstacles until thermal fluctuations help them overcome the obstacle. This is the regime of thermally-activated dislocation glide. For $\tau > \tau_0$, glide dislocations are driven continuously on the slip planes. Here, the velocity of a dislocation is moderated by drag and relativistic effects.

The dislocation mobility relation of Clifton (1970) is useful in the shock loading regime because it addresses the transition from thermally-activated dislocation glide to continuous dislocation glide in the context of macroscopic plasticity. Similar relations for the glide kinetics in single-crystal plasticity have recently been presented (Barton et al., 2009). In the following, the basic elements of Clifton's mobility relation are presented and incorporated in the constitutive model for macroscopic plasticity. We introduce a modification that alters the effective stress that drives the motion of dislocations in the continuous glide regime.

The mean velocity of the glide dislocations may be written as

$$\overline{v} = \frac{\overline{L}}{t_w + t_r} \tag{2.8}$$

where $\bar{L}$ is the average glide distance between successive obstacles on the slip planes, t_w is the time a dislocation spends waiting at an obstacle for thermal assistance, and t_r is the time a dislocation spends "running" in-between obstacles. The waiting time may be written as

$$t_w = \frac{1}{\nu_G}\left[\exp\left\{\frac{\Delta G_{dep}}{k\theta}\right\} - 1\right] \tag{2.9}$$

where ν_G is the attempt frequency of a dislocation waiting at an obstacle, ΔG_{dep} is the stress-dependent free enthalpy of activation (for dislocation depinning), and k is the Boltzmann constant. In Eq. (2.9), the conventional relation for the waiting time has been altered so that the waiting time of dislocations under continuous glide ($\Delta G_{dep} = 0$) is equal to zero.

The mean running time depends on the mean velocity of dislocations gliding in-between obstacles, $\bar{v}_r$. This quantity is derived by averaging the instantaneous velocity of a dislocation (v_r) over the prescribed spacing of obstacles. Neglecting the inertial term, the instantaneous velocity is written as

$$v_r(y) = \frac{[\tau - \tau_R(y)]b}{B} \tag{2.10}$$

where y is the position of the dislocation on the slip plane, $\tau_R(y)$ describes the (line) glide resistance profile, and B is the damping coefficient. If it is assumed that (i) the effective driving force of dislocations in continuous glide is diminished only by variations in the long-range (internal) stress field, and (ii) the long-range stress field can be described by a sinusoidal function with amplitude τ_μ and period $\bar{L}$, then it can be shown (Kocks et al., 1975) that the averaging process yields

$$B\bar{v}_r = \tau_{eff} b \tag{2.11}$$

$$\tau_{eff} \equiv \left(\tau^2 - \tau_\mu^2\right)^{1/2} \tag{2.12}$$

Here, τ_{eff} is an effective stress derived form the averaging process. In the model of Clifton (1970), it is assumed that the long-range (internal) stress field is of secondary importance in deriving a relation for $\bar{v}_r$. In that case, the effective stress is simply the applied shear stress, i.e., $\tau_{eff} = \tau$.

The relation derived for the mean dislocation velocity in continuous glide is deficient in one regard: the dislocation velocity may exceed the shear wave speed c_s for high values of τ. This concern is addressed by modifying the damping coefficient according to the relativistic relation

$$B = \frac{B_0}{1-\left(\bar{v}_r / c_s\right)^2} \tag{2.13}$$

where B_0 is the nominal value of the damping coefficient for the current thermodynamic state. This modification essentially forces τ towards large values as $\bar{v}_r \to c_s$. Solving the quadratic equation that is obtained by substituting Eq. (2.13) into Eq. (2.11) leads to

$$\bar{v}_r = c_s h \tag{2.14}$$

where

$$h = \left(\xi^2 + 1\right)^{1/2} - \xi \tag{2.15}$$

$$\xi = \frac{B_0 c_s}{2\tau_{eff} b} \tag{2.16}$$

The mean dislocation velocity given in Eq. (2.8) can now be written as

$$\bar{v} = \frac{c_s h}{\left(\exp\left\{\Delta G_{dep} / k\theta\right\} - 1\right)\left(c_s h / \nu_G \bar{L}\right) + 1} \quad \text{for} \quad \tau > \tau_\mu \tag{2.17}$$

A schematic of the mobility relation given in Eq. (2.17) is provided in Figure 2.1, where pressure, temperature, and the mechanical threshold stress have been held constant. The mobility relation without the relativistic effect introduced by Eq. (2.13) is also depicted. Here, the mean dislocation velocity has been normalized by the shear wave speed and the shear stress has been normalized by the mechanical threshold stress. There is a fairly sharp increase in dislocation velocity for shear stresses in the range of τ_μ to τ_0, which corresponds to the regime of thermally-activated dislocation glide. For shear stresses in the vicinity of the mechanical threshold (and greater), dislocation drag and the relativistic effect influence mobility.

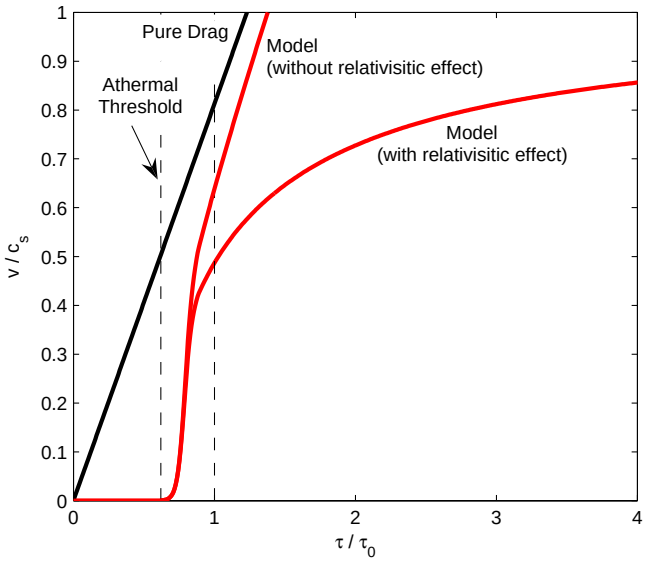

Figure 2.1: The normalized mean dislocation velocity given by Eq. (2.17) is plotted and labeled as the model (with relativistic effect). The athermal threshold, drag-controlled velocity in an obstacle-free lattice, and the model (without relativistic effect) are also plotted for reference.

2.3.2. Threshold stresses for pure fcc metals

The mechanical threshold stress τ_0 is an evolving state variable that depends on material structure. In pure polycrystalline metals the main obstacles to dislocation glide are lattice friction, the dislocation network, and the grain boundaries. The friction stress of the lattice is negligibly small in fcc metals. In fcc metals with micron-size grains, we assume the dislocation network controls the glide resistance in the shock-loading regime. This assumption is based on the fact that shock waves generate high densities of dislocation line segments as they propagate in metals. Therefore, the dense network of dislocations behind the leading edge of the shock front provides the main obstacles to continued dislocation glide instead of the considerably larger spacing of micron-scale grain boundaries. This assumption is supported by experimental work that has shown the strength of microcrystalline metals in the shocked state (Huang and Asay, 2005) and in quasi-isentropic compression waves (Asay et al., 2008) is relatively insensitive to the initial grain size. Thus, the mechanical threshold stress is written using the Taylor relation, i.e.,

$$\tau_0 = \tau_{dis,0} = \alpha_0 \mu_0 b \sqrt{N} \tag{2.18}$$

Here, $\tau_{dis,0}$ is the glide resistance of the dislocation network at 0 K, α_0 is the dislocation interaction constant, μ_0 is the shear modulus at 0 K, and N is the dislocation density. This relation is observed to hold whenever flow is controlled by dislocation-dislocation interactions, regardless of the precise arrangement of dislocations (Kocks and Mecking, 2003).

The main short-range obstacles to dislocation glide in fcc metals are forest dislocations (i.e., dislocations that pierce the glide plane). Accordingly, τ_0^* is identified as the peak resistance provided by the forest dislocations at 0 K. The long-range resistance to dislocation glide in pure metals is then attributed to dislocations arranged in cell walls, sessile Lomer-Cottrell locks, and the line tension of bowed-out glide segments. Indeed, there is evidence of long-range stress fields in pure metals (Conrad, 1970). When pure metals are deformed at a given strain rate and temperature, the Cottrell-Stokes law implies the rate- and temperature-sensitive part of the flow stress scales with the total flow stress (after a few percent deformation), i.e., $\tau^* \propto \tau$. This suggests that the short-range and long-range resistance components depend on the dislocation substructure in a similar manner, and that these resistance components should display the same functional dependence on the dislocation density. According to the decomposition of the mechanical threshold stress in Eq. (2.7), this indicates $\tau_{\mu 0} \propto \tau_0$. Therefore, the athermal threshold stress may be written as

$$\tau_\mu = \frac{\mu}{\mu_0}\left(\beta_0 \tau_{dis,0}\right) \tag{2.19}$$

where β_0 is a proportionality constant. The limiting case β_0=0 reflects a situation where the dislocation network does not provide any long-range stress fields that oppose the glide of dislocations.

2.3.3. Threshold stresses for fcc-based alloys

In alloys, the precipitates and solid solutions present additional obstacles to dislocation glide. The glide resistance of the precipitate field depends on a number of factors, e.g., the size, shape, spacing, stiffness, surface energy, and degree of coherency of the precipitates. The solid solution strengthening depends on the concentrations of alloying elements in solution. The precipitate characteristics and the solid solution depend, in turn, on the process history (e.g., heat treatment). As such, models for strengthening

mechanisms should be specialized to each alloy microstructure of interest. In this work, we treat age-hardening alloys with non-shearable precipitates and relatively weak solid solution strengthening. This subset of characteristics is of interest because it corresponds roughly to alloys in the peak-aged condition (optimal hardening).

A first-order approximate model is sought to describe the primary strengthening mechanisms in the alloys of interest. Let $\tau_{p,0}$ denote the glide resistance of precipitates at 0 K. Since non-shearable precipitates are treated, glide dislocations overcome the precipitates by the (athermal) Orowan looping mechanism. There is also a strengthening contribution from the network of dislocations, as given in Eq. (2.18). Solid solution strengthening is neglected because it is small in comparison to other strengthening mechanisms. For simplicity, it is assumed that the resistance of precipitates and the dislocation substructure superpose linearly. Therefore, the mechanical threshold stress is written as

$$\tau_0 = \tau_{p,0} + \tau_{dis,0} \tag{2.20}$$

One might consider superposing the glide resistance of the dislocation substructure and the non-shearable precipitates using a quadratic relation, which does have a physical basis (Koppenaal and Kuhlmann-Wilsdorf, 1964). However, the linear relation has been utilized in prior work and it appears sufficient (Myhr et al., 2001).

The main short-range obstacles to dislocation glide are again forest dislocations. This is because the alloying additions provide no new thermally-activated obstacles to dislocation glide in our conceptualization of the problem. If an alloy contains Guinier-Preston (GP) zones or small shearable precipitates (both of which may be overcome with thermal assistance), the description of short-range resistance to glide must be modified. The long-range glide resistance is due to the non-shearable precipitates and the parts of the dislocation network that cannot be readily overcome with the aid of thermal fluctuations. Therefore, the athermal threshold is written as

$$\tau_\mu = \frac{\mu}{\mu_0}\left(\tau_{p,0} + \beta_0 \tau_{dis,0}\right) \tag{2.21}$$

2.4. Substructure evolution

Models for the evolving dislocation substructure in metals have been proposed for quasistatic and mildly dynamic loading rates. An approach based on the total dislocation density was introduced by Mecking and Kocks (1981) and further developed; an excellent review of this work is available (Kocks and Mecking, 2003). Models that distinguish certain components of the dislocation density sometimes provide better descriptions of substructure evolution. For example, Estrin and Kubin (1986) constructed a model that distinguished the mobile and immobile components of dislocation density in order to capture fast transients in the deformation responses of metals. While these approaches form a useful basis for modeling substructure evolution at very high rates of deformation, the unique conditions found in shock waves require additional consideration. In particular, the intense generation of dislocations in the shock front must be taken into account. Therefore, the integration of earlier work with the emerging understanding of dislocation nucleation under shock conditions is relevant.

The starting point of our model of dislocation substructure is the distinction of mobile and immobile dislocation segments, i.e.,

$$N = N_m + N_{im} \tag{2.22}$$

where N_m and N_{im} are the mobile and immobile dislocation densities, respectively. The behavior of dislocations in a shock wave is conceptualized as follows. The rise in shear stress behind the leading edge of the shock front serves as the driving force for dislocation generation (nucleation and multiplication) and migration. If the shear stress approaches the ideal strength of the lattice, dislocation loops are nucleated homogeneously in the shock front. A large fraction of the homogeneously-nucleated loops travel a distance $\bar{x}_{hom}$ and are immobilized by interactions with other dislocations, forming a fine scale network of dislocations (Bandak et al., 1992). If the shear stress is well below the ideal strength of the lattice, the rate of homogeneous nucleation is negligibly small, but the rate of heterogeneous dislocation nucleation may be appreciable. Here, dislocation segments are emitted from defective regions of the lattice which experience stress concentrations. The mobile dislocation segments glide on the slip plane until they are annihilated or immobilized by obstacles. Behind the shock front (in the plateau region of the stress wave), the shear stress may drive a certain amount of thermally-activated dislocation glide and substructure rearrangement.

According to this conceptualization of dislocation behavior, evolution equations for the mobile and immobile components of the dislocation density may be written as

$$\dot{N}_m = \chi_{hom}\dot{N}_{hom} + \dot{N}_{het} + \dot{N}_{mult} - \dot{N}_{ann} - \dot{N}_{trap} \tag{2.23}$$

$$\dot{N}_{im} = \left(1-\chi_{hom}\right)\dot{N}_{hom} + \dot{N}_{trap} - \dot{N}_{rec} \tag{2.24}$$

Here, the subscripts *hom, het, mult, ann*, *trap*, and *rec* refer to the homogeneous nucleation, heterogeneous nucleation, multiplication, annihilation, trapping, and recovery of dislocation segments, respectively, and χ_{hom} is the fraction of homogeneously-nucleated dislocations that remain mobile after traveling a prescribed distance, $\overline{x}$. The evolution equations have been framed quite generally and we wish to discuss some simplifications regarding dislocation nucleation. If the shear stress is significantly lower than the ideal strength of the lattice, the homogeneous nucleation terms drop out naturally. Alternatively, if the shear stress is high enough to drive homogeneous nucleation at an appreciable rate, the heterogeneous nucleation term is suppressed so that the nucleation behavior is governed by a single mechanism. Thus, depending on the level of shear stress, either homogeneous dislocation or heterogeneous nucleation will typically dominate.

It is now possible to specify the nucleation-accommodated plasticity term in the generalized Orowan equation. The part of the plastic shearing rate Φ that is controlled by nucleated dislocation line segments may be written as

$$b\dot{N}\,\overline{x} = b\dot{N}_{hom}\overline{x}_{hom} \tag{2.25}$$

Here, it is assumed that homogeneous dislocation nucleation is the only contribution, since dislocation segments that are generated by heterogeneous nucleation and multiplication remain mobile and contribute to the glide-accommodated part of Φ.

Although time-resolved measurements of the dislocation density components typically cannot be measured in experiments, Eqs. (2.23) and (2.24) provide a logical, mechanistic framework for approximating their evolutionary behavior. Furthermore, dislocation dynamics simulations are starting to address the evolution of dislocation substructure in shock waves (Shehadeh et al., 2006) and other high-strain-rate (10^6 s^{-1}) loading conditions (Wang et al., 2009). In the latter reference, the mobile and immobile

dislocation populations of Cu single crystals have been distinguished and it has been shown that crystal orientation has a significant influence on the heterogeneity of substructure evolution.

2.4.1. Criteria for the type of dislocation nucleation

In this section, a methodology is developed to determine the type of dislocation nucleation (homogeneous vs. heterogeneous) that is expected for a given shock stress amplitude (σ^-) and microstructure. For homogeneous dislocation nucleation to occur at an appreciable rate, the shear stress must approach the ideal strength of the lattice. As mentioned earlier, heterogeneous nucleation encompasses dislocation emission from defective regions of the lattice which experience stress concentrations, and therefore occurs at lower shear stresses. Criteria are developed to identify the shock stress range wherein homogeneous dislocation nucleation is expected. Heterogeneous dislocation nucleation is then expected at lower shock stresses.

A planar shock wave in an isotropic homogeneous medium induces a state of uniaxial strain. For a planar shock wave, there is a minimum shock stress below which homogeneous dislocation nucleation does not occur at an appreciable rate. This minimum shock stress may be written as

$$\sigma_{Min} = \left(\frac{1-\nu}{1-2\nu} \right) 2\chi_{ath}\tau_{ath} \tag{2.26}$$

where ν is Poisson's ratio and $\chi_{ath}\tau_{ath}$ is the minimum shear stress required to drive homogeneous dislocation nucleation at an appreciable rate (e.g., $\tau_{ath} \simeq \mu/15$ and $\chi_{ath} \simeq 0.8$). Equation (2.26) expresses the longitudinal stress that corresponds to $\tau = \chi_{ath}\tau_{ath}$ in uniaxial elastic deformation. Deformation twinning occurs for shock stresses greater than the twinning threshold σ_{Twin}. To isolate the stress range where homogeneous dislocation nucleation is most likely, while avoiding the convoluting effects of twinning, σ_{Twin} is taken as an upper bound. Thus, the first criterion for the occurrence of homogeneous dislocation nucleation is $\sigma^- \in (\sigma_{Min}, \sigma_{Twin})$. However, this criterion alone is insufficient because it does not ensure that the shear stress in the shock front will reach levels high enough for homogeneous dislocation nucleation.

If the shear stress is to approach the ideal strength of the lattice, plastic deformation in the shock front (prior to nucleation) must be limited. Otherwise, the shear stress will be relaxed by the glide of dislocation segments. It is proposed that homogeneous nucleation is likely to occur when the shock front width (w) falls below the minimum spacing of sources that emit dislocations (λ), which relax the stress state. Therefore, the second criterion for the occurrence of homogeneous dislocation nucleation is $w/\lambda < 1$. In pure metals, the dislocation sources are the grain boundaries and the initially-resident dislocations (e.g., Frank-Read mills and dislocation cell walls). Dislocations behind the shock front are not to be considered because they cannot keep up with the shock front (even if they travel at the shear wave speed). In alloys, the precipitates also serve as dislocation sources. Thus, the criteria for the occurrence of homogeneous dislocation nucleation are expressed as $\sigma^- \in (\sigma_{Min}, \sigma_{Twin})$ and $w/\lambda < 1$. This is illustrated graphically in Figure 2.2 for a generic metal. Here, the shock front width has been estimated as

$$w = D\Delta t = \Delta u / \dot{\varepsilon} \tag{2.27}$$

where D is the shock wave speed, Δt is the shock rise time, $\Delta u = \Delta u(\sigma^-)$ is the jump in material velocity across the wave front, and $\dot{\varepsilon}$ is the maximum strain rate in the shock front that is expressed using the fourth-power law (Swegle and Grady, 1985), i.e., $\dot{\varepsilon} \propto (\sigma^-)^4$. In Figure 2.2, the gray-shaded region indicates the shock stress range where homogeneous dislocation nucleation is expected. The region to the left indicates the regime of heterogeneous dislocation nucleation.

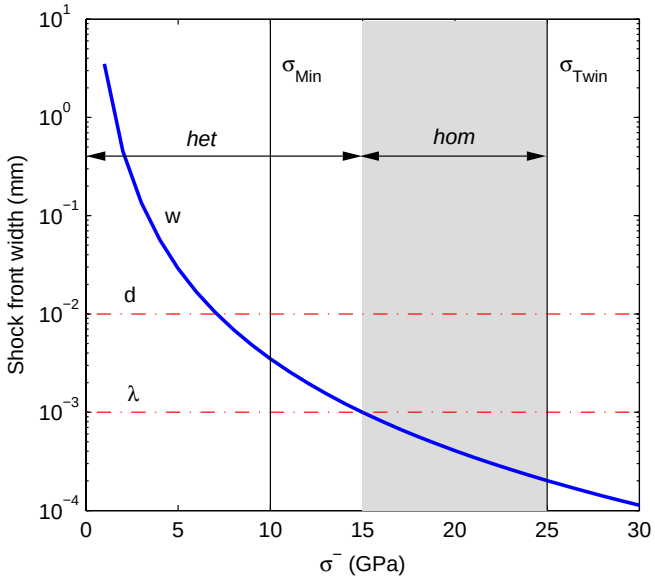

Figure 2.2: Illustration of the homogeneous dislocation nucleation criteria for a generic metal. The shock stress ranges where homogeneous and heterogeneous dislocation nucleation are expected are depicted.

2.4.2. Homogeneous dislocation nucleation

In small volumes of the lattice that are free of defects, dislocation loops are nucleated homogeneously when the shear stress approaches the ideal shear strength of the crystal. Following the treatment of Hirth and Lothe (1968), the homogeneous dislocation nucleation rate may be written as

$$\dot{N}_{hom} = n_c \omega Z \ell \tag{2.28}$$

where n_c is the equilibrium concentration of embryonic dislocation loops on the verge of criticality, ω is the frequency with which atoms on the periphery of critical-sized loops join the loop (thus rendering it super-critical), Z is a factor related to the non-equilibrium character of the process, and ℓ is the dislocation segment length introduced by a single nucleation event. The homogeneous nucleation rate given in Eq. (2.28) may be re-written as

$$\dot{N}_{hom} = \dot{N}_0 \exp\left\{\frac{-\Delta G_{hom}}{k\theta}\right\} \tag{2.29}$$

where the pre-exponential term is defined as

$$\dot{N}_0 = \frac{\alpha_{hom} \nu_D b}{\Omega} \tag{2.30}$$

Here, ΔG_{hom} is the stress-dependent free enthalpy of activation for homogeneous nucleation, ν_D is the Debye frequency, Ω is the atomic volume, and α_{hom} is a scaling factor. It has been shown that homogeneous dislocation nucleation is thermally-activated in the shock loading regime (Xu and Argon, 2000; Meyers et al., 2008). This dependence is embedded in Eq. (2.29), which is precisely the relation that has been utilized by Armstrong et al. (2007; 2009) to address shock-induced plastic flow. Similar relations have also been identified to address the thermally-activated nucleation of dislocations from free surfaces (Zhu et al., 2008) and the nucleation of sub-critical stacking faults and dislocation loops in atomistic simulations performed on single crystals (Tschopp and McDowell, 2008b).

2.4.3. Heterogeneous dislocation nucleation

In polycrystalline metals and alloys, heterogeneous dislocation nucleation may occur at nominal shear stresses considerably lower than the ideal shear strength of the lattice. Here, stress concentrators raise the nominal shear stress to that required to emit dislocations from a source (e.g., a grain boundary or precipitate-matrix interface). In our model, the heterogeneous nucleation rate accounts for dislocations emitted from sources due to a distribution of stress concentrations. Stress concentrators that are present in polycrystalline metals and alloys include GB steps, triple junctions, microscopic cracks, voids, impurity atoms, and precipitates. Incompatible deformation fields at GBs also engender stress concentrations. For example, pile-ups of glide dislocations on the GBs and the elastic anisotropy of neighboring misoriented grains act as stress concentrators. Atomistic simulations have been useful is studying the heterogeneous nucleation of dislocations due to some of these stress concentrators. For example, the work of Farkas and Curtin (2005) has confirmed that dislocations are emitted from regions of the boundary that can be characterized as containing a dislocation. The simulations of Van Swygenhoven et al. (2006) have shown that tangible stress concentrations due to atomic-sized steps in grain boundaries lead to the emission of dislocations. Capolungo et al. (2007) have shown that the critical stress required for dislocation nucleation is reduced when a small step (~1 nm in height) is introduced to the GB in atomistic simulations performed on Cu bicrystals. Finally, the atomistic simulations of Tschopp and McDowell (2008a) have confirmed the

idea that the stress field of dislocations that compose a GB may combine with the applied stress to nucleate a dislocation loop in the lattice near the GB (Varin et al., 1987), although technically this is homogeneous nucleation instead of heterogeneous nucleation because the loop is not topologically-connected to a pre-existing defect at its inception.

Models for the heterogeneous nucleation of dislocations in shock waves have been proposed by Gupta et al. (1975) for Mg-doped LiF single crystals. We have adapted the stress-based probabilistic approach of Gupta et al. to address heterogeneous nucleation in polycrystalline metals and alloys. In a stress-based approach, a dislocation segment is emitted from a source when the local shear stress, $K\tau$, reaches a critical value (K is a stress concentration factor that varies in space throughout the microstructure). Let the critical value of the *nominal* shear stress at which a dislocation is nucleated from a source, τ_{cr}, be a random-distributed variable. The probability that τ_{cr} falls in the range $(0,\tau]$ is given as

$$\int_0^{\tau} f\left(\tau_{cr}\right) d\tau_{cr} = \left(\frac{n}{\mathcal{N}}\right)_{\tau_{cr}\in(0,\tau]} \tag{2.31}$$

where $f\left(\tau_{cr}\right)$ is the probability distribution function (PDF) that characterizes the spectrum of critical shear stress required for the emission of dislocations. The right-hand-side of Eq. (2.31) represents the fraction of sources that emit dislocations in the stress range $(0,\tau]$. Here, n is the number of sources that have emitted a dislocation and $\mathcal{N}$ is the total number of potential sources. Differentiating Eq. (2.31) with respect to τ yields

$$f\left(\tau\right) d\tau = \frac{1}{\mathcal{N}} dn \tag{2.32}$$

Thus, $f(\tau)d\tau$ is interpreted as the increment in the fraction of sources that emit dislocations as the shear stress is raised from τ to $\tau + d\tau$. The differential length of dislocation line segment that is generated by heterogeneous nucleation in volume V may be written as

$$\dot{N}_{het} V dt = \bar{\ell}\, dn \tag{2.33}$$

where $\bar{\ell}$ is the mean dislocation segment length generated by a source. The combination of Eqs. (2.32) and (2.33) yields

$$\dot{N}_{het} = \alpha_{het}\, f\left(\tau\right) \dot{\tau} \tag{2.34}$$

where $\alpha_{het} = (\mathcal{N}/V)\,\overline{\ell}$. A comment regarding the numerical implementation of this relation is now in order. It is understood that heterogeneous nucleation occurs only when the stress rate $\dot{\tau}$ in Eq. (2.34) is positive with respect to its projection on the plastic shearing rate since stress rates of opposite sign (which develop if the dynamic shear stress relaxes to an equilibrium value) do not produce negative rates of dislocation generation.

To apply the heterogeneous dislocation nucleation relation to a pure metal or alloy, one must consider the range of shear stress over which dislocations are emitted from the GBs and precipitate-matrix interfaces (if present) and the shape of the PDF, $f(\tau_{cr})$, in that range. Let τ_a and τ_b be the lower and upper bounds of τ_{cr}, respectively. Since dislocations are thought to be emitted from GB ledge sources at initial yielding, it seems reasonable to take $\tau_a = Y_0/2$ where Y_0 is the initial yield strength. The upper limit of the PDF corresponds to the upper limit of GB strength. This is estimated as $\tau_b = \mu/30$, which is in agreement with atomistic calculations of the resolved shear stress at which a dislocation is emitted from an equilibrium GB in a pure Cu bicrystal under tension (Spearot et al., 2007).

In the range $\tau_a \le \tau_{cr} \le \tau_b$, the heterogeneous nucleation of dislocations occurs at stress concentrations introduced primarily by the GBs, triple junctions, and precipitates. It is useful to consider the magnitudes of these stress concentrations. Kurzydlowski (1982) used the finite element method to compute relevant stress concentration factors (SCFs) associated with GBs. The results may be summarized as follows: (i) for an elastically-anisotropic tricrystal of Cu (which has a high anisotropy coefficient), the SCF at the triple junction for the most-conspicuous misorientation of grains never exceeds 3; (ii) for a planar GB in an elastically-anisotropic bicrystal of Cu, the SCF never exceeds 3; (iii) for a non-sliding bicrystal GB that contains a step, the maximum SCF is approximately 3; (iv) for a sliding bicrystal GB containing a step, the SCF is inversely related to the step height and can be as high as 400 for small steps. If the precipitates are idealized as rigid spherical inclusions in an isotropic matrix, the SCF in plane strain is 2.5. If GB sliding is neglected, which is a reasonable assumption for micron-scale grains under high pressure, the relevant SCFs fall in the range of 1–3. Therefore, we expect nominal shear stresses down to $\mu/90$ are capable of nucleating dislocations in sites subjected to the most-intense stress concentrations. Since the SCFs vary with GB structure, one might expect that dislocations are emitted from the GBs and

triple junctions over the entire interval $\left[\tau_a, \tau_b\right]$ for a polycrystalline metal. Although the precise shape of the PDF is unknown, it seems reasonable to assume that a relatively simple function could capture the gross (macroscopic) effect of the heterogeneous nucleation of dislocations, e.g.,

$$f\left(\tau_{cr}\right) = \begin{cases} \dfrac{m+1}{\left(\tau_b - \tau_a\right)^{m+1}}\left(\tau_{cr} - \tau_a\right)^m & \tau_a < \tau_{cr} \le \tau_b \\ 0 & \text{otherwise} \end{cases} \tag{2.35}$$

Here, the PDF has been selected as a power law that integrates to unity over its limits. The material constant m determines the shape of the PDF ($m \ge 0$). More sophisticated descriptions of the PDF would presumably lead to descriptions of heterogeneous nucleation that are more accurate. If a linear PDF is assumed ($m = 1$), the nucleation relation proposed by Gupta (1975) is recovered, i.e., $\dot{N}_{het} \propto \left(\tau - \tau_a\right)\dot{\tau}$.

2.4.4. Multiplication

Dislocation line length may be generated by the multiplication of pre-existing dislocation segments. In fact, atomistic simulations have shown that multiplication precedes the intense nucleation of dislocations in shock waves propagating in crystals that contain an initial set of sources (Bringa et al., 2006). We employ the phenomenological relation of Johnston and Gilman (1960) to model dislocation multiplication, i.e.,

$$\dot{N}_{mult} = \delta N_m \overline{v} \tag{2.36}$$

where δ is the multiplication coefficient. The relation given above expresses the idea that the dislocation segment length generated by multiplication is proportional to the area swept out on the slip plane by the glide dislocations.

2.4.5. Annihilation and recovery

The mutual annihilation of mobile dislocation segments may be important if many mobile segments are generated by the shock wave. We have adopted the relation of Roters et al. (2000) to model dislocation annihilation. Here, mobile dislocations of opposite sign on parallel slip planes annihilate when they pass within a certain capture distance. Accordingly, the annihilation rate is written as

$$\dot{N}_{ann} = \alpha_{ann} b N_m^2 \overline{v} \tag{2.37}$$

where α_{ann} is a material constant related to the number of active slip systems and the capture distance.

Dislocation line length may be recovered by rearrangement of the dislocation substructure (e.g., cell wall dislocations) into lower-energy configurations. However, these rearrangements rely heavily on thermally-activated mechanisms such as dislocation climb. Since these processes are inhibited at high rates of deformation, it is assumed that dislocation recovery may be neglected, i.e., $\dot{N}_{rec} = 0$.

2.4.6. Trapping

Mobile dislocation segments may be immobilized (or *trapped*) when they interact with obstacles on the slip plane. As shown in Eqs. (2.23) and (2.24), mobile dislocation segments that are trapped by obstacles are transferred to the immobile dislocation population. A statistical approach to dislocation trapping is adopted in our model. Statistical trapping is based on the notion that some part of a mobile dislocation segment is immobilized once it has swept out a certain area on the glide plane (Kocks, 1966). According to this interpretation, the dislocation trapping rate is written as

$$\dot{N}_{trap} = \frac{N_m \bar{v}}{\Lambda} \tag{2.38}$$

where Λ is the effective mean free path of statistical trapping. The obstacles that trap glide dislocations in pure polycrystalline metals are the dislocation network and grain boundaries. In alloys, the non-shearable precipitates also trap mobile segments. The effective mean free path of statistical trapping may be constructed as the harmonic average of the individual obstacle mean free paths (Estrin, 1996), which, in the most general case, may be written as

$$1/\Lambda = 1/\Lambda_{dis} + 1/\Lambda_{p} + 1/\Lambda_{gb} \tag{2.39}$$

where Λ_{dis}, Λ_{p}, and Λ_{gb} denote the mean free paths of the dislocation network, precipitates, and grain boundaries, respectively. Since an inverse mean free path of trapping is defined as the length of glide dislocation immobilized per area swept out on the glide plane, Eq. (2.39) may be re-written more specifically as

$$\frac{1}{\Lambda} = \alpha_{dis}\sqrt{N} + \frac{\alpha_p \pi d_p}{\left(\lambda_p + d_p\right)^2} + \frac{1}{d} \tag{2.40}$$

where α_{dis} and α_p are material constants, λ_p and d_p are the mean surface-to-surface spacing and size of the precipitates, respectively, and d is the mean grain size. All terms in the substructure evolution equations have now been defined.

2.4.7. Maximum permissible rate of deformation

It is useful to consider the upper limit of the rate of deformation that can be handled in the constitutive model. From the theory of thermally-activated dislocation nucleation, the following relation is obtained when the activation volume v^* does not depend on the applied stress:

$$\tau = \tau_{ath} - \frac{k\theta}{v^*} \ln\left(\frac{\dot{\psi}_0}{\dot{\psi}}\right) \tag{2.41}$$

Here, τ_{ath} is the athermal nucleation stress and $\dot{\psi}_0$ is the upper limiting value of the plastic strain rate. It may be shown that

$$\dot{\psi}_0 = \hat{\dot{\psi}} \exp\left\{\frac{\tau_{ath} v^*}{k\theta}\right\} \tag{2.42}$$

where $\hat{\dot{\psi}}$ is the strain rate that yields $\tau = 0$ in Eq. (2.41). The value of $\hat{\dot{\psi}}$ can be estimated from a plot of τ vs. $\ln\dot{\psi}$, where the thermally-activated nucleation relation is fit to the upturn in experimental data ($\hat{\dot{\psi}} \simeq 10^4$ s^{-1}). Taking $v^* = b^3$, $\tau_{ath} = \mu/15$, and μb^3=5 eV yields $\dot{\psi}_0 \simeq 4\times10^9$ s^{-1}. Since b^3 is a lower bound on the activation volume and since μb^3 may vary by a factor of 2 for the fcc metals of interest, we take the upper limit of the plastic rate of deformation that can be handled in the constitutive model as $\dot{\psi}_0 \simeq 10^{10}$ s^{-1}.

2.5. Conclusions

A dislocation-based constitutive model has been presented for the viscoplastic response of fcc metals and alloys in the shock loading regime. Shock stress amplitudes below the twinning threshold have been addressed, which correspond to rates of deformation in the range of 10^4–10^{10} s^{-1}. Here, the mode of plastic deformation is slip. The model has been developed by enriching classical plasticity relations with terms that address the unique conditions and mechanisms in shock waves. We have focused on a

macroscopic description of dynamic plasticity, although relations have also been provided to formulate the model in terms of crystal plasticity. The main features of the constitutive model are now summarized:

- The kinematics of slip are framed in terms of the generalized Orowan relation (Eq. (2.3)) which provides a dislocation-based description of nucleation- and glide-accommodated plastic deformation.
- The kinetic relation for dislocation glide (Eq. (2.17)) describes a transition from the regime of thermally-assisted obstacle bypassing (at lower shear stresses) to the dynamic regime of continuous dislocation glide (at higher shear stresses). In the dynamic regime, the glide kinetics are governed by phonon drag and the relativistic effect.
- Microstructure-sensitive relations for the glide resistance of polycrystalline fcc metals (Eq. (2.18)) and peak-aged fcc-based alloys (Eq. (2.20)) have been provided. Here, the pressure-dependence of material strength enters through the shear modulus in the Taylor relation.
- The mobile and immobile dislocation densities have been assigned as internal state variables and a logical framework has been constructed for their evolution (Eqs. (2.23) and (2.24)) based on the nucleation, multiplication, annihilation, and trapping of dislocations in shock waves.

The constitutive model respects the asymptotic limits of viscoplastic response, i.e., thermally-activated dislocation glide kinetics at lower stresses and thermally-activated homogeneous dislocation nucleation at higher stresses. Regarding the treatment of alloys, the main strengthening mechanism is due to coherent, fine-scale, non-shearable precipitates. The precipitates impede the motion of dislocations on the slip plane, serve as heterogeneous nucleation sources, and trap (immobilize) dislocations.

The main innovative feature of this work is the treatment of the dislocation substructure in the shock loading regime. In this regard, a new model of heterogeneous dislocation nucleation has been derived, which is based on a statistical distribution of dislocation source strength. Microstructure-sensitive criteria have been developed that address the shock stress ranges where heterogeneous and homogeneous dislocation nucleation are expected in planar shock waves. In this model, we have paid special attention to the distinction of mobile and immobile dislocation density. This distinction is often overlooked or avoided

in constitutive modeling, but is perceived as important under highly dynamic loading condition. Path-dependent evolution equations have been formulated for the mobile and immobile dislocation density components. This allows quantification of (i) the part of the dislocation population responsible for the viscoplastic flow rate and (ii) the glide resistance of (microcrystalline) fcc metals. In the past, equation-of-state relations have been used to quantify dislocation density in the shock wave (for example, the model of Meyers (1978; 2002)). We prefer the use of path-dependent relations because they incorporate history effects and are usually more amenable to the inclusion of mechanistic descriptions of substructure evolution.

In the next chapter, the constitutive model developed here is applied to three fcc metals (Cu, Ni, and Al) and one precipitate-hardening alloy (6061-T6). The constitutive model is then incorporated in simulations of steady plastic waves to compare the model to experiments. In later work, the viscoplastic constitutive model will be utilized in numerical simulations of shock wave propagation in discrete Ni/Al particle mixtures.

CHAPTER 3

APPLICATION OF THE VISCOPLASTIC CONSTITUTIVE MODEL

In this chapter, the viscoplastic constitutive model (presented in Chapter 2) is applied to three fcc pure metals (Cu, Ni, and Al) and one fcc-based precipitate-hardening alloy (6061-T6). To demonstrate the capabilities and performance of the constitutive model, shock waves will be simulated in these materials. This will facilitate comparison of the model to experiments. A few methods are available for evaluating the performance of constitutive models in shock waves. These methods include the simulation of (i) elastic precursor wave decay, (ii) steady plastic waves, (iii) material unloading from the peak stress state, and (iv) Rayleigh-Taylor surface instabilities. One must recognize that pressure, temperature, and the rate of deformation are not constant in the wave front. Therefore, the method of simulation should properly take account of these conditions if meaningful comparisons to experiments are to be made. In this work, the viscoplastic constitutive model is integrated in simulations of steady plastic waves. The model is applied to 6061-T6 Al alloy first because there are more experimental data available to calibrate the model and assess its performance. The model is then applied to the pure fcc metals (Cu, Ni, and Al).

3.1. Steady plastic wave analysis

A framework that treats the propagation of transient elastic-viscoplastic waves has been constructed by Clifton (1970). Here, a Lagrangian formulation is used to address planar shock waves of finite strain in isotropic materials. Molinari and Ravichandran (2004) specialized the framework of Clifton to steady planar shock waves. The plastic waves are steady in the sense that they propagate at constant velocity and the shape of the wave does not change over time. Our analysis of steady plastic waves is based on the framework of Molinari and Ravichandran (2004). However, the current work (i) incorporates different constitutive relations for viscoplastic deformation and (ii) retains the temperature-dependence of the solution. Since the structure of a steady plastic wave depends on the viscoplastic deformation that occurs during the transition, this simulation method serves as a tool that can be used to evaluate the

performance of the constitutive model. The basic elements of the steady plastic wave framework are presented in this section. The reader may consult the aforementioned literature for further details.

Let us consider a planar compressive shock wave that propagates in the $\mathbf{e}_1$-direction of a Lagrangian coordinate system. Since the spatial dependence of the deformation is one-dimensional, the field variables are functions of the Lagrangian coordinate in the $\mathbf{e}_1$-direction and time, i.e., (X,t). The wave introduces a state of uniaxial strain wherein the deformation gradient is composed of elastic and plastic parts, i.e.,

$$\mathbf{F} = \mathbf{F}^e \cdot \mathbf{F}^p \tag{3.1}$$

The principal values of $\mathbf{F}$, $\mathbf{F}^e$, and $\mathbf{F}^p$ are the total stretch ratios, λ_i, the elastic stretch ratios, λ_i^e, and the plastic stretch ratios, λ_i^p, respectively. The rate of plastic stretching in a compressive wave of uniaxial strain is written as

$$\frac{\dot{\lambda}_1^p}{\lambda_1^p} = -\frac{2}{3}\Phi \tag{3.2}$$

where $\dot{\lambda}_1^p / \lambda_1^p$ is the longitudinal component of the plastic rate of deformation tensor, $\mathbf{D}^p$, and Φ is the plastic shearing rate, which is defined by the constitutive law. The temperature in the wave front is expressed as

$$\theta = \theta_0 + \Delta\theta^e + \Delta\theta^p \tag{3.3}$$

where θ_0 is the initial temperature, $\Delta\theta^e$ is the temperature change produced by elastic compression, and $\Delta\theta^p$ is the temperature change produced by plastic work.

In the case of steady plastic waves, the solution in the wave front can be obtained using the method of characteristics. Here, the governing equations are transformed into a coordinate system (ξ) that is attached to the plastic wave front, which moves at the constant Lagrangian shock wave velocity, D (i.e., the wave speed with respect to the material ahead of the front). This transformation is expressed as $\xi = X - Dt$. Applying this transformation to the equations for the conservation of mass and momentum yields the Rayleigh line equations, i.e.,

$$u = u^+ - D\left(\lambda_1 - \lambda_1^+\right) \tag{3.4}$$

$$T_1 = T_1^+ + \rho_a D^2 \left(\lambda_1 - \lambda_1^+ \right) \tag{3.5}$$

Here, ρ_a is the initial mass density, u is the material velocity in the longitudinal direction, T_1 is the longitudinal component of the first Piola-Kirchoff stress tensor, $\mathbf{T}$, and the (+) and (–) superscripts refer to the thermodynamic states ahead of and behind the main plastic wave front, respectively. The elastic constitutive law is written as

$$\mathbf{T} = \rho_a \frac{\partial U}{\partial \mathbf{F}^e} \tag{3.6}$$

where U is the specific internal energy function, which is third-order in the elastic strains. Therefore, third-order elastic constants are utilized in these calculations. When entropic contributions to the stress are negligible (a reasonable assumption for shock waves of moderate amplitude), the stress tensor may be written as $\mathbf{T} = \mathbf{T}(\lambda_1, \lambda_1^p)$ and it has been shown that λ_1 may be written explicitly in terms of λ_1^p (Molinari and Ravichandran, 2004). The shock wave velocity D is defined using an empirical relation that is observed to hold for many metals, i.e.,

$$D = c^+ + s_1 \left(u^- - u^+ \right) \tag{3.7}$$

Here, c^+ is the acoustic wave speed of the material compressed to the (+) state and s_1 is a material constant determined from experiments. The value of c^+ can be obtained by making a pressure correction to the commonly-reported value of acoustic wave speed in the ambient state (c_0). The maximum shear stress is written as

$$\tau = \frac{1}{2}\left(T_1 - \frac{1}{\lambda_1} T_2 \right) \tag{3.8}$$

where T_2 is the transverse component of stress.

Applying the coordinate transformation to (i) the viscoplastic flow rule (Eq. (3.2)), (ii) the conservation of energy, and (iii) the substructure evolution equations yields the following set of differential equations:

$$\frac{d\lambda_1^p}{d\xi} = \frac{2}{3} \frac{\lambda_1^p}{D} \Phi \tag{3.9}$$

$$\frac{d}{d\xi}\left(\Delta\theta^{p}\right)=\frac{4}{3}\frac{\beta\lambda_{1}\tau}{\rho_{a}c_{\eta}D}\Phi \tag{3.10}$$

$$\frac{dN_{m}}{d\xi}=-\frac{\dot{N}_{m}}{D} \tag{3.11}$$

$$\frac{dN_{im}}{d\xi}=-\frac{\dot{N}_{im}}{D} \tag{3.12}$$

Here, c_{η} is the specific heat at constant elastic configuration, and β is the Taylor-Quinney factor (i.e., fraction of plastic work that is converted to heat). Equations (3.11) and (3.12) account for the evolution of material substructure and are necessary because Φ is a path-dependent function that depends on λ_{1}^{p}, $\Delta\theta^{p}$, N_{m}, and N_{im}. Relations for $\dot{N}_{m}$, $\dot{N}_{im}$, and Φ have been defined in Chapter 2.

Equations (3.9)–(3.12) comprise a set of coupled ordinary differential equations that may be solved by integrating from the initial state (+) to the final state (–). The (–) state corresponds to the equilibrium state behind the main plastic wave front, i.e., a point on the Hugoniot. In this analysis, the peak shock stress (i.e., the Hugoniot stress $\sigma_{1}^{-}=-T_{1}^{-}$) is imposed as a loading condition. To define the (+) state, the structure of the shock wave must be considered. For shock stresses below the overdriven threshold stress, Σ, a compressive shock pulse splits into a precursor wave and the main plastic wave, as illustrated in Figure 3.1(a). This is the weak shock loading regime. The elastic precursor compresses the material from the ambient state (a) to the Hugoniot elastic limit (HEL), which is indicated as state (b) in the figure. In many cases, experimentally-measured wave profiles exhibit a plastic precursor wave, which is depicted as the solid line connecting states (b) and (c) (Wallace, 1980a). The plastic precursor contains any material hardening that occurs prior to the arrival of the main plastic wave. If there is no hardening in the precursor wave, the dashed line in the figure is followed. The main plastic wave compresses the material from state (c) to the final equilibrium state on the Hugoniot (e). Thus, in the case of weak shock waves ($\sigma_{1}^{-}<\Sigma$), the (+) state is taken as state (c). If the shock stress exceeds the overdriven threshold, the main plastic wave travels faster than the elastic precursor wave. In this case, the jump across the wave front corresponds to a transition from state (a) to state (e), as shown in Figure 3.1(b). Thus, in the case of overdriven shock waves ($\sigma_{1}^{-}>\Sigma$), the (+) state corresponds to state (a). With the (+) and (–) states now defined, the governing

differential equations are solved using a fourth-order Runge-Kutta method. The solution that is obtained allows all other field variables in the shock front to be computed.

An artificial viscosity is *not* used in these simulations of steady plastic waves. This is an important consideration because artificial viscous stresses would (i) obscure the actual shear responses that are the focus of our study, and (ii) introduce an artificial dependence of the results on the numerical grid. However, there is one somewhat artificial constraint that is introduced by the steady wave framework. Since equilibrium is enforced at the trailing edge of the shock front, plastic deformation comes to an end at the (–) state. In actuality, some plastic deformation likely continues in the shocked state (i.e., behind the shock front). This is supported by experiments that show dislocation cell structures in polycrystalline Ni are more fully-developed for shock pulse durations of 1 μs versus 0.5 μs (Murr and Kuhlmann-Wilsdorf, 1978).

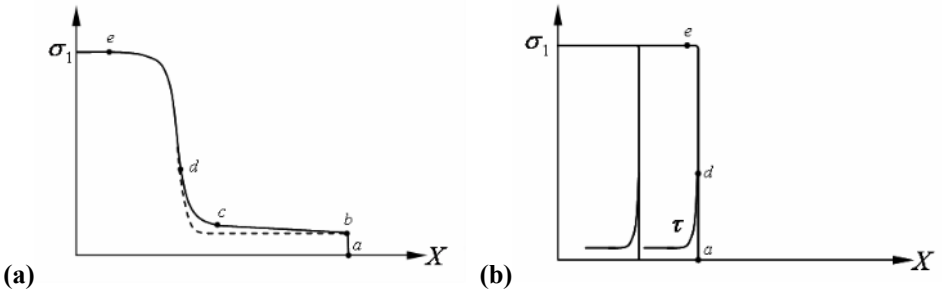

Figure 3.1: The structures of (a) weak and (b) overdriven shock waves.

3.2. Application to 6061-T6 Al alloy

The constitutive relations are now applied to 6061-T6 Al alloy. We have chosen to simulate the response of this alloy because there is a fair amount of experimental data available for the shock loading regime. The material properties and model parameters that are utilized in the constitutive relations and the steady plastic wave simulations are provided in the sections that follow.

3.2.1. Alloy composition and microstructure

The 6061 alloy is a polycrystalline Al-Mg-Si age-hardening alloy. The initial microstructure of 6061 alloy (i.e., the grain size, precipitate distribution, solute concentrations, and dislocation structure) depends on the prior working and heat-treatment. To demonstrate the constitutive model, a composition and set of microstructure attributes are selected that is typical of 6061-T6 in the peak-aged condition. The alloy composition is provided in Table 3.1. In the peak-aged condition, the fine-scale β'' (MgSi) precipitates are the primary strengthening precipitates (Polmear, 2006). The β'' precipitates are coherent needles or coherent cylindrical rods with typical dimensions of $4 \times 4 \times 35$ nm^3 according to measurements compiled by Zander and Sandstrom (2008).

It is assumed that the fine-scale β'' precipitates are wholly responsible for the precipitate strengthening of the alloy. Strengthening due to coarse-scale particles is neglected because their spacing is considerably larger. Here, the fine-scale β'' precipitates are idealized as spheres. This simplification seems admissible because prior analysis of the strengthening of rod-shaped β'' precipitates yielded results that are quite similar to the strengthening of equivalent spheres (Myhr et al., 2001). Finally, it is assumed that the fine-scale precipitates are not sheared by glide dislocations. This assumption is justified because the precipitates are of critical size in the peak-aged condition. Additionally, high-resolution TEM images of 6061-T6 specimens deformed to 2% plastic strain reveal many loops and bowed-out segments at the length scale of the fine precipitates (Douin et al., 2001), which indicates the Orowan bowing mechanism is operative.

Table 3.1: 6061-T6 Al alloy composition

Element	wt.%
Mg	1.10
Si	0.68
Fe	0.49
Cu	0.38
Cr	0.16
Mn	–
Zn	–
Ti	–
Al	bal.

Table 3.2: Grain size and MgSi precipitate distribution for 6061-T6

d	μm	40
λ_p	μm	70×10^{-3}
d_p	μm	10×10^{-3}

The shear stress required to overcome the fine-scale precipitates (at 0 K) by Orowan looping may be written as

$$\tau_{p,0} = \beta_p \left(\frac{\mu_0 b}{\lambda_p} \right) \tag{3.13}$$

where λ_p is the mean (surface-to-surface) spacing of precipitates and β_p is a coefficient on the order of unity. The value of β_p depends on factors such as the precipitate size, the dislocation line tension approximation, and the interaction of dislocation segments surrounding a precipitate. We take $\beta_p \simeq 0.84$ as a representative value (Hull and Bacon, 2001). In the peak-aged condition of a 6005 Al alloy, Myhr (2001) measured the mean volume and number density of the fine-scale β'' precipitates using micrographic analysis. The mean precipitate radius was $\bar{r}$ ~5 nm (for equivalent spheres) and the precipitate volume fraction was f_p ~0.0105. Using the Friedel relation, the mean precipitate spacing is calculated as $\bar{\lambda}$ ~80 nm, which is in agreement with the TEM images. Correcting for precipitate size, $\lambda_p = \bar{\lambda} - 2\bar{r}$, where the mean precipitate size is $d_p = 2\bar{r}$ (values are provided in Table 3.2). We select a grain size of 40 μm as being representative of an alloy with micron-scale grains. Different microstructure parameters can be selected to simulate the response of other alloys, provided the model assumptions are respected.

Solid solution strengthening has been neglected in the constitutive model. We now demonstrate that solid solution strengthening in 6061-T6 is small compared to the other strengthening mechanisms. The solid solution strengthening term may be written as

$$\tau_{sol} = \sum k_i c_i \tag{3.14}$$

where c_i are the concentrations of the alloying elements and k_i are material constants. This relation has been observed to hold for age-hardening Al alloys with compositions similar to 6061 alloy (Zhu and Starink, 2008). According to the composition provided in Table 3.1, the maximum solid solution strengthening contribution is about 9.6 MPa (assuming there is no precipitation of Mg and Si out of solution). In the peak-aged condition, however, much of the Mg and Si have precipitated out to form the fine-scale precipitates, which provide a strengthening contribution that is at least ten times as strong as the maximum solid solution strengthening contribution. Therefore, the solid solution strengthening of this alloy may be neglected.

3.2.2. Material properties

The relevant material properties of 6061-T6 are given in Table 3.3. The shear and longitudinal wave speeds in the ambient state are written as c_{sa} and c_{La}, respectively. There are two material properties that require attention: the shear modulus and the damping coefficient. The shear modulus is written in terms of a first-order expansion in pressure and temperature about the ambient state, which is identical to the relation of Steinberg et al. (1980), i.e.,

$$\mu = \mu_a \left[1 + \frac{1}{\mu_a}\frac{\partial \mu}{\partial p}\left(p - p_a\right)\eta^{-1/3} + \frac{1}{\mu_a}\frac{\partial \mu}{\partial \theta}\left(\theta - \theta_a\right) \right] \tag{3.15}$$

where $\mu_a = \rho_a c_{sa}^2$ is the shear modulus in the ambient state $\left(p_a, \theta_a\right) = \left(0,\ 300\ \text{K}\right)$ and $\eta = \rho/\rho_a$ is the compression. The volumetric correction to the pressure-dependent term in the expansion reflects the asymptotic behavior of the shear modulus at ultra-high pressure (in accordance with Thomas-Fermi theory).

The dominant mechanism of dislocation for θ>300 K is phonon damping (Kocks et al., 1975; Nadgornyi, 1988). The temperature dependence of the phonon damping coefficient is incorporated using the expression derived by Leibfried (1950), i.e.,

$$B_0 = \frac{3k\theta z}{20 c_s b^2} \tag{3.16}$$

where z is the number of atoms per unit cell and c_s is the current shear wave speed. The damping coefficient in the ambient state, $B_0\left(p_a, \theta_a\right)$, is provided in Table 3.3. For stronger shocks the model of

Wolfer (1999) would be useful since a 10-fold increase in the damping coefficient of Al is expected for stress amplitude of ~100 GPa.

It is assumed that all plastic work in the shock wave is converted to heat. Therefore, the Taylor-Quinney factor β is taken as unity in the steady plastic wave analysis. Additionally, the specific heat at constant elastic configuration c_η is taken as the specific heat at constant volume c_V.

Table 3.3: Material properties for 6061-T6

		6061-T6
ρ_a	g cm^{-3}	2.703
c_{sa}	mm μs^{-1}	3.197
c_{La}	mm μs^{-1}	6.368
b	mm	2.86×10^{-7}
μ_a	GPa	27.6
$1/\mu_a\,(\partial\mu/\partial p)$	GPa^{-1}	65.0×10^{-3}
$1/\mu_a\,(\partial\mu/\partial\theta)$	K^{-1}	-0.62×10^{-3}
$B_0\,(p_a,\theta_a)$	GPa μs	1.0×10^{-8}
ν_D	μs^{-1}	8×10^{6}
Σ	GPa	13
c_η	J mg^{-1} K^{-1}	0.880×10^{-3}
β		1
κ	J (mm μs K)$^{-1}$	167×10^{-9}
θ_m	K	926
$\partial\theta_m/\partial p$	K GPa^{-1}	41.2
ΔH_{fus}	J mg^{-1}	390×10^{-3}

3.2.3. Thermally-activated dislocation glide

In the model of thermally-activated dislocation depinning and glide, the free enthalpy of activation is written using the phenomenological form suggested by Kocks et al. (1975), i.e.,

$$\Delta G_{dep} = g_{dep,0}\mu b^3\left[1-\left(\tau/\tau_0\right)^p\right]^q \tag{3.17}$$

Here, $g_{dep,0}$ is the normalized free enthalpy required to overcome the dislocation forest when the applied stress is equal to zero, and p and q are parameters that determine the statistically-averaged shape of the

obstacle resistance profile. The relevant thermal activation parameters ($g_{dep,0}$, p, and q) for Al have been obtained by Kocks and Mecking (2003) based on review of experimental work cited therein. The free enthalpy of activation may also be written strictly in terms of the short-range stress components, i.e., $\Delta G_{dep} = \Delta G_{dep}(\tau^* / \tau_0^*)$. However, the activation parameters in this relation have not been determined experimentally. It is assumed that $\nu_G \overline{L} = \chi_{dep} \nu_D b$ where χ_{dep} is a constant of proportionality; this assumption is fairly standard in models of thermally-activated dislocation glide (see, for example, the work of Nes (1998)). The value of χ_{dep} could depend on material structure, but it is taken as a constant for simplicity. The parameters for the model of thermally-activated dislocation depinning are given in Table 3.4.

3.2.4. Threshold stress parameters

Measurements and theory show the value of the dislocation interaction coefficient, α_0, should be about 1/2 (within a factor of 2) for single-crystalline and polycrystalline fcc metals (Mecking and Kocks, 1981; Kuhlmann-Wilsdorf, 1999). The value of the parameter β_0, which quantifies the long-range glide resistance provided by the dislocation network, has been estimated by Basinski (1959) in experiments performed on single-crystalline and polycrystalline Al. The values of α_0 and β_0 used in the model are provided in Table 3.4.

Table 3.4: Model parameters for 6061-T6

			6061-T6
Thermal-depinning			
$g_{dep,0}$			0.65
p			1/2
q			2
χ_{dep}	†		0.05
Threshold stresses			
α_0			0.5
β_0			0.7
Substructure evolution			
Y_{HEL}		GPa	0.212
N^+		mm^{-2}	2×10^8
f^+	†		0.006
α_{hom}			0
α_{het}	†	mm^{-2}	7.4×10^7
m			1
δ	†	mm^{-1}	350
α_{ann}			0.5
α_{dis}	†		0.015
α_p	†		0.020
Equation of state			
c_0		mm μs^{-1}	5.35
s_1			1.34
Γ_0			2.0

† Model parameters that have been adjusted to fit shock profile data

3.2.5. Evaluation of dislocation nucleation criteria

The dislocation nucleation criteria presented in Chapter 2 are now analyzed to determine the stress ranges where heterogeneous and homogeneous dislocation nucleation are expected for 6061-T6. Recall that the criteria for homogeneous dislocation nucleation is $\sigma_1^- \in (\sigma_{Min}, \sigma_{Twin})$ and $w/\lambda < 1$. The situation for 6061-T6 is illustrated graphically in Figure 3.2. Gray and Follansbee (1988) observed twins in 6061-T6 shocked to 13 GPa. This stress level is taken as an estimate of the twinning threshold of 6061-T6. The twinning threshold of pure Al (which has higher stacking fault energy) is also plotted for reference. The

material length scales of interest are the spacing of fine-scale precipitates, λ_p, and the spacing of dislocations in the unshocked material, $\lambda_0 = N_0^{-1/2}$. It can be seen that $w/\lambda_p > 1$ for shock stresses all the way up to the twinning threshold of pure Al. Therefore, homogeneous dislocation nucleation is not expected in 6061-T6 for shock stresses up to at least 30 GPa. In the weak shock regime ($\sigma_1^- < \Sigma$), plastic deformation should be accommodated by the glide of dislocations in the shock front, including those segments nucleated heterogeneously from precipitates and grain boundaries. In the overdriven shock regime ($\sigma_1^- > \Sigma$), twinning is also expected.

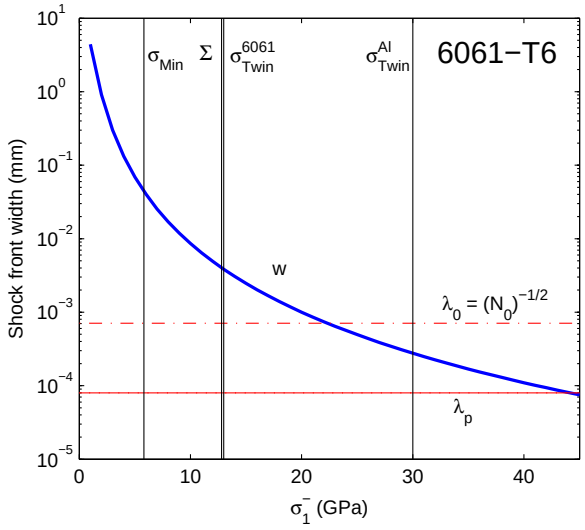

Figure 3.2: The criteria for homogeneous dislocation in 6061-T6.

3.2.6. Substructure parameters

Material constants related to substructure evolution are provided in Table 3.4. In this section, quantities evaluated at the HEL and the (+) state are discussed. This is followed by discussion of the parameters utilized in the substructure evolution equations. The wave profiles in 6061-T6 that have been obtained by Johnson and Barker (1969) indicate the yield stress at the HEL is $Y_{HEL} = 2\tau_{HEL} \simeq 0.212$ GPa. This is in agreement with the measurements of Huang and Asay (2005) in which Y_{HEL} fell in the range of

0.130–0.320 GPa for grain sizes of 5–50 μm and the measured value cited by Steinberg et al. (1980), i.e., 0.290 GPa. The experimental wave profiles display material hardening in the plastic precursor waves. The conditions at the (+) state have been extracted from the experimental profiles using the analysis of Wallace (1980a). Here, $\tau^+ \simeq 0.155$ GPa and $u^+ \simeq 0.042$ mm/μs. Additionally, we have calculated the effective plastic strain rate, $\dot{\psi}^+ \simeq 8\times10^3$ s^{-1}, and the effective plastic strain, $\psi^+ \simeq 6\times10^{-4}$. The dependence of these quantities on the peak shock stress is weak enough for the aforementioned values to be representative of all wave profiles in the range of experimental shock stresses (2.1–9.0 GPa). The dislocation density at the HEL can be estimated using the relation $\tau_{HEL} = (\tau_p + \tau_{dis})_{HEL}$, which yields $N_{HEL} \simeq 8\times10^6$ mm^{-2}. This is a reasonable value for the initial dislocation density of an age-hardening alloy that has been cold-worked and annealed. The dislocation density of the material at the (+) state can be estimated using the constitutive model. The assumption that viscoplastic flow is controlled by thermally-activated dislocation glide prior to the arrival of the main plastic wave yields $N^+ \simeq 2\times10^8$ mm^{-2} (a reasonable value considering the work-hardening of the material in the plastic precursor wave). The mobile dislocation density at the (+) state is written as a small fraction of the total dislocation density, i.e., $N_m^+ = f^+ N^+$.

As discussed earlier, homogeneous dislocation nucleation is not expected in 6061-T6 for shock stresses up to 30 GPa. Therefore, the homogeneous nucleation coefficient, α_{hom}, is set to zero. In the weak shock regime, heterogeneous dislocation nucleation prevails. The adjustable parameter in the heterogeneous nucleation model depends on the number density of sites that emit dislocations and the mean length of dislocation segment that is emitted, i.e., $\alpha_{het} = (\mathcal{N}/V)\bar{\ell}$. It may be estimated based on the size and spacing of the fine scale precipitates. Taking $(\mathcal{N}/V) = (\lambda_p + d_p)^{-3}$ and $\bar{\ell} = \pi d_p$ yields $\alpha_{het} \simeq 6\times10^7$ mm^{-2}, which is very close to the (fitted) value used in the model. The PDF exponent, m, is taken as unity for simplicity.

The multiplication coefficient δ is related to the efficiency of multiplication mechanisms such as double-cross-slip and Frank-Read mills. Johnson and Barker (1969) found that δ =350 mm^{-1} provided the best fit to experimental data in their model of 6061-T6. This value is adopted in our model. The annihilation coefficient α_{ann} can be estimated on a physical basis according to the model of Roters et al.

(2000). It can be shown that this parameter should be on the order of unity for an fcc polycrystal. The dislocation trapping coefficient α_{dis} is an adjustable parameter that is on the order of 0.01 (Kocks and Mecking, 2003) since a unit length of glide dislocation interacts with hundreds of dislocations before it is immobilized. The precipitate trapping coefficient α_p is a parameter that quantifies the deviation of the actual precipitate trapping behavior from idealized Orowan looping around the precipitates ($0 \le \alpha_p \le 1$). Since parts of the glide dislocations may avoid the precipitates (e.g., by cross slip) and since the cross-section of the precipitate that intersects the glide plane will, in general, be less than the maximum diameter, an adjustable parameter seems justified.

3.2.7. Equation of state

The parameters of the EOS for 6061-T6 are provided in Table 3.4. These parameters have been determined from shock compression experiments (Marsh, 1980). A small correction has been applied to Eq. (3.7) to reduce the shock wave speed (by ~1%) for low shock stresses. This correction brings the shock wave speed into agreement with the measurements of Johnson and Barker (1969) for shock stresses below 4 GPa.

3.2.8. Discussion of adjustable model parameters

Although all model parameters are truly adjustable from material to material, we wish to make a distinction between those model parameters that are "set" and those that are "adjusted" to fit specific data. The values of the set parameters have been selected based on experimental data and model assumptions pertaining to 6061-T6; these values have *not* been calibrated to fit the model to measured shock wave profiles, which are presented later for model validation. On the other hand, the values of the adjustable model parameters have been selected to fit the model to experimentally-measured shock wave profiles. In Table 3.4, a dagger symbol has been placed next to parameters that have been adjusted. Since each adjustable parameter has a physical interpretation, it is possible to estimate an acceptable range of values for each parameter. The values of all adjustable parameters (six in total for 6061-T6) fall within the acceptable ranges. Considering the complexity of deformation in the shock loading regime and the rich,

microstructure-sensitive description that is provided by the constitutive model, we believe the use of six adjustable parameters for 6061-T6 is acceptable.

3.3. Results for 6061-T6 Al alloy

Results from simulations of steady plastic waves in 6061-T6 are presented in the sections that follow. The stress amplitudes achieved in the experiments of Johnson and Barker (1969) have been simulated. Additional model calculations will be presented for stress amplitudes up to 21 GPa.

3.3.1. Preliminary results

In this section, a few basic results are given to verify the jump conditions and illustrate the simulation procedure. In Figure 3.3, the Hugoniot curve that is computed for 6061-T6 using the steady wave analysis is compared to experimental measurements. It can be seen that the Hugoniot is accurately reproduced. This is expected because the EOS parameters were obtained from these experimental data. This result simply verifies that the jump conditions in the steady wave simulations are calculated with sufficient accuracy.

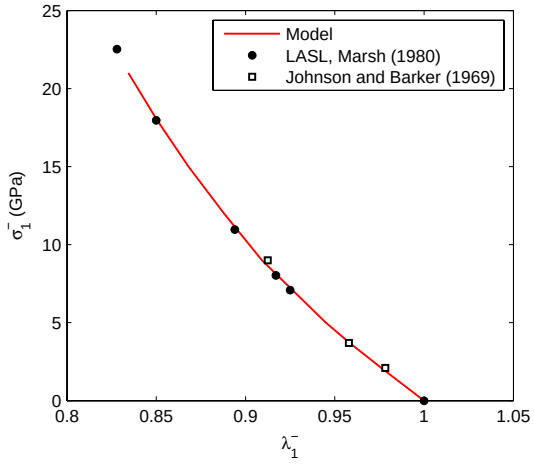

Figure 3.3: The Hugoniot curve that is computed for 6061-T6 is compared to the shock compression measurements.

Fixed-point time histories of the stretch ratios λ_1 and λ_1^p are shown in Figure 3.4(a) for the shock stress σ_1^-=3.7 GPa. The (+) state and the plastic transition leading to the Hugoniot (–) state are indicated. As mentioned earlier, the structure of λ_1^p is governed by the viscoplastic constitutive law. In Figure 3.4(b), the variation of the longitudinal stress component, σ_1, the transverse stress components, $\sigma_2 = \sigma_3$, the magnitude of the (maximum) shear stress, τ, and the pressure, p, are plotted for a 9.0 GPa shock as the material is compressed from λ_1^+ to λ_1^-. Here, the Cauchy stress components are taken as positive in compression, i.e., $\sigma_1 = -T_1$ and $\sigma_2 = -T_2 / \lambda_1$. It can be seen that σ_1 follows the Rayleigh line and that the maximum shear stress experienced by the material occurs near the center of the wave front.

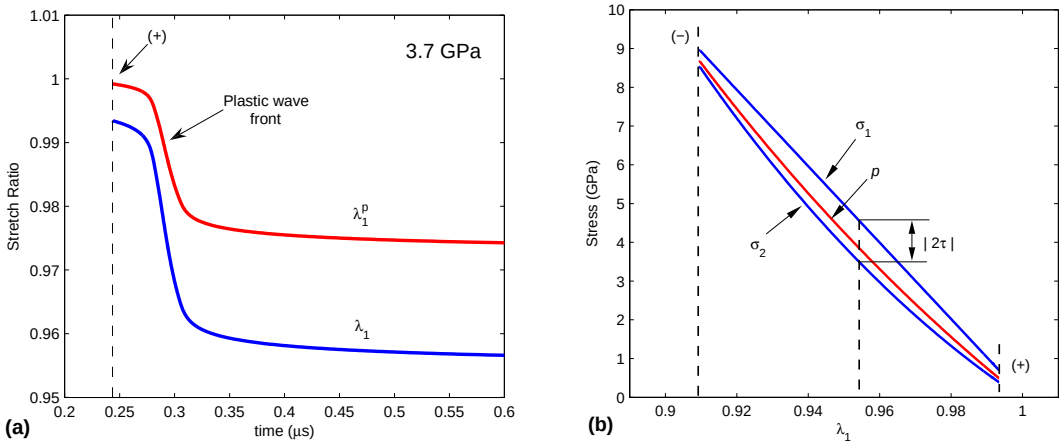

Figure 3.4: (a) Time histories of the stretch ratios for a 3.7 GPa shock in 6061-T6; (b) the pressure, stress components, and maximum shear stress in 6061-T6 loaded from the (+) state to the equilibrium state on the Hugoniot (–) for a 9.0 GPa shock.

3.3.2. Material velocity profiles

Steady plastic waves in 6061-T6 have been obtained in plate impact experiments performed by Johnson and Barker (1969). Here, free-surface velocity profiles were measured for peak stress amplitudes of 2.1, 3.7, and 9.0 GPa. Experimental records of the material velocity $u(t)$ are provided in Figure 3.5. Model calculations of the material velocity are also plotted in Figure 3.5. The profiles do not extend back to the first data points of the experimental records because the initial conditions in the steady plastic wave

calculations are for the (+) state instead of the HEL. This is necessary because the plastic precursor waves are unsteady. The shock front structures that are computed using the model agree with experiments for all stress amplitudes considered. For example, the rather gradual plastic transition of the 2.1 GPa shock is computed with relatively minor overshoot in material velocity at the terminal state. The same can be said for the stronger shock waves, although the shock structure could not be fully resolved in the 9.0 GPa shock wave measurements because the rise time was too short. All three profiles have been plotted on a common time scale in Figure 3.5(d). It can be seen that the model is successful in reproducing shock front structures for rise times ranging from approximately 5–500 ns, and Hugoniot material velocities u^- ranging from 0.1–0.6 mm/μs. Since the structure of the shock front is sensitive to the viscoplastic deformation that occurs in the front, these results provide support for the constitutive relations.

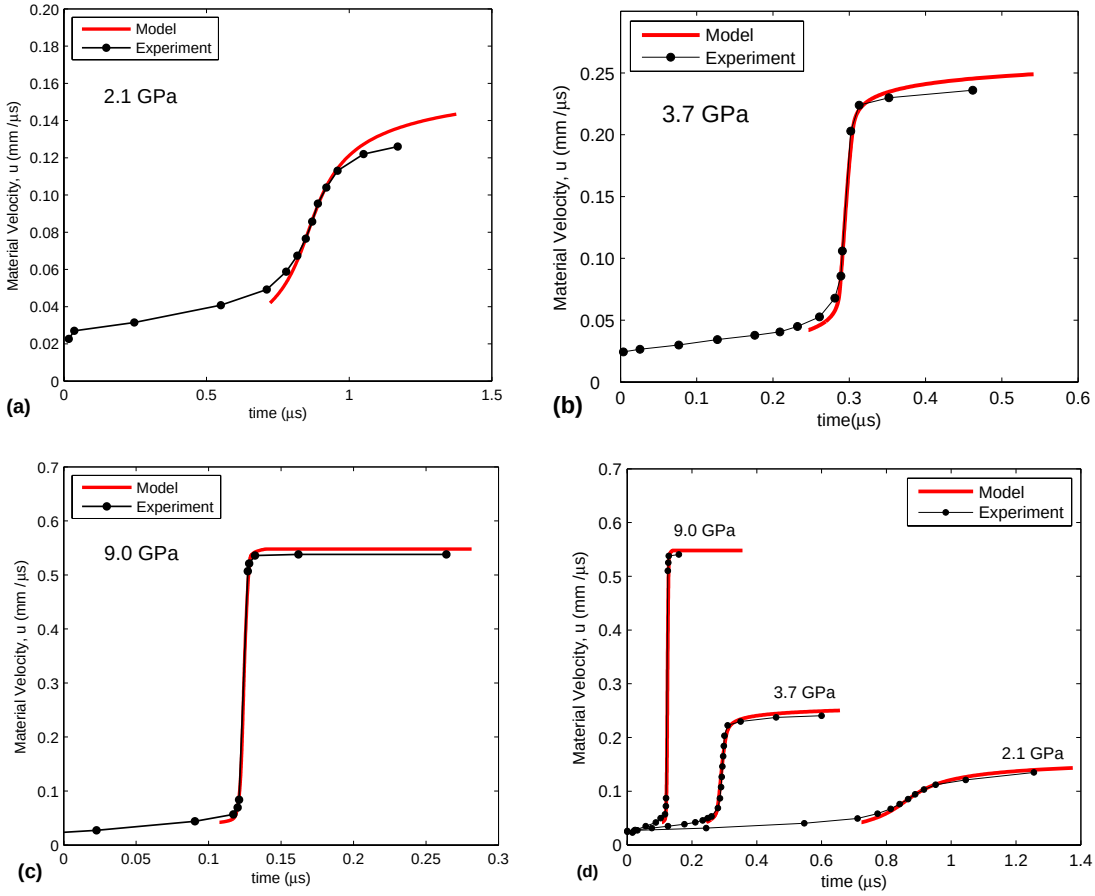

Figure 3.5: Fixed-point material velocity profiles that are computed using the steady wave analysis are compared to experimental measurements for shock stress amplitudes of (a) 2.1 GPa, (b) 3.7 GPa, and (c) 9.0 GPa; (d) material velocity profiles plotted on common axes. Lines that connect experimental data points are plotted to guide the eye.

3.3.3. Viscoplastic flow in the shock front

In Figure 3.6, model computations of τ/τ_0 are plotted versus the effective plastic strain, ψ, which is the time-integrated value of $\dot{\psi} = \sqrt{(2/3)\mathbf{D}^p : \mathbf{D}^p}$. The value of τ/τ_0 determines whether or not mobile dislocations are in continuous glide. When τ/τ_0 is less than unity, the mobile dislocations wait at obstacles to be activated by fluctuations in thermal energy (i.e., $\Delta G_{dep} > 0$). When τ/τ_0 exceeds unity, the mobile dislocations are not held up at short-range obstacles (i.e., $\Delta G_{dep} = 0$). In the 2.1 GPa shock, viscoplastic flow in the shock front is controlled by thermally-activated dislocation glide. In the 9.0 GPa shock, dislocations are in continuous glide for most of the profile. It can be seen that the 3.7 GPa shock is an intermediate case.

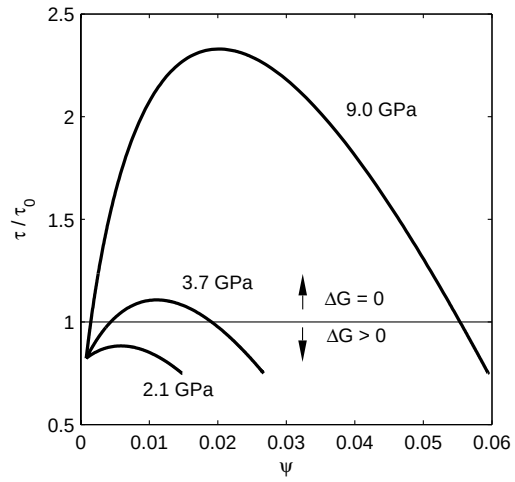

Figure 3.6: The ratio of shear stress to the mechanical threshold stress is plotted as a function of the effective plastic strain through the shock front for the 2.1 GPa, 3.7 GPa, and 9.0 GPa shock waves. The horizontal line separates the regimes of thermally-activated dislocation depinning and continuous glide.

In Figure 3.7, model calculations of the longitudinal component of the plastic rate of deformation, $D_1^p = \dot{\psi}$, are plotted versus the effective plastic strain ψ in the shock front. The model is compared to the D_1^p profiles that have been obtained by Wallace (1980a) from the measured free-surface velocity profiles of Johnson and Barker (1969). The calculations that have been performed by Wallace (1980b; 1980a) are

essentially transformations of the experimental measurements using a thermodynamic framework. Constitutive relations for the plastic deformation of the material are *not* utilized in the thermodynamic framework; therefore, the results obtained by Wallace may be viewed as indirect experimental data. The plateau in the data is an estimate of the maximum rate of plastic deformation in the shock front. The error bar (which extends over the entire plateau region of the profile) represents the uncertainty that stems from the scatter in experimental records. The ψ -axis in each plot begins at the (+) state, i.e., the starting point of the main plastic wave. In all cases, model calculations are compatible with the experimental data. All plastic rate of deformation peaks fall within the uncertainty bars and the profile shapes are in fairly good agreement. This is encouraging because accurate calculation of the viscoplastic flow profiles in the shock front serve as a fairly rigorous test of the constitutive model. It is noted that the shape of the D_1^p profile evolves in proportion to the quantity $N_m \overline{v}$, which indicates this quantity is reproduced fairly well by the model for the shock stresses considered. Finally, we wish to point out that the terminal value of ψ on the Hugoniot (i.e., ψ^-) is not imposed in the model calculations. Rather, ψ^- is a natural outcome of the integration process in the steady wave calculation. In Figure 3.7 it can be seen that the computed values of ψ^- (indicated by an open symbol) agree with the experimental data in all cases.

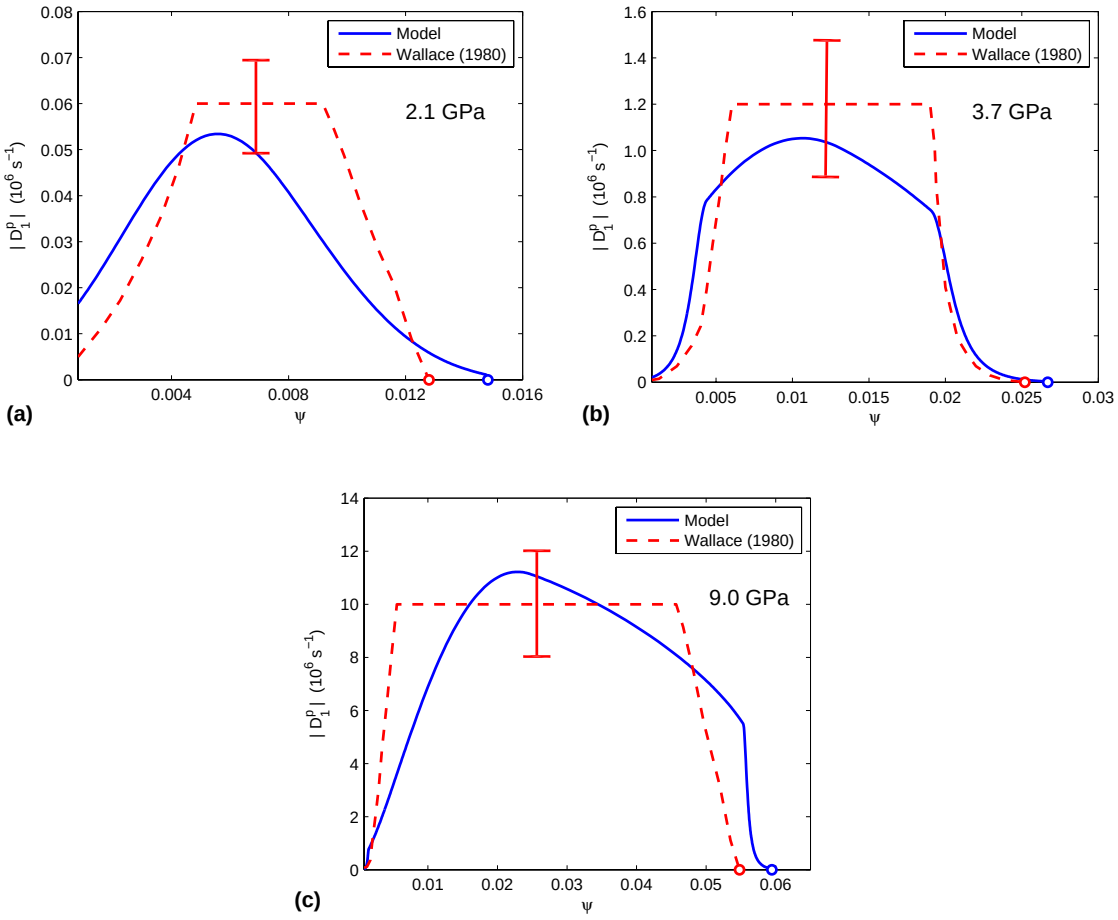

Figure 3.7: Profiles of the plastic rate of deformation that are computed using the model are compared to experimental data for the (a) 2.1 GPa, (b) 3.7 GPa, and (c) 9.0 GPa shocks. The uncertainty bars extend over the entire plateau of the (indirectly) measured profiles.

Experiments have shown that a number of metals exhibit a one-fourth power-law relation between the maximum (nominal) strain rate in the shock front, $\dot{\varepsilon}$, and the peak shock stress, i.e., $\sigma^{-} \propto \dot{\varepsilon}^{1/4}$ (Swegle and Grady, 1985). In fact, it is thought that this scaling law is universal. In Figure 3.8, we have constructed a Swegle-Grady plot for 6061-T6 using results generated by the model. The quantity $\dot{\varepsilon}$ is the maximum value of $\left|\dot{\lambda}_1\right|$ in a steady plastic wave. The best-fit line to the model calculations has a slope of 0.30 and a correlation coefficient r^2=0.98 for shock stresses in the range of 2-20 GPa and $\dot{\varepsilon}$ in the range of 10^4–10^8 s^{-1}. This agrees reasonably well with the expected slope of 1/4.

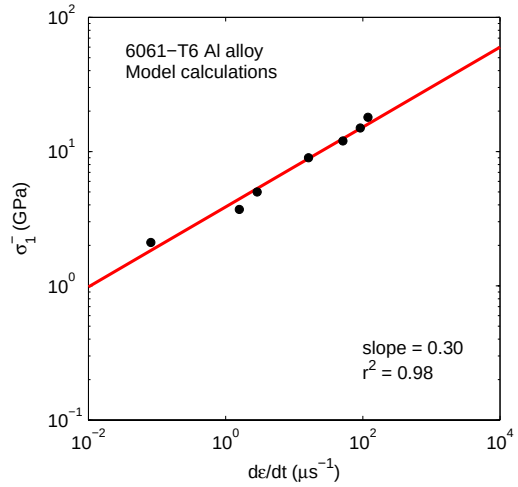

Figure 3.8: The Swegle-Grady plot that is obtained from the model for 6061-T6.

3.3.4. Temperature calculations

The temperature increase through the shock front ($\Delta\theta$) is plotted in Figure 3.9(a) for stress amplitudes of 2.1, 3.7, and 9.0 GPa. In all three cases the temperature increase due to elastic compression ($\Delta\theta^e$) is larger than that due to plastic work ($\Delta\theta^p$). Model calculations of the Hugoniot temperature are plotted versus the Hugoniot stress in Figure 3.9(b). The model calculations are in agreement with the data points calculated by Wallace (1980a). It can be seen that a 10 GPa shock increases the temperature on the Hugoniot by ~100 K. For this increase in temperature, the damping coefficient is increased by about 30%.

Although the shear modulus softens as the temperature is increased, the concurrent rise in pressure leads to an overall 60% increase of the shear modulus.

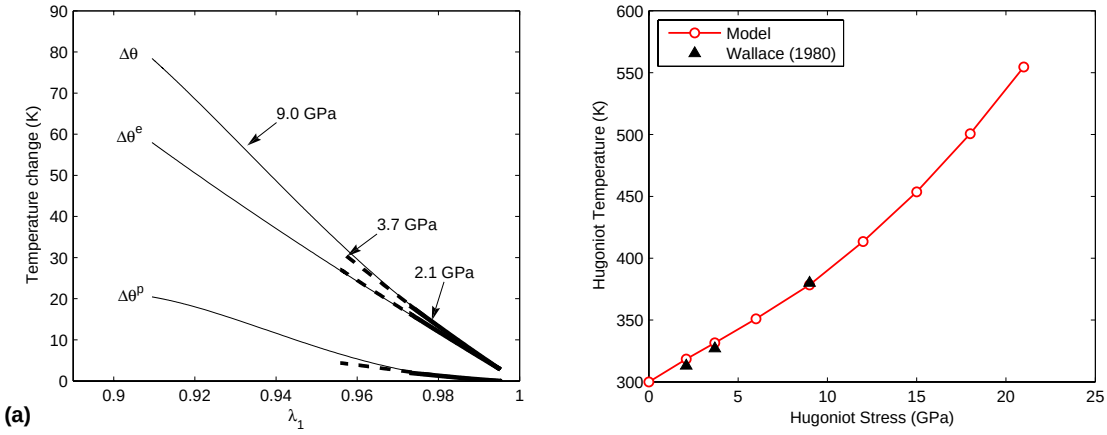

Figure 3.9: (a) The computed temperature increments due to elastic and plastic work are plotted through the plastic wave front for shock stress amplitudes of 2.1, 3.7, and 9.0 GPa; (b) the computed temperature on the Hugoniot compared to experimental data.

3.3.5. Substructure evolution

The substructure evolution rates that are computed using the constitutive model are plotted in Figure 3.10. To our knowledge, this represents the first attempt to quantify the distinct mechanisms that drive rate- and path-dependent evolution of the mobile and immobile dislocation densities in shock waves. The vertical dashed line in each figure indicates the (+) state. For a 2.1 GPa shock, the (heterogeneous) nucleation and annihilation rates are negligibly small, while the multiplication and trapping rates are modest. For a 3.7 GPa shock, the nucleation rate is low but discernible. For a 9.0 GPa shock, there is a considerable increase in the heterogeneous nucleation rate (it should be noted that the vertical axes are scaled by roughly a factor of ten as the shock stress is increased from 2.1 to 3.7 to 9.0 GPa). The multiplication and trapping rates are also increased for the 9.0 GPa shock wave. Since the shear stress in the shock front reaches 0.5–0.6 GPa in this case, it is envisioned that dislocations are emitted from multiple source types (i.e., the GBs, triple junctions, and precipitate-matrix interfaces). For a 12 GPa shock, the heterogeneous nucleation rate now surpasses the multiplication rate at the leading edge of the shock front.

In Figure 3.10, it can be seen that dislocation multiplication and trapping control substructure evolution until shear stresses are high enough to drive the heterogeneous nucleation of dislocations. The multiplication and trapping rates scale with Φ ; hence the similarity of these profiles to the D_1^p profiles. It can be seen that the effects of multiplication and trapping are basically offsetting for shock stresses up to about 9 GPa. This yields essentially constant mobile dislocation density for mild deformations, which is a common assumption at lower deformation rates. For all stress amplitudes, the trapping rate is higher than the multiplication rate. It can also be seen that the effect of annihilation remains small for stress amplitudes up to 12 GPa. Therefore, in this deformation regime the model could be simplified by omitting the annihilation term in the substructure evolution equations.

Model calculations of the dislocation density on the Hugoniot are plotted versus the peak shock stress of the simulated waves in Figure 3.11. Measurements of the residual dislocation density from shock-recovery experiments performed on polycrystalline Ni (Murr and Kuhlmann-Wilsdorf, 1978) and polycrystalline Cu (Murr, 1978; Murr, 1981) are also plotted for comparison. The purpose of this comparison is to show that the dislocation density computed by the model is the same order of magnitude as the dislocation density that has been measured for other fcc polycrystalline metals (since we are not aware of any such data for Al or Al alloys).

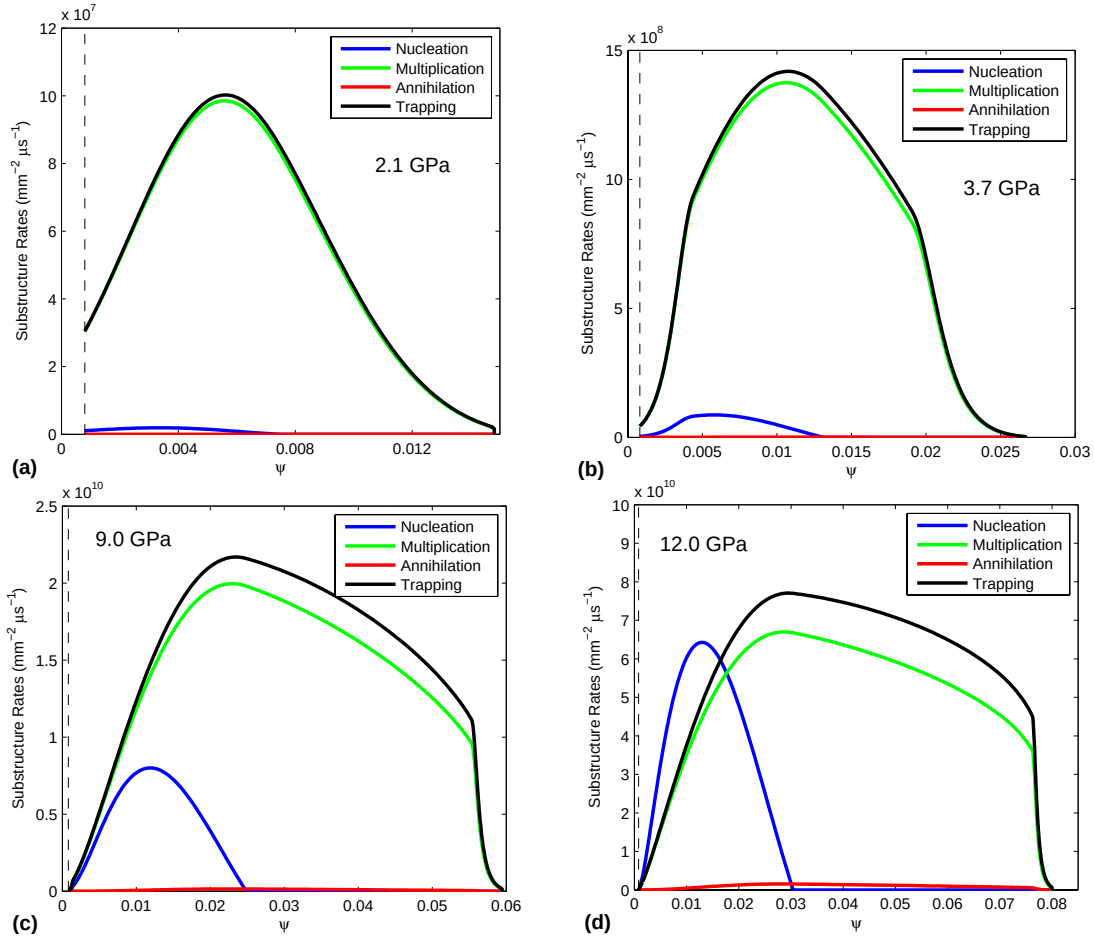

Figure 3.10: Substructure evolution rates computed in the model are plotted for stress amplitudes of (a) 2.1 GPa, (b) 3.7 GPa, (c) 9.0 GPa, and (d) 12.0 GPa.

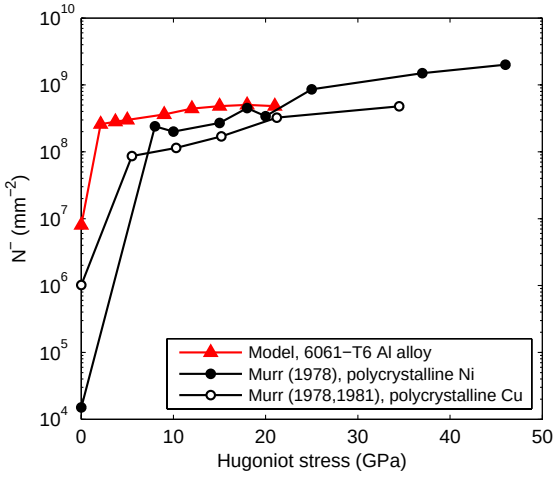

Figure 3.11: Model calculations of dislocation density on the Hugoniot for 6061-T6 are compared to experimental measurements of the residual dislocation density of shock-recovered Ni and Cu. Lines connecting the data points are plotted to guide the eye.

3.3.6. Dynamic stress-strain curves

In Figure 3.12, model calculations of the dynamic shear stress τ and the athermal threshold stress τ_μ are plotted versus the effective plastic strain ψ. In the shock front, dislocation glide is driven by an overstress, i.e., a measure of stress in excess of the athermal threshold. Thus, τ is interpreted as the non-equilibrium shear stress and τ_μ is interpreted as the equilibrium shear stress required for dislocation glide (at the current temperature). The rise in τ is a consequence of limited plasticity at the onset of the shock transition. Here, the density of dislocation line segments that are available for glide is limited, and the dislocations can travel only so fast. The decrease in τ from its peak value corresponds to the relaxation that occurs due to the generation and migration of dislocation line segments. The shear stress returns to the athermal threshold behind the shock front because the flow rate in a steady wave is zero on the Hugoniot. The $\tau(\psi)$ data that have been calculated by Wallace (1980a) from the experimental records are plotted for comparison. The agreement of the model with experimental data is rather good for all stress amplitudes considered. The maximum deviation of the model occurs for the 9.0 GPa shock; the magnitude of this deviation is ~55 MPa. Considering the highly nonlinear response of the material in the shock front, this level of agreement is encouraging. The importance of the rate-dependence of τ can be seen in this figure, as the peak shear stress in the shock front is about 3 times as high as the shear strength on the Hugoniot for a 9.0 GPa shock wave. Finally, the relatively weak strain-hardening of 6061-T6 is reflected in the τ_μ profiles computed using the model. It is noted that the computed values of shear stress and effective plastic strain on the Hugoniot, i.e., (ψ^-, τ^-), are of some concern for the 9.0 GPa shock since they deviate from the final data point in the experimental record. It will be shown later that measurements of the shear strength in the shocked state that have performed by Asay and Chhabildas (1981) are in better agreement with the value of τ^- computed by the model for the 9.0 GPa shock.

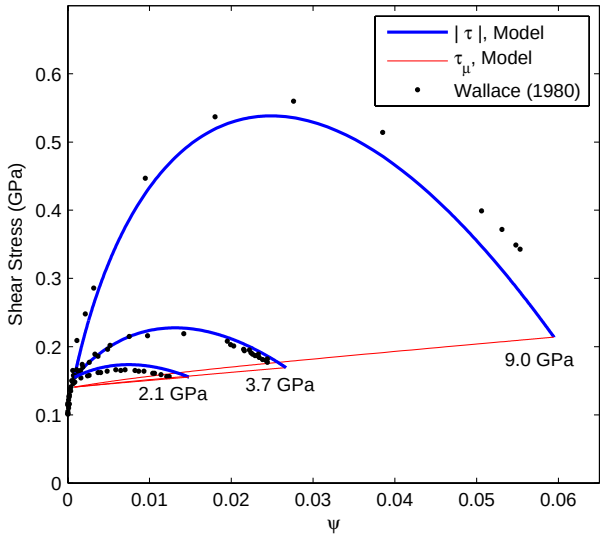

Figure 3.12: The dynamic shear stress profiles computed in the model are compared to experimental data for the 2.1, 3.7, and 9.0 GPa shock waves. The athermal threshold is also plotted to illustrate the return to equilibrium behind the shock front.

3.3.7. Shear strength on the Hugoniot

The shear strength of 6061-T6 in the shocked state has been measured using a few methods. Asay and Chhabildas (1981) and Huang and Asay (2005) used shock/re-shock and shock/release experiments to estimate the shear strength of 6061-T6 for a few different grain sizes. Here, the yield strength in the shocked state is determined from quasi-elastic waves that are propagated upon reloading. Vecchio and Gray (1994) measured the strength of shock-prestrained 6061-T6 using quasistatic reloading experiments. Here, a specimen was shocked to 27 GPa and carefully recovered. The yield strength of the recovered specimen was measured using a quasistatic reloading test (under ambient conditions). The reported value of strength has been scaled by $\mu(p)/\mu(p=0)$ to provide an appropriate measure of strength in the high-pressure state of the shock wave. Finally, Millett et al. (2009) determined the strength of 6082-T6 Al alloy in the shocked state via direct measurement of longitudinal and transverse stress components. In these experiments, blocks of the alloy were sectioned in half and lateral stress gages were embedded in an epoxy layer that was used to reconstruct the blocks. Longitudinal and transverse stresses were measured simultaneously during shock wave propagation; this permits direct calculation of the maximum shear

stress. These measurements of strength are plotted in Figure 3.13 along with the τ^- data points calculated by Wallace (1980a). The strength values at zero shock stress correspond to the Hugoniot elastic limits of the materials. It can be seen that the experimental data appear to follow two distinct trends. The strength measured using lateral stress gages (Millett et al., 2009) increases sharply with shock stress, whereas the strength measured using the re-shock and release method (Asay and Chhabildas, 1981; Huang and Asay, 2005) and the quasistatic reloading method (Vecchio and Gray, 1994) follows a lower trajectory in this space. A discussion of this discrepancy is deferred until later, where it is observed again for pure metals.

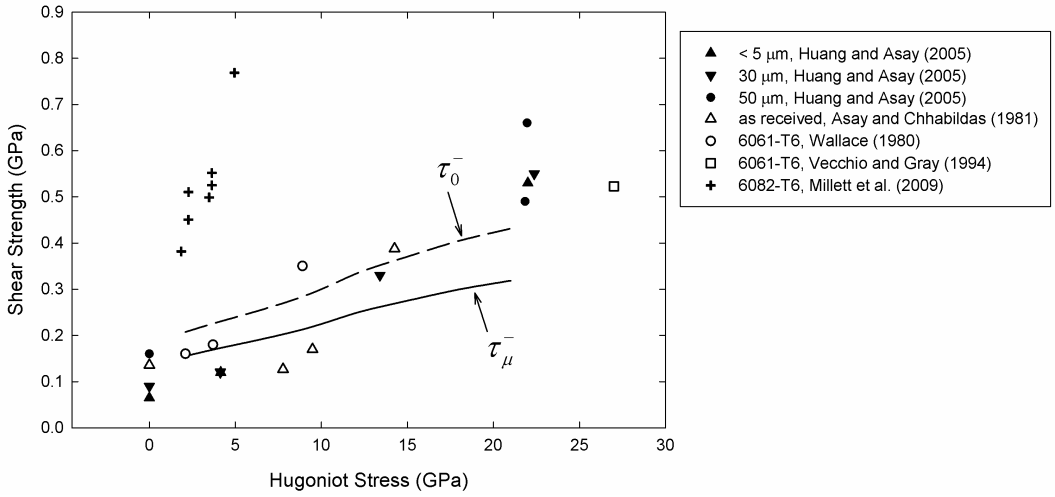

Figure 3.13: Measurements of the shear strength of 6061-T6 in the shocked state are compared to model bounds of strength.

In the model, the critical shear stress required for the onset of viscoplastic flow corresponds to the athermal threshold τ_μ. However, the shear strength of the material on the Hugoniot will appear higher than τ_μ^- if the viscoplastic flow rate is greater than zero. An upper bound of the shear stress in the regime of thermally-activated dislocation glide is the mechanical threshold stress τ_0. Accounting for the possibility of thermally-activated dislocation glide during the peak stress-hold of the shock wave, the shear strength on the Hugoniot should fall in-between τ_μ^- and τ_0^-. Model computations of these bounds are

plotted in Figure 3.13 for comparison to experimental data. The model bounds of strength are in agreement with the re-shock/release measurements for shock stresses up to about 15 GPa. Additionally, the computed value of τ_{μ}^{-} for a shock stress of 9.0 GPa agrees with the data set of Asay and co-workers, which should alleviate the concern about the computed values of (ψ^{-}, τ^{-}) in Figure 3.12. However, the deviation of the model from the strength measurements at shock stresses greater than 20 GPa cannot be explained by the possibility of plastic flow in the shocked state. Instead, it is thought there is a transition from pure slip to concurrent slip and twinning deformation. Gray and Follansbee (1988) observed twins in 6061-T6 that was shocked to 13 GPa. This corresponds to the stress level where the model begins to deviate from the experimental data. Since twins serve as additional barriers to dislocation glide, the strength of the material would be increased as a result of twinning deformation. Thus, the inclusion of a twin component in the strength relations may bring the model into better agreement with experiments at stresses greater than 15 GPa.

3.4. Application to pure fcc metals (Cu, Ni, and Al)

In this section, the constitutive model is applied to three pure fcc metals: Cu, Ni, and Al. The model has been applied to these metals to investigate their dynamic responses at high rates of deformation (10^4–10^8 s^{-1}) and to compare the model to experiments. Furthermore, we are specifically interested in using the viscoplastic constitutive model in highly-resolved simulations of shock wave propagation in mixtures of Ni and Al particles. The material properties and model parameters that are utilized in the constitutive relations and the steady plastic wave simulations are provided in the sections that follow. The application of the model to the pure metals follows many of the same procedures outlined in Section 3.2, which may be referenced for any details not provided here.

3.4.1. Initial microstructure

The purity, processing, and initial grain size of the materials considered in this study are provided in Table 3.5. Two distinct Cu materials have been considered because relevant experimental measurements are available for each. A representative grain size of 40 μm has been selected for all of the metals. This is consistent with the mean grain size of the Cu specimens studied in experiments that are reported later.

3.4.2. Material properties

The relevant material properties for Cu, Ni, and Al are given in Table 3.6. Expressions for the shear modulus (Eq. (3.15)) and the phonon damping coefficient (Eq. (3.16)) have been provided earlier. The pressure- and temperature- derivates of the (isotropic) polycrystalline shear modulii have been determined by Guinan and Steinberg (1974).

Table 3.5: Pure fcc metals of interest

	Purity	Material processing	Initial grain size (d)
OFE Cu	>99.99% Cu	Annealed	40 μm
OFHC Cu	>99.99% Cu	Cold-worked (half-hard)	40 μm
Ni	>99.6% Ni	200 series; annealed	40 μm
Al	>99% Al	1000 series; annealed	40 μm

Table 3.6: Material properties for the pure fcc metals

		Cu	Ni	Al
ρ_a	g cm^{-3}	8.924	8.875	2.712
c_{sa}	mm μs^{-1}	2.33	3.13	3.16
c_{La}	mm μs^{-1}	4.76	5.79	6.38
b	mm	2.56×10^{-7}	2.49×10^{-7}	2.86×10^{-7}
μ_a	GPa	48.4	86.9	27.1
$1/\mu_a\,(\partial\mu/\partial p)$	GPa^{-1}	28.0×10^{-3}	16.0×10^{-3}	69.0×10^{-3}
$1/\mu_a\,(\partial\mu/\partial\theta)$	K^{-1}	-0.38×10^{-3}	-0.33×10^{-3}	-0.54×10^{-3}
$B_0\,(p_a,\theta_a)$	GPa μs	1.7×10^{-8}	1.4×10^{-8}	1.0×10^{-8}
ν_D	μs^{-1}	10^7	10^7	10^7
Σ	GPa	24	42	13
σ_{Twin}	GPa	20	30	>30
c_η	J (mg K)$^{-1}$	0.385×10^{-3}	0.460×10^{-3}	0.904×10^{-3}
β		1	1	1
κ	J (mm μs K)$^{-1}$	401×10^{-9}	90.9×10^{-9}	222×10^{-9}
$\theta_{m,a}$	K	1358	1728	926
$\partial\theta_m/\partial p$	K GPa^{-1}	25.4	12.6	41.2
ΔH_{fus}	J mg^{-1}	209×10^{-3}	306×10^{-3}	390×10^{-3}

3.4.3. Evaluation of dislocation nucleation criteria

The dislocation nucleation criteria presented in Chapter 2 are now analyzed to determine the stress ranges where heterogeneous and homogeneous dislocation nucleation are expected. Recall that the criteria for homogeneous dislocation nucleation are $\sigma_1^- \in (\sigma_{Min}, \sigma_{Twin})$ and $w/\lambda < 1$. The situations for OFE Cu, Ni, and Al are illustrated graphically in Figure 3.14. For Cu and Ni, the minimum spacing of dislocation "sources" corresponds to the spacing of dislocations ahead of the main plastic wave, i.e., $\lambda^+ = (N^+)^{-1/2}$. The situation in Al is slightly more complicated because shock waves are overdriven at lower stress levels. In the weak shock regime ($\sigma_1^- < \Sigma$), the material length scale of interest is λ^+, as above. For overdriven shock waves ($\sigma_1^- > \Sigma$), the material length scale of interest is the initial spacing of dislocations in virgin material, $\lambda_0 = (N_0)^{-1/2}$. This is because there is no precursor wave in the overdriven case. In Figure 3.14, the stress ranges that satisfy the homogeneous dislocation nucleation criteria are shaded gray. Heterogeneous dislocation nucleation is expected for the stress ranges that fall below the gray shaded regions. It can be seen that homogeneous nucleation is expected in all three metals for shock stresses greater than ~15 GPa. Homogeneous nucleation above the twinning threshold is certainly possible; however, we have excluded it at this point for simplicity.

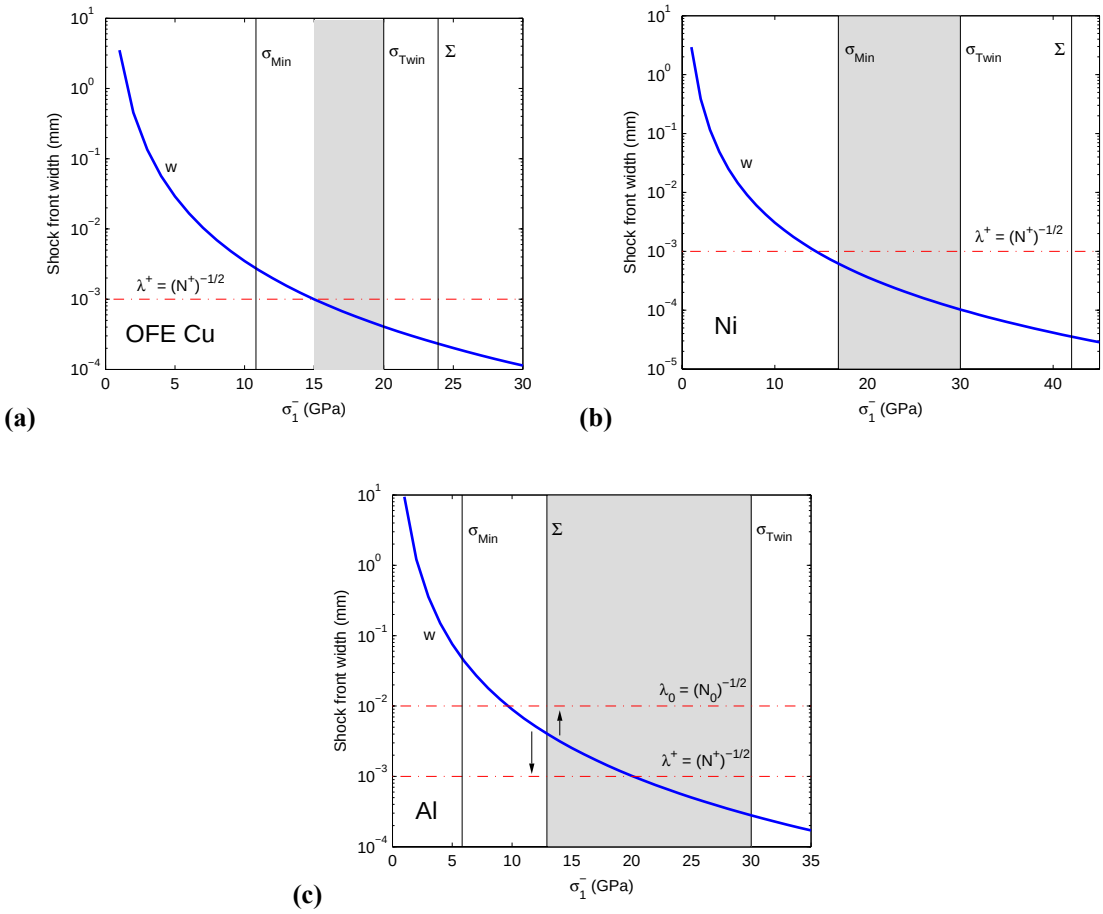

Figure 3.14: The criteria for homogeneous dislocation is illustrated for (a) OFE Cu, (b) Ni, and (c) Al.

3.4.4. Homogeneous dislocation nucleation

In the model of thermally-activated homogeneous dislocation nucleation, the free enthalpy of activation is written as

$$\Delta G_{hom} = g_{hom,0}\mu b^3\left(1-\tau/\tau_{ath}\right) \tag{3.18}$$

where $g_{hom,0}$ is the normalized free enthalpy required to nucleate a dislocation loop and τ_{ath} is the athermal nucleation threshold. Here, it has been assumed that the activation volume $v^* \equiv -\partial\Delta G/\partial\tau$ does not depend on the shear stress. The expression given in Eq. (3.18) is analogous to the activation energy prescribed in the model of Armstrong et al. (2007). According to Hirth and Lothe (1968), $\tau_{ath} \simeq \mu/15$ for Cu and Al at 300 K. For simplicity, we take $\tau_{ath} = \mu_a/15$ (i.e., the pressure-dependence of the shear modulus is currently neglected). The nucleation-accommodated part of the plastic shearing rate ($b\dot{N}_{hom}\bar{x}_{hom}$) now requires specification of the mean displacement of nucleated dislocation loops. For simplicity, we take $\bar{x}_{hom} = \eta_{hom}b$ where η_{hom} is a constant. The parameters for the model of homogeneous dislocation nucleation are provided in Table 3.7.

According to this relatively simple model, the activation energy (at zero applied stress) is $\Delta G_{hom,0} = g_{hom,0}\mu b^3$ and the activation volume is $v^* = \Delta G_{hom,0}/\tau_{ath}$. The model parameters that have been selected for Cu, Ni, and Al yield $\Delta G_{hom,0}$ in the range of 0.6–1.4 eV and v^* in the range of 1–5 b^3. These values are in general agreement with those calculated in atomistic simulations of homogeneous dislocation nucleation in Cu monocrystals (Tschopp and McDowell, 2008b), i.e., $\Delta G_{hom,0}$ in the range of 1–2 eV and v^* in the range of 0.5–2 b^3. It is worth noting that these atomistic simulations have revealed a significant degree of tension-compression asymmetry in the stresses at which dislocations are homogeneously nucleated. Here, the resolved shear stress required for homogeneous nucleation increases if the compressive stress normal to the slip plane is increased. This effect can be incorporated in the model when grain orientations are resolved. For example, the athermal nucleation stress for the α^{th} slip system τ_{ath}^{α} may be prescribed in such a way that takes into account the normal stress on the slip plane.

Table 3.7: Model parameters for the pure fcc metals

			Cu	Ni	Al
Thermal-depinning					
$g_{dep,0}$			0.87	0.74	0.65
p			1/2	1/2	1/2
q			2	2	2
χ_{dep}	†		0.05	0.05	0.05
Threshold stresses					
α_0	*		1	1	1
β_0			0.7	0.7	0.7
Substructure evolution					
Y_{HEL}		GPa	0.040[(a)], 0.120[(b)]	0.060	0.040
N^+		mm^{-2}	2.6×10^{6}[(a)], 3×10^{7}[(b)]	1.9×10^{6}	6.4×10^{6}
f^+			0.01	0.01	0.01
α_{hom}	†		9×10^{-5}	16×10^{-5}	10^{-5}
$g_{hom,0}$	†		0.12	0.08	0.33
χ_{hom}	†		0.008	0.008	0.008
η_{hom}	†		50	40	40
α_{het}	†	mm^{-2}	1.4×10^{9}	2.4×10^{9}	6.4×10^{8}
m	†		0.70	0.70	0.85
δ	†	mm^{-1}	42	56	88
α_{ann}			0.5	0.5	0.5
α_{dis}	†		0.012	0.017	0.017
α_p			–	–	–
Equation of state					
c_0		$mm\ \mu s^{-1}$	3.91	4.59	5.38
s_1			1.51	1.44	1.34
Γ_0			2.0	1.8	2.2

[(a)] OFE Cu, annealed
[(b)] OFHC Cu, half-hard
† Adjusted to fit experimental data
* Value is modified at high shock stresses (cf. Section 3.4.6)

3.4.5. Thermally-activated dislocation glide

The parameters of the model of thermally-activated dislocation depinning and glide are provided in Table 3.7. The thermal activation parameters ($g_{dep,0}$, p, and q) for Cu, Ni, and Al have been obtained by Kocks and Mecking (2003) based on a review of experimental measurements. The scaling coefficient χ_{dep} can be selected by fitting model results to experimentally-measured shock wave profiles when thermally-activated dislocation glide is the primary mechanism of plastic deformation. For Cu, this led to χ_{dep} =0.05, which is in agreement with the value found previously for 6061-T6. Unfortunately, experimental profiles that would allow calibration of χ_{dep} for Ni and Al are not available. For simplicity, the same value of χ_{dep} has been assumed.

3.4.6. Threshold stress parameters

The parameters for the threshold stresses of Cu, Ni, and Al are provided in Table 3.7. The dislocation-obstacle interaction coefficient, α_0, depends on the configuration of the dislocation substructure (Olivares and Sevillano, 1987) and the overall dislocation density (Kuhlmann-Wilsdorf et al., 1962). In our dynamic simulations, we have found $\alpha_0 = 1$ seems to work best when the dislocation density is less than 10^{16} m^{-2}. This value is reasonable considering the value of α_0 under quasistatic loading conditions should be about 1/2 (within a factor of 2) for single-crystalline and polycrystalline fcc metals (Mecking and Kocks, 1981; Kuhlmann-Wilsdorf, 1999). In fact, values as high as $\alpha_0 = 2$ have been used in theoretical developments that address the shock loading of metals (Johnson et al., 1992; Johnson, 1993). When the dislocation density exceeds 10^{16} m^{-2}, it has been found necessary to reduce the value of α_0 to prevent unrealistically-high predictions of material strength. This is necessary, for example, when there is intense homogeneous dislocation nucleation. According to Kuhlmann-Wilsdorf theory, the dislocation interaction coefficient scales with dislocation density as $\alpha_0 \sim \ln(3/bN^{1/2})$. If the dislocation density is increased by 3 orders of magnitude, α_0 is reduced by a factor of ~2. Therefore, we have found $\alpha_0 = 0.4$ provides reasonable results for stress amplitudes in the homogeneous nucleation regime.

3.4.7. Substructure parameters

The model parameters that define substructure evolution are provided in Table 3.7. When experimental wave profiles are available, the (+) state can be determined by correcting the HEL based on the amount of hardening in the plastic precursor wave. This has been done for OFE and OFHC Cu. However, steady wave profiles are not available for pure Ni or Al, so it is assumed that there is no material hardening in the precursor wave. That is, the (+) state is taken as the HEL. The dislocation density, N^+, is calculated based on the value of τ^+.

The homogeneous dislocation nucleation parameters have been discussed earlier. In the model of heterogeneous dislocation nucleation, the scaling coefficient, α_{het}, and the PDF exponent, m, for pure polycrystalline metals are expected to be somewhat different than those for precipitate-hardening alloys. In pure polycrystalline metals, dislocations are emitted from the grain boundaries (GBs) and triple junctions. To estimate of α_{het}, suppose $\overline{\ell} \propto nd$ where n is the number of dislocations emitted from a source, and $\mathcal{N}/V \propto \Gamma/d^2$ where Γ is the linear density of sources in the GB. If it is assumed the spacing of potential GB sources is ~5 nm, the heterogeneous nucleation coefficient α_{het} is estimated to be in the range 10^8–10^9 mm^{-2} for micron-sized grains. The shape of the PDF that characterizes dislocation emission stress is also expected to be slightly different for pure metals and alloys. In alloys, the precipitates introduce stress fields that inhibit the emission of dislocations from GB sources, especially if dislocation segments are hung-up on precipitates in close proximity to the boundary. The continued operation of GB sources in alloys then requires progressively higher levels of shear stress, which is reflected by higher values of the PDF exponent m. Since we have found $m = 1$ for 6061-T6, it stands to reason that $m < 1$ should hold for the pure metals.

The dislocation multiplication coefficients for Cu, Ni, and Al are adjustable parameters that have been selected according to the relative stacking fault energies of the materials. The coefficients have been ordered with respect to stacking fault energy because dislocation multiplication under dynamic loading conditions is thought to be primarily due to the double cross-slip mechanism (Johnston and Gilman, 1960). The values of α_{ann} and α_{dis} have been estimated according to the procedure described earlier.

3.4.8. Equation of state

The EOS parameters for Cu, Ni, and Al are provided in Table 3.7. These parameters have been determined from shock compression experiments (Marsh, 1980). Small corrections have been applied to the EOS parameters of Al to reduce the shock wave speed (by about 1-2%) for low shock stresses. This correction brings the shock wave speed into better agreement with the aforementioned data for shock stresses below 6 GPa.

3.4.9. Discussion of adjustable model parameters

The model parameters that have been *set* are again distinguished from model parameters that have been *adjusted*. In Table 3.7, a dagger symbol has been placed next to the adjustable parameters. There are now 9 adjustable parameters in total since homogeneous nucleation is incorporated. However, we have found χ_{hom}=0.008 and $\eta \simeq 40$ for all three metals, which indicates χ_{hom} and η may be considered *set* instead of adjustable. Considering the complexity of deformation and substructure evolution in the shock loading regime and the rich, microstructure-sensitive description that is provided by the constitutive model (including distinction of heterogeneous and homogeneous dislocation nucleation), we believe the use of 7-9 nine adjustable parameters is acceptable for pure fcc metals. Since each adjustable parameter has a physical interpretation, it is possible to estimate an acceptable range of values for each parameter. The values of all adjustable parameters fall within the acceptable ranges. Of course, there is some uncertainty in the precise values of the parameters since they are integrated simultaneously in the steady wave calculations. Slightly different sets of parameters might provide equally-good fits to the available data.

3.5. Results for pure fcc metals (Cu, Ni, and Al)

Steady plastic waves have been simulated in Cu, Ni, and Al using the framework presented in Section 3.1. Stress amplitudes up to 30 GPa have been simulated for each material. Model results are examined in the sections that follow.

3.5.1. Hugoniot curves

The Hugoniot curves that are computed in the steady wave analysis are compared to experimental measurements in Figure 3.15. This result simply verifies that the jump conditions in the steady wave simulations are calculated with sufficient accuracy.

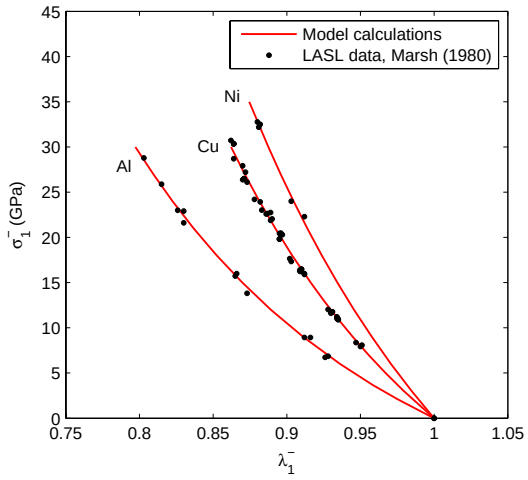

Figure 3.15: The Hugoniot curves computed in the steady wave framework are compared to shock compression measurements.

3.5.2. Material velocity profiles

Steady waves have been achieved in plate impact experiments performed on Cu. The peak stress amplitudes in these shock compression experiments were ~3 GPa (Warnes and Tonks, 1989) and 10 GPa (Johnson et al., 1992) in OFE Cu, and 5.4 GPa in OFHC Cu (Swegle and Grady, 1985). Experimental records of the material velocity, $u(t)$, are provided in Figure 3.16. The three profiles measured by Warnes and Tonks (1989) were similar, so only the velocity trace from the 3.2 GPa shock wave is shown. Model calculations of the material velocity for OFE Cu and OFHC Cu are plotted in Figure 3.16. The plastic transition of the 3.2 GPa shock is well-captured by the model. For the 5.4 GPa shock, the model agrees with the measured profile for the first half of the shock rise, but deviates from the experimental profile near the knee of the curve. The model deviates because there is a rather abrupt change in the slope of the

experimental profile near the center of the plastic transition. An explanation for this change in slope has not been reported, but one may speculate that it is due to some unforeseen experimental complication or deformation that is accommodated by some mechanism other than slip. The model captures the sharpness of the plastic transition for the 10 GPa shock. Unfortunately, the time resolution of these measurements is insufficient to further assess the structure of the shock front at this stress amplitude. The material velocity that is computed on the Hugoniot agrees with experimental data in all cases. In summary, the model is mostly successful in reproducing shock front structures for rise times ranging from approximately 10–200 ns and Hugoniot material velocities u^- ranging from 0.090–0.250 mm/μs. Since the structure of the shock front is sensitive to the viscoplastic deformation that occurs in the front, these results provide support for the constitutive relations.

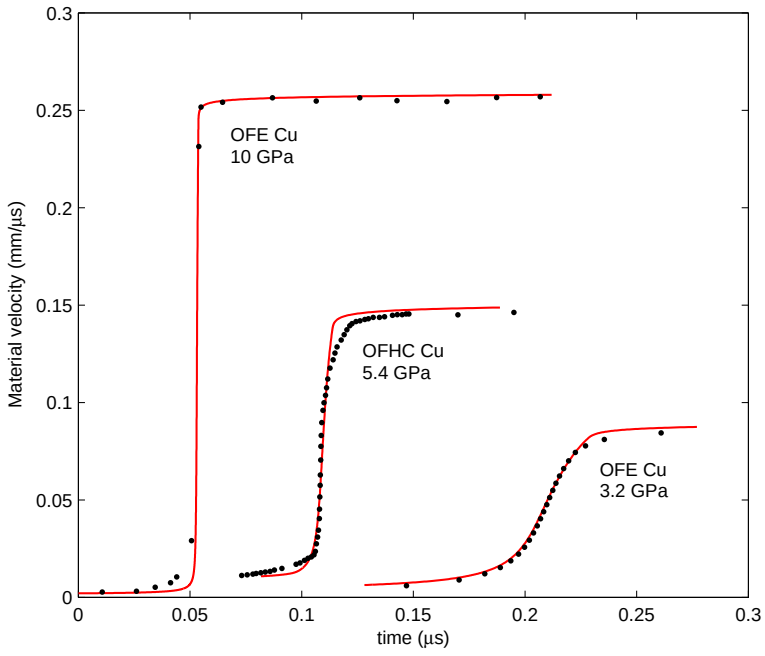

Figure 3.16: Fixed-point material velocity profiles that are computed in the steady wave analysis are compared to experimental measurements for shock stress amplitudes of 3.2 and 10 GPa for OFE Cu and 5.4 GPa for OHFC Cu.

3.5.3. Viscoplastic flow in the shock front

Model calculations of the longitudinal plastic rate of deformation, D_1^p, are plotted versus the effective plastic strain, ψ, in Figure 3.17 for Cu. The model is compared to profiles that have been extracted from the experimental $u(t)$ records using the analysis of Wallace (1980a), which has been discussed earlier (cf. Section 3.3.3). For the 3.2 GPa shock in OFE Cu, the agreement between the experimental and computed $D_1^p(\psi)$ profiles is excellent. In fact, one can even discern evidence of the presumed transition from continuous glide back to thermally-activated dislocation glide in the experimental profile (near $\psi = 0.011$). In the model, this transition is identified by a discontinuity in the slope of $D_1^p(\psi)$ near the end of the plastic transition. For the 5.4 GPa shock in OFHC Cu, the computed profile does not agree with the experimental profile. This discrepancy is due to the abrupt change in the slope of the experimental $u(t)$ profile since the rate of deformation is proportional to $\dot{u}$. In both cases, the terminal plastic strain ψ^- (which is not imposed but rather a natural outcome of the integration process) is in agreement with experiments.

To examine the plastic rate of deformation in stronger shocks, the D_1^p profiles that have been computed for OFE Cu and Ni subjected to stress amplitudes up to 15 GPa are depicted in Figure 3.18. Here, the D_1^p profiles remain roughly self-similar as the shock stress is increased, the peak rate of plastic deformation being maintained over much of the transition. Unfortunately, measured free-surface velocity profiles are not available for steady waves in Ni or Al, so the Wallace analysis cannot be used to compute shock profile data for comparison.

The mean velocity of glide dislocations in the shock front is plotted in Figure 3.19 for Al shocked up to 12 GPa. The shear wave speed c_S is the commonly-accepted upper-limit of dislocation velocity. It can be seen that relativistic effects comes into play for stress amplitudes near 9 GPa. This affects the mean dislocation velocity profile significantly, which has a direct impact on the plastic strain rate in the shock front.

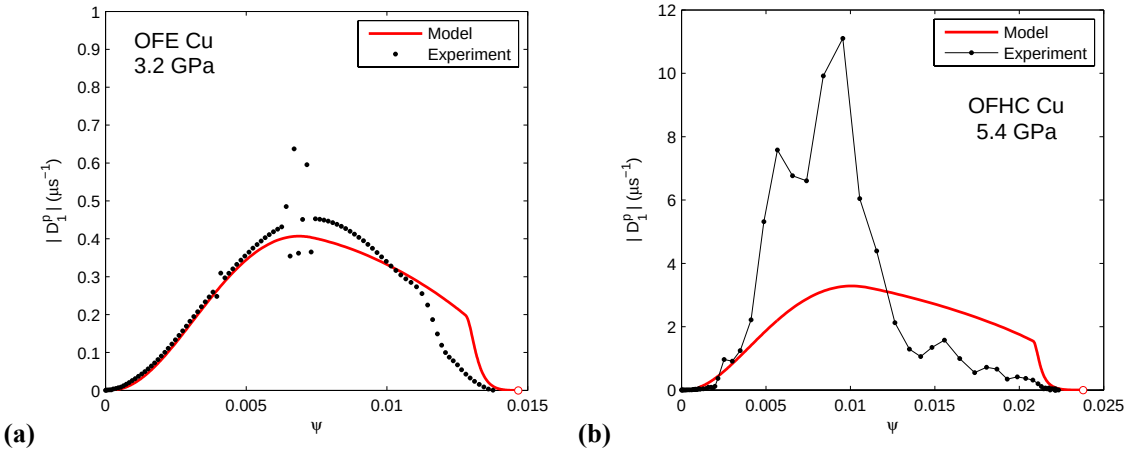

Figure 3.17: Profiles of the plastic rate of deformation that are computed using the model are compared to experimental data for (a) the 3.2 GPa shock in OFE Cu and (b) the 5.4 GPa shock in OFHC Cu.

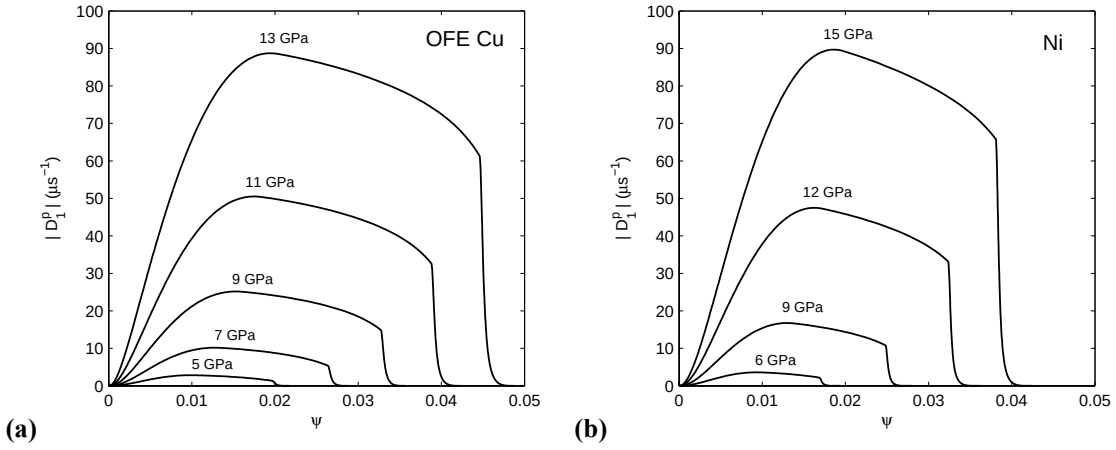

Figure 3.18: The plastic rate of deformation profiles that are computed for (a) OFE Cu and (b) Ni shocked up to 15 GPa.

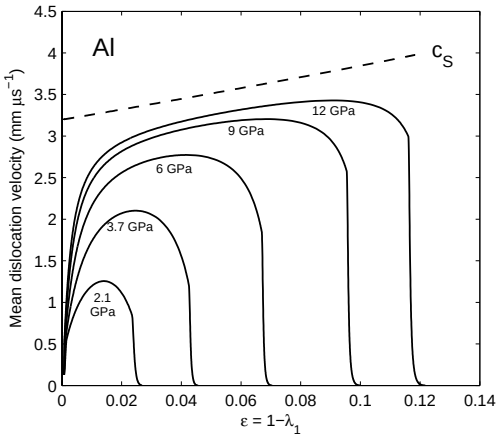

Figure 3.19: The mean dislocation velocity is plotted versus nominal compressive strain for Al shocked up to 12 GPa. The current shear wave speed is indicated by the dashed line.

3.5.4. Substructure evolution in the heterogeneous nucleation regime

In this section, the substructure evolution rates that are computed for Cu, Ni, and Al are presented. Two shock stress amplitudes have been considered for each material: one that is rather low (a few GPa) and one that is higher (~10 GPa). In all cases shown here, the shock stress is too low for homogeneous dislocation nucleation. Therefore, the nucleation rates that are plotted correspond to the heterogeneous nucleation of dislocations from GB sources. The mobile and immobile components of dislocation density, which are obtained by integrating the substructure evolution rates, are also presented.

The substructure evolution rates that are computed for OFE Cu subjected to shocks of 3.2 GPa and 10 GPa are plotted in Figure 3.20. For the 3.2 GPa shock, the rates of heterogeneous dislocation nucleation, multiplication, and trapping are comparable in magnitude. As discussed earlier, the nucleation rate goes to zero near the center of the shock front because the model does not allow heterogeneous dislocation nucleation during the stress relaxation part of the shock front (i.e., where $\dot{\tau} < 0$). The point at which the nucleation rate returns to zero corresponds to the peak in the dynamic stress-strain curve. At this point, many mobile dislocation segments have been generated and are available for migration. Multiplication proceeds by cross slip of the newly-generated dislocation segments. As shown in the inset of Figure 3.20(a), the mobile density rises to a peak value near the center of the front while the immobile density increases monotonically. The total dislocation density increases by almost one order of magnitude

for the 3.2 GPa shock. For the 10 GPa shock, the peak rate of heterogeneous dislocation nucleation is significantly greater than the multiplication rate. It can also be seen that the peak heterogeneous nucleation rate of the 10 GPa shock is about 1000 times greater than that of the 3.2 GPa shock. Dislocation nucleation dominates substructure evolution near the leading edge of the shock front and the trapping (immobilization) rate now rises above the multiplication rate for the entire deformation. Although the annihilation rate is somewhat significant for the 10 GPa shock, Figure 3.20 indicates that one might be justified in neglecting dislocation annihilation for shock stresses up to (at least) 10 GPa. As shown in the inset of Figure 3.20(b), the mobile density rises very quickly during the first part of the wave front, forcing the total dislocation density to a saturated value of $\sim 10^{8}$ mm^{-2} for this shock stress. This constitutes an overall 50-fold increase in total dislocation density for the 10 GPa shock. The calculations of mobile dislocation density are speculative; however, the evolution equations for dislocation generation are based on physical mechanisms and the computed values of dislocation density on the Hugoniot appear reasonable.

The substructure evolution rates that are computed for Ni and Al are plotted in Figure 3.21 and Figure 3.22, respectively, for the stress amplitudes indicated. In both cases, a quantitative description of substructure evolution is nearly identical to that given above for OFE Cu, with the exception that the peak dislocation density in Al is somewhat higher for the higher shock stress.

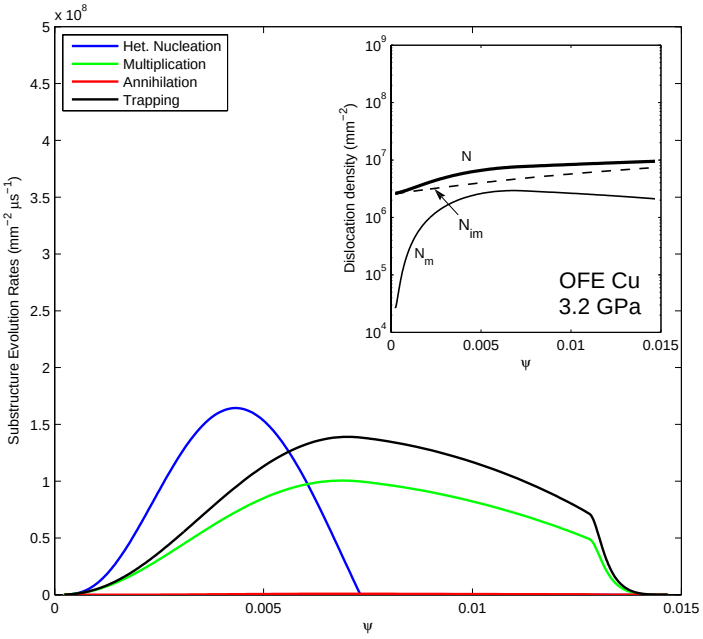

(a)

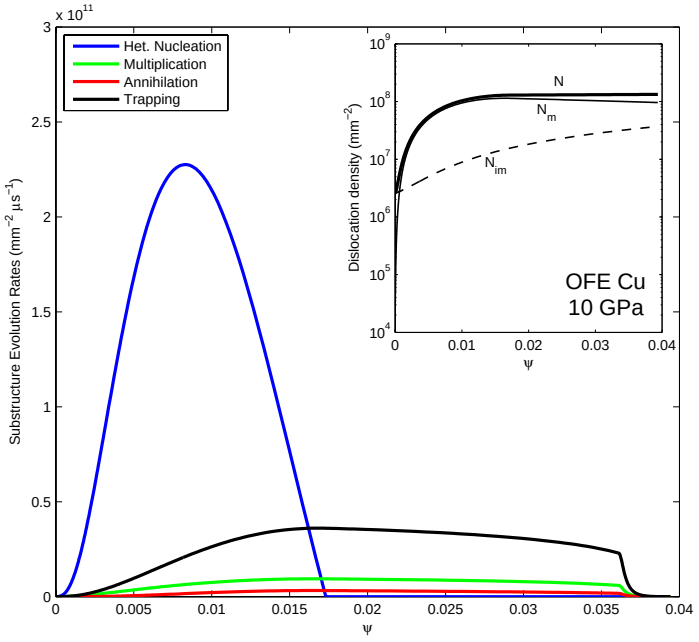

(b)

Figure 3.20: Substructure evolution rates in the shock front for peak stress amplitudes of (a) 3.2 GPa and (b) 10 GPa in OFE Cu. The inset figures are plots of the dislocation density components.

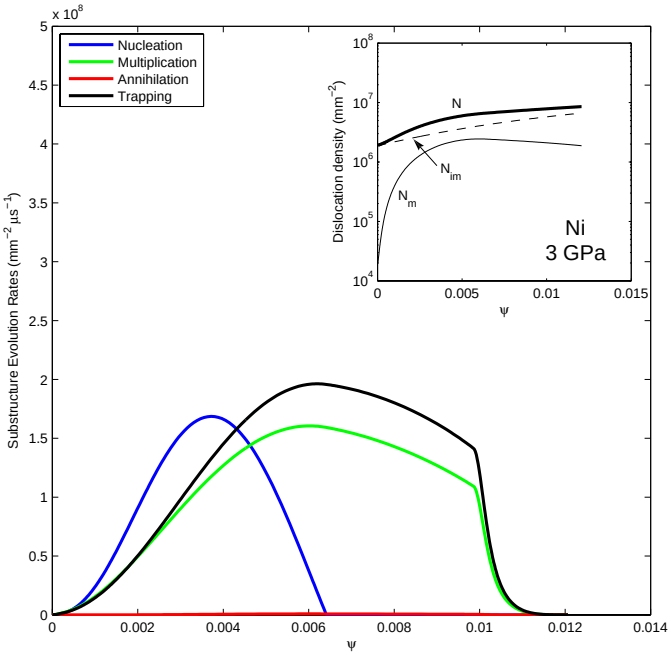

(a)

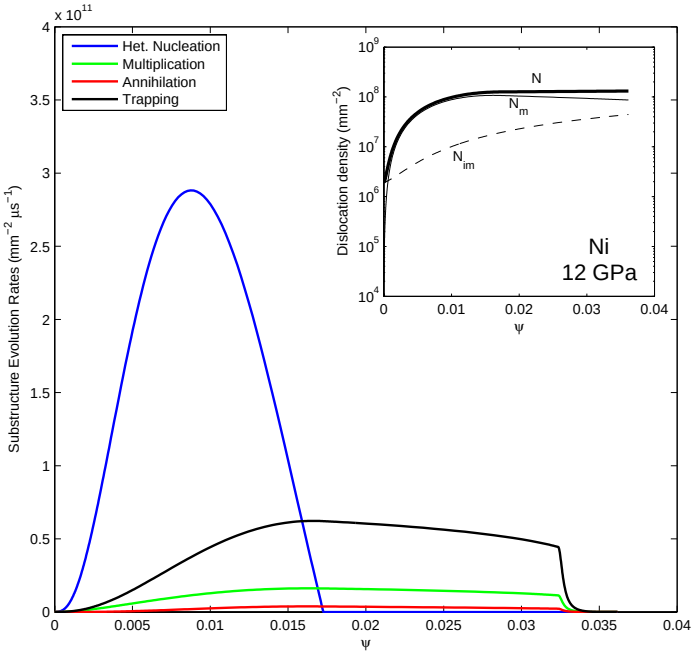

(b)

Figure 3.21: Substructure evolution rates in the shock front for peak stress amplitudes of (a) 3 GPa and (b) 12 GPa in Ni. The inset figures are plots of the dislocation density components

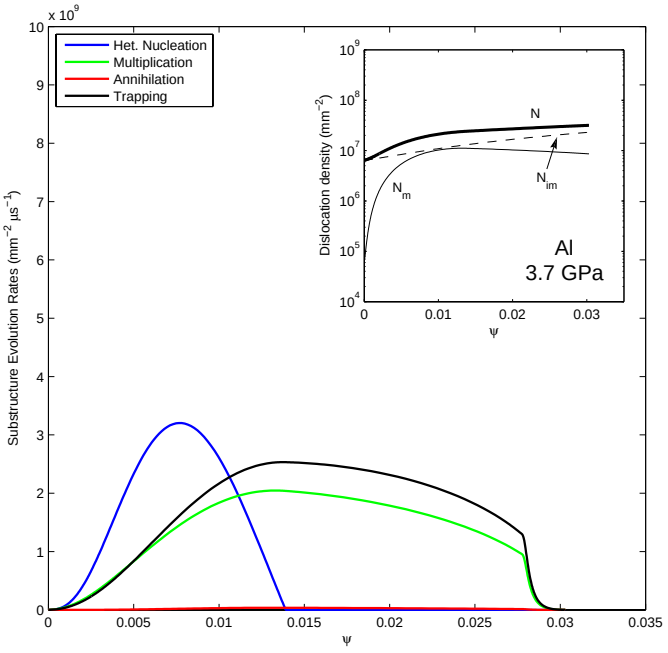

(a)

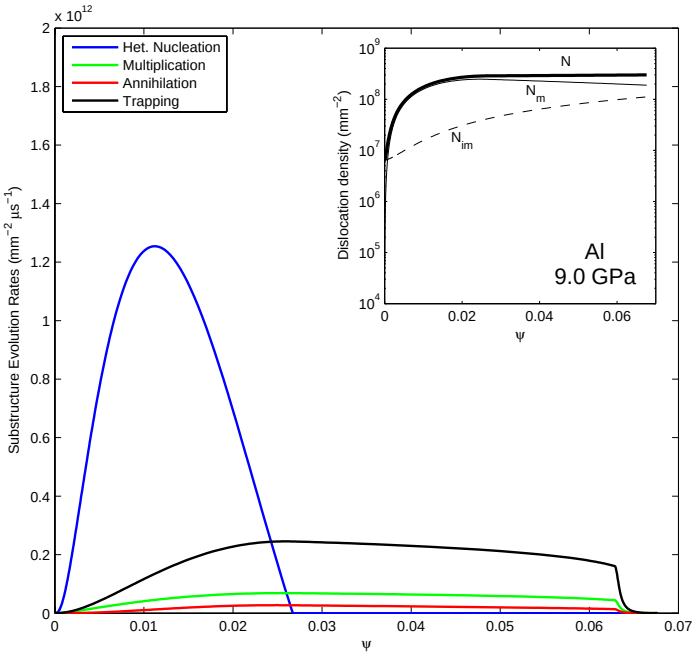

(b)

Figure 3.22: Substructure evolution rates in the shock front for peak stress amplitudes of (a) 3.7 GPa and (b) 9 GPa in Al. The inset figures are plots of the dislocation density components.

3.5.5. Simulation of homogeneous dislocation nucleation

Dislocations are nucleated homogeneously when the shear stress reaches a significant fraction of the athermal nucleation stress, τ_{ath}. The shear stress in the shock front approaches τ_{ath} when the deformation is nearly elastic. To simulate homogeneous dislocation nucleation, the steady wave framework has been modified to suppress plastic flow (which relaxes the shear stress) prior to the onset of homogeneous nucleation. Here, it is assumed that the deformation is purely elastic prior to state (d), which is depicted in Figure 3.1. State (d) is defined as that where homogeneous nucleation begins to occur at an appreciable rate. We have chosen the shear stress at state (d) to be 80% of τ_{ath}. In the steady wave simulations, the (+) state is now taken as state (d). All other aspects of the calculations remain the same. Thus, the modified framework simulates the elastic deformation of small volumes in the shock front which are relaxed by the nucleation and glide of dislocation segments.

In this section, simulation results are presented for Al in the homogeneous nucleation regime. The results for Cu and Ni are quite similar and therefore omitted for brevity. Shear stress profiles for Al are plotted in Figure 3.23(a) for shock stresses that span the heterogeneous and homogeneous nucleation regimes. The shear stress profiles in the homogeneous nucleation regime (σ_1^->13 GPa) illustrate the elastic response (up to $0.8\tau_{ath}$) and the subsequent relaxation by nucleation and glide. In Figure 3.23(b), the nucleation- and glide-accommodated parts of the plastic shearing rate are depicted as $\Phi_{hom} = \dot{N}_{hom} b\bar{x}_{hom}$ and $\Phi_{glide} = bN_m\bar{v}$. For shock stresses greater than 15 GPa, Φ_{hom} reaches an upper limit because ΔG_{hom} has been reduced to zero. It can be seen that dislocation glide accommodates a modest fraction of the plastic shearing rate in the homogeneous nucleation regime.

The substructure evolution rates that are computed for a 15 GPa shock in Al are plotted in Figure 3.24. Homogeneous dislocation nucleation dictates much of the substructure behavior. At its peak, the rate of homogeneous dislocation nucleation is 4 orders of magnitude greater than the multiplication and trapping rates. The homogeneous nucleation rate falls to zero as τ is relaxed by plastic flow. As shown in the inset of Figure 3.24, the dislocation density increases by about four orders of magnitude, settling on a very high value in the shocked state (~10^{16} m^{-2}). A large fraction of these dislocation segments are immobile.

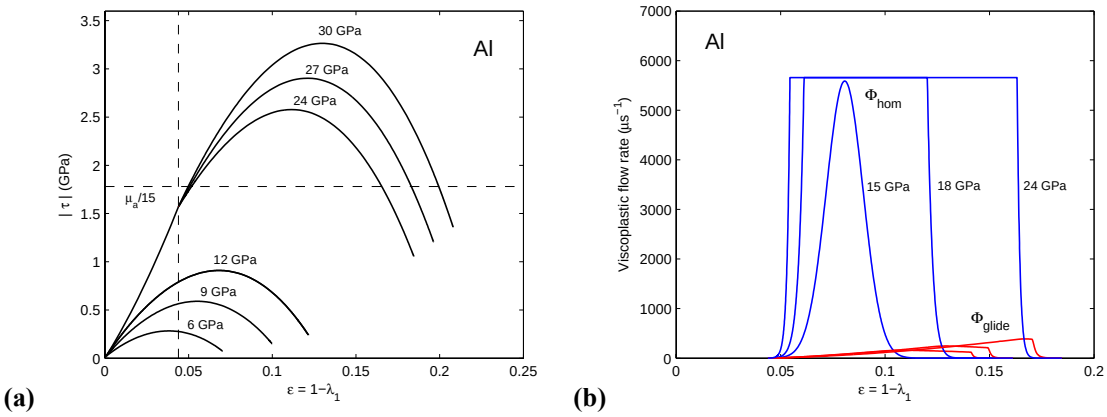

Figure 3.23: In part (a), the shear stress is plotted versus compression (ε) for the shock stress indicated next to each curve. In part (b), the nucleation- and glide-accommodates parts of the overall plastic shear rate are plotted versus compression for the stress amplitudes indicated.

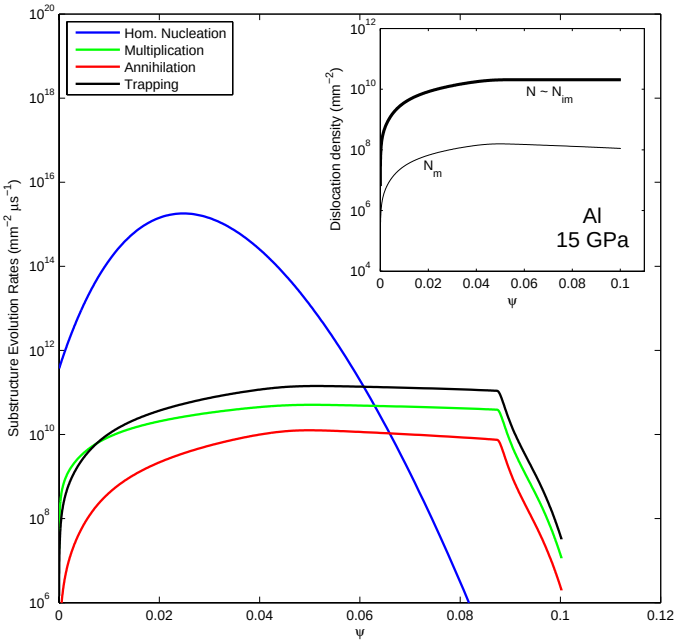

Figure 3.24: Substructure evolution rates for a 15 GPa shock wave in Al. The inset figures are plots of the dislocation density components.

3.5.6. Dislocation density on the Hugoniot

Model calculations of dislocation density on the Hugoniot are plotted versus peak shock stress for Ni, OFE Cu, and Al in Figure 3.25. The regions that are shaded gray correspond to stress ranges where homogeneous dislocation nucleation is expected (cf. Section 3.4.3). In these stress ranges, homogeneous dislocation nucleation has been simulated in the model. At lower stresses, the heterogeneous nucleation of dislocations (from GB sources) has been simulated. Measurements of residual dislocation density from shock-recovery experiments and dislocation densities that have been calculated in atomistic and dislocation dynamics simulations are plotted for comparison. For the single crystal data sets, the crystallographic direction of shock wave propagation is indicated.

For Ni, the computed values of N^{-} in the heterogeneous nucleation regime (σ_1^{-}<16 GPa) compare favorably with shock-recovery experiments performed on microcrystalline Ni (Murr and Kuhlmann-Wilsdorf, 1978). There is a precipitous increase in N^{-} when homogeneous nucleation is simulated using the model. Here, it can be seen that the dislocation density in the shocked state exceeds 10^{16} m^{-2} and is trending toward the atomistic results at higher shock stresses. In the atomistic simulations of shock wave propagation in monocrystalline Ni (Holian and Lomdahl, 1998; Jarmakani et al., 2008) the dislocation density has been estimated from the *shock-induced plasticity*, a_0 / ℓ, where a_0 is the lattice parameter and ℓ is the average spacing of stacking faults (Holian and Lomdahl, 1998). An interesting feature of the atomistic work of Jarmakani et al. (2008) is the simulation of crystal unloading (release). Here, many partial dislocation loops disappear after the specimen is unloaded (presumably, the stacking faults have collapsed). As indicated by the arrows in Figure 3.25(a), unloading reduces the dislocation density by about one order of magnitude, which brings the atomistic results into better agreement with the shock-recovery experiments performed on microcrystalline Ni (Murr and Kuhlmann-Wilsdorf, 1978) and nanocrystalline Ni (Wang et al., 2006). The compatibility of the model with experimental measurements (at lower stresses) and atomistic results (at higher stresses) is encouraging from a constitutive modeling perspective. Higher shock stresses have not been simulated in Ni because we wish to avoid the possibility of shock-induced twinning.

For OFE Cu, the computed values of N^- in the heterogeneous nucleation regime (σ_1^- <15 GPa) agree with shock-recovery experiments performed on polycrystalline Cu (Murr, 1978; Murr, 1981). Again, there is a large increase in N^- when homogeneous nucleation is simulated using the model. Although the upper limit of the homogeneous nucleation regime for OFE Cu is 20 GPa (according to the criteria stated earlier) we have simulated homogeneous dislocation nucleation for shock stresses up to 30 GPa to facilitate comparison of the model to the numerical results at higher stresses. Therefore, the constitutive model, which is based on crystallographic slip, has been extended to a stress range where twinning is a concurrent (or possibly dominant) mode of deformation. The computed values of N^- in the homogeneous nucleation regime are comparable to the dislocation densities that are calculated in atomistic simulations of shock waves in monocrystalline Cu (Holian and Lomdahl, 1998; Bringa et al., 2006; Cao et al., 2007) and nanocrystalline Cu (Bringa et al., 2005) and dislocation dynamics simulations of shock waves in monocrystalline Cu (Shehadeh et al., 2006).

For Al, the model values of N^- in the heterogeneous nucleation regime (σ_1^- <13 GPa) have been compared to the aforementioned shock-recovery experiments performed on Ni and Cu, since we are not aware of any such data for Al. The purpose of this comparison is to show that the dislocation density computed by the model is in general agreement with measurements for other fcc polycrystalline metals. In the homogeneous nucleation regime, the computed values of N^- are in agreement with estimates of dislocation density from atomistic simulations of shock waves in monocrystalline Al (Holian and Lomdahl, 1998). This makes sense because homogeneous nucleation is the predominant mechanism of dislocation generation in atomistic simulation of shocked monocrystals.

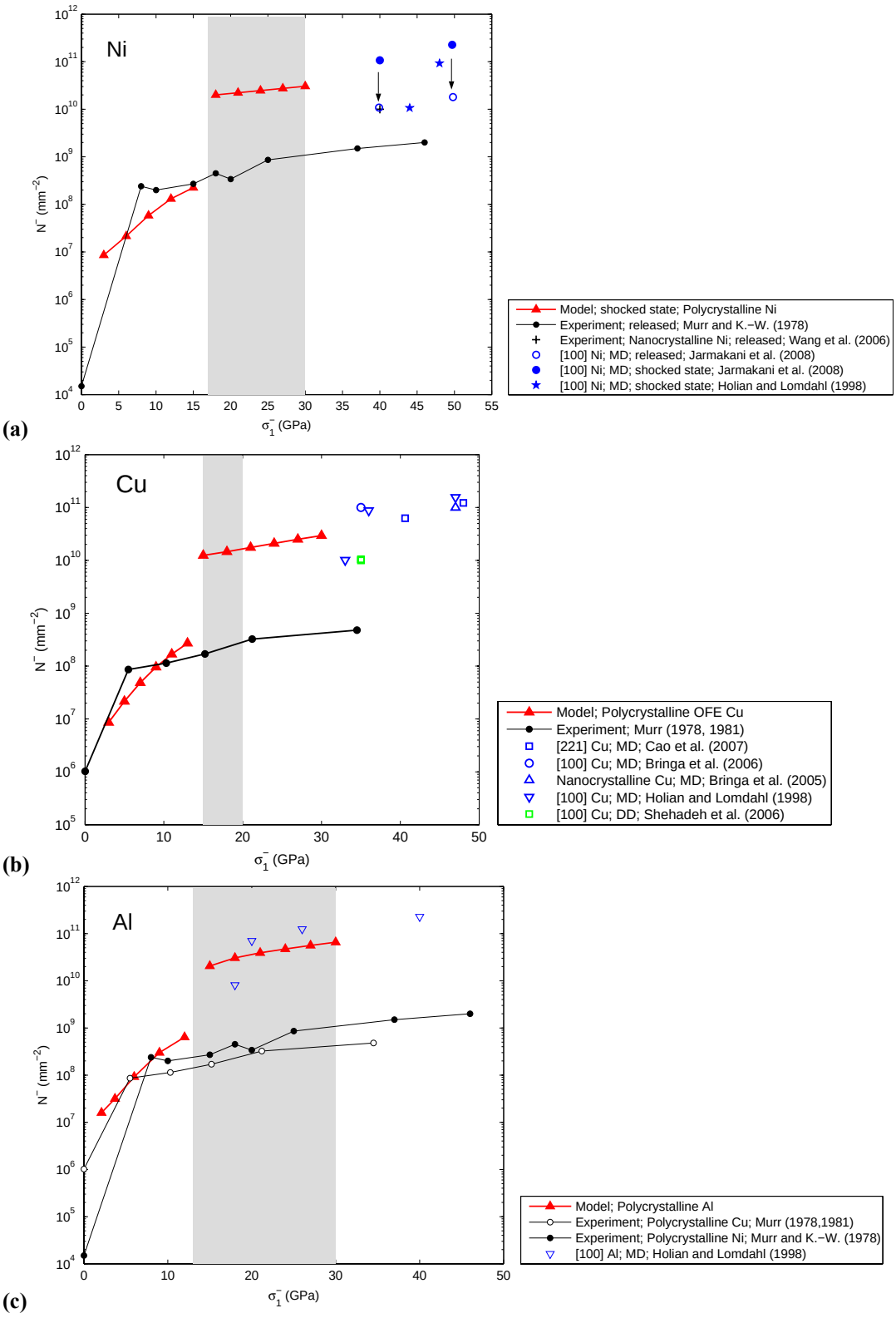

Figure 3.25: The dislocation density in the shocked state that is computed using the model is plotted as a function of shock stress. Simulated results for (a) Ni, (b) OFE Cu, and (c) Al are compared to experimental measurements of the residual dislocation density of shock-recovered Cu and Ni and dislocation densities calculated using molecular dynamics (MD) and dislocation dynamics (DD).

3.5.7. Swegle-Grady plots

In Figure 3.26, plots have been constructed using results generated by the model for OFE Cu, Ni, and Al to illustrate the one-fourth power law between shock stress and strain rate, i.e., $\sigma_1^- \propto \dot{\varepsilon}^{1/4}$ (Swegle and Grady, 1985). Here, shock stress amplitudes range from 2–30 GPa and maximum (nominal) strain rates range from about 10^6–10^{10} s^{-1}. The model-generated results are correlated by lines with slopes of 1/4. This indicates that the viscoplastic constitutive model respects the one-fourth scaling law (which is thought to be universal for metals) over a considerable range of shock stress. It is should be noted that the upper part of the stress range is governed by thermally-activated (homogeneous) dislocation nucleation, whereas the lower part of this stress range is governed by heterogeneous nucleation and glide.

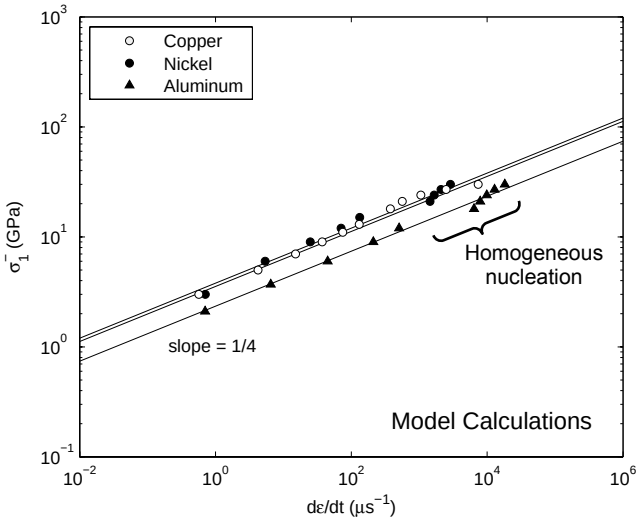

Figure 3.26: Swegle-Grady plots constructed from model-generated results illustrate the one-fourth power law for Cu, Ni, and Al.

3.5.8. Dynamic stress-strain curves

In Figure 3.27, model calculations of the dynamic shear stress, τ, the athermal threshold stress, τ_μ, and the mechanical threshold stress, τ_0, are plotted for OFE and OFHC Cu. The $\tau(\psi)$ data that have been extracted from the experimental $u(t)$ profiles are plotted for comparison. The agreement of the

model with experimental data is rather good for both materials, the largest deviations occurring near the end of the plastic transition in each case. As discussed earlier, dislocation glide in the shock front is driven by an overstress, and the kinetics of glide are influenced by phonon damping and the relativistic effect. It can be seen that τ exceeds τ_0 for most of the deformation, indicating that thermally-activated dislocation glide (thermal-depinning) plays a small role in the shock front for these stress levels.

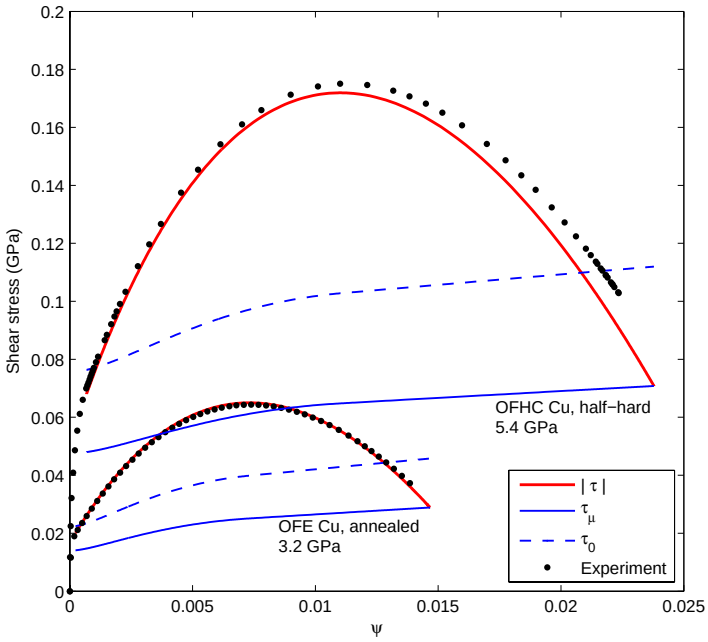

Figure 3.27: Dynamic shear stress profiles are compared to experimental data for the 3.2 GPa shock in OFE Cu and the 5.4 GPa shock in OFHC Cu. The computed values of the athermal threshold stress and the mechanical threshold stress are also plotted.

In Figure 3.28, time histories of shear stress, $\tau(t)$, and shear stress profiles, $\tau(\psi)$, are plotted for selected shock stresses in Cu, Ni, and Al. For all three metals, the time histories indicate the weakest shocks are relatively gradual (occurring over ~100 ns) and exhibit mild peaks, while the plastic transitions of the strongest shocks occur rapidly (< 10 ns), displaying pronounced peaks in shear stress followed by quick relaxation to the equilibrium (Hugoniot) state. The strain-rate-dependence of τ is illustrated by these Figures since higher shear stresses are required to drive higher rates of deformation in stronger

shocks. The rate-dependence of structure evolution (material hardening) is illustrated by the $\tau_\mu(\psi)$ profiles since τ_μ depends on dislocation density. For a given value of ψ, stronger shocks produce higher rates of dislocation generation, and thus higher values of τ_μ. Finally, we wish to consider the relative proportions of τ and σ_1 in the shock front. At the peak of the $\tau(\psi)$ curve for the 12 GPa shock in Al, the shear stress is ~15% of the longitudinal stress σ_1 (which has not yet reached its maximum value). Therefore, the material does not behave as an inviscid fluid here. On the Hugoniot, τ is ~2% of σ_1.

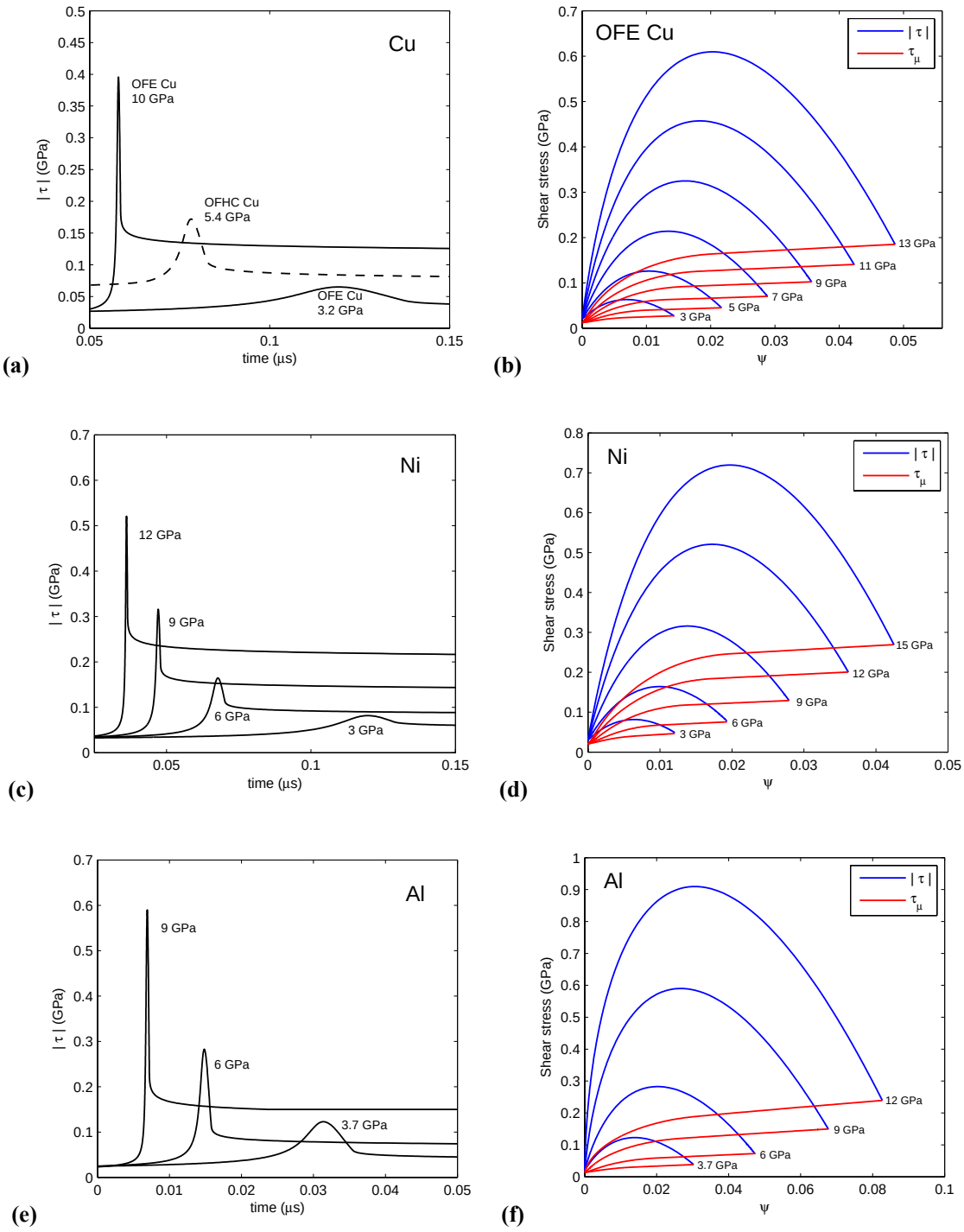

Figure 3.28: Shear stresses in Cu, Ni, and Al for shock stresses up to 15 GPa. Time histories of the shear stress are plotted in (a), (c), and (e). Profiles of the shear stress and the athermal threshold stress are plotted versus the effective plastic strain in (b), (d), and (f).

3.5.9. Shear strength on the Hugoniot

In this section, the model bounds of shear strength in the shocked state are compared to experimental measurements for Cu, Ni, and Al. The strength of shocked Cu has been measured using a few methods. Turneaure and Gupta (2009) determined the strength of Cu monocrystals shocked in the [111] direction using real time synchrotron x-ray diffraction (XRD). In these experiments, longitudinal lattice strain was measured at the instant the longitudinal stress was completely released (at which point the transverse stresses were not yet zero). This permitted calculation of material strength near ambient pressure. Follansbee and Gray (1991a) measured the strength of shock-prestrained Cu using quasistatic reloading experiments. Here, OFE Cu specimens (annealed; 40 μm grain size) were shock loaded to 10 GPa for ~1 μs and recovered "softly" using special techniques (Gray et al., 1989). Quasistatic compression tests (10^{-3} s^{-1}) were then performed on specimens extracted from the shock-recovered discs. The reloading yield strength (at ambient pressure) may be related to material strength in the shocked state provided careful soft recovery techniques are used to minimize reversed plastic flow during unloading. Finally, Millett et al. (1997) determined the strength of shocked polycrystalline Cu (cold-rolled and annealed; 10–20 μm grain size) using the direct method (i.e., simultaneous measurement of longitudinal and transverse stress components). In these experiments, Cu discs were sectioned in half and lateral stress gages were embedded in an epoxy layer that was used to reconstruct the disc. Longitudinal and transverse stresses were measured simultaneously during shock wave propagation, which permits direct calculation of the maximum shear stress. The measurements of Cu strength are plotted in Figure 3.29(a). The values reported from the XRD and quasistatic reloading experiments have been scaled by $\mu(p)/\mu(p=0)$ to provide an appropriate measure of strength in the high-pressure state of the shock wave. The uncertainty that is reported for the XRD measurements is rather small (± 0.006 GPa); the uncertainty in the quasistatic reloading measurements was not reported.

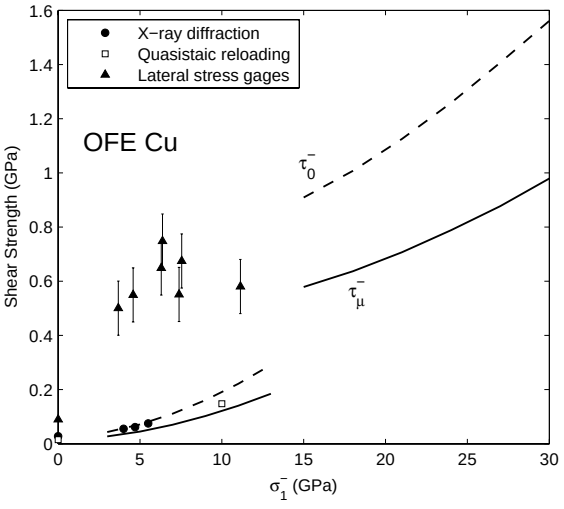

(a)

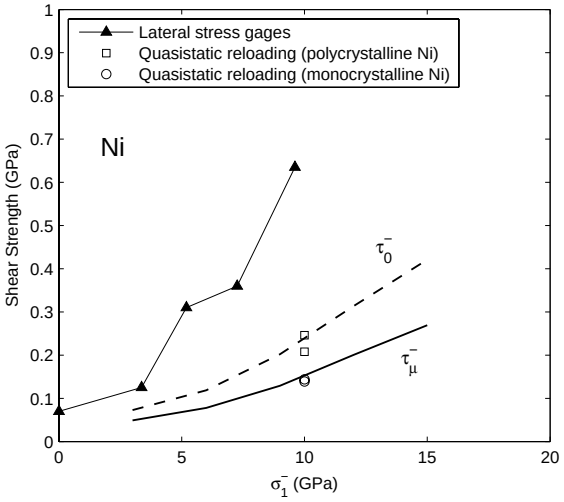

(b)

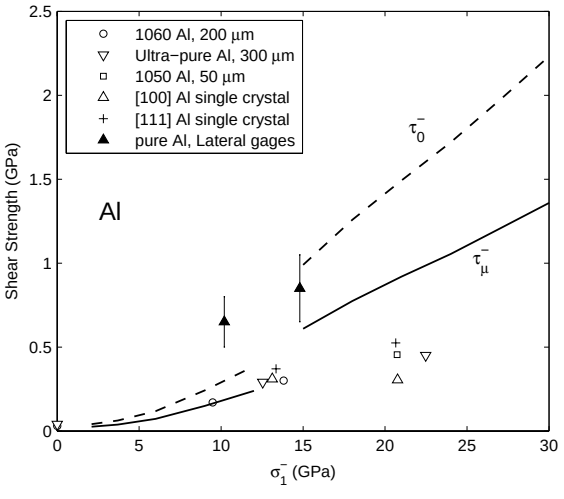

(c)

Figure 3.29: Model bounds of the shear strength in the shocked state for (a) OFE Cu, (b) Ni, and (c) Al are compared to measurements from shock compression experiments performed on mono- and polycrystalline specimens.

Model bounds of the shear strength of OFE Cu in the shocked state are compared to the experimental data in Figure 3.29(a). The breaks in the curves correspond to the shock stresses above which homogeneous dislocation nucleation has been simulated in the model. The occurrence of homogeneous dislocation nucleation leads to much higher dislocation densities, and thus, higher material strength. In the heterogeneous nucleation regime ($\sigma_1^- <15$ GPa), the model bounds are in agreement with the XRD measurements and the quasistatic reloading measurements, while the strengths measured using lateral stress gages are significantly higher. It is currently unclear as to why the measurements of strength differ by so much. The elevated strength measurements cannot be explained by the higher initial yield strength of the cold-rolled Cu specimens, which was estimated from the reported hardness measurement and is plotted at zero stress. Unfortunately, experimental data are not available for comparison in the homogeneous nucleation regime.

The strength of Ni in the shocked state has been measured using two of the above methods. Follansbee and Gray (1991b) measured the strength of shock-prestrained Ni using the quasistatic reloading method. In these experiments, two polycrystalline Ni specimens (grain sizes of 40 μm and 225 μm) and two monocrystalline Ni alloys, i.e., [100] Ni (0.43 wt% C) and [111] Ni (0.72 wt% C), were tested. The shock stress was 10 GPa and the pulse duration was ~1 μs. The reloading yield strengths reported for the polycrystals were converted to maximum shear stresses ($Y = 2\tau$) for plotting purposes; values of the critical resolved shear stresses that were reported for single crystals were plotted directly. Again, the quasistatic reloading data were scaled by $\mu(p)/\mu(p=0)$ to facilitate comparison of the experimental data to model values in the shocked state. Millett et al. (2007) measured the shear strength of pure Ni (forged bar stock; ~200 μm grain size) just behind the shock front using embedded lateral stress gages. The uncertainty in these measurements (± 0.015 GPa, at most) is much smaller than that of the previous Cu measurements. The measurements of Ni strength are plotted in Figure 3.29(b).

Model bounds of the shear strength of Ni in the shocked state are compared to the experimental data in Figure 3.29(b). Again, the model bounds are compatible with quasistatic reloading measurements, but not the measurements that utilize lateral stress gages. Here, we have only plotted results in the heterogeneous nucleation regime ($\sigma_1^- <16$ GPa). Material strength in the homogeneous dislocation

nucleation regime is considerably higher, i.e., about 1.5–2 GPa for shock stresses in the range of 20–30 GPa. It is not plotted here because this makes it difficult to compare the model to available experimental data at lower stresses.

The strength of Al in the shocked state has been measured (indirectly) using the shock/re-shock and shock/release method (Huang and Asay, 2005; Huang and Asay, 2007) and lateral stress gages (Bat'kov et al., 2000). These data are plotted for mono- and polycrystalline Al in Figure 3.29(c). As discussed by Huang and Asay (2007), the polycrystalline results are consistent with the averaged responses of the monocrystals, and grain size seems to have a small effect on the plastic response. Model bounds of the shear strength of Al in the shocked state are compared to the experimental data in Figure 3.29(c). Again, the breaks in the curves correspond to the shock stress above which homogeneous dislocation nucleation has been simulated. In the heterogeneous nucleation regime ($\sigma_1^- <13$ GPa), the model bounds are in agreement with the re-shock and release measurements. The strength measurements that were obtained using lateral stress gages are again significantly higher. In the homogeneous nucleation regime, the model bounds of strength appear to be in agreement with the lateral stress gage data point at 15 GPa, and not with the re-shock and release measurements.

The levels of strength that are measured using the direct stress method (i.e., suitably-oriented stress gages) in shocked Cu (Millett et al., 1997), Ni (Millett et al., 2007), Al (Bat'kov et al., 2000) and precipitate-hardening Al alloys (Millett et al., 2009) are consistently higher than the strengths measured in the same materials using other non-invasive methods (i.e., real-time XRD, quasistatic reloading of shock-prestrained materials, and reshock and release methods). The reason for these rather substantial differences is currently unknown. However, finite element simulations of the lateral stress gage experiments have demonstrated that the interpretation of these experimental results is not a trivial matter (Winter and Harris, 2008). Here, simulations of wave propagation in the specimen assembly show that the epoxy layer (which encapsulates the lateral stress gage) introduces perturbations to the local stress field. These perturbations are caused by the difference of shock wave speed in the metal and the epoxy layer. Thus, the simulated gages register time-dependent lateral stresses that are distinct from the far-field lateral stresses in the metal for some period of time. Although these simulations help address the issue of material hardening (or

softening) in the shock wave, the large discrepancy in strength measurements cannot be explained by these local stress perturbations.

According to our model for pure metals, any difference in material strength should be explained by a difference in dislocation density. Therefore, we have searched for a reason as to why the dislocation density in the lateral stress gage experiments might be higher than the dislocation density in the other experiments. Recall the atomistic simulations of Jarmakani et al. (2008), where it was demonstrated that dislocation density is reduced by one order of magnitude when single crystals are unloaded from the shocked state. Here, the resolved shear stresses in the shocked state hold open many (sub-critical) stacking faults, which collapse when the stress wave is released. This effect is not limited to single crystals since atomistic simulations of shock waves in nanocrystalline Ni also demonstrated that ~40% of the partial dislocations emitted from the GBs are reabsorbed back into the boundaries upon release (Jarmakani et al., 2008). Since the XRD and quasistatic reloading measurements are reckoned in the unloaded state and the lateral stress gage measurements are reckoned in the shocked state, this is a possible reason for an order-of-magnitude difference in the dislocation density in these experiments. If the model bounds of shear strength in Figure 3.29 are scaled by a factor of $\sqrt{10}$, they are brought into better agreement with the lateral stress gage experiments. The scaled bounds for Ni and Al exhibit rather good agreement with the lateral stress gage data, while the scaled bounds for Cu agree only with the data point of highest shock stress. The model could be calibrated to the lateral stress gage measurements if sub-critical dislocation nucleation is accounted for in the constitutive model. However, the re-shock/release measurements (Huang and Asay, 2005; Huang and Asay, 2007) are also reckoned in the shocked state, and they yield measurements of strength that are considerably lower than the lateral stress gage experiments. Therefore, it appears that a difference in dislocation density does not resolve the issue.

3.6. Conclusions

The viscoplastic constitutive model presented in Chapter 2 has been applied to three fcc metals (Cu, Ni, and Al) and one fcc-based precipitate-hardening alloy (6061-T6). The constitutive model was then incorporated in simulations of steady plastic waves in these metals to demonstrate the model and compare results to experimental data. These calculations resolved the structure of the shock front, including all

relevant field variables and dislocation substructure components. The results of the steady wave analysis may be summarized as follows:

- Model calculations are in agreement with the experimentally-measured shock profile data that are available for 6061-T6 and Cu, i.e., direct measurements of material velocity, $u(t)$, and indirect measurements of the plastic rate of deformation, $D_1^p(\psi)$, and shear stress, $\tau(\psi)$, for shock stresses in the range of 2–10 GPa.
- For shock stresses in the heterogeneous dislocation nucleation regime ($\sigma^- \lesssim 15$ GPa), model calculations of dislocation density in the shocked state, N^-, are in agreement with measurements of dislocation density in shock-recovery experiments.
- For shock stresses in the homogeneous dislocation nucleation regime ($\sigma^- \gtrsim 15$ GPa), model calculations of dislocation density in the shocked state, N^-, are in agreement with atomistic simulations of shock wave propagation in Cu, Ni, and Al.
- The model respects the one-fourth power law of Swegle and Grady (1985) for shock stresses that span the regimes of heterogeneous and homogeneous dislocation nucleation, which corresponds to strain rates in the range of 10^6–10^{10} s^{-1}.
- Model calculations of shear strength in the shocked state, τ^-, are in agreement with experiments that use non-invasive techniques to measure strength for shock stress amplitudes up to ~15 GPa in Cu, Ni, Al, and 6061-T6 (e.g., shock/re-shock and shock/release experiments, quasistatic reloading of shock prestrained specimens, and real-time XRD).

Since the shock structure is sensitive to the viscoplastic response of the material, the agreement of model calculations with available shock profile data provides support for the proposed constitutive model. Regarding dislocation density and shear strength, the agreement between the model and experiments (and atomistic simulations) indicates the substructure evolution equations are producing reasonable results, and that our interpretation of material strength (i.e., the resistance provided by the dislocation network) is

justifiable. Thus, the model appears to yield very reasonable results for the pure fcc metals and 6061-T6 Al alloy.

The rate-dependence of the shear stress τ and of substructure evolution have been addressed in Section 3.5.8. In the model, the shear stress in the shock front must be increased to drive dislocation generation and dislocation glide in the presence of phonon drag and the relativistic effect. The model also predicts higher rates of dislocation generation for stronger shock waves. Therefore, the model is in agreement with the notion that the abrupt increase in strain-rate sensitivity ($\partial \ln \tau / \partial \ln \dot{\gamma}$) at $\dot{\varepsilon} \sim 10^4$ s^{-1} is due to higher rates of structure evolution (Regazzoni et al., 1987; Follansbee and Kocks, 1988; Armstrong et al., 2007).

In formulating substructure evolution equations for shock waves, it was essential to address dislocation nucleation. The homogeneous dislocation nucleation criteria presented in Chapter 2 has been applied to all metals considered here. In the pure metals, dislocation sources in the wave front are extremely limited for shock stresses greater than ~15 GPa. Therefore, homogeneous nucleation is expected at higher stresses and heterogeneous nucleation is expected at lower stresses. In 6061-T6, homogeneous nucleation is not expected for shock stresses up to 30 GPa due to the close spacing of sources (precipitates) that emit dislocations. Thus, heterogeneous nucleation prevails in 6061-T6 for the stress amplitudes considered here. The constitutive model could not be brought into acceptable agreement with experiments (for any of the metals) if heterogeneous nucleation was not taken into account. At higher shock stresses, substructure evolution is driven primarily by homogeneous dislocation nucleation. A novel contribution of this work is the distinction of various mechanisms that drive the evolution of the dislocation structure in shock waves.

To our knowledge, this work represents the first plastic wave analysis that incorporates a dislocation-based constitutive law with rate- and path-dependent substructure evolution and microstructure-sensitive glide resistance, including explicit treatment of heterogeneous and homogeneous dislocation nucleation. In addition, the model addresses how material length scales and the structure (width) of the shock front affect the viscoplastic response (in terms of the activation of heterogeneous vs. homogeneous dislocation nucleation). The accuracy of calculations in the weak shock regime indicates the proposed constitutive model may be useful in numerical simulations of high-strain-rate phenomena. One area in

particular that stands to benefit is the simulation of high-rate viscoplastic deformation at small length scales. For example, micro- and nanoscopic structures (or material systems) may have geometric features comparable in size to the width of the shock front. To resolve the deformation of these systems in the shock front, an accurate model of viscoplasticity is essential. This, in fact, has been the primary motivation for the development of this constitutive model since the deformation and mixing of micron-sized Ni and Al particles in (and closely behind) the shock front is of concern to us.

We now wish to consider how the constitutive model might be extended to (i) nanocrystalline materials, and (ii) stress amplitudes where twinning deformation is expected. To apply the model to nanocrystalline fcc metals, one must reformulate the mechanical threshold stress, τ_0, which is no longer governed solely by the dislocation network. The spacing of grain boundaries now has a strong influence on the resistance to dislocation glide. One must also re-examine the homogeneous dislocation nucleation criteria, as the grain boundaries now serve as closely-spaced sources of dislocations. In this case, homogeneous nucleation should be deferred to higher shock stresses. The values of the heterogeneous nucleation parameters, α_{het} and m, will also require alteration to reflect the dislocation emission process in nanoscopic grains, as the number of dislocation sources (per unit volume) and the mean length of emitted dislocation segment will now be different. To address twinning deformation, the kinematics could be framed in terms of concurrent phase transformations (twinning) and crystallographic slip within these transformed domains (Barton et al., 2005). The kinetics of twinning could be described using a model of thermally-activated twin nucleation (Armstrong et al., 2007). The kinetics of glide would retain the same form, although the threshold stress should account for the density of twins, which serve as additional barriers to dislocation glide.

CHAPTER 4

SHOCK WAVE CHEMISTRY OF METALLIC POWDER MIXTURES

We now turn our attention to the chemical reaction of metallic powder mixtures that are subjected to shock wave loading. Shock compression experiments performed on reactive metal powder mixtures have demonstrated the occurrence of high-yield chemical reactions during the stress pulse. However, reaction mechanisms and reaction initiation thresholds are not generally understood in these material systems. To harness these material systems as energetic materials, it is desirable to develop a fundamental understanding of shock-induced reactions in this regard. In this chapter, experimental investigations of shock wave chemistry in metal powder systems are reviewed, with specific emphasis on the Ni/Al system. This is followed by a discussion of mechanisms that have been hypothesized to account for the high rates of mixing in shock-induced reactions.

4.1. Literature review

4.1.1. Distinction of reaction types in shock-compressed media

Chemical reactions in shock-compressed media have been classified according to the time scale on which they occur (Thadhani, 1994). *Shock-induced* chemical reactions occur in the shock front or shortly-behind it (in the stress pulse) during the time scale of mechanical equilibration (< 1 μs). *Shock-assisted* chemical reactions occur on the longer time scale of bulk temperature equilibration (> 10 μs) after the state of stress has been released. In the shock-assisted case, the stress wave modifies the powder mixture and reactions initiate upon the introduction of sufficient thermal energy. Here, *modification* refers to the production of defects and mixing of the constituents due to the shock deformation. The thermal energy may be provided by the irreversible work performed in the shock wave or subsequent thermal treatment of recovered specimens. The primary mechanism of shock-assisted chemical reactions is temperature- and defect-enhanced mass diffusion (Thadhani, 1994), where, for example, one constituent melts and the other

is dissolved in it. This is analogous to the reaction mechanism of self-propagating high-temperature synthesis (SHS).

The mechanisms of shock-induced chemical reactions are currently unclear. Shock-induced reactions result in nearly full conversion of reactant particles (~10 μm in size) to product phases in a sub-microsecond time span. However, the characteristic length of mass diffusion in the shock wave (for a metal with saturated dislocation density and near the melting temperature) is only about 0.1 μm (Horie and Sawaoka, 1993). Therefore, a purely diffusive mechanism of mixing is orders of magnitude too slow to account for shock-induced reactions. Thermally-activated mechanisms are generally inhibited in the shock wave because the time scale is short. Therefore, it is thought that shock-induced reactions are mechano-chemical in nature, rather than thermo-chemical. That is, large scale reactions in the shock wave are the result of strongly-driven mechanical processes instead of the generation and re-distribution of thermal energy. Elevated temperatures might enable isolated reactions at particle interfaces; however, the bulk of the reactant phases remain segregated and unreacted if the intensity of mechanical mixing is insufficient.

Shock-induced chemical reactions are detected using time-resolved measurements of the Hugoniot state. In powder mixtures, the deviation of measurements from the expected inert Hugoniot of the mixture indicates the occurrence chemical reaction in the shock wave. Signatures of shock-induced chemical reactions may take the form of (i) volume expansion (Batsanov et al., 1986), (ii) excess pressure (Bennett et al., 1992), and/or (iii) an increase in the shock wave velocity (Thadhani et al., 1997) due to the heat of reaction and phase transformation. In order for deviations from the inert mixture Hugoniot to be detected by instrumentation, the degree of conversion must be significant, e.g., greater than 30% (Batsanov, 1996). A partial list of experiments that have detected shock-induced chemical reactions in powdered metal systems is provided in Table 4.1. It is now relevant to review the experimental body of work for the Ni/Al powder system, which includes explosive loading and recovery experiments and instrumented (time-resolved) plate impact experiments.

Table 4.1: Experimental observations of shock-induced chemical reactions in powder mixtures

Material System	Researchers
Sn/S	Batsanov et al. (1986)
Fe_2O_3/Al	Boslough (1990)
Mg/S, Al/S, Fe/S, Ti/S	Gogulya et al. (1991)
Ni/Al	Bennett et al. (1992)
Ni/Al	Yang et al. (1997)
Ti/Si	Thadhani et al. (1997)
Mo/Si	Vandersall and Thadhani (2003)
Ni/Al	Eakins and Thadhani (2006)

4.1.2. Shock recovery experiments

Early studies of shock wave chemistry in the Ni/Al powder system centered on the explosive shock loading and recovery of powder mixtures which were then analyzed using microscopy. In these experiments, powder specimens were placed in recovery capsules and subjected to shock waves generated by the detonation of high explosive materials (see Figure 4.1). The drawbacks of this technique are (i) the lack of temporal resolution, and (ii) complex shock conditions (non-uniform pressure and temperature) that are created by wave interactions between the fixture and the powder. However, microscopic analysis of shock-recovered specimens can be useful for inspecting the deformation of the microstructure just below the threshold for reaction initiation.

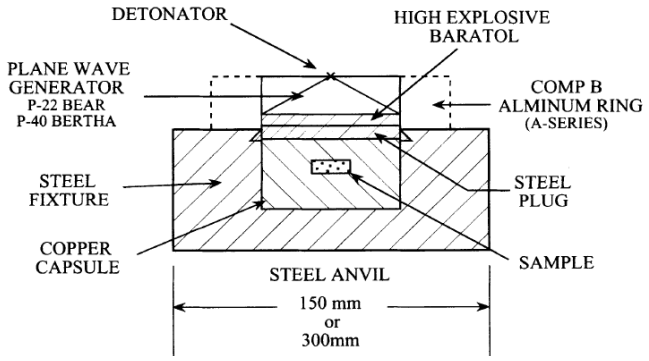

Figure 4.1: Cross sectional view of the Sandia explosive shock recovery fixture (Graham and Webb, 1984).

The shock synthesis of nickel-aluminides from powder mixtures was first demonstrated by Horie et al. (1985). Here, an explosive loading fixture was used to shock mixtures of spherical Ni + Al powders. Microscopic analysis performed on the recovered powder compacts revealed regions of near homogenous Ni_3Al in the corners of the compacts, indicating the occurrence of large scale (non-localized) chemical reaction. The regions of large scale reaction corresponded to the regions of highest temperature in the shocked compact. In the micrographs, a sharp transition between fully-reacted and unreacted regions of the mixture was observed. Additionally, the hardness of fully-reacted regions was significantly elevated, similar to that of a rapidly-solidified metal. These observations suggest that large scale reactions occurring during shock compression were quenched by unloading; however, this does not serve as definitive proof of *shock-induced* chemical reaction.

A subsequent study of shock synthesis in the Ni/Al system (Horie et al., 1986) considered two distinct powder mixtures. The first mixture contained mechanically-blended spherical Ni + Al particles. The second mixture was composed of spherical Al particles that have a Ni coating (hereafter referred to as *composite* particles). Again, an explosive fixture was used to generate the shock waves. Large "pockets" of fully-reacted regions were observed in the mechanically-blended powders, while only localized reactions were observed in the shock-recovered composite powders. The difference in reactivity is presumably due to differences in the mixing conditions. The mechanically-blended mixtures permit mixing of the constituents in the collapsing pore space. This produces volumes of intensely-deformed Al and Ni that are in intimate contact and are subjected to elevated temperatures. In the composite powder mixtures, the collapsing pores do not draw in both constituents. Consequently, the degree of mixing of Ni and Al is comparatively limited. A micrograph from an unreacted region of a mechanically-blended powder mixture is shown in Figure 4.2(a). Here, the Ni particles have been etched to reveal the fine subgrain crystallites that are produced by the shock deformation. The subgrain crystallites result from intense dislocation generation. An interesting feature of this micrograph is the character of deformation about the periphery of the Ni particles, in particular, the topology of the Ni/Al interface. In some regions, the interface is reminiscent of classical surface instabilities that are encountered in fluid mechanics (e.g., Kelvin-Helmholtz, Rayleigh-Taylor, and Richtmyer-Meshkov surface instabilities). The appearance of a local chemical reaction in a shock-recovered composite powder mixture is shown in Figure 4.2(b). Here, it

appears that the Ni shell penetrates into the Al core, perhaps by interface instability or jetting. The product phase ("A" in the micrograph) exhibits a vortical or "whirling" flow structure. Electron probe micro-analysis (EPMA) of the mechanically-blended powders revealed significant penetration of Ni into Al (tens of microns deep). In the composite powder, EPMA showed that the phases remained segregated. Hence, the initial spatial arrangement of the constituent phases can have a rather strong influence on the occurrence of large scale chemical reaction.

The degree of mixing and activation of shocked Ni/Al powder mixtures has been quantified using differential thermal analysis (DTA) (Hammetter et al., 1988). When non-shocked powder mixtures are heated, reaction exotherms are observed after one constituent melts and the other dissolves in it. When shock-pretreated (but unreacted) powder mixtures are subjected to the same heating schedule, the reaction exotherms occur at lower temperatures because the effective mass diffusivity has been increased by the intimate mixing of constituents with high defect densities. The shape and position of the reaction exotherm depends on the factors that control the level of mixing and activation, namely the shock intensity and the initial powder configuration.

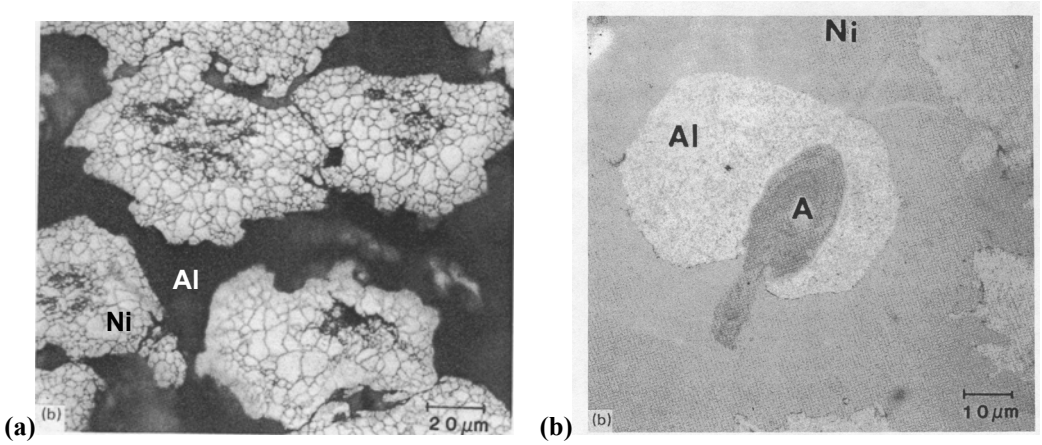

Figure 4.2: Micrographs of shock-recovered Ni/Al powder mixtures (Horie et al., 1986); (a) mechanically-blended powders; (b) composite powder mixtures.

A variety of Ni/Al powder configuration were studied by Thadhani (1990) using the explosive loading and recovery technique. Here, emphasis was placed on determining how particle size and morphology affects the likelihood of large scale chemical reaction. For nominally fixed loading conditions, flaky Ni + spherical Al powder mixtures and the smallest spherical Ni + Al powder mixtures that were considered (each constituent ~1 μm in diameter) exhibited complete reaction of the compact. The Ni flakes in these mixtures are basically plates of sub-micron thickness. All other spherical Ni + Al powder mixtures (larger particle sizes) exhibited high-yield reactions in the corners of the compacts, but remained largely unreacted. The study of particle morphology effects in the Ni/Al was continued in experiments performed on a Sawaoka explosive fixture (Song and Thadhani, 1992). Again, flaky Ni + spherical Al mixtures were more prone to react when compared to the spherical Ni + Al powder mixtures. Additionally, it was observed that the stoichiometry of product phase depended on the shock loading intensity, and therefore, the intensity of mass mixing. It has been suggested that irregular particle morphologies (e.g., flaky particles) tend to promote larger degrees of (bulk) particle deformation, while mixtures composed of spherical or rounded particles tend to have deformation concentrated at the particle surfaces (Thadhani, 1993). Extensive bulk deformation of the particles may enable reactions to penetrate all the way through particles, while deformation localized in the vicinity of particle interfaces may lead to partial surface reactions only.

The role of mixture composition and particle morphology in the Ni/Al system was considered by Dunbar et al. (1993). Here, shock recovery experiments were performed for a range of volumetric distributions (Ni+3Al, Ni+Al, Ni+3Al) that were composed of either fine or coarse spherical Ni + Al powders or flaky Ni + spherical Al powders. Micrographs of certain shock-recovered mixtures are provided in Figure 4.3. The flaky Ni mixtures exhibited large scale reactions for all volumetric distributions. This is in agreement with prior observations and is rationalized by the simultaneous (coordinated) deformation of the Ni and Al phases and the large surface area of intimate contact. The fine spherical powder mixtures exhibited large scale reactions in the corners of the Ni-rich and the near-equivolumetric mixtures, while only sparse localized reaction were observed in the Al-rich mixtures. The coarse spherical powder mixtures exhibited large scale reactions only in corner of the Ni-rich specimen. Thus, it appears that chemical reactions in this system are promoted by increased volume fractions of Ni.

This is because the Ni particles serve as a hard phase that promotes coordinated deformation of both constituents. On the other hand, Al-rich mixtures experience concentrated plastic flow in the softer Al phase, which leaves the bulk regions of the reactants largely separated.

Parallel plate impact experiment performed on composite Ni/Al powder mixtures revealed a critical threshold above there is an abrupt change in the mixing behavior of the constituents (Horie and Sawaoka, 1993). Recovered specimens are shown in Figure 4.4 for impact velocities (stainless steel plates) ranging from 500 m/s to 800 m/s. In micrographs (A) though (C), the deformation of the composite particles is relatively mild. As the flyer velocity is increased, the growth of a product interphase can be identified by the reduction of pure aluminum (the dark phase in the micrographs). These chemical reactions are due to the shock activation and heating of the powder mixtures. When the flyer velocity reaches 800 m/s, there is a rather abrupt change in the character of the particle deformation, as seen in micrograph (D) of Figure 4.4. The mixing of the constituent phases appears chaotic or turbulent. It is thought that this sudden loss of regularity in the packing arrangement is due to surface instability along the Ni/Al interfaces. Although the temporal aspect of shock-induced chemical reactions was not investigated in these experiments, the enhanced mixing in powders shocked above the threshold condition indicates that a mechanism similar to classical surface instabilities and/or adiabatic shear localization may be the precursors to ultra-fast chemical reactions in the shock wave.

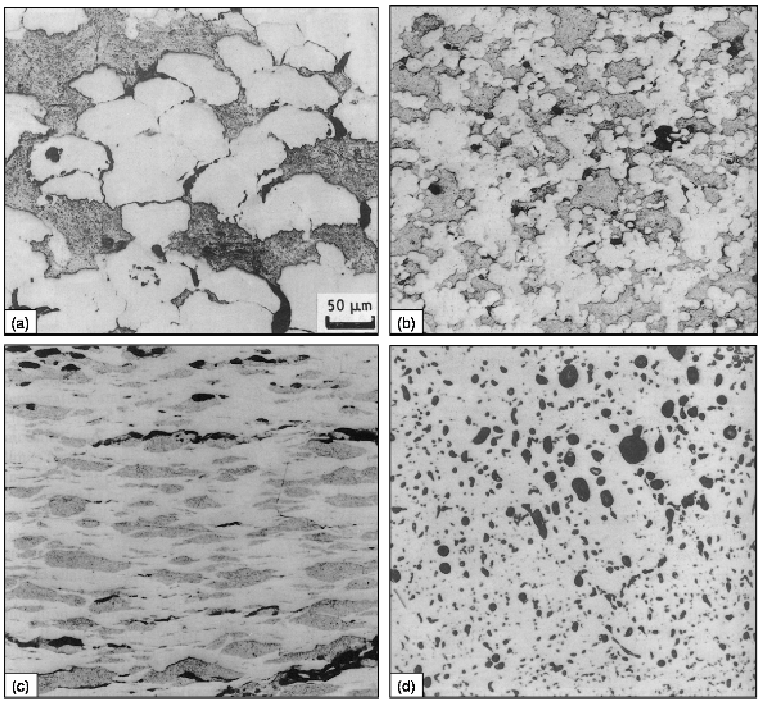

Figure 4.3: Micrographs from shock recovered 3Ni+Al powder mixtures (Dunbar et al., 1993). In unreacted regions, the Ni phase displays bright contrast and the Al phase displays dark contrast; (a) coarse spherical powders; (b) fine spherical powders; (c) flaky Ni + spherical Al powder mixture; (d) fully-reacted region displaying uniform contrast of the product phase with (dark) interspersed solidification pores.

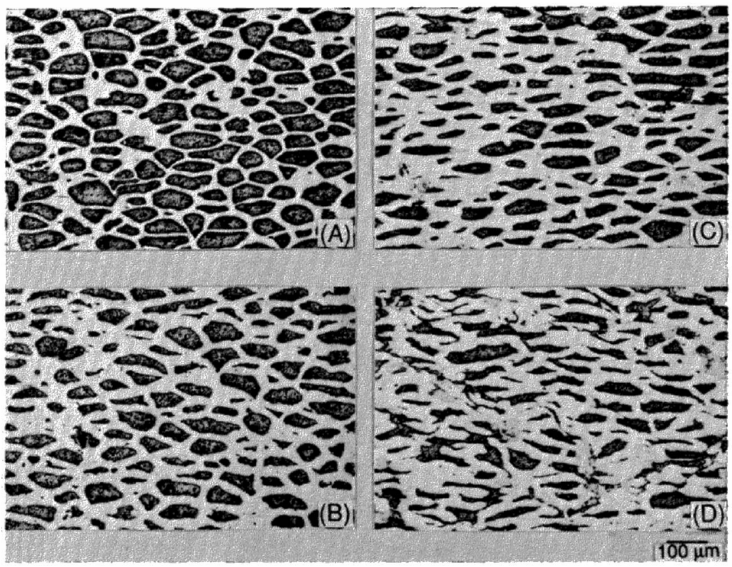

Figure 4.4: Micrographs of Ni/Al composite powder mixtures recovered from plate impact experiments (Horie and Sawaoka, 1993). The initial velocity of the stainless steel flyer plate varied from 500 m/s to 800 m/s for micrographs (A) through (D). The deformation pattern in micrograph (D) has been attributed to flow instability.

4.1.3. Instrumented plate impact experiments

The first experimental observations of *shock-induced* chemical reactions in the Ni/Al powder system were made by Bennett et al. (1992). In these experiments, a stainless steel flyer plate accelerated by a gas gun impacted a plate assembly containing a mixture of spherical Ni + Al powders (5 μm sized Ni particles + 20 μm sized Al particles mixed in a volumetric ratio of 1.7 Ni:Al, 55%TMD). Planar shock waves were generated in the specimens and gages were used to monitor the pressure in the backer plate of the target assembly. A schematic of these instrumented plate impact experiments is shown in Figure 4.5. For flyer velocities greater than ~1075 m/s, pressures in excess of the expected inert response of the powder mixture were recorded (see Figure 4.6(a)). The excess pressure (~5 GPa in these experiments) is due to the heat of reaction and the volume expansion due to compound formation. Since this excess pressure is recorded in the time-resolved pressure profile, it is interpreted as the signature of chemical reactions occurring in the shock wave. The occurrence of shock-induced chemical reactions is further corroborated by microscopic analysis of the recovered specimens, which reveal full conversion of Al; the product phase was predominantly $NiAl_3$.

Yang et al. (1997) performed similar plate impact experiments on the same Ni/Al powder mixtures. Again, an excess pressure (~5 GPa) was observed for stainless steel flyer plates that were accelerated to velocities above ~1075 m/s. Thus, the earlier experimental observations of Bennett et al. (1992) are corroborated by these experiments, which were performed using a different gas gun. These experiments also demonstrated that the structure of the shock wave (i.e., the shock ring-up process) can influence whether or not shock-induced chemical reactions occur in the powder mixture. If a high-impedance material was used as the backer plate in the target assembly, chemical reactions were detected in the first reflected wave provided the stress jump upon reflection was greater than ~14 GPa. However, chemical reactions were not detected if a low-impedance plate was inserted behind the powder, even for impact velocities well above the previous threshold. Since the low-impedance backer plate alters the ring-up sequence (effectively changing a single shock into a series of smaller stress jumps) while leaving the shock energy essentially unchanged, this suggests (i) a stress jump of sufficient magnitude is required to initiate reactions in this experiment, and (ii) the reaction mechanism is intimately tied to mechano-chemical

effects such as the details of particle deformation and mixing in the shock wave, and not just the total energy deposited in the mixture.

Eakins and Thadhani (2006) performed instrumented plate impact experiments on three distinct equivolumetric Ni/Al powder mixtures: (a) micron-scale spherical Ni + Al powders (60% TMD), (b) flaky Ni + spherical Al powders (45% TMD), and (c) nano-scale spherical Ni + Al powders (35% TMD). The measurements obtained from the spherical powder mixtures followed the inert mixture Hugoniot for Cu flyer velocities up to ~1000 m/s. Recovery micrographs from the micron-scale spherical powder mixture showed localized reactions for the impact velocity of 998 m/s; however, the lack of reaction signature in the Hugoniot measurements (combined with the observation of no particle boundaries in the Al phase) indicates that these reactions occurred by melting of Al and dissolution of Ni in the melt. Therefore, these reactions appear to be shock-assisted instead of shock-induced. Alternatively, the flaky Ni mixture exhibited deviations from the inert mixture Hugoniot for shock stresses greater than ~3.5 GPa. This indicates that shock-induced chemical reactions occurred in the flaky Ni mixture, likely due to the favorable mixing conditions that were discussed earlier. It was suggested that reactions did not occur in the micron- or nano-scale spherical powders because the mixing intensity was not strong enough. For example, the bulk Ni and Al phases remained separated by large distances in the micron-scale powders, while the incomplete densification of the nano-scale powders suppressed the intimate mixing of the constituents.

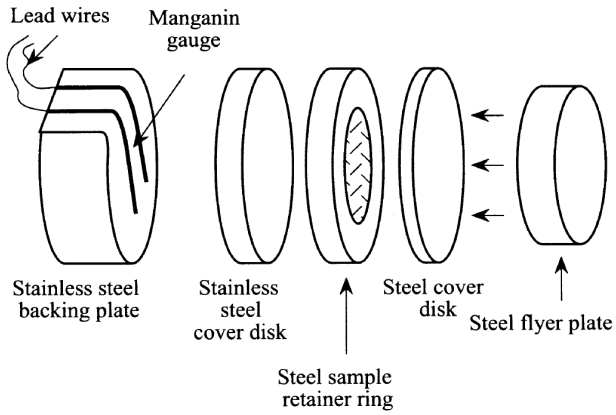

Figure 4.5: Schematic of the instrumented plate impact experiments of Bennett et al. (1992) that were used to generate a sequence of planar shock waves in the powder specimen. The powder specimen is contained within the steel sample retainer ring.

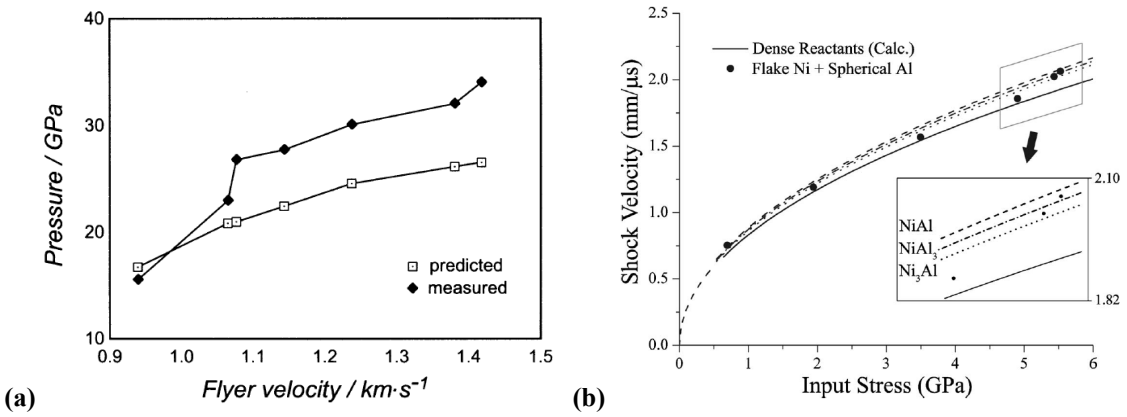

Figure 4.6: Experimental observations of shock-induced reaction signatures; (a) measurements of shock pressure in excess of the predicted inert mixture response (Horie and Sawaoka, 1993); (b) measurements of shock wave speed that deviate from the inert mixture Hugoniot of flaky Ni + spherical Al powders for (input) shock stresses greater than ~3.5 GPa (Eakins and Thadhani, 2006).

4.2. Potential mechanisms of ultra-fast mass mixing

Experimental observations that have been presented for the Ni/Al powder system indicate that shock-induced reactions require certain levels of constituent mixing in the shock wave. It has been seen that the degree of mixing depends on factors such as particle morphology, phase distribution (including porosity), and shock wave intensity. The purpose of this section is to discuss mechanisms that have been proposed to account for the ultra-fast rates of mixing that are required for shock-induced reactions.

The first attempt to explain shock-induced reactions on a mechanochemical basis appears to be due to Dremin and Breusov (1968). According to their *ROLLER* model, when two reactant layers are displaced relative to one another, the product phase that nucleates between them may be regarded as a fast-spinning mechanical roller that draws in the reactants (see Figure 4.7(a)). Thus, the rate of chemical reaction in the shock wave would be greatly accelerated by zones of intense shear deformation. This mechanism of micromixing is in sharp contrast to conventional mass diffusion where phases interpenetrate by random walk of vibrating atoms. Calculations show that the rollers can be composed of approximately 30,000 atoms, reaching approximately 3 μm in size (Dremin and Breusov, 1968).

A conceptual framework that provides a mechanochemical interpretation of the processes leading to shock-induced reactions was proposed by Graham (1989). In this framework, this initial configuration of the material is taken through a transition to the final compressed state. The details of material behavior in the transition zone determine whether or not shock ignition is achieved. The transition zone (i.e., the shock rise to peak stress) involves *Con*figuration changes, *M*ixing, *A*ctivation, and *H*eating; hence, the framework is known as the *CONMAH* model. The initial configuration of the material system (e.g., particle morphology and phase distribution) is an important factor because it has a strong influence on the nature of particle deformation and energy localization. The configuration changes refer to the character of particle deformation in the shock front. Mixing refers to the evolution of reactant boundaries, encompassing both macromixing and micromixing. Shock activation characterizes the increased solid-state reactivity (enhanced mobility of species) due to defect generation and processes such as cleansing of reaction surfaces. Here, the concentration and structure of defects is important since solid-state reactivity is affected by the presence of vacancies, dislocations, stacking faults, twins, and cracks. Finally, heating refers to the thermal energy generated by plastic deformation and chemical reaction, and its transport

through the microstructure. This scheme addresses the mechanochemical factors that control whether or not shock ignition is achieved; however, the mechanism(s) of shock-induced reactions are not identified.

The shock compression of granular media has been described as a "catastrophic" process, i.e., a highly non-equilibrium process of slip, damage nucleation and growth, particle fracturing, and high-speed material jetting (Duvall, 1985). The most promising mechanisms of shock-induced reactions appear to be related to the heterogeneous nature of deformation in shocked powder mixtures. For example, Batsanov (1994) suggested that the distinct physical properties of binary mixture components lead to differences in particle velocity, which, under sufficiently high shock stress, cause the particles to interpenetrate (see Figure 4.7(b)). This process of interpenetration would be aided by particle fracturing in the shock front, which may be accommodated by strong strain gradients and high defect concentrations (Batsanov, 1986). The forced interpenetration of subgrain crystallites ~10 nm in size would cause surface reactions that are nearly instantaneous and would account for degrees of conversion in the range of 20–40%.

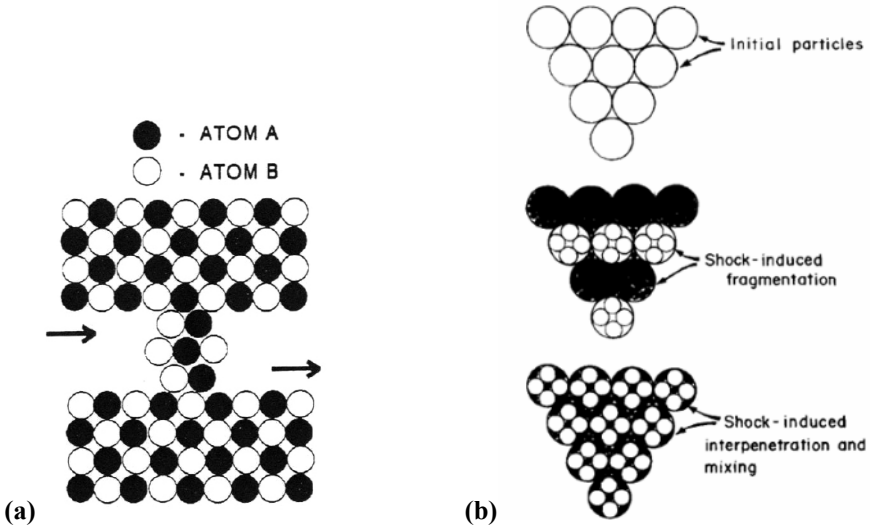

Figure 4.7: Schematics of potential ultra-fast mixing mechanisms; (a) the *ROLLER* model (Dremin and Breusov, 1968) and (b) the model of forced crystallite interpenetration (Batsanov, 1996).

In the Ni/Al system, local chemical reactions go to completion in small regions of intense mixing that exhibit some common flow structures in recovery micrographs (Horie, 1993). The mixing in these regions appears to be due to some type of flow instability, e.g., adiabatic shear localization, surface instability, material jetting, or vortical flow fields. The sources of flow instability are related to the heterogeneous nature of the material system and the heterogeneity of plastic deformation. For example, the collapsing pores in shocked powder mixtures tend to produce high-speed material jets that impact neighboring particle surfaces; this is thought to have a potent mixing effect as one material is driven into another. It has also been shown that shear bands contain evidence of intense constituent mixing (e.g., particle comminution and vortical flow patterns) (Nesterenko et al., 1994); these zones of intense shearing may serve as the nuclei of shock-induced reactions. Finally, a shock wave propagating in a heterogeneous medium does not remain planar. Instead, it will bow out as it encounters material with higher wave speed. The local curvature of the front induces rotational flow fields (Horie and Sawaoka, 1993) and high rate vortical flows have the potential to expose large reactant interfaces that are primed for chemical reaction.

Evidence of surface instability in shocked Ni/Al powder mixtures has been presented earlier (cf. Figure 4.2 and Figure 4.4). The unstable behavior of these interfaces may be due to highly defective surfaces or localized deformation. A model of shock-wave-induced surface instability has been proposed by Horie (1995) based on the non-uniform velocity fields that develop in heterogeneous material systems. Here, the kinetic energy associated with particle velocity fluctuations are transformed to the energy required to created new reactant surface area. This is accompanied by a simultaneous reduction in the mixing length scale. If the length scale of mixing is small enough, defect- and temperature-enhanced solid-state diffusion may be rapid enough to explain shock-induced reactions.

It may be natural to think that shock-induced melting would promote large scale reactions. In fact, a reaction initiation criterion in silicide systems (Nb/Si and Mo/Si) was proposed based on a critical bulk melt fraction of Si (Meyers et al., 1994). However, it has been shown experimentally (Vandersall and Thadhani, 2003) and computationally (Tamura and Horie, 1998) that shock-induced melting ultimately suppresses the occurrence of large-scale reactions in the shock wave. Shock-induced reaction signatures were not detected in plate impact experiments performed on Mo/Si powder mixtures apparently because the melting of Si limited the plastic deformation of the Mo phase and hence the overall mixing of the

constituents (Vandersall and Thadhani, 2003). The numerical simulations of shear bands in the Nb/Si system showed that melting reduces the chance of shock ignition by reducing the energy dissipated in shear bands (Tamura and Horie, 1998).

The overarching theme of this chapter is that the mechanically-driven mixing of powder constituents is the most important factor that determines if chemical reactions are initiated within the time scale of shock compression. The mixing response is sensitive to the initial configuration of the mixture (i.e., the particle morphology and phase distribution) and the details of deformation at the particle level. One of the goals of this research is to resolve the thermomechanics of particle deformation in the shock wave via numerical simulation. In the next chapter, numerical methods used to simulate shock wave propagation at the particle level are presented.

CHAPTER 5

NUMERICAL METHODS FOR DISCRETE PARTICLE SIMULATION

The mechanically-driven mixing of powder constituents is the most important factor that determines whether or not large scale chemical reactions are initiated in the shock wave. Current experimental methods cannot resolve (in space and time) the shock-induced deformation and mixing of the particles. Therefore, it is attractive to study the problem using direct numerical simulation. The focus of this chapter is the development of numerical methods that are used to resolve the particle-level responses in shocked powder mixtures. In particular, the finite element (FE) method will be used to simulate shock wave propagation in discrete micron-scale Ni/Al powder mixtures. Since the deformation of the reactant phases during the shock transition is relevant to the initiation of ultra-fast chemical reactions, the advanced constitutive model that has been developed in Chapters 2 and 3 is incorporated in this simulation framework. Direct numerical simulation is an effective way to study how the initial configuration of the powder mixture affects the shock-induced deformation and mixing of the constituents. For example, certain features of the initial configuration may be isolated and varied; the simulations then reveal how this feature affects local and collective mixing responses.

5.1. Prior work

Finite element simulation has been used in the past to gain insight to the deformation of shocked powder mixtures. It appears that Williamson (1990) performed the first numerical simulations of shock wave propagation in spatially-resolved (discrete) powder mixtures. In that work, an Eulerian finite difference code was used to calculate thermal and mechanical responses of a small set of ordered, periodic, micron-scale stainless steel particles. Benson (1994; 1995b) progressed this field of study by considering volumes elements of randomly-distributed, micron-scale Cu particles. Here, numerical simulations of shock wave propagation were performed using a multi-material Eulerian FE code (Benson, 1995a). The simulations showed that rectangular Cu particles exhibit substantially lower levels of "turbulent" flow in

comparison to cylindrical Cu particles (Benson, 1994) and that Cu powder mixture Hugoniots could be extracted from the simulations (shock wave velocity – particle velocity relations were computed) (Benson, 1995b). Benson and co-workers went on to study shock wave propagation in a variety of material systems, e.g., Ti/SiC powder mixtures (Benson et al., 1995), Ni-based alloy powders and stainless steel powders (Benson et al., 1997), and distributions of HMX crystals (Benson and Conley, 1999). In the simulation work performed on HMX, the initial configuration of the material system was defined by importing the geometry of the HE crystallites from a digitized experimental micrograph. Thus, the actual morphology of a 2D section of the material was simulated instead of an idealized geometric representation. In previous work, shock waves have been simulated in idealized Al/Fe_2O_3/epoxy composites to resolve local thermomechanical responses and to compute Hugoniot curves (Austin et al., 2006). Recently, Eakins and Thadhani (2007; 2008) simulated shock waves in spherical Ni + Al powder mixtures and flaky Ni + spherical Al powder mixtures (of varying porosity) wherein initial particle morphologies were imported from digitized micrographs. In that work, the simulated Hugoniot curves were shown to be in agreement with measurements and detailed calculations of the shock front and particle deformation (which, in some cases, appeared highly fluidic) were presented for each of the powder mixtures.

The simulation work referenced above addresses the thermomechanics of shocked powder mixtures. Do and Benson (2000; 2001) incorporated heterogeneous chemical reaction kinetics in FE simulations of shock waves in discrete Nb/Si powder mixtures. Here, a kinetic law was postulated for the rate of reaction in cells (pools) containing reactants. This enabled the calculation of coupled thermo-mechano-chemical responses of the powder mixture in the shock wave. However, a mechanism of mass mixing was not addressed in their kinetic law. Instead, it was assumed that mass was instantaneously transported through the interfacial product layer. This is somewhat incongruous with mechanistic interpretations of shock-induced chemical reactions because the mixing of reactants is the overall rate-limiting step.

The discrete element method has also been used to simulate the shock-wave-induced responses of powder mixtures and other heterogeneous media. Here, the rigid body equations of motion are solved for a set of mass particles that interact through rheological elements (springs, dampers, etc.). This method of simulation is especially useful for resolving certain mixing characteristics because additional models and/or

assumptions need not be introduced for fracture, as in the case of continuum methods. Tamura and Horie (1998) used the discrete element method to simulate mechano-chemical interactions in shear banding regions of Nb/Si and Ni/Al material systems. It was assumed that local chemical reactions were initiated when reactants in contact exceeded a threshold temperature. Signatures of classical thermal explosion were calculated when there was sufficient mixing of reactants in the shear bands. Here, reductions in material thickness (which are accompanied by increases in surface area) led to more intimate mixing as compared to fragmentation processes, since pores tended to develop around large fragments. Yano and Horie (1998) used the discrete element method to study the shock-induced responses of Ni/Al and Ti/Teflon powder mixtures. In these simulations, the dispersion of particle velocity in the shock wave was computed. Based on these velocity perturbations, it was shown the length scale of mass mixing may be reduced to ~60 nm, which is small enough to rationalize shock-induced reactions on the basis of diffusive mass transport.

5.2. The Eulerian finite element method

In the present work, the simulations of shock wave propagation are performed using *Raven* (Benson, 1995a), a 2D multi-material arbitrary Lagrangian-Eulerian (ALE) finite element code. An Eulerian formulation is utilized because pure Lagrangian formulations typically cannot handle the severity of deformation that is encountered in the shock compression of porous material systems. In this section, a brief description of the numerical methods in *Raven* is provided. The literature may be consulted for further details; see, for example, the comprehensive review article on Lagrangian and Eulerian hydrocodes that has been compiled by Benson (1992).

The conservation of mass, momentum, and energy may be written in an Eulerian coordinate system as

$$\frac{\partial \rho}{\partial t} + \nabla \cdot \left(\rho \boldsymbol{u} \right) = 0 \tag{5.1}$$

$$\frac{\partial \left(\rho \boldsymbol{u} \right)}{\partial t} + \nabla \cdot \left(\rho \boldsymbol{u} \otimes \boldsymbol{u} \right) = \nabla \cdot \boldsymbol{\sigma} + \rho \boldsymbol{b} \tag{5.2}$$

$$\frac{\partial \left(\rho e \right)}{\partial t} + \nabla \cdot \left(\rho e \boldsymbol{u} \right) = \boldsymbol{\sigma} : \boldsymbol{L} + \rho H - \nabla \cdot \boldsymbol{q} \tag{5.3}$$

where ρ is the mass density, $\boldsymbol{u}$ is the material velocity, $\boldsymbol{\sigma}$ is the Cauchy stress, $\boldsymbol{b}$ is the specific body force, e is the specific internal energy, $\boldsymbol{L}$ is the velocity gradient, H is the specific rate of heat generation from sources, and $\boldsymbol{q}$ is the heat flux. The conservation equations may be cast as general transport equations, which are decoupled and solved sequentially through operator splitting (Benson, 1995a). The operator split decomposes the solution into a Lagrangian step and an Eulerian step. During the Lagrangian step, the solution is marched forward in time with the Lagrangian mesh following the deformation of the material. During the Eulerian step, solution variables are advected between the cells of the Eulerian mesh while time remains constant, thus reconciling the two computational meshes. The advantage gained here is the avoidance of severe element distortions; thus, arbitrarily large deformations can be handled. *Raven* is classified as an arbitrary Lagrangian-Eulerian code because the motion of the Eulerian mesh may be prescibed.

The spatial domain is discretized using a logically regular (structured) mesh, which simplifies the data structures and transport alogrithms. Time integration is performed explicitly. The maximum permissible time step is determined by the Courant stability criterion, which limits the time step to the minimum time necessary for an acoustic wave to traverse the smallest element edge. Finally, artifical viscosity is used to smear the shock front over a transition region that is sharp but continuous. The artificial viscosity damps out oscillations near the shock front, which, if left unchecked, can destroy the solution.

5.2.1. The Lagrangian step

The computational sequence of the Lagrangian step adheres broadly to the framework used in many second-order-accurate explicit Lagrangian hydrocodes. There is, however, a complicating factor: the allowance of more than one material in a single element. The multi-material elements are handled by introducing a mixture theory for the sub-element thermodynamics and algorithms that track material interfaces. These material interfaces are perfectly-bonded in the code. The solution is marched forward in time according to the procedures given in **Box 5.1**. Here, the subscripts n and $n+1$ refer to the beginning

and end of the time step, respectively; the superscipt m denotes the value of a quantiy for the m^{th} material in the element.

5.2.2. The Eulerian step

The deformed state of the material (i.e., all solution variables and material coordinates) is described by the Lagrangian mesh at the end of a time increment. During the Eulerian step, the material description contained in the Lagrangian mesh is remapped to the Eulerian mesh while time remains constant. The computational sequence of the Eulerian step is provided in Box 5.2. The transport of material between the elements is handled with advection algorithms. Solution variables (e.g., mass density, internal energy, and stress) are advected using the MUSCL (Monotone Upwind Scheme for Conservation Laws) transport algorithm developed by Van Leer (1977). The interfaces in multi-material elements are reconstructed using the method of Youngs (1982).

Box 5.1: Procedures for the Lagrangian step

1. At time t_n, the nodal forces $\boldsymbol{f}_n$ are calculated from the stress state $\boldsymbol{\sigma}_n$, surface tractions $\boldsymbol{\tau}_n$, and body forces $\boldsymbol{b}_n$.
2. The nodal accelerations $\boldsymbol{a}_n$ are calculated from the nodal forces and the (lumped) mass matrix.
3. The acceleration field is integrated to obtain the velocity field $\boldsymbol{u}_{n+1/2}$.
4. The velocity field is integrated to obtain the updated positions of the material points $\boldsymbol{x}_{n+1}$.
5. The rate of deformation is calculated from the velocity gradient, i.e., $\boldsymbol{D}_{n+1/2} = sym\left(\boldsymbol{L}_{n+1/2}\right)$, and partitioned among the materials in an element according to the mixture theory.
6. The deviatoric stress in each material $\boldsymbol{s}^m_{n+1}$ is updated using an objective stress rate. Here, the stress increment from the constitutive model is added at the midpoint of the time step.
7. The artificial viscous stress q^m_{n+1} is calculated based the elemental velocity jump.
8. The pressure of each material p^m_{n+1} is calculated from the equation of state, i.e., $p^m_{n+1} = p\left(v^m_{n+1}, e^m_{n+1}\right)$, where v^m_{n+1} is the updated specific volume.
9. The internal energy of each material e^m_{n+1} is updated based on the work done during the time step.
10. Based on the stress in each material, i.e., $\boldsymbol{\sigma}^m_{n+1} = \boldsymbol{s}^m_{n+1} - (p^m_{n+1} + q^m_{n+1})\boldsymbol{I}$, the mean elemental stress $\boldsymbol{\sigma}_{n+1}$ is calculated according the mixture theory.
11. The next time step Δt_{n+1} is calculated according to the Courant stability criterion.

Box 5.2: Procedures for the Eulerian step

1. The volume transported between neighboring elements is calculated based on mesh motion.
2. The values of the solution variables associated with the transported volumes are calculated and advected.
3. The material interfaces within mixed elements are reconstructed.
4. The meshes are reconciled and the calculation proceeds to the next Lagrangian step.

5.2.3. The heat transfer step

The heat transfer steps are staggered in-between the Lagrangian (deformation) steps. The internal energy is updated according to the heat fluxes that are computed over the spatial domain. The temperature θ is calculated from the thermal energy content of a material, i.e.,

$$\theta = \frac{e - e_c(\eta)}{c_p} \tag{5.4}$$

where c_p is the specific heat at constant pressure and e_c is the cold compression energy, which is a function of the compression $\eta = \rho/\rho_0$. Equation (5.4) is adjusted to incorporate the latent heat of fusion if the material is (partially) melted.

5.3. Methods for simulating shock waves in discrete powder mixtures

The methods specific to our simulation of shock waves in discrete Ni/Al powder mixtures are now presented. The simulations are performed on *statistical volume elements* (SVEs) of powder mixture because representative volume elements (RVEs) are likely too large for simulation with available resources. Here, multiple instantiations of a given powder mixture are simulated to build up statistical descriptions (ensemble averages) of material response. In the sections that follow, we discuss (i) the specific Ni/Al powder mixtures that are considered in this work, (ii) the method of generating initial powder geometries, (iii) the thermal and mechanical constitutive laws for each phase, and (iv) the initial-boundary value problem that is used to simulate shock wave propagation in discrete particle mixtures.

5.3.1. Powder mixtures of interest

The initial configuration of a powder mixture is determined by the volumetric distribution of phases and their arrangement in space. In this work, the simulated Ni/Al powder mixtures are characterized by:

- Mixture composition (volume fractions of the constituents)
- Relative density of the mixture (%TMD)
- Particle morphology (size and shape)
- Spatial arrangement of phases

The relative density (%TMD) is the mass per unit volume of the porous mixture relative to that of the fully densified mixture. The mixtures that have been selected for simulation are summarized in Table 5.1. The powder mixtures have been grouped into classes. Mixture class B contains variants of powder mixtures with large Al particles and smaller Ni particles. Mixture class C contains variants of the composite powders (i.e., Al particles with Ni coatings). Mixture class E contains variants of powder mixtures with equal-sized Ni and Al particles. The simulated powder mixtures have been selected to facilitate comparison to experiments and to explore the role of powder configuration for a fixed set of constituent volume fractions. Mixture B1 corresponds to the experimental powder mixture that displayed signatures of shock-induced chemical reactions above a critical shock threshold (Bennett et al., 1994; Yang et al., 1997). Mixture C1 corresponds to the experimental powder mixture that displayed extensive flow instability above a critical shock threshold (Horie, 1993; Horie, 1995). These experiments were not time-resolved, so the issue of whether or not chemical reactions occurred during the stress pulse was not addressed; however, the micrographs from recovery specimens (cf. Figure 4.4) indicate that large scale reactions did not occur in these mixtures. Mixture E2 corresponds roughly to one of the powder mixtures considered in the experiments of Eakins and Thadhani (Eakins and Thadhani, 2006; Eakins, 2007). In these instrumented plate impact experiments, shock-induced chemical reactions were not detected for Cu flyer velocity up to ~1.0 km/s. In the equivolumetric Ni/Al powder system that is 60% TMD, four distinct powder configurations have been selected for simulation (mixtures B2, C2, E1, and E2).

Table 5.1: Simulated Ni/Al powder mixtures

Mixture	Molar composition	Volumetric ratio (Ni:Al)	% TMD	Particle shape	Mean particle size (μm)	
					Ni	Al
E1	1.5 Ni + 1 Al	1	60	spherical Ni / spherical Al	5	5
E2	1.5 Ni + 1 Al	1	60	spherical Ni / spherical Al	20	20
B1	2.6 Ni + 1 Al	1.7	55	spherical Ni / spherical Al	5	20
B2	1.5 Ni + 1 Al	1	60	spherical Ni / spherical Al	5	20
C1	1.8 Ni + 1 Al	1.2	65	composite particles	60 (outer dia.)	
C2	1.5 Ni + 1 Al	1	60	composite particles	60 (outer dia.)	

5.3.2. Generating powder mixtures for simulation

The simulation of a large set of fully-3D powder mixtures is prohibitively expensive for our purposes. Therefore, the complexity of the problem has been reduced by considering the propagation of shock waves in 2D representations of the powder mixtures. In the 2D approximation, the actual spherical particles are represented as circular cross sections in the plane of interest. Plane strain is assumed, so the particle cross sections are extended as cylinders out of the plane. The main drawback of the 2D approximation is that out-of-plane particle motions are constrained. However, the 2D simulations are still useful for (i) quantifying the deformation of idealized constituents and (ii) comparing the relative responses of distinct powder mixtures. Furthermore, it is reasonable to speculate that 2D simulations are capable of picking up hints of the mechanisms that enable shock-induced reactions.

A flexible algorithm has been developed to generate the initial geometry of a user-defined powder mixture. This algorithm has been used to generate 2D representations of the powder mixtures listed in Table 5.1. Here, sets of particles are randomly generated according to the volume fractions of the Ni and Al phases. The particle diameters for each phase are drawn from lognormal distributions (the mean and variance are prescribed). For the powder mixtures in Table 5.1, the standard deviation of each size distribution was 5-10% of the mean particle size. The particles are placed in a volume element (of prescribed size) using a random sequential addition process (Torquato, 1991). The locations of the particle centroids are randomly drawn from a uniform distribution, subject to the constraint that particle cross sections do not overlap excessively. The allowance of small overlaps creates a distribution of particles with small indentations in regions where they contact other particles, similar to that of a pressed powder. Finally, spatially-periodic instantiations of a powder mixture are obtained through appropriate treatment of particles that fall on the boundaries of the SVE (i.e., a particle that intersects the left-hand surface is completed on the right-hand surface).

Spatial correlations among the phases may be achieved by adjusting the positions of the particle centroids using a simulated annealing procedure (Austin, 2005). This is not pursued in the current work because (i) the spatial correlation functions are higher-order descriptors of the powder mixtures, and (ii) no such data have been reported for the Ni/Al powder mixtures of interest. Therefore, as a first step we focus on the effects of basic powder configuration for sets of randomly arranged particles.

An instantiation of the 20 μm equal-sized Ni/Al powder mixture (E2) that has been generated is shown in Figure 5.1. This powder mixture is similar to the spherical –325 mesh Ni/Al powders that have been considered in instrumented plate impact experiments (Eakins and Thadhani, 2006; Eakins, 2007). A purpose of simulating this powder mixture is to quantitatively compare results obtained from idealized powder mixtures to experiments performed on particle mixtures that have more complex morphologies. Explicit rendering of the actual particle morphology in shock wave simulations has been considered in prior work (Eakins and Thadhani, 2007; Eakins and Thadhani, 2008) and is not repeated here. The geometry of the mixture E1 is similar the geometry of the mixture E2. The only difference is that all dimensions are reduced by a factor of four when these powder mixtures are generated. The equal-sized Ni/Al powder mixtures provide an opportunity to examine a few size-dependent effects related to particle deformation. For example, the grain size of the polycrystalline particles is an inherent material length scale that may be held fixed as the mean particle diameter is varied. The mean pore size is another length scale of interest since the nature of particle deformation and energy localization are sensitive to the configuration of pores.

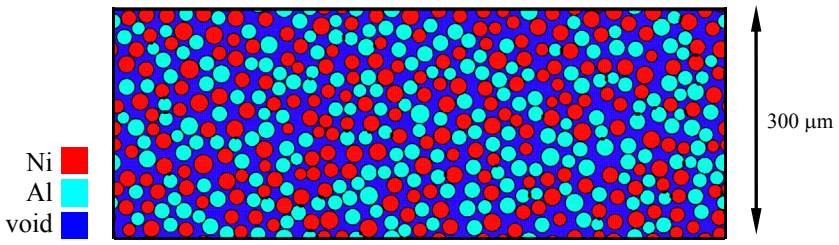

Figure 5.1: A randomly-generated instantiation of the 20 μm equal-sized powder mixture (E2).

Instantiations of the large-Al powder mixtures (B1 and B2) are shown in Figure 5.2. Mixture B1 was generated according to the powder mixtures considered in the instrumented plate impact experiments of Bennett et al. (1994) and Yang et al. (1997). The large-Al powder mixtures allow one to probe the effect of relative particle size. The effect of Al content can be assessed through comparison of the simulated responses of mixtures B1 and B2; however, this comparison would not be ideal because the porosity of these mixtures differs slightly.

Instantiations of the composite powder mixtures (C1 and C2) are shown in Figure 5.3. Mixture C1 corresponds to the powder mixture considered in the plate impact experiments of Horie (1995). The composite powder mixtures provide an opportunity to investigate the effect of phase arrangement, specifically how Ni coatings influence the mixing of constituents during pore collapse. For a fixed particle size and porosity, the volumetric distribution of reactants is altered by adjusting the shell thickness. Two Ni shell thicknesses have been selected for study (~10 μm and ~9 μm). The effect of Al content in the mixtures could be assessed; but again, this comparison would not be ideal because the porosity of these mixtures differs slightly. It is relevant to note the pore configuration (size and shape) is distinct for each of the mixture classes (B, C, and E).

The dimensions of SVEs were selected to include (what is judged) a sufficient number of particles for each phase. Accordingly, the transverse (vertical) dimension of an SVE was selected to be at least 10 times the size of the largest mean particle diameter. The longitudinal (horizontal) dimension of the SVE was made at least 2 times as large as the transverse dimension. This procedure yields SVEs that contain hundreds of particles, and allows shock waves propagated in the longitudinal direction to approach quasi-steady conditions.

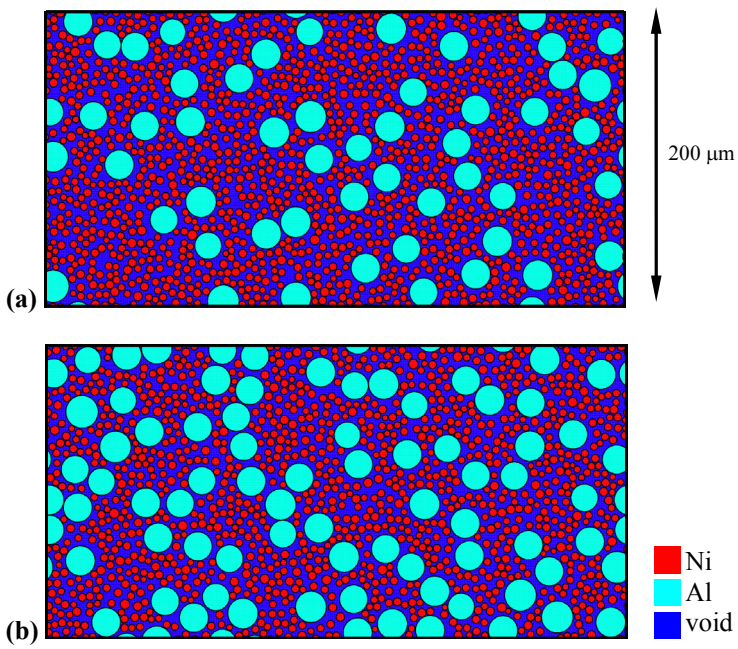

Figure 5.2: Randomly-generated instantiations of the large-Al powder mixtures; (a) mixture B1; (b) mixture B2.

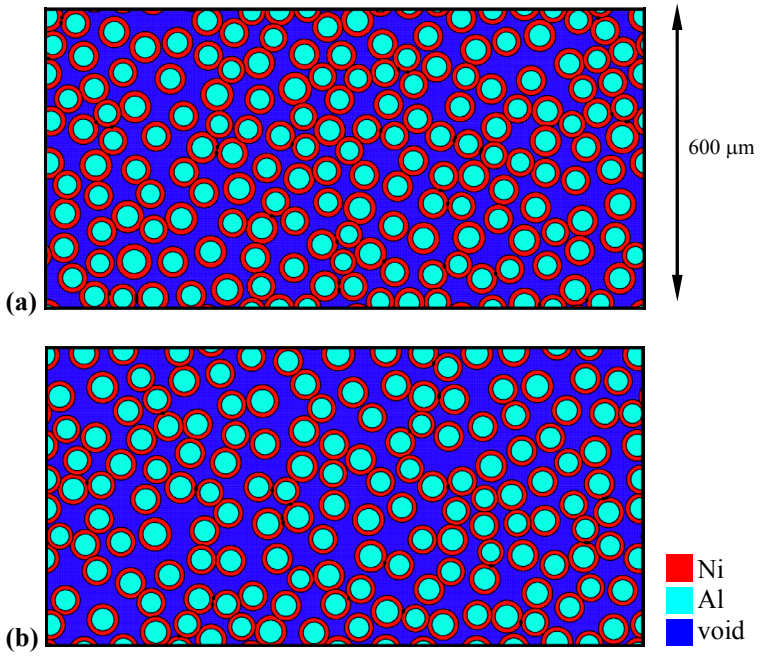

Figure 5.3: Randomly-generated instantiations of the composite powder mixtures; (a) mixture C1; (b) mixture C2. The coating thickness is ~10 μm for mixture C1 and ~9 μm for mixture C2.

5.3.3. Initial-Boundary Value Problem

The problem of interest is the propagation of a nominally planar shock wave in a powder mixture. This is achieved through specification of the boundary conditions and initial conditions. A schematic of the initial-boundary value problem is shown in Figure 5.4. The shock is delivered to the powder mixture by a deformable flyer plate that is assigned an initial velocity. All other components of the SVE are initially stationary. The top and bottom surfaces of the SVE are restrained by rigid frictionless walls, i.e., $\boldsymbol{u} \cdot \boldsymbol{n} = 0$ and $\boldsymbol{n} \cdot \boldsymbol{\sigma} \cdot \boldsymbol{t} = 0$, where $\boldsymbol{u}$ is the material velocity, $\boldsymbol{\sigma}$ is the Cauchy stress, and $\boldsymbol{n}$ and $\boldsymbol{t}$ are the surface normal and tangential unit vectors, respectively. The left and right surfaces of the SVE have transmitting boundary conditions in the normal direction and unconstrained tangential displacements. The transmitting boundary conditions allow a shock wave to pass freely through the boundary without any wave reflection. This is achieved by adjusting the normal stress on the boundary according to the local jump in material velocity (McGlaun, 1982), i.e.,

$$\boldsymbol{n} \cdot \boldsymbol{\sigma} \cdot \boldsymbol{n} = \int_0^t \rho D \left(\boldsymbol{u} \cdot \boldsymbol{n} \right) dt' \tag{5.5}$$

where D is the shock wave velocity. Thus, the initial-boundary value problem is analogous to a miniature plate impact experiment, with the simulation window fixed on the powder mixture. In these simulations, both the incident and reflected waves are compressive pulses.

It would be ideal to apply periodic boundary conditions to the top and bottom surfaces of the volume element. In fact, the initial geometries of the powder mixtures have been generated in a periodic manner specifically for this purpose. However, a current limitation of the FE code is a conflict that arises in the corners of the domain when periodic and transmitting boundary conditions are applied in the desired way. Therefore, rigid frictionless walls are utilized to approximate the macroscopic state of uniaxial strain in a shock wave. The Lagrangian boundary conditions impose a set of physical constraints on the material contained within the SVE. One must also prescribe the motion of the Eulerian mesh and the extrapolation method for materials crossing the boundary of the Eulerian mesh. In this work, the Eulerian mesh is fixed in space for the duration of the simulation and material is permitted to flow only through the left and right boundaries of the SVE.

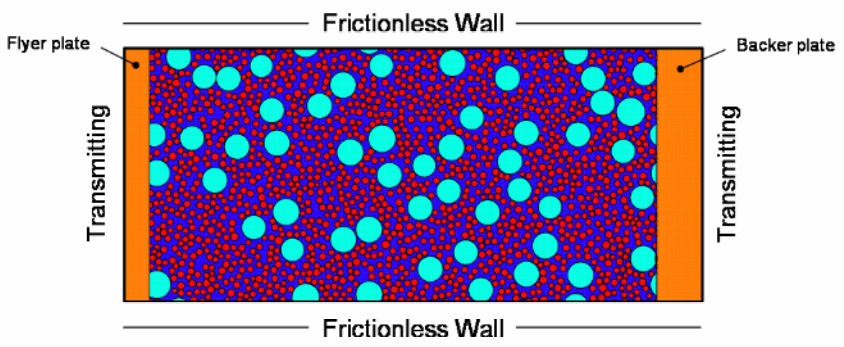

Figure 5.4: The initial-boundary value problem for planar shock wave propagation in the Ni/Al powder mixtures. The initial velocity of the flyer plate is prescribed.

Instrumented plate impact experiments have detected shock-induced reactions in the first reflected wave of the ring-up sequence in shocked Ni/Al powder mixtures (Bennett et al., 1992; Yang et al., 1997). It has been suggested that sufficiently large jumps in shock stress are required to drive the particle-level deformation that initiate these reactions. Therefore, a backer plate (of finite impedance) is included to simulate reflected waves in the densified powder mixtures. The plate material was selected according to what was used in the corresponding plate impact experiments. The width of the backer plate and the simulation time window were selected to allow one full reflection of the shock wave without any particles exiting the Eulerian mesh. Simulation times range from ~120 ns (for the smallest equal-sized powder mixtures) to ~1000 ns (for the composite powder mixtures). The simulation times, which depend on SVE size and shock intensity, should be sufficiently long for studying mechanical processes responsible for the initiation of reactions in the shock waves.

5.3.4. Meshing

The spatial domain is discretized using a uniform rectangular array of 2D solid quadrilateral elements. The elements have a single integration point with viscous hourglass control. As mentioned earlier, interface trackers resolve material interfaces in multi-material elements. It is desirable to use the same element size in all simulations to facilitate comparison of the distinct powder mixtures. However, it is impractical to use a fixed element size when one considers the range of SVE and particle sizes that are

considered in this work. We have found that an element size of ~1 μm provides an agreeable balance between spatial resolution and computational time. The powder mixtures generated for simulation have been meshed using element sizes ranging from 0.5 μm (mixture E1) to 2 μm (mixtures C1 and C2). In previous simulation work, it was recommended that the smallest particles should be spanned by at least 2–3 elements (Benson, 1995b). In our simulations, the smallest particles are spanned by at least 6 elements (typically, particles are spanned by 10 elements or more). In the worst case scenario (mixture C2), the Ni coating is spanned by 4 elements.

5.3.5. Constitutive models

The stress is decomposed into volumetric and deviatoric parts, i.e., $\boldsymbol{\sigma} = \boldsymbol{s} - (p+q)\boldsymbol{I}$, where p is the pressure, and q is the artificial bulk viscous stress. The pressure is calculated according to an equation of state (EOS). The Gruneisen EOS is used for the Ni and Al phases and the plate materials, i.e.,

$$p - p_H = \frac{\Gamma}{v}(e - e_H) \tag{5.6}$$

where the reference state falls on the Hugoniot (denoted by a subscript *H*), v is the specific volume, $\Gamma \equiv v(\partial p/\partial e)_v$ is the isotropic Gruneisen parameter. The following constitutive assumption is invoked: $\Gamma/v = \Gamma_0/v_0$. The EOS of the regions that are void of material is simply $p = 0$. In actuality, the pores are usually filled with air (e.g., the experiments mentioned earlier were not performed in a vacuum). Gas that is trapped in the collapsing pores will be compressed to a high degree, and its temperature will be raised. This is neglected in the current calculations.

The deviatoric responses of the Ni and Al phases are defined by the viscoplastic constitutive model that was presented in Chapters 2 and 3. This constitutive relation is sensitive to the rate of deformation in the shock wave and the material microstructure (i.e., the dislocation substructure and grain size). It has been developed with special consideration of the mechanisms of shock-wave-induced viscoplasticity. The constitutive model has been added to the FE code as a user-material subroutine. Here, the deviatoric stress, plastic loading parameter, and internal state variables are updated using forward-Euler time integration, which is consistent with the time integration procedure of the FE code in explicit mode.

The numerical implementation of the constitutive model has been verified by simulating planar shock waves in homogeneous slabs of Ni and Al.

For the micron-scale particles considered in this work, the initial yield strength of the materials may depend on particle size. This is neglected in the current work because the initial yield strength is a feature that is buried in the lower left hand corner of the stress-strain diagram. The large strains and high dislocation densities that are encountered in the shock deformation quickly negate the effect of initial yield strength in Ni and Al. That is, the particles have a quickly-fading memory of initial strength. The subsequent strength is modeled according to the evolving dislocation substructure.

The deviatoric responses of the driver and backer plates are defined by the Steinberg-Guinan model for OFHC Cu and stainless steel (304 SS) (Steinberg et al., 1980). The use of a rate-independent strength model for the compression plates is acceptable because the deformation of the plates is not of interest; the plates serve only to deliver and reflect the shock waves. The deviatoric stress in voided regions is null.

The conduction of heat in shock waves is sometimes significant. The characteristic length of thermal diffusion (for pulsed excitation) is $x_t = 2\sqrt{\alpha t}$ where α is the thermal diffusivity and t is the elapsed time. For the time scale of shock wave propagation (100–1000 ns), x_t is in the range of 6–20 μm for Al, which is comparable to the particle size. Therefore, heat transfer is modeled using Fourier's law of heat conduction. The thermal conductivity, κ, of Ni and Al is reported in Table 3.6. The pores are modeled as insulators, i.e., $\kappa = 0$.

The melting temperature of the constituents, θ_m, is approximated using a linear expansion in pressure about the ambient state, i.e.,

$$\theta_m = \theta_{m,a} + \left(\partial\theta_m/\partial p\right)\max\left(p, 0\right) \tag{5.7}$$

The initial melting temperature, $\theta_{m,a}$, the slope of the melting curve, $(\partial\theta_m/\partial p)$, and the latent heat of fusion, ΔH_{fus}, are reported for Ni and Al in Table 3.6. The values of $(\partial\theta_m/\partial p)$ were estimated by fitting lines to the diamond anvil cell data for Ni (Lazor et al., 1993) and Al (Boehler and Ross, 1997) in the range of 0–60 GPa. After a material is fully melted (i.e., the phase transition is completed) the strength of the

material is reduced to zero and the deviatoric response of the liquid metal is framed as $\boldsymbol{s} = 2\mu_v \boldsymbol{D}'$, where μ_v is the melt viscosity. The melt viscosity of Ni and Al are taken as $\mu_v \sim 2\times10^{-7}$ GPa μs.

It would be desirable to model the chemical reaction of the Ni and Al phases during shock wave propagation. However, the mechanism of mass mixing that enables shock-induced chemical reactions is currently unclear (cf. Chapter 4). The arbitrary assignment of fast reaction kinetics in the FE simulations wouldn't necessarily further our understanding of the reaction mechanism. In fact, the chemical reactions might obscure the particle-level deformation processes that initiate the reactions in the first place. Therefore, it is pertinent to model the thermomechanics of shock wave propagation in the Ni/Al powders in the absence of chemical reactions to gain a better understanding of the mechanical processes leading up to reaction initiation. In this work, the chemical reaction of Ni and Al is not modeled in the FE simulations. Since intermetallic reactions in the Ni/Al system release heat and expand volume, the deformation and mixing that is calculated in the FE simulations will be underestimated when compared to actual volumes of material that undergo reaction.

5.3.6. Material properties and model parameters

Relevant material properties and constitutive model parameters for Ni and Al are provided in Table 3.6 and Table 3.7. A few modifications are required for the discrete particle shock simulations. The grain size of the polycrystalline Ni and Al particles is taken as 2 μm based on visual inspection of SEM images of the powders (Eakins, 2007). Additionally, the homogeneous nucleation term in the viscoplastic constitutive law is deactivated because there are many heterogeneous nucleation sources (particle surfaces and grain boundaries) in the shock front (i.e., $w/\lambda > 1$). The heterogeneous dislocation nucleation term remains active in the constitutive law. The results of the shock wave simulations are presented and analyzed in the next chapter.

CHAPTER 6

ANALYSIS OF DISCRETE PARTICLE SIMULATION RESULTS

Shock wave propagation has been simulated in discrete Ni/Al powder mixtures according to the methods presented in Chapter 5. In this chapter, the simulation results are presented and analyzed. As a first step, the Hugoniot curves of the simulated powders are computed and validated against available experimental data. Next, deformation fields for the equal-sized powders (mixture class E), large-Al powders (mixture class B), and composite powders (mixture class C) are plotted for a range of impact velocities. Special attention is paid to the Ni/Al interfaces in these simulations. The macromixing of reactants is quantified by computing, for example, (i) the shocked surface area per unit volume of the Ni/Al interface and (ii) histograms (reckoned over the Ni/Al interface) of quantities relevant to constituent mixing. Simulated responses in the reflected waves are also investigated, as this is where shock-induced chemical reactions have been experimentally detected in certain Ni/Al powder mixtures.

6.1. Preliminaries

The volume elements considered here are statistical volume elements (SVEs) of the powder mixtures, as they are too small to be considered representative volume elements (RVEs). Therefore, multiple instantiations of each powder mixture are simulated to quantify the variability in response. In this work, four randomly-generated instantiations of each powder mixture (cf. Table 5.1) have been subjected to a range of impact velocities. A matrix of the simulated impact velocities (and the plate materials that have been utilized) is provided in Table 6.1. The simulation impact velocities corresponding to experimental impact velocities are highlighted in gray. In total, 96 simulations have been performed (6 powder mixtures $\times$ 4 impact velocities per mixture $\times$ 4 instantiations per impact). In the sections that follow, simulated impact velocities are referenced using a single significant decimal place (e.g., 1.2 km/s).

Table 6.1: Simulated impact velocities

	Equal-sized particles		Large-Al particles		Composite particles	
Mixture	E1	E2	B1	B2	C1	C2
Flyer/backer plate material	OFHC Cu	OFHC Cu	SS-304	SS-304	SS-304	SS-304
Impact velocity (km/s)	0.618	0.618		0.600	0.500	0.600
	0.804	0.804	0.846	0.800	0.800	0.800
	0.998	0.998	1.008	1.000	1.000	1.000
			1.101			
	1.200	1.200	1.216	1.200	1.200	1.200

6.2. Hugoniot curves

The Hugoniot curves for each of the simulated powder mixtures have been computed. The computed Hugoniot curves can be compared to experimental measurements to establish that the simulations respect the macroscopic responses of the powder mixtures. The longitudinal material velocity, u, and longitudinal stress, σ, on the Hugoniot are calculated by volume-averaging the heterogeneous fields behind the shock front (just prior to wave reflection). The shock wave velocity, D, is calculated by tracking the position of the shock front over time. The average position of the shock front (in the incident wave) is taken as $x_s = V_s / A$, where V_s is the volume of material that is shocked and A is the cross-sectional area of the volume element. The wave speed is calculated by fitting a line to the $x_s(t)$ profile after the slope of the profile has stabilized. In the simulated powder mixtures, steady wave speeds are achieved after the first few hundred nanoseconds of wave propagation.

In Figure 6.1(a), the Hugoniot curves computed for the equivolumetric Ni/Al powders are plotted in the shock stress – material velocity space. The relation that has been measured for an equivolumetric Ni/Al powder mixture (–325 mesh spherical particles, 60% TMD) is also plotted for reference (Eakins, 2007). Mixture E2 is the simulated powder mixture that is closest to the experimental powder mixture in terms of particle size and shape. The $\sigma - u$ relation that is computed for mixture E2 is in agreement with the measurements. The computed data points fall mostly within the uncertainty bars of the measurements; a quadratic that was fit to the simulated mixture is displaced from the experimental relation by about 0.5 GPa. The Hugoniot curves calculated for the other equivolumetric powder mixtures (B2, C2, and E1) fall along roughly the same $\sigma - u$ relation. The $\sigma - u$ relations computed for the Ni-rich mixtures (B1 and

C1) are plotted in Figure 6.1(b). In these plots, each data point corresponds to a distinct simulation. Therefore, these plots quantify the variation in simulated response that is computed for powder mixtures that are randomly-generated using identical mixture parameters.

The computed Hugoniots in the shock velocity – material velocity space are plotted for the equivolumetric Ni/Al mixtures in Figure 6.2(a) and the Ni-rich powder mixtures in Figure 6.2(b). The $D-u$ relation that is computed for mixture E2 exhibits reasonable agreement with the experimental data, although it appears to be shifted slightly upward. The source of this discrepancy is thought to be the 2D representation of the powders and the idealized particle shapes. The shock velocity – material velocity relation is commonly expressed using the linear relation, $D = c_0 + su$. Lines fit to the experimental and simulated data yield parameters are given in Table 6.2. Mixture theories based on the volume fractions of constituents would predict identical $D-u$ relations for these powders. However, the simulations indicate the $D-u$ relation depends (weakly) on powder configuration. The lines fitted to the simulated data for the composite particles (C2) and the 5-μm sized particles (E1) are offset by about 0.1 km/s. Similar variations in wave speed are said to be observed for shock wave simulations in (fully-dense) Ni/Al laminates, where the stacking direction has been varied relative to the direction of wave propagation (Thadhani, 2010). The large difference in mean pore size for mixtures C2 and E1 seems to be a viable explanation for the difference in shock wave speed, as pore size affects the interconnectedness of the particles.

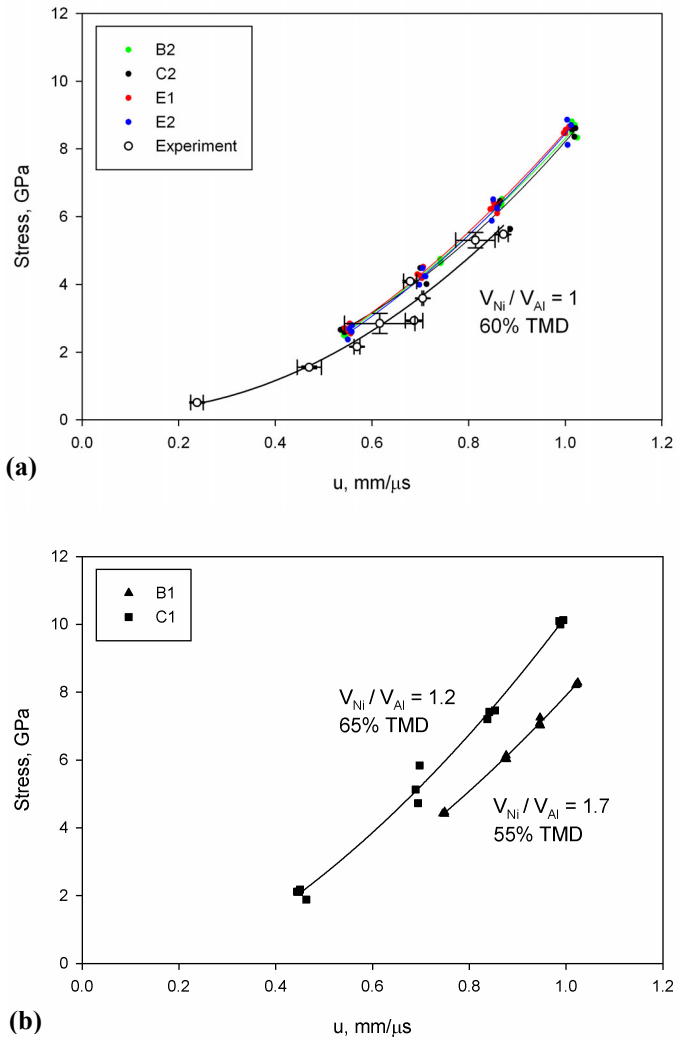

Figure 6.1: The shock stress – material velocity relation for (a) the equivolumetric Ni/Al powder mixtures, and (b) the Ni-rich powder mixtures.

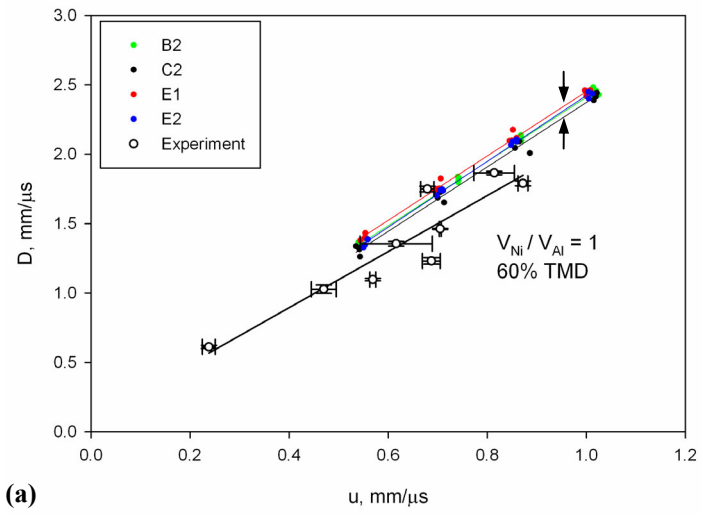

(a)

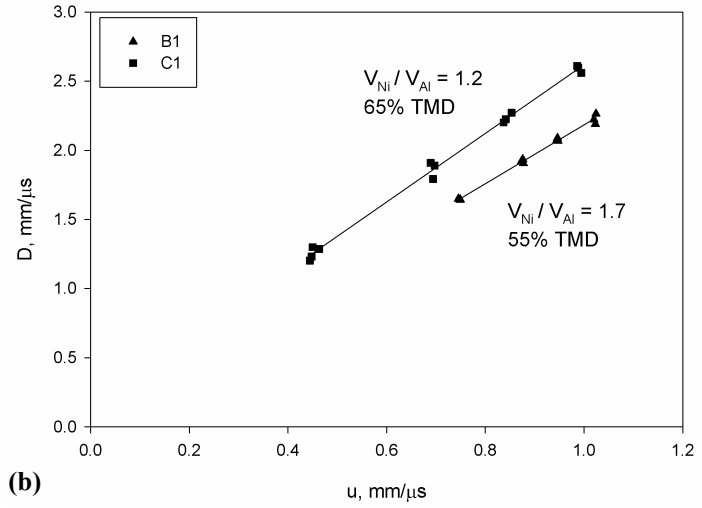

(b)

Figure 6.2: The shock wave velocity – material velocity relation for (a) the equivolumetric Ni/Al powder mixtures, and (b) the Ni-rich powder mixtures.

Table 6.2: EOS parameters calculated from the simulations ($D = c_0 + su$)

Equivolumetric Ni/Al powders (60% TMD)	c_0 (km/s)	s
E1	0.133	2.319
E2	0.051	2.373
B2	0.098	2.312
C2	0.052	2.321
Experiment[(a)]	0.086	2.019
Ni-rich powders (variable porosity)	**c_0 (km/s)**	**s**
B1	0.057	2.128
C1	0.138	2.481

[(a)] Eakins (2007)

The rise times of the shock waves have been measured in the experimental powder (equivolumetric Ni+Al, –325 mesh spherical particles, 60% TMD) (Eakins, 2007). In the experiments, the rise time is taken as the time required for (average) shock stress to increase from 10% to 90% of its peak value. The rise times that are measured from the input and propagated stress gages (which sandwich the powder specimen) are plotted in Figure 6.3. The shock rise times in the simulations have been calculated according to the experimental definition. As shown in Figure 6.3, the simulated rise time in mixture E2 falls in-between the rise times measured in the experiments. Thus, the computed Hugoniot curves and shock rise times indicate that the simulations are reproducing the basic macroscopic features of shock wave propagation. In the sections that follow, mesoscale simulation results for each mixture class are presented.

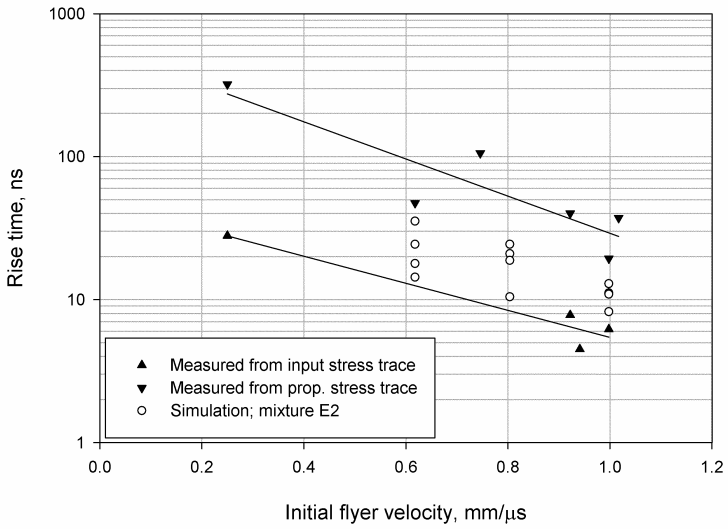

Figure 6.3: The shock rise times simulated in mixture E2 are compared to the rise times measured in experiments.

6.3. Equal-sized powder mixtures

Recall that mixture E2 is an equivolumetric Ni/Al mixture (60% TMD) with mean particle sizes of 20 μm for both phases. Mass density fields for mixture E2 are plotted in Figure 6.4 to illustrate the deformation of the Ni and Al phases in the incident shock pulse. In this Figure, the exact same powder mixture instantiation has been subjected to impact velocities of 0.6 and 1.2 km/s. For the 0.6 km/s impact, the particle deformation is relatively mild. It appears that the pores have collapsed in a relatively gentle manner, producing smooth interfaces between the particles. The deformation field for the 1.2 km/s impact clearly exhibits deformation character that is distinct from the lower impact velocity. Both phases are deformed to a greater extent; however, the deformation of the Al particles is particularly severe. In some locations there is intense flow of Al through the channels defined by the Ni particles, and in other regions there is entrapment of Al within clusters of Ni particles. In Figure 6.5, an enlarged view of the powder deformation is shown just behind the shock front for an intermediate impact velocity (1.0 km/s). The Al phase flows into the spaces between the Ni particles and in some cases the Al particles are flattened and spread over the surfaces of the Ni particles. The marker on the right-hand-side of Figure 6.5 indicates a region where two Al particles have been necked down and are flowing in-between two Ni particles. This is

similar to a flow feature that has been simulated by Eakins and Thadhani (2007), which they refer to as the "cooperative focused flow" of Al. The marker closer to the center of the figure indicates a region where Al has been drawn into a cluster of Ni particles in a vortical-type motion. In earlier simulations performed on spherical Ni+Al powders, Eakins and Thadhani (2007) observed vortices which persisted well behind the shock front. Finally, tiny fragments of Al are found deep within Ni particles and *vice versa*. This is an artifact of the simulation, which occurs when phases are deformed so intensely that tiny fragments are "numerically-detached" from parent particles.

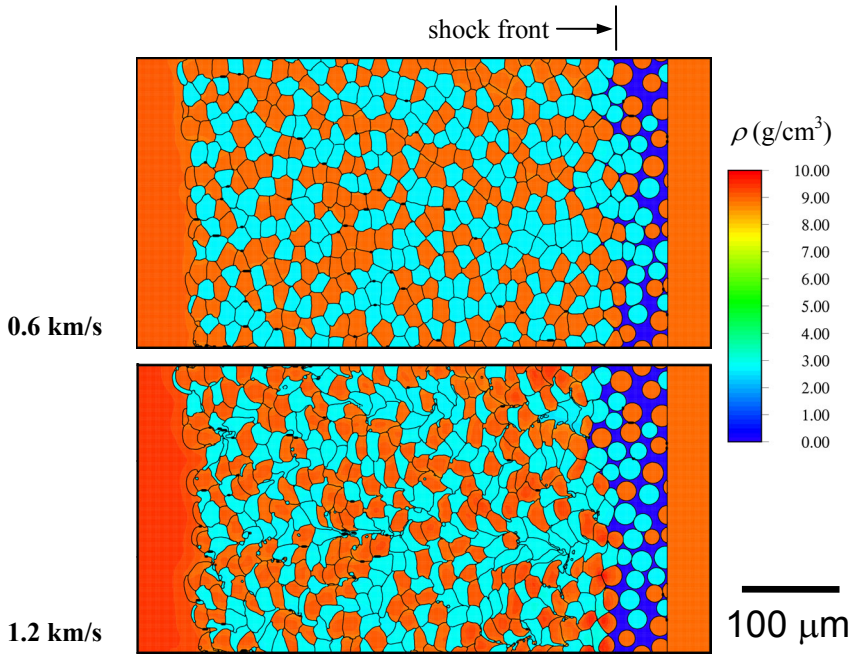

Figure 6.4: Mass density fields for mixture E2 impacted at 0.6 and 1.2 km/s. The light blue phase is Al, the orange phase is Ni, and the dark blue phase is void of material.

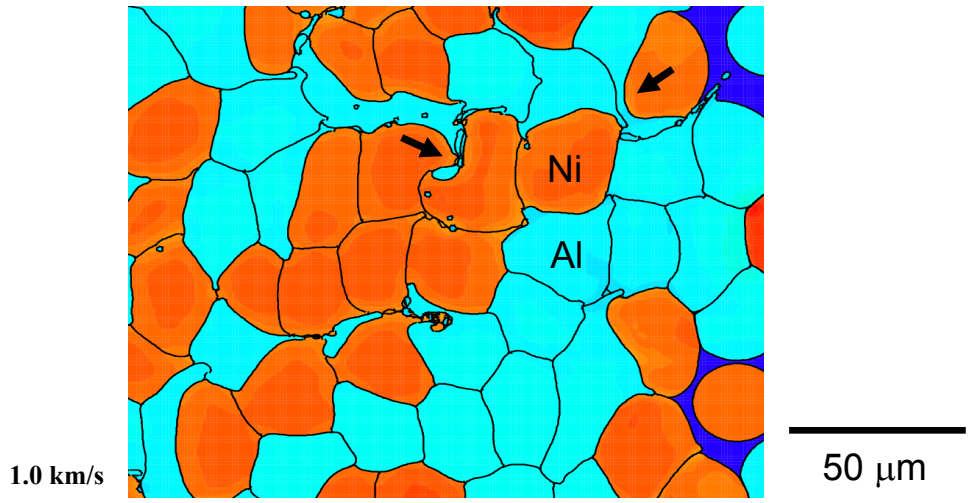

Figure 6.5: An enlarged view of the deformation in mixture E2 impacted at 1.0 km/s.

The temperature field for mixture E2 impacted at 1.0 km/s is plotted in Figure 6.6(a). There is a significant rise in temperature in each phase, which is caused by inelastic deformation. The temperatures in the Al phase range from 900-1500 K, while the Ni particle interiors remain at lower temperatures. The corresponding distribution of melt fractions is shown Figure 6.6(b). The melt fraction characterizes the progress of the phase transformation from solid to liquid. After the melting temperature is reached, the melt fraction is calculated according to how much energy has been added to the system relative to the latent heat of fusion of the material. Melt fractions equal of unity indicate volumes of material that are fully-melted. In Figure 6.6(b), most of the melting is concentrated in the Al phase, although there are small isolated volumes of partially-melted Ni throughout the shocked volume element. The overall volume fraction of the powder that is melted in the incident wave is ~8%. It is noted that any frictional heating due to sliding of interfaces is not taken into account because the interfaces are perfectly-bonded in these simulations. It is known that frictional sliding can have a potent heat effecting. However, under high pressure, it is not unreasonable to think the particle surface would be stuck together, and relative motion achieved by inelastic deformation in volumes of material located near the interfaces.

In Figure 6.7, the dislocation density field is plotted for a sub-element of mixture E2 impacted at 1.0 km/s. The average dislocation density of the Ni particles is more than an order of magnitude greater than that of the Al particles. The dislocation density of the Ni particles in void-collapsed regions is significantly elevated, reaching values of $\sim 5 \times 10^{10}$ mm^{-2}. This value of dislocation density is approaching the upper-limit of dislocation density ($\sim 10^{11}$ mm^{-2}) for a crystalline material (Cotterill, 1977).

Mixture E1 is an equivolumetric Ni/Al mixture (60% TMD) with mean particle sizes of 5 μm for both phases. The deformation fields of mixture E1 are qualitatively similar to those presented earlier for mixture E2 (cf. Figure 6.4) and are not repeated here. Quantification of the shocked response of mixture E1 relative to mixture E2 (and other powder mixtures) is deferred to Section 6.7.

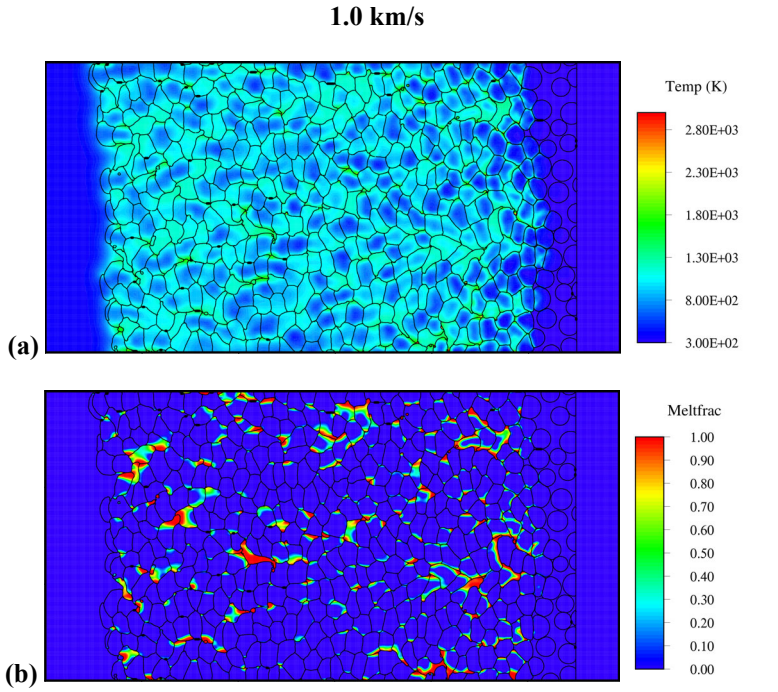

Figure 6.6: The temperature field (a) and the melt fractions (b) for mixture E2 impacted at 1.0 km/s.

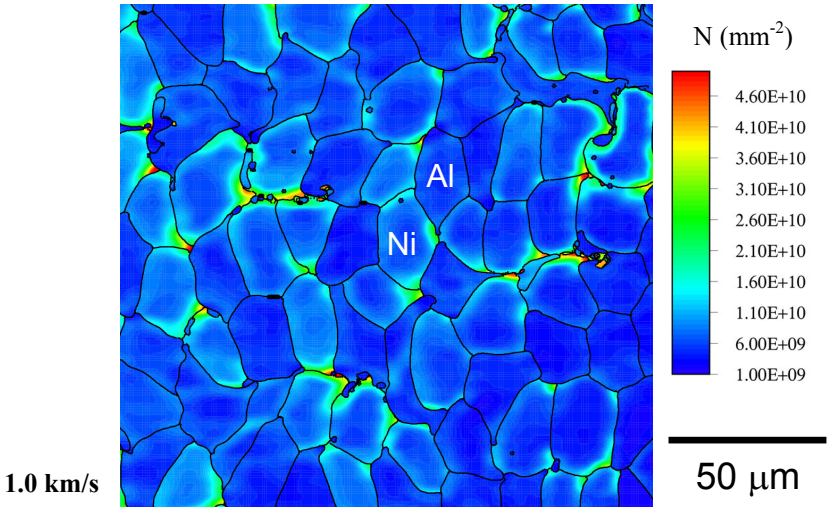

Figure 6.7: The dislocation density field for mixture E2 impacted at 1.0 km/s.

6.4. Large-Al powder mixtures

Mixture B1 is a Ni-rich powder composed of 20-μm size Ni particles and 5-μm size Al particles (the volumetric ratio of Ni to Al is 1.7 and the mixture is 55% TMD). Mixture B1 corresponds to the powder mixtures that were utilized in the shock compression experiments of Bennett et al. (1992) and Yang et al. (1997). In these time-resolved experiments, shock-induced chemical reactions were detected in the reflected wave pulses for (stainless steel) flyer plate velocities greater than ~1.075 km/s. Therefore, simulated responses in the reflected waves are considered below and above this critical impact velocity.

In Figure 6.8, the mass density fields for mixture B1 are plotted in the incident and reflected shock pulses for impact velocities of 0.8 and 1.2 km/s. Here, the exact same powder mixture instantiation has been subjected to impact velocities below and above the experimentally-observed threshold for shock-induced reactions. This Figure illustrates the deformation of the Ni and Al phases. For the 0.8 km/s impact, the deformation of the Ni and Al phases is relatively mild. In the incident and reflected waves the Al particles remain approximately circular in the sectioning plane. For the 1.2 km/s impact, the Al particles are flattened to a greater extent, appearing more ellipsoidal in shape. It also appears that the Ni particles are driven further into the Al particles. The Ni particles now form indentations in the Al particles and trap small volumes of Al about the particle peripheries.

Temperature fields in the reflected waves are plotted in Figure 6.9 for mixture B1 impacted at 0.8 and 1.2 km/s. For the 0.8 km/s impact, the Al particles are embedded in a Ni matrix that has an average temperature of ~1000 K. As the impact velocity is increased to 1.2 km/s, the temperature of the Ni matrix is increased to ~1500 K. Some of the void-collapsed regions among the smaller Ni particles exhibit temperatures approaching 3000 K. The effect of heat conduction can be seen in Figure 6.9 (b), as the large Al particles near the flyer plate display nearly uniform temperature fields, while those close to the backer plate have cooler interior regions. The melting of constituents is negligible for the 0.8 km/s impact. For the higher impact velocity, there are some regions of full melting about the periphery of Al particles.

Dislocation density fields in the reflected shock pulses are shown in Figure 6.10 for the 0.8 and 1.2 km/s impact velocities. The particle boundaries have been removed in these plots to provide unobstructed views of the fields. For the 0.8 km/s impact, the large Al particles can be identified by their lower values of dislocation density ($<10^9$ mm^{-2}). The Ni matrix attains a higher average dislocation density

(~1.5x10^{10} mm^{-2}). As the impact velocity is increased to 1.2 km/s, the dislocation density of the Al phase rises to ~5x10^{9} mm^{-2}, while the dislocation density of the Ni phase is increased to ~3x10^{10} mm^{-2}, with certain local void-collapsed regions reaching 5x10^{10} mm^{-2}. For the stronger wave, it appears the Al particles are embedded in a highly-dislocated matrix of Ni. In both cases, the levels of dislocation density are highest near the flyer plate because the substructure evolution equations are time-dependent, and these particles have spent the longest amount of time under shock compression. The regions of very high dislocation density in the Ni phase may be prone to fragmentation (fracture). This is relevant to the problem of shock-ignition because particle fragmentation would enable accelerated mixing rates.

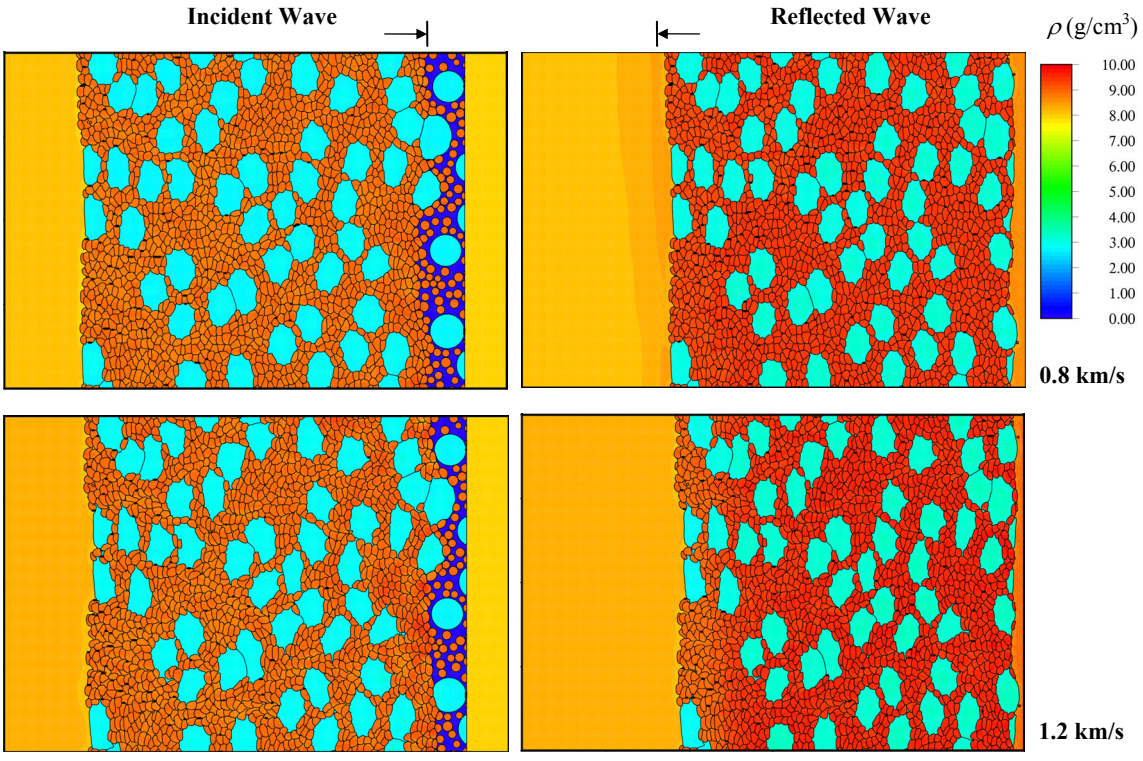

Figure 6.8: Mass density fields for mixture B1 in the incident and reflected shock waves. The initial flyer plate velocities are indicated. In experiments, shock-induced chemical reactions are detected in the reflected wave for flyer velocities greater than ~1.1 km/s.

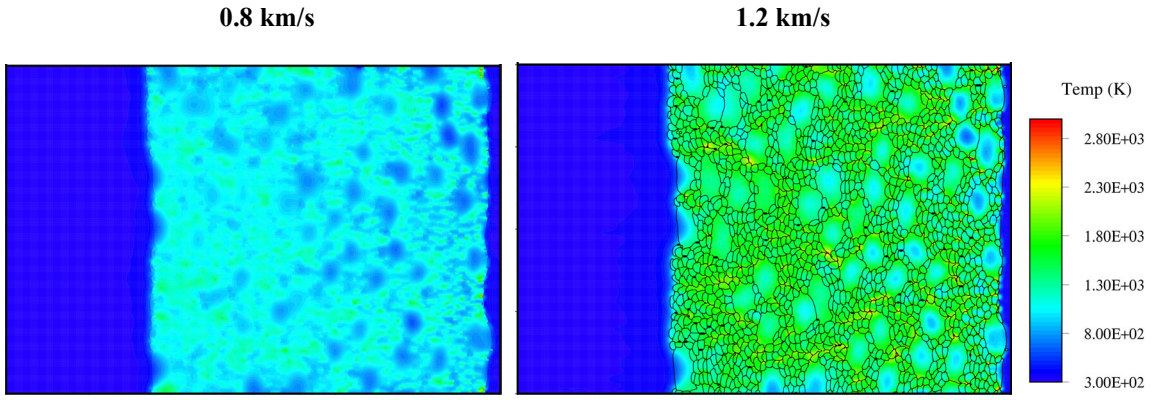

Figure 6.9: Temperature fields in the reflected waves for mixture B1 impacted at 0.8 (left) and 1.2 km/s (right). The particle boundaries have been removed in the left-hand pane.

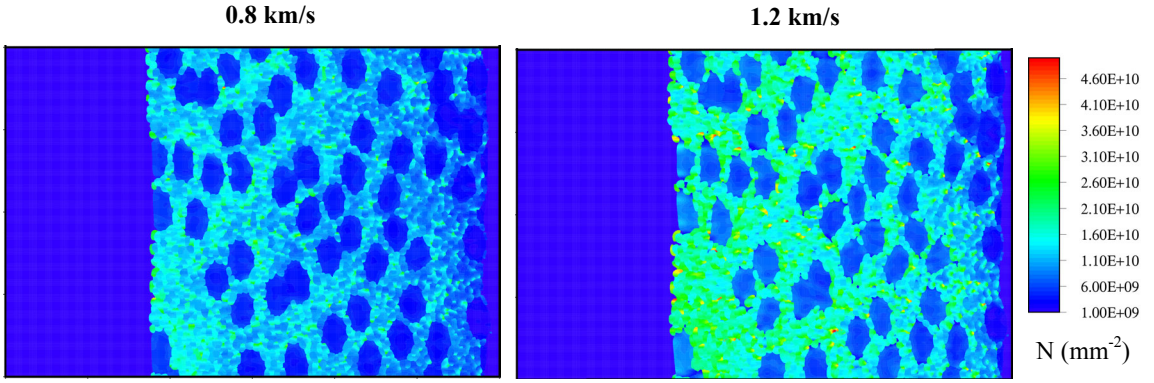

Figure 6.10: Dislocation density fields in the reflected waves for mixture B1 impacted at 0.8 (left) and 1.2 km/s (right). The particle boundaries have been removed to provide unobstructed views of the fields.

Mixture B2 is composed of the same 20-μm size Ni particles and 5-μm size Al particles; however, this mixture contains equal volumes of Ni and Al and is 60% TMD. The deformation fields of mixture B2 are qualitatively similar to those presented earlier for mixture B1 (cf. Figure 6.8) and are not repeated here. The main difference is that the Al particles of mixture B2 appear deformed to a lesser extent than those of mixture B1 due to the higher volume fraction of (softer) Al. Further quantification of the shocked response of mixture B2 is deferred to Section 6.7.

6.5. Composite powder mixtures

Recall that mixture C1 is a Ni-rich powder composed of composite particles 60 μm in size (the volumetric ratio of Ni to Al is 1.2 and the mixture is 65% TMD). This powder provides a distinct spatial arrangement of reactants (i.e., spherical Al cores with Ni coatings). Mixture C1 corresponds to the powder mixture that was studied in the plate impact experiments of Horie (1995).

The mass density fields of mixture C1 in the incident and reflected shock pulses are plotted in Figure 6.11 for impact velocities of 0.5 and 1.2 km/s. For the 0.5 km/s impact, the pores are not compressed entirely out of the powder in the incident wave, but the powder is fully-densified upon wave reflection. In this case, the overall particle deformation is rather mild, all interfaces remaining intact. The deformation field in the reflected wave can be compared to the shock recovery micrograph shown in Figure 4.4(A). It can be seen that the deformed particle morphologies are similar, although the range of particle size in the experimental powder (53–88 μm) is larger than that in the simulation (50–70 μm). The Al cores in the simulation appear slightly less flattened than those in the micrograph; this is attributed to the representation of the actual spherical particles as cylindrical particles in the simulations and the perfect bonding of the interfaces. For the 1.2 km/s impact, there is a noticeable change in the character of deformation in the shock waves. This Figure shows strongly-driven deformation of the Ni phase. In some regions, the Ni shells are fully ruptured and Ni is found deep within the Al cores. A magnified image of the deformation at the shock front is shown in Figure 6.12(a). At the shock front of the incident wave, high-speed jets of Ni (~3 km/s) form as the pores are collapsed. As shown near marker "1", these jets impinge on particles in the front, causing extensive deformation and sometimes penetration of neighboring Ni

shells. As shown near marker "2", the deforming Ni follows the initial jet producing a bulge in the Al core of the impacted particle. A shock recovery micrograph from the corresponding experimental composite powder (Horie et al., 1985) is shown in Figure 6.12(b). In this micrograph a surface instability has propagated from the Ni/Al interface into the Al core. The intensity of mixing in this region was strong enough for a local chemical reaction to occur (the product phase is marked as 'A' in the micrograph). The simulated flow morphology is similar to that in the experimental micrograph. Thus, the mechanism described above is a potential explanation of the surface instabilities that are observed in the experimental composite powders. Additionally, the deformation character in the reflected wave for the 1.2 km/s impact is indicative of a precursor to the flow instability seen in an experimental recovery micrograph (cf. Figure 4.4(D)). However, the impact velocity in the experiment was only 0.8 km/s. The difference in flow morphology may be partially due to local chemical reactions along the Ni/Al interface in the experiment, although it seems likely that there is some mechanism that is yet to be accounted for in the simulation.

The temperatures and melt fractions of mixture C1 in the incident wave are plotted in Figure 6.13(a) and (b), respectively, for an impact velocity of 1.2 km/s. The temperature field is quite heterogeneous because (i) there is preferential deformation of the Ni phase in pore-collapsed regions, and (ii) there is insufficient time for thermal equilibration in the fairly large Al cores (~40 μm). Fully-melted material is found in pore-collapsed regions (especially in regions where the high-speed Ni jets have formed), although the overall volume fraction of melted material is rather modest. In Figure 6.13(c) the corresponding dislocation density field is plotted. Here, the particle boundaries have been removed for clarity. Regions of high dislocation density ($>5x10^{10}$ mm^{-2}) develop in the Ni phase, while the Al inclusions exhibit lower dislocation density ($<10^{9}$ mm^{-2}). Again, the Ni phase may be prone to fragmentation or surface instability in regions of very high dislocation density.

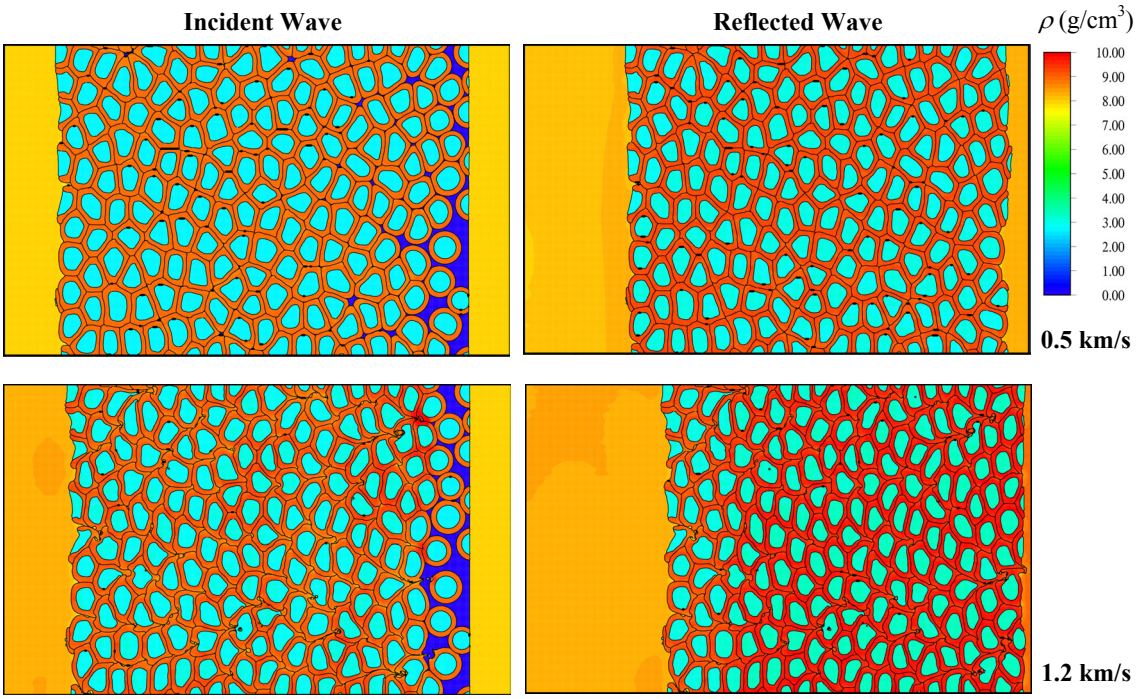

Figure 6.11: Mass density fields for mixture C1 in the incident and reflected shock waves. The initial flyer plate velocities are indicated.

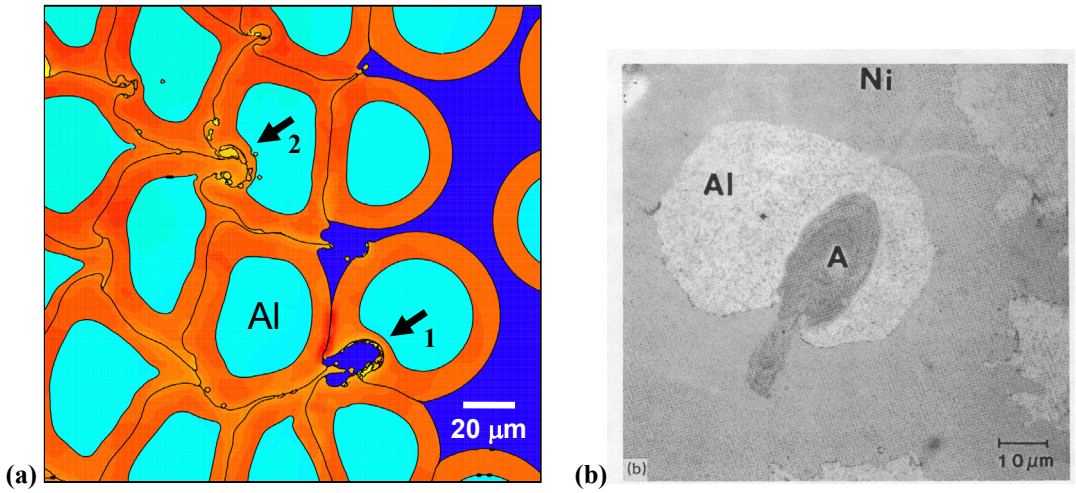

Figure 6.12: An enlarged view of the simulated deformation near the shock front for mixture C1 (impacted at 1.2 km/s) is shown in part (a). Notice the formation of Ni jets that impact shells within the shock front and the bulging of Ni into Al cores. A recovery micrograph from the corresponding experimental powder (Horie et al., 1985), which displays similar flow morphology, is shown in part (b). In the experimental micrograph, local chemical reaction has results in a product phase that is marked 'A'.

1.2 km/s

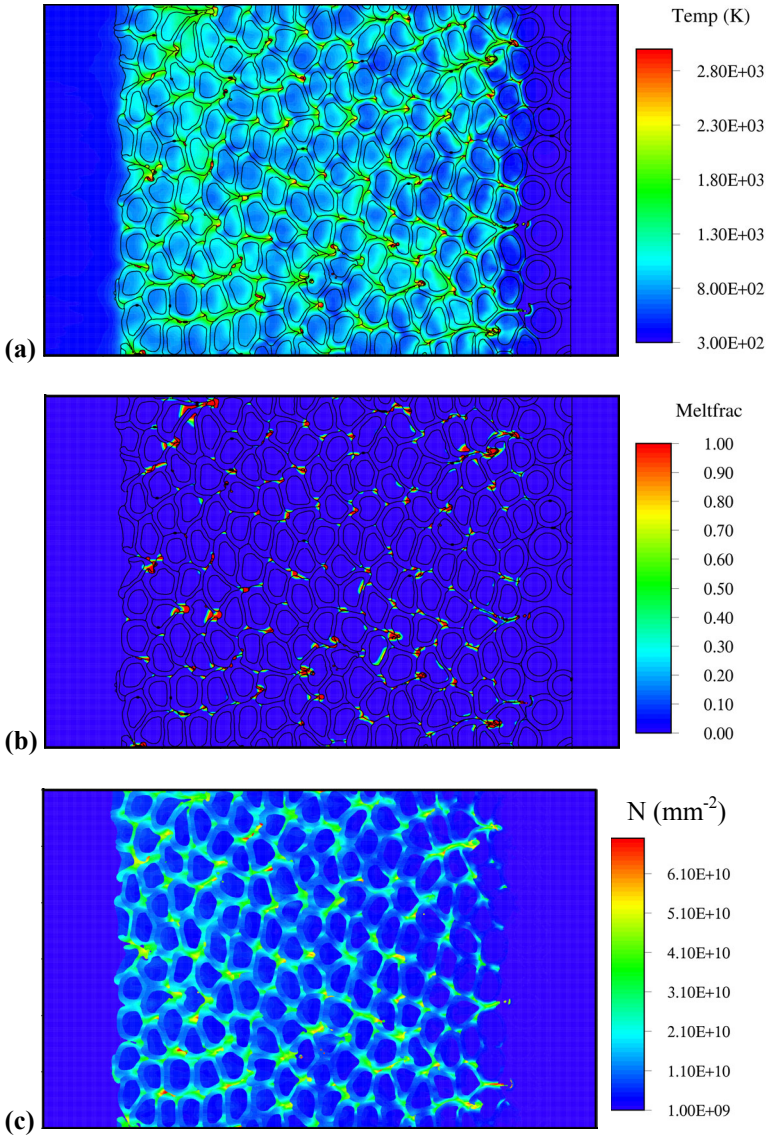

Figure 6.13: The (a) temperature field, (b) melt fractions, and (c) dislocation density of mixture C1 impacted at 1.2 km/s. The fields are plotted in the incident wave.

Mixture C2 is composed of similar composite particles; however, this mixture contains equal volumes of Ni and Al and is 60% TMD. Additionally, the Ni coatings in mixture C2 are ~1 μm thinner than those of mixture C1. In Figure 6.14, the mass density field of mixture C2 (in the incident shock pulse) is plotted for an impact velocity of 1.2 km/s. The deformation fields of mixture C2 are similar to those of C1, although the thinner Ni coatings promote higher levels of shell penetration. There is, however, a new observation for mixture C2. There are now a fair number of Ni shells that have been ruptured by the stretching (and thinning) of the Ni phase. To quantify the likelihood of unstable flow in mixtures C1 and C2, the fractions of particles with non-convex Al cores have been calculated for the range of simulated impact velocities. The results, shown in Figure 6.15, confirm that the severity of deformation is greater for the composite particles with thinner Ni coating (mixture C2).

1.2 km/s

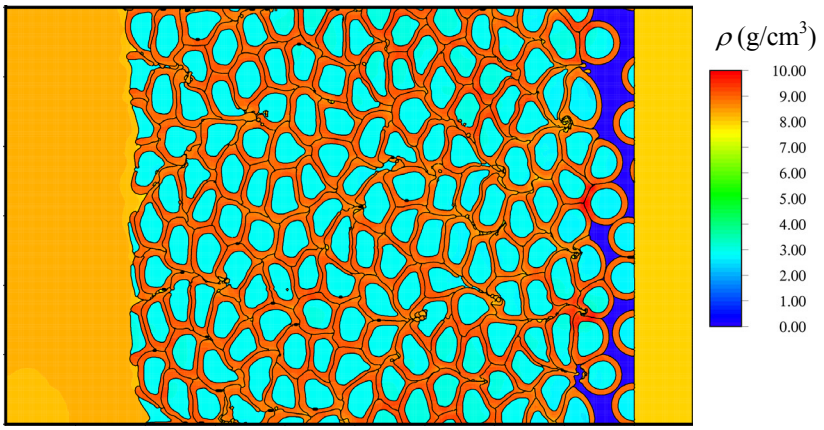

Figure 6.14: The mass density field for mixture C2 impacted at 1.2 km/s. Strongly-driven deformation of Ni shells into the Al cores is observed.

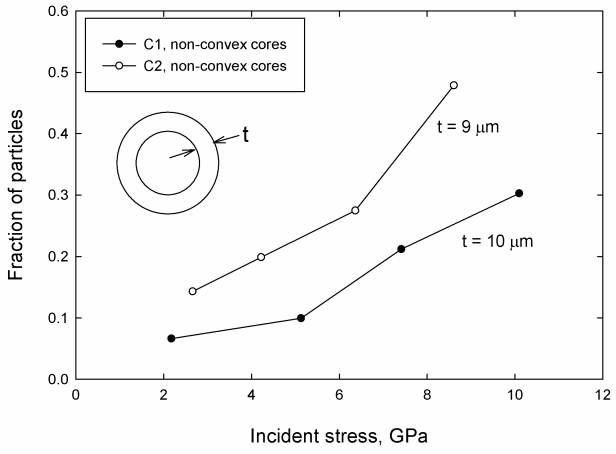

Figure 6.15: The fractions of Al cores that have been rendered non-convex by shock deformation in the simulated composite powder mixtures.

6.6. Shock simulations with a rate-independent constitutive law

In Chapters 2 and 3, emphasis was placed on the importance of the rate-dependence of plastic deformation in the shock front. Significant rate-dependent effects were demonstrated (and validated against experimental data) for homogeneous media. In this section, we investigate the usage of rate-dependent and rate-independent constitutive relations in the discrete particle shock simulations.

Let us first consider a Ni/Al powder that has been studied in experiments. Shock compression experiments have been performed on micron-scale (–325 mesh) Ni/Al powder mixtures that were initially pressed to 60% TMD (Eakins, 2007). A recovery micrograph from one such powder mixture that was impacted by a Cu flyer plate traveling at 0.998 km/s is shown in Figure 6.16(a). This experiment has been simulated numerically. Mixture E2 is an idealized version of the experimental powder and the loading conditions (impact velocity and flyer plate material) have been matched. Two simulations have been performed on the exact same instantiation of mixture E2. In one simulation, the (rate-independent) Steinberg-Guinan model (1980) is utilized as the deviatoric stress-strain relation for the Ni and Al phases. In the other simulation, the high-rate viscoplasticity relation that has been developed in this work (cf. Chapter 2) is utilized. The Steinberg-Guinan (SG) model parameters for Ni and Al (actually, 6061-T6)

have been taken from the original reference. The viscoplasticity (VP) model parameters for Ni and Al are provided in Chapter 3.

The shock-wave-induced deformation that is computed using the SG model is illustrated in Figure 6.16(b). Here, the mass density field has been plotted to identify the phases. It can be seen that the Ni and Al phases are highly-deformed, exhibiting a somewhat fluidic-type flow. The Ni particles are severely flattened, in some cases being reduced to ~1/10 of their original size. Additionally, there are high levels of numerical fragmentation for both phases. The shock wave deformation that is computed using the VP model is shown in Figure 6.16(c). Here, the Ni an Al phases are deformed to lesser extents. The deformed particle morphologies that are calculated using the VP model appear to be more in line with those observed in the (unreacted) recovery micrographs. In particular, the extensive deformation of the Ni phase that is calculated using the SG model (Figure 6.16(b)) is not observed in the recovery micrograph.

The deformation that is computed using the SG model is more severe because the non-equilibrium stresses that are required to drive the high rates of deformation in the shock front are not taken into account. That is, the rate-dependence of plastic deformation in the shock front is neglected. The simulations that are performed using the VP model display lower levels of particle deformation because the rate-dependent nature of the material in the shock front is addressed. This is illustrated in Figure 6.17. In the shock front, the apparent strength of a rate-dependent material is higher than that of the rate-independent material; therefore, the rate-dependent material is deformed to a lesser extent. The SG model is a perfectly acceptable model of material strength *behind* the shock front. However, a rate-independent description of plastic deformation in the shock front does not seem appropriate. This is an important point to consider because the deformation and mixing of particles in the shock front (or closely behind it) is relevant to the initiation of shock-induced chemical reactions.

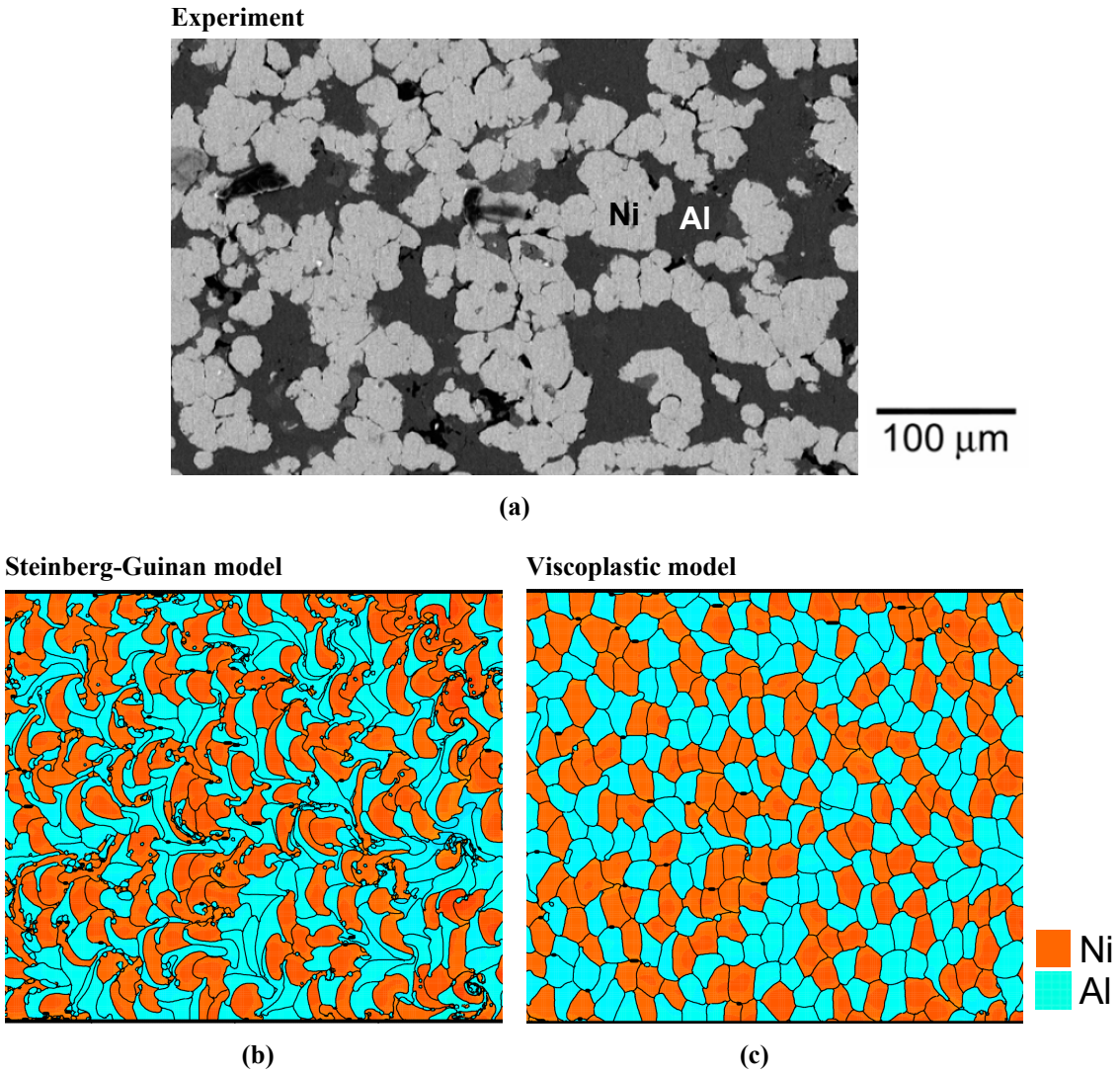

Figure 6.16: Comparison of (a) the experimental micrograph to the simulations performed using (b) the Steinberg-Guinan model and (c) the high-rate viscoplasticity model. The exact same powder instantiation has been subjected to the experimental impact velocity (1.0 km/s). The direction of shock wave propagation is from left to right.

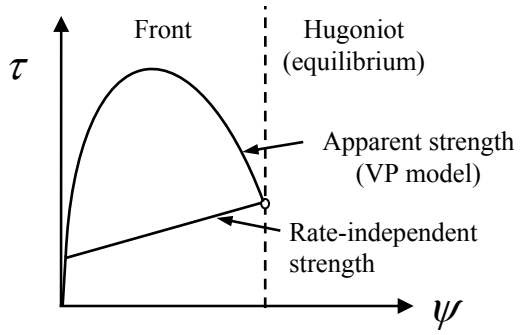

Figure 6.17: The stress-strain curves that are computed in the shock front using rate-dependent and rate-independent constitutive models.

6.7. The Ni/Al interface

The level of constituent mixing is the factor that determines whether or not large scale chemical reactions occur in the shock wave. Since chemical reactions originate at the surfaces where Ni and Al come into direct contact, it is useful to develop methods to quantify the Ni/Al interface in the simulated powder mixtures. As a first step, time histories of the surface area per unit volume of Ni/Al contact, $S_V(t)$, were calculated during wave propagation. Here, the normalizing volume is strictly that of shocked Ni and Al. An example $S_V(t)$ profile is depicted in Figure 6.18. The simulated volume elements were selected to be large enough to allow the values of S_V to stabilize prior to wave reflection (the stabilized value of S_V in Figure 6.18 is demarcated by the open circle). In Figure 6.19(a), the stabilized values of S_V are plotted versus the incident stress for the simulated powder mixtures. Regression lines have been fit to the data. The simulation data indicates a rank-ordering of mixtures based on $S_V(\sigma)$. On a per unit volume basis, the composite powder mixtures (C1 and C2) form the smallest Ni/Al interfaces, while the elemental mixtures (E2, B1, and B2) yield larger Ni/Al interfaces. Mixture E1 (5-μm sized particles) forms the largest surface area per unit volume (about 200–300 mm^{-1}); however, these results are not plotted in Figure 6.19(a) because they tend to obscure the other results. The slopes of the $S_V(\sigma)$ diagrams for the elemental powder mixtures are consistently higher than those of the composite powders, indicating greater stress-sensitivity of Ni/Al surface formation for these powders.

To consider interface formation form a different perspective, a measure of surface amplification has been constructed. Let $S_{V,0}$ be defined as the smaller of the Ni and Al surface areas (per unit volume) in the initial configuration. The quantity $S_V / S_{V,0}$ is then interpreted as a measure of how much the limiting surface is amplified by the shock deformation. In Figure 6.19(b), the values of $S_V / S_{V,0}$ just prior to wave reflection are plotted versus the incident stress for each of the powder mixtures. The rank-ordering of powders that was established on the basis of S_V is now rearranged. Mixture E1 exhibits the smallest surface amplification over the entire shock stress range. The surface amplifications for mixtures E1 and E2 are about 10% and 20%, respectively, for the strongest shocks considered. The surface amplifications for the composite powders are nearly independent of the shock stress. The greatest surface amplification is achieved by mixture B1 (i.e., mixture B1 makes the most efficient use of the original Al surface). The reason for this response can be seen in Figure 6.8. Here, the small Ni particles are pressed into the flattened Al particles, which produces a considerable amplification of the initial surface area.

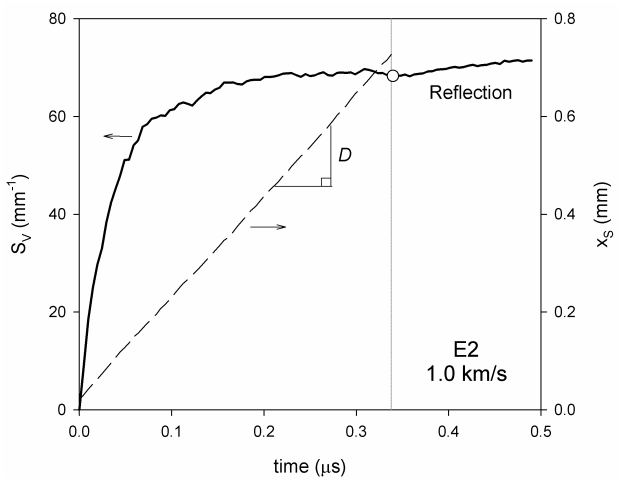

Figure 6.18: The time history of S_V for mixture E2 impacted at 1.0 km/s. The stabilized value of S_V in the incident shock wave is indicated by the open circle. The average shock front position, x_s, is also plotted to demonstrate constant shock wave speed.

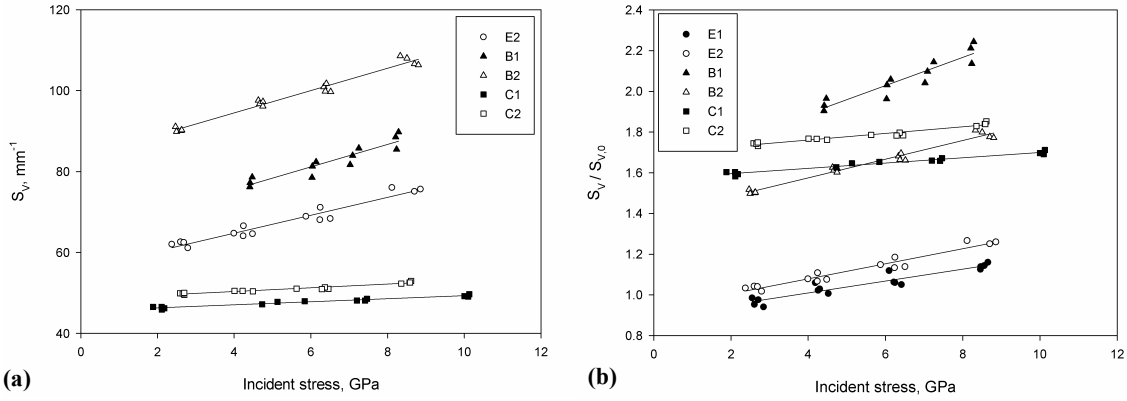

Figure 6.19: The Ni/Al surface area per unit volume is plotted for the simulated powder mixtures in part (a). The measure of surface amplification is plotted in part (b).

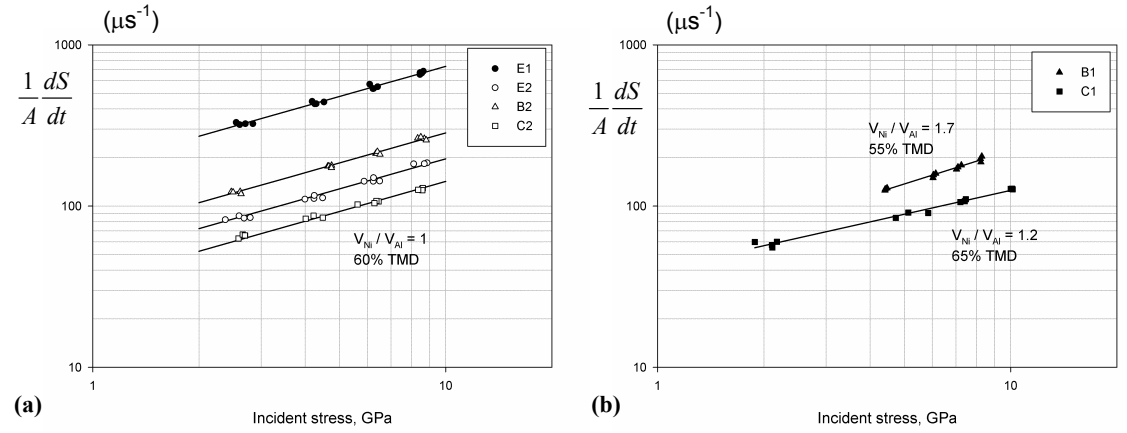

Figure 6.20: The normalized rate of Ni/Al interface creation for (a) the equivolumetric powder mixtures and (b) the Ni-rich powder mixtures.

We now consider the growth rate of Ni/Al interfaces. For a shock wave that advances into a powder at constant speed, D, and produce a stabilized surface area per unit volume, S_V, the (normalized) rate of Ni/Al interface creation may be written as

$$\frac{1}{A}\frac{dS}{dt} = S_V D \tag{6.1}$$

Here, S is the surface area of the Ni/Al interface and the normalizing area, A, is the transverse cross-sectional area of the volume element (i.e., the surface normal to the direction of wave propagation). In Figure 6.20, the normalized rates of Ni/Al interface creation are plotted for the equivolumetric and Ni-rich powder mixtures. When plotted in log-log space, $1/A \cdot (dS/dt)$ displays a linear dependence on the shock stress, σ, for all powder mixtures that were simulated. Interestingly, the results for the equivolumetric powder mixtures (Figure 6.20(a)) are well-described by a set of lines with identical slopes. This indicates the existence of a power-law scaling relation, e.g.,

$$\frac{1}{A}\frac{dS}{dt} = B\sigma^n \tag{6.2}$$

where the exponent, n, is constant for a given phase distribution. The coefficient, B, depends on the initial powder configuration (i.e., particle shape, size, etc.). The scaling relation parameters that have been determined for the simulated powder mixtures are provided in Table 6.3. By extension, a scaling relation for the shocked surface area per unit volume may be derived from Eq. (6.2), i.e., $S_V = B\sigma^n / D$ where $D = D(\sigma)$. The scaling relation for the rate of Ni/Al interface growth may find utility in macroscopic analyses that do not resolve the explicit deformation of the phases, e.g., treatments of large-scale reaction initiation and scoping analyses that are performed in the design of energetic materials.

Table 6.3: Scaling parameters (Ni/Al interface growth rate)

Equivolumetric Ni/Al powders (60% TMD)	B ($\text{GPa}^{-n}\mu\text{s}^{-1}$)	n
E1	176.4	0.62
E2	47.1	–
B2	68.2	–
C2	34.1	–
Ni-rich powders (variable porosity)	**B ($\text{GPa}^{-n}\mu\text{s}^{-1}$)**	**n**
B1	45.2	0.69
C1	40.2	0.49

Thus far, the overall size and rate of formation of the Ni/Al interface have been quantified. The state of the interface and its underlying microstructure are relevant to the mixing that occurs across the interface. Therefore, histograms of the Ni/Al surface temperature and dislocation density have been computed through dynamic tracking of the entire (disjointed) Ni/Al interface within the shocked volume element. The procedures that were used to construct these histograms are now briefly described. The relevant data were extracted from the simulations just prior to wave reflection. In elements containing part of the Ni/Al interface, the elemental surface temperature, θ_{surf}, was calculated based on the mass-averaged thermal energy of the Ni and Al contained in the element, i.e.,

$$\theta_{surf} = \theta_0 + \frac{1}{\bar{c}}\left[\phi_{Ni} c_{Ni}\left(\theta_{Ni} - \theta_0\right) + \phi_{Al} c_{Al}\left(\theta_{Al} - \theta_0\right)\right] \tag{6.3}$$

Here, θ_0 =300 K is the reference temperature, ϕ_i, c_i, and θ_i are the mass fractions, specific heats, and temperatures of the constituents (Ni and Al), respectively, and $\bar{c}$ is the volume-averaged specific heat of the constituents contained in the element. The elemental surface dislocation density (i.e., the number of dislocations that pierce the Ni/Al interface per unit area) is simply

$$N_{surf} = N_{Ni} + N_{Al} \tag{6.4}$$

where N_i are the elemental dislocation densities of the constituents. Sets of bins were created for the Ni/Al surface temperature and dislocation density. The simulation data were processed by sweeping over the Ni/Al interface and placing the elemental Ni/Al surface areas in the appropriate bins based on elemental

values of surface temperature and dislocation density. The data were then normalized, so the histograms are to be interpreted as the fractions of the Ni/Al surface that fall within the designated bins.

Histograms of the Ni/Al surface temperature (in the incident wave) are plotted in Figure 6.21(a) for the equal-sized powders (E2), the large Al powders (B1), and the composite powders (C1). The number next to each histogram indicates the simulated impact velocity. The data points correspond to the midpoints of the bins. Lines connecting the data points have been drawn to guide the eye. In mixtures E2 and B1, the tails of the distributions for the highest impact velocity extends beyond 2000 K. Alternatively, the temperature distribution for mixture C1 is biased towards lower surface temperatures. The process of void collapse is responsible for this difference. In the elemental powder mixtures (E2 and B1), Ni and Al are drawn into the void space simultaneously. This produces severe plastic deformation and heating of both phases. In the composite powder (C1), the voids are filled primarily by the Ni phase. Therefore, the material in close proximity to the Ni/Al interface is less deformed and resides at lower temperature. Histograms of the Ni/Al surface dislocation density (in the incident wave) are plotted in Figure 6.21(b) for the aforementioned powders. The powders exhibit incremental shifts in the interface dislocation density as the impact velocity is increased, with the upper tails of the distributions all approaching 10^{11} mm^{-2}. The histograms of the composite powders (C1) exhibit the widest range, which indicates there are distinct fractions of the Ni/Al interface that experience relatively mild and severe deformations. The reason for this behavior has been explained in terms of pore collapse. Finally, it is noted that these histograms have been calculated from single instantiations of the powder mixtures for the purpose of demonstration. More robust histograms can be constructed through appropriate averaging of the data extracted from multiple SVEs subjected to a given impact velocity. However, this is a tedious calculation and only marginal differences among the histograms are expected since the Ni/Al surface that is sampled in each SVE is fairly large.

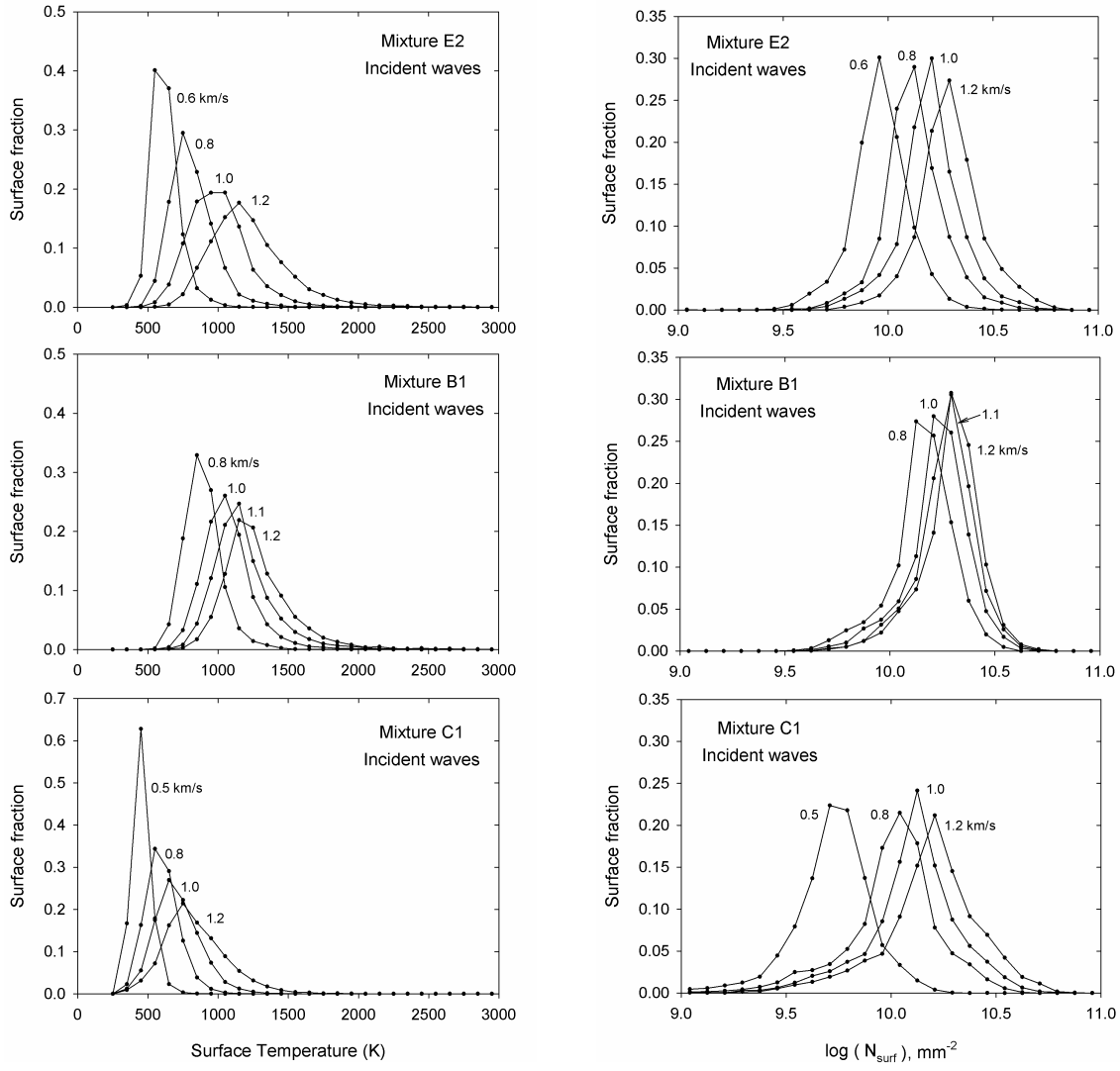

Figure 6.21: Histograms of (a) the Ni/Al surface temperature and (b) the Ni/Al surface dislocation density for mixtures the equal-sized powders (mixture E2), large Al powders (mixture B1), and the composite powders (mixture C1). The number next to each histogram indicates the simulated impact velocity (in km/s).

To consolidate the Ni/Al interface data, the mean values of surface temperature and dislocation density have been calculated for the simulated impact velocities. The mean Ni/Al surface temperature, $\bar{\theta}_{surf}$, and mean Ni/Al surface dislocation density, $\bar{N}_{surf}$, are the expected values of the histograms plotted in Figure 6.21. In Figure 6.22(a), $\bar{\theta}_{surf}$ is plotted as a function of the incident shock stress, σ, for the simulated powder mixtures. In log-log space, the mean Ni/Al surface temperatures of the elemental powders (mixture classes B and E) are well fit by a single line, while the composite powders (mixture class C) exhibit lower mean Ni/Al surface temperatures. Recall that mixtures E1, E2, B2, and C2 have identical volume fractions of all constituents. These results hint at a power-law scaling relation, e.g., $\bar{\theta}_{surf} \propto \sigma^m$, where the exponent is constant for a given phase distribution and the scaling coefficient depends on particle configuration. However, it seems premature to draw this conclusion based on somewhat sparse statistics. The simulation results indicate elemental powders may be more prone to shock-initiation due to the higher surface temperature; however, thermal response should not be viewed as the sole determining factor of reaction initiation. In Figure 6.22(b), $\bar{N}_{surf}$ is plotted as a function of the incident shock stress. The different particle configurations simulated in this work yield only marginal shifts in mean Ni/Al interface dislocation density in the shocked state. The interface dislocation density reaches ~2×10^{10} mm^{-2} for shock stresses of 8–10 GPa, which is on the order of the saturated dislocation density of a metal.

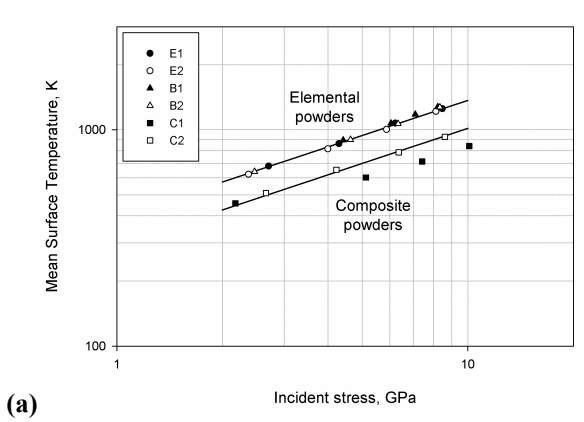

(a)

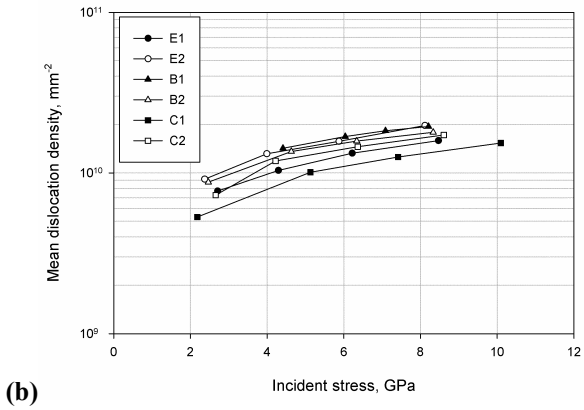

(b)

Figure 6.22: The mean values of (a) Ni/Al surface temperature and (b) Ni/Al surface dislocation density plotted as functions of shock stress.

The melting behavior of the Ni/Al interface in the shock wave is of interest. It is known that self-propagating high-temperature synthesis (SHS) reactions in the Ni/Al system occur by melting of Al and dissolution of Ni into the melt. However, shock compression experiments performed on reactive powders indicate that melting actually inhibits the occurrence of the ultra-fast (shock-induced) chemical reactions (Vandersall and Thadhani, 2003). Therefore, the degree of melting along the Ni/Al interface has been quantified in the shock wave simulations. In Figure 6.23, the fraction of the Ni/Al interface that is composed of fully melted Al is plotted versus the incident shock stress. The Ni phase remains, for the most part, solid along the Ni/Al interface. The elemental powders exhibit higher levels of Al melting because the pore configurations allow for extensive deformation of Al particles. In the composite powders, the Al cores tend to remain encapsulated within the Ni shells, which prevent extensive flow of Al in the void

space. If large scale melting of the Al phase (greater than 50%) is to be avoided, the shock stress should be kept below ~8 GPa in the elemental powder mixtures. The composite powders can be shocked to higher stresses without large scale melting of Al along the Ni/Al interfaces.

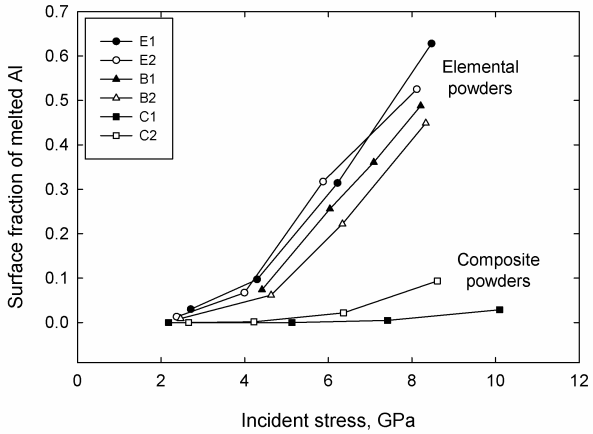

Figure 6.23: The fraction of the Ni/Al interface that is composed of fully melted Al.

6.8. Observations in the reflected waves

In time-resolved plate impact experiments, shock-induced chemical reactions have been detected during the propagation of sufficiently strong reflected waves in certain Ni/Al powder mixtures (Bennett et al., 1992; Yang et al., 1997). Therefore, special attention has been paid to the simulated responses in the reflected waves (i.e., the second jump in stress for the powder situated in-between the flyer and backer plates). In Figure 6.25, the longitudinal material velocity (u_1) fields are plotted for the reflected shock pulses in an equal-sized powder mixture (E2), a large Al powder mixture (B1), and a composite powder mixture (C1). Please notice that the simulation windows are not drawn to scale. The impact velocity in these simulations was 1.2 km/s. In these plots the wave fronts are now propagating from right to left. The particle boundaries have been removed in mixtures E2 and C1 to provide unobstructed views of the velocity fields. There are two phenomena of specific interest. The first is the appearance of two distinct wave fronts. There is now a quasi-elastic precursor wave that detaches from the main reflected wave. This

occurs because the powders are fully densified (and hardened). The second feature of interest is the non-planarity of the main reflected wave. The undulations in the shock front form because the wave travels faster in the Al particles (the intrinsic waves speed of Al is higher than that of Ni). The particle boundaries have been rendered in mixture B1 (the middle pane of Figure 6.25) to illustrate this phenomenon.

Due to the non-planarity of the main reflected wave front, there are gradients (or fluctuations) in material velocity in-between the fingers of the advancing front. These velocity fluctuations occur across Ni/Al interfaces in many places. The average velocity fluctuations across the Ni/Al interfaces, $\langle \Delta u \rangle$, have been computed for each powder mixture from the full velocity fields in the reflected waves. The results are plotted as a function of impact velocity in Figure 6.24. The velocity fluctuations follow distinct trends for the elemental and composite powder mixtures; this is due to differences in initial phase arrangement and subsequent shock deformation. For an impact velocity of 1.2 km/s, the average velocity difference across the Ni/Al interfaces is ~0.130 km/s for the equal-sized powders (mixture class E) and the large-Al powders (mixture class B) and ~0.060 km/s for the composite powders (mixture class C). These velocity fluctuations may serve as the driving forces for ultra-fast mixing processes at the Ni/Al interfaces. For example, the heterogeneous velocity fields may result in shear-driven surface instabilities, shear localization, and/or particle comminution. This is discussed further in Section 6.9.

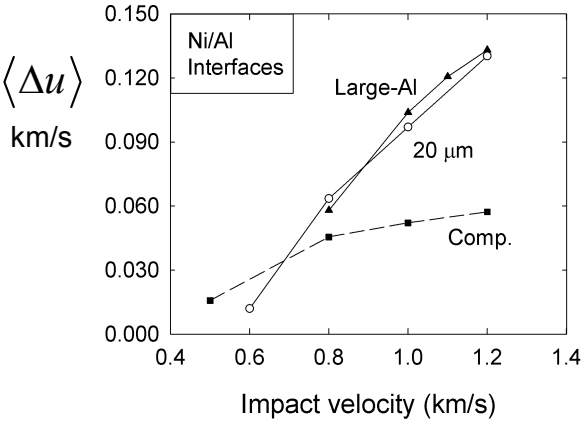

Figure 6.24: Average velocity fluctuations across the Ni/Al interfaces in the large-Al powder mixture (B1), the 20 μm equal-sized powder mixture (E2), and the composite powder mixture (C1).

In Figure 6.26, the longitudinal rate of deformation (D_{11}) fields are provided for the reflected shock pulses in the same powder mixtures as above. Here, the compressive fields ($D_{11} < 0$) are plotted for two impact velocities: 0.8 and 1.2 km/s. Again, the wave fronts are propagating from right to left and the particle boundaries have been removed to present unobstructed views of the fields. The coherency and intensity of the reflected shock front are of interest here. That is because the simultaneous (coordinated) deformation of Ni and Al tends to (i) expose fresh surfaces that are available for reaction, and (ii) induce higher defect densities in volumes of material near the Ni/Al interfaces. These deformation features are desirable for achieving shock-induced reactions. In mixture B1, there is preferential deformation of the softer Al particles at the lower impact velocity. At the higher impact velocity, (i) a coherent shock front is formed that spans the transverse dimension of the SVE and (ii) there are some bands of concentrated deformation on planes oriented about 45 degrees relative to the direction of wave propagation (i.e., close to the planes of maximum shear in a homogeneous medium). The deformation bands form in regions that have been weakened by material melting. However, the deformation bands are not fully-melted volumes of material (most regions of the bands retain material strength). There is a significant contribution to the banding behavior from the velocity gradients that are introduced by the non-planar shock front (cf. Figure 6.25). As such, these deformation bands tend to form along the Ni/Al interfaces. In the equal-sized powder mixture (E2) impacted at 1.2 km/s, the reflected shock front is less coherent. Again, there is evidence of distributed deformation banding, although some of these regions correspond to melt pools that were formed in the incident wave. In the composite powder mixture (C1), there is no deformation banding. Instead, there is preferential deformation of the Al cores for both impact velocities. Therefore, mixture B1 (the large-Al powder) forms the most coherent and the most intense reflected shock front of all three powders impacts at 1.2 km/s. Interesting, the large-Al powder is precisely the experimental powder mixture wherein shock-induced reactions have been detected in the reflected shock pulses for flyer velocities greater than ~1.1 km/s (Bennett et al., 1992; Yang et al., 1997). Thus, the discrete particle simulations appear to provide some hints as to which powder mixtures are most likely to undergo shock-induced chemical reaction in the reflected waves.

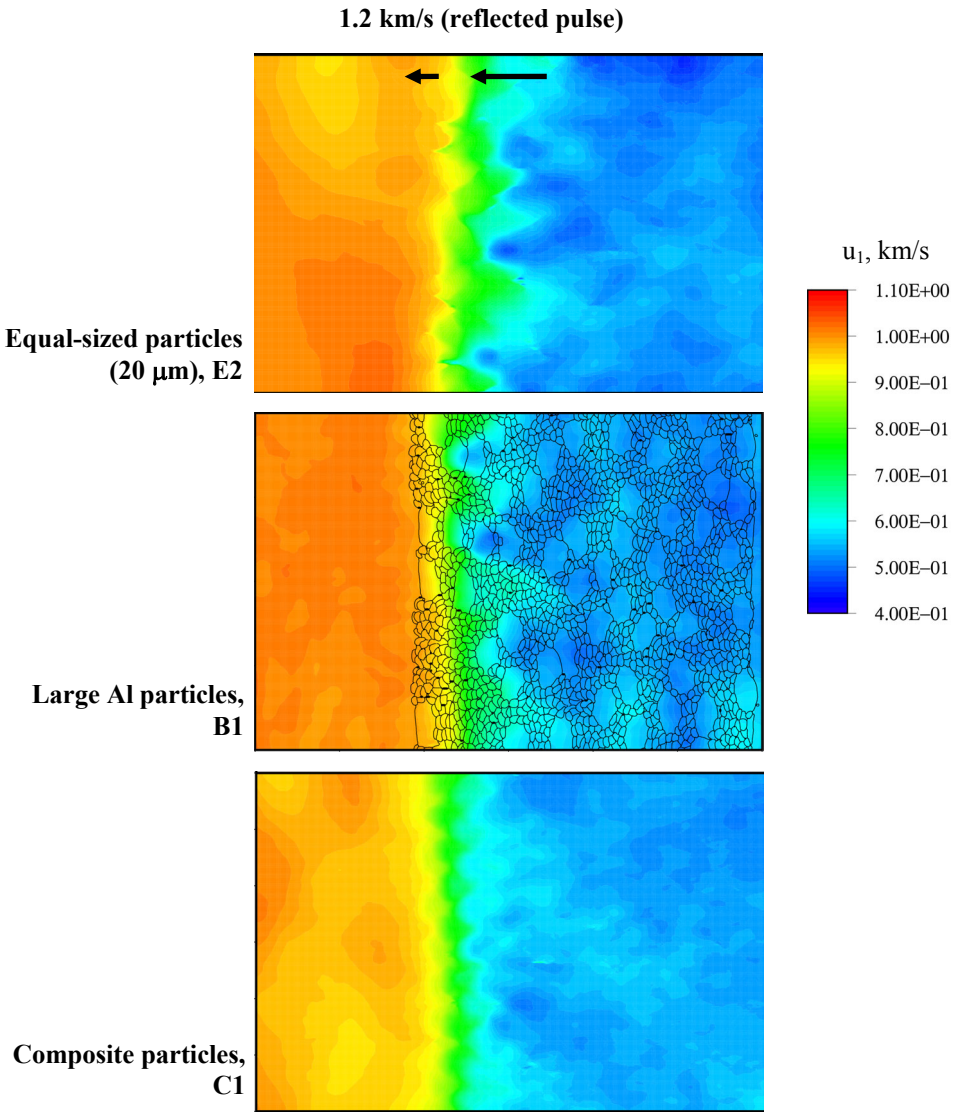

Figure 6.25: The longitudinal material velocity (u_1) fields in reflected waves are plotted for the powder mixtures indicated. The simulation windows are not drawn to scale.

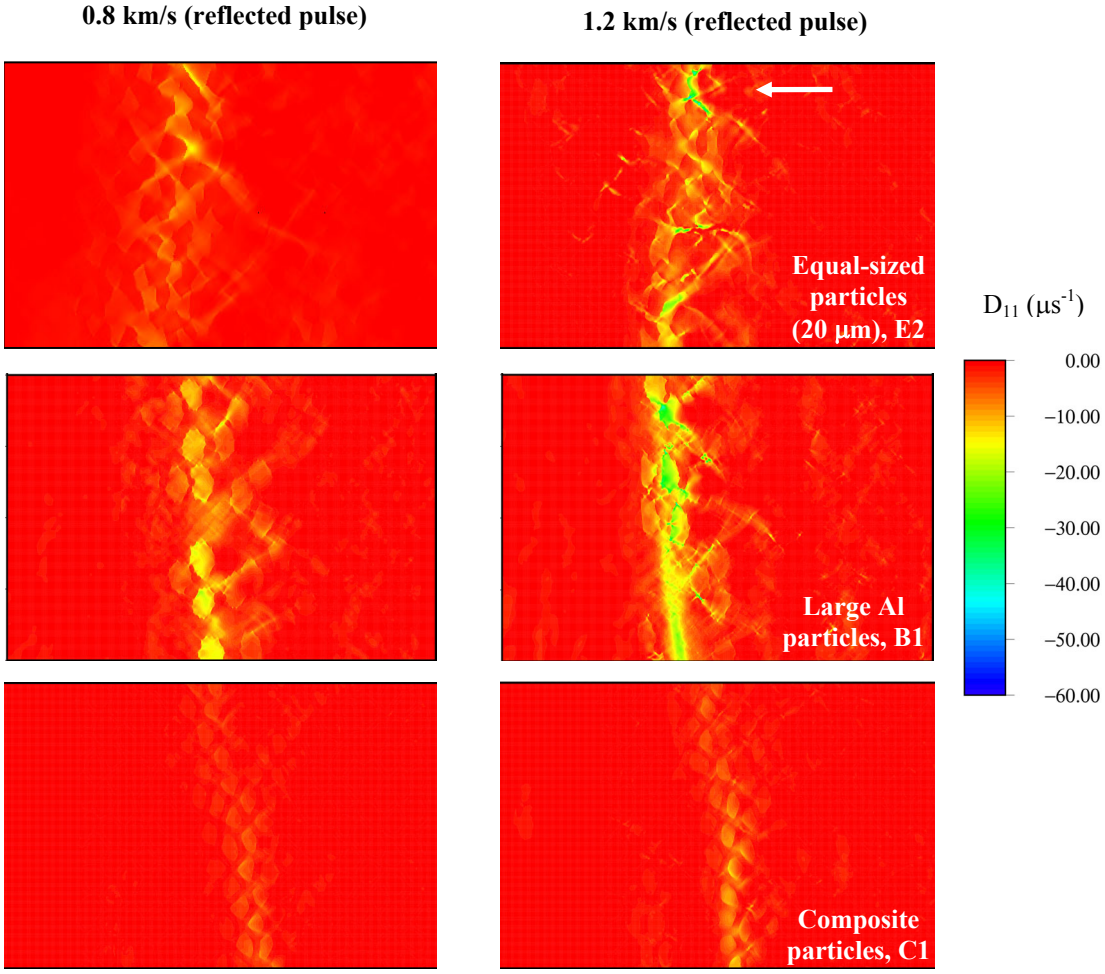

Figure 6.26: The longitudinal rate of deformation fields (D_{11}) fields in reflected waves are plotted for the powder mixtures indicated. The simulation windows are not drawn to scale.

6.9. Reduction of the mixing length scale

It has been mentioned that material velocity fluctuations in the shock wave may serve as the drive fast mixing processes such as shear localization, surface instability, and particle comminution (especially in the presence of saturated dislocation densities near the particle surfaces). However, the current framework is not well-equipped for the explicit simulation of these phenomena. Shear localization (e.g., shear banding) can be detected using the current framework, but the results depend on mesh density. To simulate the proper size, intensity, and distribution of shear bands, mesh-independent procedures are required. The simulation of particle comminution requires a method for treating extensive (shear-driven) fracture, which is a difficult feat in finite element codes. Finally, the problem involves multiple length scales. The heterogeneity of the velocity field depends on the mesoscale response of the shocked powders, while the fast mixing processes involve smaller length scales (i.e., the nanoscale). It is difficult to achieve sufficient resolution of these fine scale mixing processes in a simulated volume element that contains hundreds of particles. Therefore, the goal of this section is to provide an estimate of the reduction in mixing length scale due to material velocity fluctuations in the shock wave.

The basic assumption is some part of the kinetic energy of the velocity fluctuations is transformed to the free surface energy of a set of material fragments. This conceptualization is analogous to the model of Grady (1982), which treats the fragmentation of a rapidly expanding fluid. Recall that fluctuations in material velocity occur across the Ni/Al interfaces in the reflected shock waves (cf. Figure 6.25). The problem is idealized as two identical blocks of material that slide relative to each other with velocity jump, Δu, as shown in Figure 6.27. This is meant to represent two particles sliding relative to one another in the shock front. The mass densities of the blocks are the same, as are the masses located on either side of the interface. The volumes of material located near the interface are considered highly-dislocated (this has been demonstrated in the shock simulations). The kinetic energy of the two-block system, K, may be written in terms of the kinetic energy of the center-of-mass, K_{cm}, and the local kinetic energy of the system relative to the center-of-mass, K', i.e.,

$$K = K_{cm} + K' \tag{6.5}$$

The fragmentation process is driven by the local kinetic energy, K'. The transformation of local kinetic energy to free surface energy may be expressed as

$$\varepsilon \frac{K'}{m} = e_s \tag{6.6}$$

where ε is the fraction of local kinetic energy that is transformed to surface energy, m is the mass of the system, and e_s is the surface energy per unit mass of the system. The local kinetic energy of the two-block system is

$$K' = \frac{1}{8} m \left(\Delta u \right)^2 \tag{6.7}$$

The surface energy density of the system may be written as

$$e_s = \frac{6\lambda^2 \Gamma}{\rho \lambda^3} \phi^* \tag{6.8}$$

where it is assumed cubical (or spherical) fragments of size λ form in the zones of intense shearing (cf. Figure 6.27), ρ is the mass density of the sliding blocks, Γ is the free surface energy of the fragments, and ϕ^* is the mass fraction that participates in fragmentation. Combining Eqs. (6.6)–(6.8) yields a relation for the fragment size in terms of local velocity fluctuation, i.e.,

$$\lambda = \frac{48 \left(\Gamma / \rho \right)}{\varepsilon \left(\Delta u \right)^2} \phi^* \tag{6.9}$$

Equation (6.9) resembles a mixing length scale relation that has been proposed earlier (Yano and Horie, 1998), which is also based on the transformation of kinetic energy to surface energy. To facilitate estimates, full conversion of local kinetic energy to the surface energy is assumed (i.e., $\varepsilon = 1$), which is an upper bound. Following Yano and Horie (1998), it is also assumed that 10% of the mass in the system undergoes fragmentation (i.e., $\phi^* = 0.10$). To account for material compression, the specific free surface energy is taken as $\Gamma / \rho = \Gamma_0 / \rho_0$, where the subscript zero indicates quantities in the reference state. The (equilibrium) free surface energies of Ni and Al are 1.756×10^{-6} and 0.860×10^{-6} J/mm^2, respectively (Boyer and Gall, 1987).

The fragment size λ (i.e., the mixing length scale) is plotted for Ni and Al in Figure 6.28 over a range of relative particle velocity, Δu. In the shock simulations performed on mixture B1, the average level of velocity fluctuations in the reflected front is ~0.130 km/s for an impact velocity of 1.2 km/s. According to Figure 6.28, the mixing length scale is reduced to 50–100 nm for velocity fluctuations of this

magnitude in Ni and Al. The characteristic length of mass diffusion for two semi-infinite blocks of material that form a planar diffusion couple is $\bar{x} = 8\sqrt{D^* \Delta t}$, where D^* is the mass diffusivity and Δt is the elapsed time. The mass diffusivity is enhanced by the presence of dislocation cores and higher temperature (see the treatment outline by Horie (1993)). Based on the average dislocation density and temperature that has been calculated for the Ni/Al interface of mixture B1, the enhanced mass diffusivity is $D^* = 2 \times 10^{-10}$ mm$^2/\mu$s. For a shock pulse duration of 1 μs, the characteristic length of mass diffusion is $\bar{x}$ ~110 nm. This mass diffusion length scale is indicated in Figure 6.28. It can be seen that the fragment sizes (λ) fall below the mass diffusion length scale. As such, the particle fragments are small enough for ultra-fast chemical reactions to proceed by diffusive mass transport. Therefore, a viable explanation of the experimentally-observed shock-induced reactions is particle fragmentation that is driven by velocity fluctuations in the reflected shock front. Even if the time scale is reduced to 100 ns, the mass diffusion length scale is still a significant fraction of the fragment size, which would imply large scale (but incomplete) reactions during the shock transition. It is important to note that the precise mechanism of fragmentation has not been identified in the derivations above; only the energetic aspects of the process have been considered. Furthermore, the ductility of the constituents (Ni an Al) raises the question of whether such fragmentation (fracture) can occur at all. In light of these difficulties, fragment sizes obtained from Eq. (6.9) are viewed as rough, order-of-magnitude estimates.

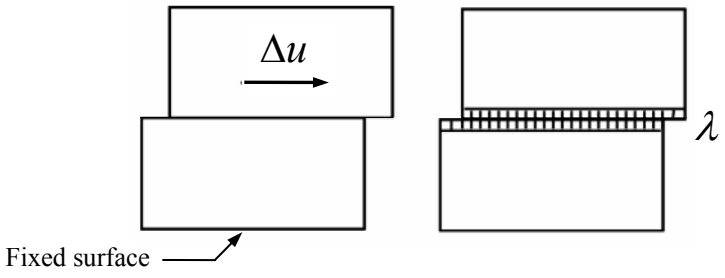

Figure 6.27: The idealized representation of particle velocity fluctuations in the shock wave (left) and subsequent fragmentation of the bodies near the interface (right).

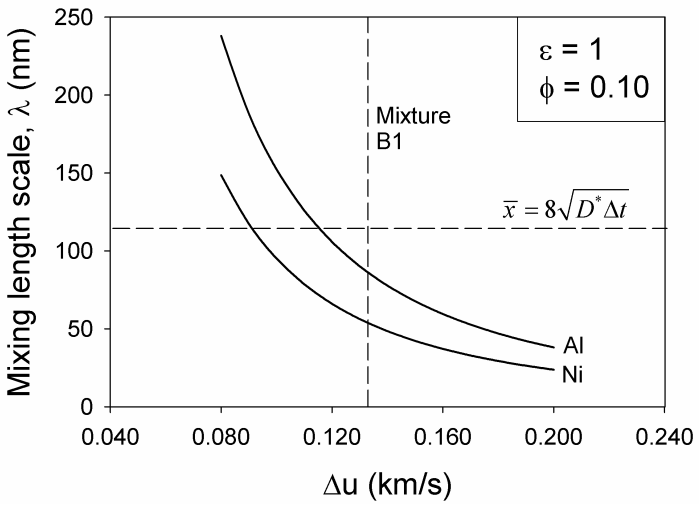

Figure 6.28: The mixing length scales (i.e., fragment sizes) for Ni and Al plotted as functions of the particle velocity fluctuation. The dashed lines indicate the average level of velocity fluctuations that are calculated in mixture B1 (for an impact velocity of 1.2 km/s) and the characteristic length of mass diffusion for a shock pulse of 1 μs.

6.10. Summary and conclusions

Shock wave propagation has been simulated at the mesoscale for 6 distinct Ni/Al powder mixtures. The Hugoniot curves and shock rise times that have been computed for an experimental powder (equivolumetric Ni/Al, 60% TMD, –325 mesh spherical particles) are in agreement with measurements. The agreement between the simulations and experimental data indicates that the mesoscale models are producing reasonable results. Interestingly, the shock velocity – particle velocity relation, $D(u)$, that is computed for the equivolumetric Ni/Al powders (60% TMD) exhibits a slight dependence on particle configuration (cf. Figure 6.2). It is thought that this dependence is due to variations in pore size among the mixtures.

Simulated deformation fields have been presented for each of the mixture classes (i.e., the equal-sized powders, the large Al powders, and the composite powders). The results highlight the differences in particle level deformation among the powder mixtures. In the composite powders, the simulated deformation indicates that high-speed jets of Ni are formed as the pores are collapsed. These jets impinge on neighboring particles in the shock front, which causes extensive deformation to the shells of those

particles. The simulated flow morphologies resemble those observed in recovery micrographs (cf. Figure 6.12). Therefore, the simulations illustrate a process through which the experimentally-observed Ni/Al surface instabilities may propagate in the composite powders.

A rank ordering of powder mixtures has been determined according to the Ni/Al surface area per unit volume, S_V, that forms in the shock waves (cf. Figure 6.19). On a per unit volume basis, the composite powders form the smallest Ni/Al interface while the smallest elemental powders form the largest Ni/Al interface. The rank ordering of powders is rearranged when a measure of the limiting surface amplification, $S_V / S_{V,0}$, is considered. Now the smallest elemental powders are the least effective while the large Al powders experience the largest amplification of surface area. This is because the large Al inclusions are encapsulated in a matrix of densified Ni particles that are pressed into the Al surfaces (cf. Figure 6.8).

A scaling relation (Eq. (6.2)) has been found for the normalized rate of Ni/Al interface creation in the shocked powder mixtures. Interestingly, the scaling exponent is the same for identical volume fractions of constituents and the scaling coefficient depends on the configuration of particles. This relation may find utility in analytical developments that do not resolve the distinct phases of powder mixtures in the shock wave.

Finally, the simulated responses in the reflected shock waves have been analyzed because shock-induced chemical reactions have been detected in the reflected stress pulses of certain Ni/Al powders (Bennett et al., 1992; Yang et al., 1997). These experiments demonstrated that the amount of energy deposited in the powder is not the key parameter, but rather mechanochemical effects (e.g., the nature of particle deformation and mixing) control whether or not large scale chemical reactions occur in the reflected pulse. In the mesoscale simulations, the heterogeneity of the material velocity fields has been quantified for the shocked Ni/Al powders. It has been shown that the non-planar reflected wave fronts (cf. Figure 6.25) introduce velocity gradients (or fluctuations) across the Ni/Al interfaces. A mixing length scale, $\lambda(\Delta u)$, was derived (Eq. (6.9)) by assuming the local kinetic energy of these particle velocity fluctuations is transformed to the surface energy of fragments in zones of intense shearing and near-saturated dislocation density. Mixture B1 is the simulated powder that corresponds to the experimental powder that undergoes shock-induced chemical reaction when the jump in shock stress (upon reflection) is

above a critical threshold (~14 GPa). When the simulated jump in shock stress (upon reflection) in mixture B1 is above this threshold, the simulated velocity fluctuations are projected to reduce the mixing length scale to 50–100 nm. At this length scale ($\lambda < \bar{x}$), diffusive mass transport is fast enough to support shock-induced chemical reactions. Furthermore, the rate of deformation in the reflected shock front is the most coherent and intense of all the simulated powder mixtures (cf. Figure 6.26). Thus, the simulations seem to indicate that mixture B1 is most prone to react in the reflected shock waves, and this is observed in the experiments.

CHAPTER 7

SUMMARY AND CONCLUSIONS

The goal of this research was to develop models that provide insight to the deformation and mixing of Ni/Al powder mixtures in shock waves. Of specific interest was the mesoscopic deformation that enables shock-induced chemical reactions (i.e., large scale chemical reactions that occur during shock compression). The problem was approached using direct numerical simulation. Here, shock wave propagation was simulated in discrete Ni/Al powder mixtures using the finite element method. In this chapter, the body of work is summarized, the novel contributions are identified, and suggestions for future work are offered.

7.1. Summary

At the outset of this work, a mechanistic model for the deviatoric stress-strain responses of metals was not available for the high strain rates that are encountered in the shock front. This was an important problem to address because the shock front in a granular material is not a discontinuity at the mesoscale. For micron-size particles, the shock front width is comparable to the particle diameter for shock stresses that are not too strong. Therefore, accurate modeling of particle deformation during the shock transition should address the highly dynamic conditions that are encountered during pore collapse (e.g., local strain rates on the order of 10^7 s^{-1}). This is especially important in the discrete particle simulations because the deformation and mixing of the constituents in (and closely behind) the shock front determines whether or not shock-induced chemical reactions are initiated in a given powder. Existing constitutive models that are based solely on thermally-activated dislocation glide (obstacle-bypassing) are only applicable for strain rates up to ~10^4 s^{-1}. Rate-independent models can provide an acceptable description of material strength behind the shock front, where the material approaches an equilibrium state. However, the situation is far from equilibrium in the shock front. Here, large non-equilibrium shear stresses drive high rates of plastic deformation during the transition. Furthermore, the marked increase in rate-sensitivity ($\partial\tau / \partial \ln \dot{\gamma}$) of fcc

metals at high strain rates ($>10^4$ s^{-1}) indicates rate-dependent descriptions of plastic deformation are necessary. Therefore, a dislocation-based constitutive model for the viscoplastic deformation of fcc metals at very high strain rates was developed in Chapter 2.

The proposed constitutive model addresses shock stress amplitudes below the twinning threshold, wherein the mode of plastic deformation is slip. In the model, the kinematics of slip are framed in terms of the generalized Orowan relation, which provides a seamless transition from glide-controlled plasticity (at lower shock stresses) to nucleation-controlled plasticity (at higher shock stresses). The kinetic relation for dislocation glide describes a transition from the regime of thermally-activated dislocation glide to the dynamic regime of continuous dislocation glide for applied stresses in excess of the mechanical threshold. In the dynamic regime, glide kinetics are governed by phonon damping and a relativistic effect, which prevents the dislocation velocity from exceeding the shear wave speed of the metal. A novel contribution of this modeling effort is the treatment of the dislocation substructure in the shock wave. The mobile and immobile dislocation densities have been assigned as internal state variables and differential equations have been constructed for their evolution based on the nucleation, multiplication, annihilation, and trapping of dislocations in shock waves. This provides a microstructure-based description of material hardening during the shock transition. Dislocation nucleation is an important issue to address in shock waves. In the model, there is a continuous transition from heterogeneous dislocation nucleation (at lower shock stresses) to homogeneous nucleation (at higher shock stresses). A new probabilistic model of heterogeneous dislocation nucleation has been developed to treat the emission of dislocation segments from sources (e.g., grain boundaries and particle surfaces). The model is based on a probability distribution of nominal source strength. The homogeneous nucleation of dislocations is modeled using a thermally-activated relation, which is analogous to the recent treatment of Armstrong et al. (2007; 2009). Additionally, microstructure-sensitive criteria have been developed to pin down the shock stress ranges where heterogeneous and homogeneous dislocation nucleation are expected. The constitutive relation that is developed in this work is applicable to shock wave loading and ramped loading that is executed at high rates (e.g., isentropic compression waves), both of which are active areas of research. Thus, the proposed model addresses a critical need for a more predictive viscoplastic constitutive law at very high strain rates.

In Chapter 3, the viscoplastic constitutive model was applied to three fcc metals (Cu, Ni, and Al) and one precipitate-hardening Al alloy (6061-T6). The constitutive model was then incorporated in simulations of steady planar waves in homogeneous slabs of these metals to compare model predictions to experimental measurements and to demonstrate the general features of the constitutive model. These calculations resolved the structure of the shock front, including all relevant field variables and dislocation density components. In contrast to other (simplified) steady wave simulations, the framework constructed here is applicable to finite deformation, retains the temperature-dependence of the solution, and integrates the microstructure evolution laws through the shock front to provide a path-dependent description of material response. Furthermore, an artificial viscosity is *not* used in these simulations. This is an important consideration because artificial viscous stresses obscure the actual shear responses that are of interest, and they introduce an artificial dependence on the grid that discretizes the domain. Therefore, the steady wave simulation framework that has been developed in this work may serve as a test bed for evaluating the performance of different candidate constitutive models in the shock loading regime.

To our knowledge, this is the first plastic wave analysis that incorporates a dislocation-based constitutive law with microstructure-sensitive glide resistance and explicit treatment of dislocation substructure evolution through the shock transition. The homogeneous dislocation nucleation criteria that are presented in Chapter 2 have been applied to all metals considered in this work. In the pure metals, the shock front width falls below the minimum spacing of dislocation sources (i.e., the dislocations themselves) for shock stresses greater than ~15 GPa. Therefore, homogeneous nucleation is expected at higher stresses and heterogeneous nucleation is expected at lower stresses. In the alloy (6061-T6), the twinning threshold (~13 GPa) is encountered before the shock front width falls below the average spacing of the precipitates (this would occur at ~30 GPa). Therefore, heterogeneous dislocation nucleation should prevail in 6061-T6 for shock stresses up to ~13 GPa. Above this stress amplitude, there is deformation twinning, which should raise the strength of the material on the Hugoniot since the twins serve as additional obstacles to dislocation glide. This appears to explain the deviation of the model from experimental measurements of strength on the Hugoniot for shock stresses greater than 13 GPa (cf. Figure 3.13) since the nucleation and growth of twin layers is not included in the constitutive model.

The steady wave simulations accurately reproduce much of the available experimental data. For shock stresses up to ~10 GPa in Cu and 6061-T6, model calculations are in agreement with direct measurements of the material velocity profiles, $u(t)$, and indirect measurements of the dynamic shear stress, $\tau(\psi)$, and plastic rate of deformation, $D_1^p(\psi)$. The latter profiles were calculated using the thermodynamic framework of Wallace (1980b; 1980a). Since (weak) shock front profiles are intimately related viscoplastic response of the material, the agreement of model calculations with available shock profile data provides support for the proposed constitutive model. Furthermore, it has been demonstrated that the constitutive model respects the Swegle-Grady scaling law over four decades of strain rate (10^6–10^{10} s^{-1}). The upper part of this strain rate regime is governed by thermally-activated homogeneous dislocation nucleation, whereas this lower part of the strain rate regime is governed by heterogeneous nucleation and glide. The model calculations of dislocation density on the Hugoniot are in agreement with recovery micrographs at lower shock stresses and atomistic calculations at higher shock stresses. Model calculations of shear strength in the shocked state, τ^-, are in agreement with experiments that use non-invasive techniques to measure strength for shock stress amplitudes up to ~15 GPa in Cu, Ni, Al, and 6061-T6. The agreement between the steady wave simulations and the corresponding experimental data indicates the viscoplastic constitutive law provides reasonable results.

The experimental work pertaining to shock wave chemistry in Ni/Al powder mixtures was reviewed in Chapter 4. Time-resolved experiments that offer definitive proof of ultra-fast (shock-induced) chemical reactions have been cited, and mechanisms that have been hypothesized for the ultra-fast mixing rates required to support these reactions have been discussed.

The mechanically-driven mixing of powder constituents is perhaps the most important factor that determines whether or not large scale chemical reactions occur in the shock wave. Current experimental methods cannot resolve (in space and time) the shock-induced deformation and mixing of the particles. Therefore, it is attractive to study this problem using direct numerical simulation. In this work, the finite element (FE) method has been used to simulate shock wave propagation in discrete micron-sized Ni/Al powder mixtures. The simulations were performed using the arbitrary Lagrangian-Eulerian (ALE) finite element code, Raven (Benson, 1995a). A summary of the numerical methods that were used in these calculations are provided in Chapter 5. The FE model that is developed in this work addresses certain

shock simulation aspects that have been ignored in previous work, in particular: (i) the rate-dependence of plastic deformation during pore collapse, (ii) the thermodynamic state and microstructure of reactant interfaces, (iii) simulated responses in reflected shock waves (where shock-induced reactions are observed in certain Ni/Al powder mixtures), and (iv) the variation of simulation results that are extracted from statistical volume elements of the powder mixtures. The viscoplastic constitutive model of Chapter 2 has been implemented in the FE code (as a user material subroutine) to define the deviatoric stress-strain responses of the Ni and Al phases. At this point, reaction kinetics have been omitted in the simulations because it is difficult to include them in a meaningful way when the mechanisms of reaction initiation and the early stages of reaction propagation are unknown. Furthermore, the inclusion of arbitrarily fast reaction kinetics might obscure the mechanically-driven mechanisms that are sought for understanding shock-induced reactions.

It is useful to distinguish the current work from previous simulation work in the Ni/Al powder system (Eakins and Thadhani, 2007; Eakins and Thadhani, 2008). Both efforts have attempted to clarify the mechanisms of shock-induced reactions (and their relation to mesoscale deformation) via discrete particle simulation. However, the prior work has focused on incorporating realistic descriptions of initial particle morphology in the shock simulations, while relying on conventional constitutive models for deviatoric material response. The incorporation of accurate particle morphology was especially useful in the flaky Ni + spherical Al powders, as this enabled correlation of the simulated deformation fields with experiments that exhibited signatures of shock-induced reactions. The current work has focused on incorporating advanced constitutive models for particle deformation in the shock simulations, while relying on idealized representation of initial particle morphology. Although some details of the precise particle shapes are sacrificed in this work, the use of idealized particle morphology enables simulation of a wide range of particle mixtures in an efficient manner. Furthermore, it has been demonstrated that the strain-rate-sensitivity of the constitutive model can have a profound effect on shocked particle morphology in the discrete particle simulations, which is relevant to the problem of reactant mixing and shock-ignition.

Shock wave propagation has been simulated at the mesoscale for 6 distinct Ni/Al powder mixtures. The discrete particle simulation results were presented and analyzed in Chapter 6. The Hugoniot curves and shock rise times that have been computed for an experimental powder (equivolumetric Ni/Al,

60% TMD, –325 mesh spherical particles) are in agreement with measurements. This indicates that the mesoscale models are producing reasonable macroscopic results. Sets of deformation fields were presented for each of the mixture classes (i.e., the equal sized powders, the large-Al powders, and the composite powders) to highlight flow morphology, dislocation density, and thermal response. The dislocation density of the shocked particles is relevant to the problem of mass mixing, and up to this point, has not been quantified in previous simulation work. The current work indicates the dislocation density in certain regions of the Ni phase approaches the upper limiting value for a crystalline material ($\sim 10^{17}$ m^{-2}) for the strongest shocks considered here. The highest dislocation densities develop in the pore-collapsed regions. In these regions of very high dislocation density, the Ni phase may be prone to fragmentation (fracture). This would expose a large amount of fresh surface area for near-instantaneous chemical reaction, and it would reduce the mixing length scale that needs to be explained by diffusive mass transport in the shock wave.

Flow morphologies that were computed using the dislocation-based viscoplastic constitutive law and the Steinberg-Guinan model have been compared to recovery micrographs extracted from the corresponding experimental Ni/Al powder (cf. Figure 6.16). The flow morphology that is computed using the viscoplastic law displays qualitative agreement with the recovery micrograph. On the other hand, the severe deformation of the Ni particles that is computed using the (rate-independent) Steinberg-Guinan model is not observed in the recovery micrograph. Rate-independent models rely on a consistency condition for determining the tensorial rate of plastic deformation (i.e., the stress state must remain on a yield surface, regardless of the rate of deformation). This leads to a response that is too soft because the non-equilibrium stresses that are required to drive high rates of plastic deformation are not taken into account. Stated another way, the rate-dependence of plastic deformation during the shock transition is neglected. This is a significant observation because rate-independent constitutive laws are commonly used in mesoscale simulations of shock waves in discrete metallic particle systems. The Steinberg-Guinan model is a perfectly acceptable model of material strength *behind* the shock front. However, a rate-independent description of plastic deformation in the shock front does not seem appropriate. This is an important point because the deformation of particles in the shock front (or closely behind it) is intimately related to the initiation of shock-induced chemical reactions. Thus, the current work is an attempt to

resolve the shock-induced deformation of particles using a constitutive model that is specialized for the high rates of deformation encountered in the shock front.

Since chemical reactions originate at the surfaces where Ni and Al come into direct contact, the entire (disjointed) Ni/Al interface has been tracked in the shock wave simulations. The size of the Ni/Al interface has been quantified by calculating its surface area per unit volume as a function of shock stress, i.e., $S_V(\sigma)$. The computed rate of Ni/Al interface creation is well-described by a power law, i.e., $\dot{S} \propto \sigma^n$, where the scaling exponent is constant for a given phase distribution and the scaling coefficient depends on the configuration of the particles. The state of the Ni/Al interface and its underlying microstructure were quantified by computing histograms of the Ni/Al surface temperature and dislocation density. The Ni/Al powder mixtures have been rank-ordered according to these measures of macromixing (cf. Chapter 6). The melting behavior of the Ni/Al interface in the shock wave is also of interest. It is known that self-propagating high-temperature synthesis (SHS) reactions in the Ni/Al system occur by melting of Al and dissolution of Ni into the melt. However, shock compression experiments performed on reactive powders indicate that melting actually inhibits the occurrence of the ultra-fast (shock-induced) chemical reactions (Vandersall and Thadhani, 2003). Therefore, the degree of melting along the Ni/Al interface has been quantified as a function of shock stress in the simulations (cf. Figure 6.23). To avoid large scale melting of Al in the equivolumetric elemental powders, the shock stress should be kept below ~8 GPa. The composite powders can be shocked to higher stresses before there is large scale melting of Al.

Finally, simulated powder responses in the reflected shock waves have been analyzed as shock-induced chemical reactions have been detected here for certain Ni/Al powders (Bennett et al., 1992; Yang et al., 1997). These experiments have been reconstructed in the simulation framework. The Ni-rich, large-Al powder (mixture B1) is the simulated powder that corresponds to the experimental powder that undergoes shock-induced chemical reaction when the jump in shock stress (upon reflection) is above a critical threshold. In the mesoscale simulations, the heterogeneity of the material velocity fields, $\mathbf{u}$, and the rate of deformation fields, $\mathbf{D} = sym(\mathbf{u}\bar{\nabla})$, have been quantified. It has been shown that non-planar reflected wave fronts introduce velocity gradients (or fluctuations) across the Ni/Al interfaces. These velocity fluctuations may drive ultra-fast mixing processes at the Ni/Al interfaces (e.g., shear localization, surface instability, and/or particle comminution). Unfortunately, the FE model is not well-equipped for

explicit simulation of these phenomena. Therefore, an estimate of a reduced mixing length scale, $\lambda(\Delta u)$, was derived by assuming the local kinetic energy of these particle velocity fluctuations is transformed to the surface energy of fragments in zones of intense shearing and near-saturated dislocation density. When the simulated jump in shock stress for mixture B1 is above the critical experimental threshold, the simulated velocity fluctuations reduce the mixing length scale to 50–100 nm. At this length scale, diffusive mass transport is fast enough to support shock-induced chemical reactions. Thus, a potential explanation of shock-induced chemical reactions in the experimental powder is particle fragmentation driven by velocity fluctuations. Furthermore, the rate of deformation fields in mixture B1 exhibit the most coherent and most intense shock fronts out of all simulated powders (cf. Figure 6.26). This is significant because the simultaneous (coordinated) deformation of constituents in the shock front is thought to be responsible, in part, for the shock-initiation of flaky Ni + spherical Al powders (Eakins and Thadhani, 2006; Eakins and Thadhani, 2007; Eakins and Thadhani, 2008). Therefore, the mesoscale simulation framework that has been developed here appears to pick up certain deformation processes that are relevant to the shock ignition of Ni/Al powder mixtures.

7.2. Design of energetic materials

The simulation tools that have been developed in this thesis provide a quantitative framework that may be used to help guide the design of energetic materials. The focus of this work has been the Ni/Al powder system. However, the framework can be applied to any reactive metal powder system, and to aggregates of high explosive (HE) crystals (with or without polymer binders). Regarding the design of reactive powder mixtures, one must first define functional requirements, the design space (e.g., admissible particle shapes, sizes, porosity, etc.), and criteria for evaluating the performance of candidate configurations. The algorithms developed in this work may then be used to:

- rapidly generate volume elements of user-defined powder configurations (intermediate to and beyond those imported from experiments),
- mesh the volume elements for FE simulation in an automated manner,
- execute concurrent shock wave simulations on distributed computational resources,

- compute the Hugoniot curves of the powder mixtures,
- track and quantify the entire reactant interface during shock wave propagation, and
- analyze particle level deformation fields that are relevant to shock initiation.

In this work, the Ni/Al interface was quantified on the basis of its surface area per unit volume, rate of growth, temperature, and dislocation density. Attention was also paid to the fluctuating velocity fields near the Ni/Al interface and the coherency and intensity of the reflected shock fronts. The scaling relations that have been found for the interface growth rate, $\dot{S}$, and the fragment size, λ, can certainly be incorporated in design calculations. A repository of simulation data has been generated for 6 distinct configurations of the Ni/Al powder system. This repository of data may serve as a reference for designers of Ni/Al powder mixtures, or as a foundation for additional simulation work that explores different configurations of the Ni/Al system.

7.3. Novel contributions

The novel contributions of this work are as follows:

Constitutive modeling

- A physically-based constitutive model has been developed for the viscoplastic response of fcc metals at very high strain rates. This enables more accurate simulation of dynamic plastic deformation, especially in heterogeneous material systems with length scales that are comparable to the wave front width.
- Mechanistic relations have been derived for the evolution of the mobile and immobile dislocation densities in the shock loading regime. These relations are integrated through the shock front to provide path-dependent descriptions of material hardening and viscoplastic deformation.
- A new model of heterogeneous dislocation nucleation has been developed for polycrystalline metals and alloys. The model is based on a statistical distribution of dislocation source strength.
- A model of homogeneous dislocation nucleation has been implemented in the steady wave calculations, which is pertinent to the strong shock regime.

- Microstructure-sensitive criteria have been developed to pin down the stress amplitudes where heterogeneous and homogeneous dislocation nucleation are expected in planar shock waves.
- The viscoplastic constitutive model parameters have been determined for three fcc metals (Cu, Ni, and Al) and a precipitate-hardening Al alloy (6061-T6).
- A framework has been constructed for simulating finite strain steady planar waves in homogeneous media. The framework serves as a test bed for evaluating the performance of constitutive models in the shock loading regime.
- The strength on the Hugoniot has been calculated for Cu, Ni, Al, and 6061-T6 using the viscoplastic constitutive law and the steady wave simulation framework. This enabled the first comparison of a rate- and path-dependent constitutive model to experimental measurements of strength in the shocked state.

Discrete particle simulation

- Shock wave propagation has been simulated in discrete Ni/Al powder mixtures using a FE model that incorporates the new viscoplastic constitutive law. These discrete particle simulations are the first to incorporate a rate- and path-dependent model of plasticity to address the high strain rates that are encountered during the collapse of pores in shocked powder systems.
- The mesoscale simulations presented in this work are the first to resolve dislocation density fields in shocked Ni/Al powder mixtures.
- Algorithms have been developed to quantify the size, rate of growth, temperature, and dislocation density of reactant interfaces that develop in shocked powder mixtures.
- A power law relation, $\dot{S} \propto \sigma^n$, has been found for the growth rate of Ni/Al interfaces. Here, the scaling exponent was found to be constant for a fixed set of constituent volume fractions, while the scaling coefficient was found to depend on powder configuration. By extension, the Ni/Al surface area per unit shocked volume may be expressed in terms of shock stress, i.e., $S_V = B\sigma^n / D$.

- Simulated responses in the reflected shock waves have been quantified in this work. In particular, velocity fluctuations that develop at the Ni/Al interfaces and the coherency and intensity of deformation in the reflected shock fronts.
- An estimate of fragment size, $\lambda(\Delta u)$, has been derived by assuming the local kinetic energy of velocity fluctuations in the shock wave is transformed to the free surface energy of fragmented (fractured) particles.
- The mesoscale FE models provide a quantitative simulation framework that may be used to help guide the design of energetic materials (cf. Section 7.2).

7.4. Conclusions

The following conclusions are drawn from the work presented in this thesis:

Constitutive modeling

- The proposed viscoplastic constitutive model is conceptually sound and in agreement with available experimental data.
- A description of material strength that is based on dislocation density (and the spacing of non-shearable precipitates, if present) is reasonable for pure fcc metals and precipitate-hardening alloys in the shock loading regime.
- Heterogeneous and homogeneous dislocation nucleation are relevant aspects of substructure evolution in the shock loading regime. Heterogeneous nucleation is dominant at lower shock stress; homogeneous nucleation is dominant at higher shock stresses.
- The material strength on the Hugoniot that is calculated using the viscoplastic law is in agreement with non-invasive techniques that have been used to measure strength in the shocked state (i.e., real-time x-ray diffraction, quasistatic reloading of shock-prestrained specimens, and reshock/release experiments).

Discrete particle simulation

- The mesoscale FE simulations can be utilized to resolve particle level deformation in the shock wave. However, this simulation framework is insufficient for resolving fine-scale mixing processes, such as fragmentation of particles down to the nanoscale or fine scale surface instability.
- Rate-independent constitutive models are inappropriate for resolving flow morphology in the shock front (e.g., during pore collapse).
- It appears that idealized particle geometries are sufficient for computing the basic characteristics of particle deformation and the surface area per unit volume of spherical Ni/Al powder mixtures and composite Ni/Al powders. However, realistic descriptions of particle geometry are likely needed for irregular particle shapes (e.g., flaky particles), which form a complex network of contacts in the initial configuration.
- In the composite Ni/Al particle mixtures, the jetting of Ni (during pore collapse) appears to play a role in the experimentally-observed surface instabilities (cf. Figure 6.12).
- The mesoscale simulations can be used to establish rank-orderings of powder mixtures based on metrics of macromixing (e.g., the surface area per unit volume of the Ni/Al interface, $S_V(\sigma)$, or the growth rate of the Ni/Al interface, $\dot{S}(\sigma)$). These measures of macromixing may find utility in treatments directed towards reaction initiation and the design of reactive powder mixtures.
- A potential mechanism of shock-induced reactions in Ni/Al powder mixtures is the fragmentation (fracture) of particles down to the nanoscale due to strong velocity fluctuation at the Ni/Al interfaces. This has been demonstrated (in principle) using the current simulation framework; however, stronger assertions of this conclusion require more rigorous treatments of fine-scale mixing processes.

7.5. Suggestions for future work

The performance of the viscoplastic constitutive model that was developed in Chapter 2 may be further evaluated in the following ways. The inclined plate impact experiments of Clifton and co-workers

may be simulated using a numerical method that incorporates the viscoplastic law. This would serve as a fairly rigorous test of the constitutive model because now the shear mode of deformation is excited to a greater extent. As another diagnostic test, the wave-induced Rayleigh-Taylor surface instabilities that develop in thin rippled metallic foils could be simulated using a finite element model that incorporates the viscoplastic law. If the constitutive model performs well, the perturbation growth factors that have measured for 6061-T6 Al alloy should be reproduced by the simulations. Recent simulations of ripple growth in 6061-T6 and vanadium indicate that the deviatoric responses that are predicted using the Steinberg-Guinan model and the Preston-Tonks-Wallace model (with default parameters) are too soft (Remington et al., 2006; Park et al., 2010).

A crystal plasticity formulation of the constitutive law may be developed and implemented in the finite element simulations. This should be fairly straight forward because relations for the average dislocation flux ($N_m \overline{v}$) have already been derived. The extension to crystal plasticity would require specialization and tracking of the dislocation fluxes ($N_m^{\alpha} \overline{v}^{\alpha}$) on each of the α^{th} slip systems. The usage of crystal plasticity in the shock wave simulations would address the anisotropic nature of grain deformation and the effects of texture.

The discrete particle simulation framework may be enhanced by developing a method for treating the fracture of particles in the shock wave. This would help address the issue of particle fragmentation driven by velocity fluctuations. However, it is a huge challenge to incorporate physically-based fragmentation schemes in finite element calculations. Other simulation tools (e.g., the discrete element method) may be better-suited for this purpose. Additionally, full 3D simulation of shock waves in the particle mixtures is an obvious extension that would provide a more accurate description of particle deformation. This is an option worth pursuing if computational resources are in place.

Finally, the reaction kinetics could be incorporated in the finite element simulations. However, one must be careful to address the issue of mass mixing in a meaningful way if this route is pursued. At this point, it may be more useful to simulate unit processes that are informed by the discrete particle simulations. For example, atomistic simulations of the sliding (or oblique impact) of blocks of Ni and Al (with some prescribed surface roughness) may provide insight to fine-scale mixing processes.

REFERENCES

Armstrong, R.W., W. Arnold and F.J. Zerilli (2007) "Dislocation mechanics of shock-induced plasticity" *Metall. Mater. Trans. A*, 38A(11), 2605-2610.

Armstrong, R.W., W. Arnold and F.J. Zerilli (2009) "Dislocation mechanics of copper and iron in high rate deformation tests" *J. Appl. Phys.*, 105, 1-7.

Asay, J.R., T. Ao, J.-P. Davis, et al. (2008) "Effect of initial properties on the flow strength of aluminum during quasi-isentropic compression" *J. Appl. Phys.*, 103, 083514.

Asay, J.R. and L.C. Chhabildas (1981) in Shock Waves and High Strain-Rate Phenomena in Metals (eds. M.A. Meyers and L.E. Murr), Plenum Press, New York.

Austin, R.A. (2005) "Numerical Simulation of the Shock Compression of Microscale Reactive Particle Systems," M.S. Thesis, Georgia Institute of Technology.

Austin, R.A., D.L. McDowell and D.J. Benson (2006) "Numerical simulation of shock wave propagation in spatially-resolved particle systems" *Modell. Simul. Mater. Sci. Eng.*, 14, 537-561.

Bandak, F.A., R.W. Armstrong and A.S. Douglas (1992) "Dislocation structure for one-dimensional strain in shocked crystal" *Phys. Rev. B*, 36(6), 3228-3235.

Barton, N.R., D.J. Benson and R. Becker (2005) "Crystal level continuum modelling of phase transformations: the alpha <->epsilon transformation in iron" *Modell. Simul. Mater. Sci. Eng.*, 13(5), 707-731.

Barton, N.R., N.W. Winter and J.E. Reaugh (2009) "Defect evolution and pore collapse in crystalline energetic materials" *Modell. Simul. Mater. Sci. Eng.*, 17(3), 035003.

Basinski, Z.S. (1959) "Thermally activated glide in face-centered cubic metals and its application to the theory of strain hardening" *Philos. Mag.*, 4(40), 393-432.

Bat'kov, Y.V., V.N. Knyazev, S.A. Novikov, et al. (2000) "Shear strength of Aluminum at shockless compression" *Shock Compression of Condensed Matter - 1999* (eds. M.D. Furnish, L.C. Chhabildas and R.S. Hixson), Melville, NY, AIP: 501-504.

Batsanov, S.S. (1986) "Inorganic Chemistry of High Dynamic Pressures" *Russ. Chem. Rev.*, 55(4), 297-315.

Batsanov, S.S. (1994) Effects of explosions on materials: Modifications and synthesis under high-pressure shock compression, Springer, New York.

Batsanov, S.S. (1996) "Synthesis and modification of materials by shock waves: real-time measurements and mechanisms of reaction" *Mater. Sci. Eng. A - Struct.*, 210, 57-63.

Batsanov, S.S., G.S. Doronin, S.V. Klochkov, et al. (1986) "Synthesis reactions behind shock fronts" *Combustion, Explosion, and Shock Waves*, 22(6), 765-768.

Bennett, L.S., Y. Horie and M.M. Hwang (1994) "Constitutive model of shock-induced chemical reactions in inorganic powder mixtures" *J. Appl. Phys.*, 76(6), 3394-3402.

Bennett, L.S., F.Y. Sorrell, I.K. Simonsen, et al. (1992) "Ultrafast chemical reactions between nickel and aluminum powders during shock loading" *Appl. Phys. Lett.*, 61(5), 520-521.

Benson, D.J. (1992) "Computational Methods in Lagrangian and Eulerian hydrocodes" *Comput. Meth. Appl. Mech. Eng.*, 99, 235-394.

Benson, D.J. (1994) "An analysis by direct numerical simulation of the effects of particle morphology on the shock compaction of copper powder" *Modell. Simul. Mater. Sci. Eng.*, 2, 535-550.

Benson, D.J. (1995a) "A multi-material Eulerian formulation for the efficient solution of impact and penetration problems" *Comput. Mech.*, 15, 558-571.

Benson, D.J. (1995b) "The calculation of the shock velocity - particle velocity relationship for a copper powder by direct numerical simulation" *Wave Motion*, 21, 85-99.

Benson, D.J. and P. Conley (1999) "Eulerian finite-element simulations of experimentally acquired HMX microstructures" *Modell. Simul. Mater. Sci. Eng.*, 7, 333-354.

Benson, D.J., V.F. Nesterenko, F. Jonsdottir, et al. (1997) "Quasistatic and Dynamic Regimes of Granular Material Deformation Under Impulse Loading" *J. Mech. Phys. Solids*, 45, 1955-1999.

Benson, D.J., W. Tong and G. Ravichandran (1995) "Particle-level modeling of dynamic consolidation of Ti-SiC powders" *Modell. Simul. Mater. Sci. Eng.*, 3, 771-796.

Boehler, R. and M. Ross (1997) "Melting curve of aluminum in a diamond cell to 0.8 Mbar: implications for iron" *Earth and Planetary Science Letters*, 153(3-4), 223-227.

Boslough, M.B. (1990) "A thermochemical model for shock-induced reactions (heat detonations) in solids" *J. Chem. Phys.*, 92(3), 1839-1848.

Boyer, H.E. and T.L. Gall, eds, (1987) Metals Handbook, ASM.

Bringa, E.M., A. Caro, Y.M. Wang, et al. (2005) "Ultrahigh strength in nanocrystalline materials under shock loading" *Science*, 309(5742), 1838-1841.

Bringa, M., K. Rosolankova, R.E. Rudd, et al. (2006) "Shock deformation of face-centered-cubic metals on subnanosecond timescales" *Nat. Mater.*, 5(10), 805-809.

Cao, B.Y., E.M. Bringa and M.A. Meyers (2007) "Shock compression of monocrystalline copper: Atomistic Simulations" *Metall. Mater. Trans. A*, 38A(11), 2681-2688.

Capolungo, L., D.E. Spearot, M. Cherkaoui, et al. (2007) "Dislocation nucleation from bicrystal interfaces and grain boundary ledges: Relationship to nanocrystalline deformation" *J. Mech. Phys. Solids*, 55(11), 2300-2327.

Clifton, R.J. (1970) "On the Analysis of Elastic/Visco-plastic Waves of Finite Uniaxial Strain," in Shock Waves and the Mechanical Properties of Solids (eds. J.J. Burke and V. Weiss), Syracuse University Press, Syracuse, NY: 73-116.

Conrad, H. (1970) "The athermal component of flow stress in crystalline solids" *Mater. Sci. Eng.*, 6(4), 265-273.

Cotterill, R.M.J. (1977) "Does dislocation density have a natural upper limit?" *Phys. Lett.*, 60A(1), 61-62.

Davison, L. and R.A. Graham (1979) "Shock Compression of Solids" *Phys. Rep.*, 55(4), 255-379.

Do, I.P.H. and D.J. Benson (2000) "Modeling shock-induced chemical reactions" *Int. J. Comput. Eng. Sci.*, 1(1), 61-79.

Do, I.P.H. and D.J. Benson (2001) "Micromechanical modeling of shock-induced chemical reactions in heterogeneous multi-material powder mixtures" *Int. J. Plasticity*, 17, 641-668.

Douin, J., P. Donnadieu, T. Epicier, et al. (2001) "Stress field around precipitates: direct measurement and relation with the behavior of dislocations" *Mater. Sci. Eng. A - Struct.*, 319, 270-273.

Dremin, A.N. and O.N. Breusov (1968) "Processes Occurring in Solids Under the Action of Powerful Shock Waves" *Russ. Chem. Rev.*, 37(5), 392-401.

Dunbar, E., N.N. Thadhani and R.A. Graham (1993) "High-pressure shock activation and mixing of nickel-aluminum powder mixtures" *J. Mater. Sci.*, 28, 2903-2914.

Duvall, G.E. (1985) "The Physics Connection" *Metallurgical Applications of Shock-wave and High-strain-rate Phenomena* (eds. L.E. Murr, K.P. Staudhammer and M.A. Meyers), CRC Press: 3-25.

Eakins, D. (2007) "Role of heterogeneity in the chemical and mechanical shock-response of nickel and aluminum powder mixtures," Ph.D. thesis, Georgia Institute of Technology.

Eakins, D. and N.N. Thadhani (2006) "Shock-induced reaction in a flake nickel plus spherical aluminum powder mixture" *J. Appl. Phys.*, 100, 113521.

Eakins, D. and N.N. Thadhani (2007) "Discrete particle simulation of shock wave propagation in a binary Ni+Al powder mixture" *J. Appl. Phys.*, 101, 043508.

Eakins, D.E. and N.N. Thadhani (2008) "Mesoscale simulation of the configuration-dependent shock-compression response of Ni plus Al powder mixtures" *Acta Materialia*, 56(7), 1496-1510.

Estrin, Y. (1996) in Unified Constitutive Laws of Plastic Deformation (eds. A.S. Krausz and K. Krausz), Academic Press, New York.

Estrin, Y. and L.P. Kubin (1986) "Local strain-hardening and nonuniformity of plastic deformation" *Acta Metall.*, 34(12), 2455-2464.

Farkas, D. and W.A. Curtin (2005) "Plastic deformation mechanisms in nanocrystalline columnar grain structures" *Mater. Sci. Eng. A - Struct.*, 412(1-2), 316-322.

Follansbee, P.S. and G.T. Gray (1991a) "Dynamic deformation of shock prestrained copper" *Mater. Sci. Eng. A - Struct.*, 138(1), 23-31.

Follansbee, P.S. and G.T. Gray (1991b) "The response of single-crystal and polycrystal nickel to quasi-static and shock deformation" *Int. J. Plasticity*, 7(7), 651-660.

Follansbee, P.S. and U.F. Kocks (1988) "A Constitutive Description of the Deformation of Copper based on the use of the Mechanical Threshold Stress as an Internal State Variable" *Acta Metall.*, 36(1), 81-93.

Frutschy, K.J. and R.J. Clifton (1998) "High-temperature pressure-shear plate impact experiments on OFHC copper" *J. Mech. Phys. Solids*, 46(10), 1723-1743.

Gogulya, M.F., I.M. Voskoboinikov, A.Y. Dolgoborodov, et al. (1991) "Interaction of sulfur with metals under shock loading" *Khimicheskaya Fizika*, 10(3), 420-427.

Grady, D.E. (1982) "Local inertia effects in dynamic fragmentation" *J. Appl. Phys.*, 53(1), 322-325.

Graham, R.A. (1989) "Issues in Shock-Induced Solid-State Chemistry" *Proceedings of the Third International Symposium on Dynamic Pressures* (ed. R. Charet), La Grande Motte, France: 175.

Graham, R.A. and D.M. Webb (1984) *Shock Waves in Condensed Matter - 1983* (eds. J.R. Asay, R.A. Graham and G.K. Straub): 211.

Gray, G.T. and P.S. Follansbee (1988) "Influence of peak pressure on the substructure evolution and mechanical properties of shock-loaded 6061-T6 aluminum" *Shock Waves in Condensed Matter - 1987* (eds. S.C. Schmidt and N.C. Holmes): 339-342.

Gray, G.T., P.S. Follansbee and C.E. Frantz (1989) "Effect of residual strain on the substructure development and mechanical response of shock-loaded copper" *Mater. Sci. Eng. A - Struct.*, 111, 9-16.

Guinan, M.W. and D.J. Steinberg (1974) "Pressure and temperature derivatives of isotropic polycrystalline shear modulus for 65 elements" *J. Phys. Chem. Solids*, 35(11), 1501-1512.

Gupta, Y.M., G.E. Duvall and G.R. Fowles (1975) "Dislocation mechanisms for stress relaxation in shocked LiF" *J. Appl. Phys.*, 46(2), 532-546.

Hammetter, W.F., R.A. Graham, B. Morosin, et al. (1988) "Effects of Shock Modification on the Self-Propagating High-Temperature Synthesis of Nickel Aluminides," in Shock Waves in Condensed Matter, 1987 (eds. S.C. Schmidt and N.C. Holmes), Elsevier Science, Amsterdam: 431-434.

Hirth, J.P. and J. Lothe (1968) Theory of Dislocations, McGraw-Hill, New York.

Holian, B.L. and P.S. Lomdahl (1998) "Plasticity induced by shock waves in nonequilibrium molecular-dynamics simulations" *Science*, 280, 2085-2088.

Horie, Y. (1993) "Shock-Induced Chemical Reactions in Inorganic Powder Mixtures," in Shock Waves in Materials Science (ed. A.B. Sawaoka), Springer-Verlag, Tokyo: 67-101.

Horie, Y. (1995) "Mass mixing and nucleation and growth of chemical reactions in shock compression of powder mixtures," in Metallurgical and Materials Applications of Shock-Wave and High-Strain-Rate Phenomena (eds. L.E. Murr, K.P. Staudhammer and M.A. Meyers), Elsevier Science: 603-614.

Horie, Y., R. Graham and I.K. Simonsen, eds., (1986) Observations on the Shock-Synthesis of Intermetallic Compounds, Metallurgical Applications of Shock-wave and High-strain-rate Phenomena, CRC Press, New York.

Horie, Y., R.A. Graham and I.K. Simonsen (1985) "Synthesis of nickel aluminides under high-pressure shock loading" *Mater. Lett.*, 3(9-10), 354-359.

Horie, Y. and A.B. Sawaoka (1993) Shock Compression Chemistry of Materials, KTK Scientific Publishers, Tokyo.

Huang, H. and J.R. Asay (2005) "Compressive strength measurements in aluminum for shock compression over the stress range of 4-22 GPa" *J. Appl. Phys.*, 98(3), 033524.

Huang, H. and J.R. Asay (2007) "Reshock and release response of aluminum single crystal" *J. Appl. Phys.*, 101(6), 063550.

Huang, S. and R.J. Clifton (1985) *Macro- and Micro-mechanics of High Velocity Deformation and Fracture* (eds. K. Kawata and J. Shioiri), Tokyo, IUTAM: 63.

Hull, D. and D.J. Bacon (2001) Introduction to Dislocations, Butterworth-Heinemann, Oxford.

Jarmakani, H.N., E.M. Bringa, P. Erhart, et al. (2008) "Molecular dynamics simulations of shock compression of nickel: From monocrystals to nanocrystals" *Acta Mater.*, 56(19), 5584-5604.

Johnson, G.R. and W.H. Cook (1985) "Fracture characteristics of 3 metals subjected to various strains, strain rates, temperatures and pressures" *Engineering Fracture Mechanics*, 21(1), 31-48.

Johnson, J.N. (1993) "Micromechanical considerations in shock compression of solids," in High-Pressure Shock Compression of Solids (eds. J.R. Asay and M. Shahinpoor), Springer-Verlag, New York: 217-264.

Johnson, J.N. and L.M. Barker (1969) "Dislocation dynamics and steady plastic wave profiles in 6061-T6 Aluminum" *J. Appl. Phys.*, 40(11), 4321-4334.

Johnson, J.N., R.S. Hixson, G.T. Gray, et al. (1992) "Quasi-elastic release in shock-compressed solids" *J. Appl. Phys.*, 72(2), 429-441.

Johnston, W.G. and J.J. Gilman (1960) "Dislocation multiplication in Lithium Fluoride crystals" *J. Appl. Phys.*, 31(4), 632-643.

Klepaczko, J.R. (1975) "Thermally activated flow and strain rate history effects for some polycrystalline fcc metals" *Mater. Sci. Eng.*, 18(1), 121-135.

Kocks, U.F. (1966) "A statistical theory of flow stress and work-hardening" *Philos. Mag.*, 13(123), 541-566.

Kocks, U.F., A.S. Argon and M.F. Ashby (1975) "Thermodynamics and Kinetics of Slip" *Prog. Mater. Sci.*, 19, 1-281.

Kocks, U.F. and H. Mecking (2003) "Physics and Phenomenology of Strain Hardening: the FCC case" *Prog. Mater. Sci.*, 48, 171-273.

Koppenaal, T.J. and D. Kuhlmann-Wilsdorf (1964) "The effect of prestressing on the strength of neutron-irradiated copper single crystals" *Appl. Phys. Lett.*, 4(3), 59-61.

Kuhlmann-Wilsdorf, D. (1999) "The theory of dislocation-based crystal plasticity" *Philos. Mag. A*, 79(4), 955-1008.

Kuhlmann-Wilsdorf, D., R. Maddin and H.G.F. Wilsdorf (1962) "Strengthening Mechanisms in Solids," in (ed. J.J. Harwood).

Kurzydlowski, K. (1982) "Finite-element analysis of stress-concentrations on the grain-boundary in anisotropic bicrystals" *Res. Mech.*, 5(2), 89-99.

Lazor, P., G. Shen and S.K. Saxena (1993) "Laser-heated diamond-anvil cell experiments at high-pressure - melting curve of nickel up to 700 kbar" *Physics and Chemistry of Minerals*, 20(2), 86-90.

Leibfried, G. (1950) "Uber den einfluss thermisch angeregter schallwellen auf die plastische deformation" *Z. Phys.*, 127(4), 344-356.

Li, C.H. (1981) PhD Thesis, Brown University.

Marsh, S.P., ed. (1980) LASL Shock Hugoniot Data, University of California Press, Berkeley, CA.

McGlaun, J.M. (1982) "Improvements in CSQII: a transmitting boundary condition," Sandia National Laboratories (Report # SAND82-1248).

Mecking, H. and U.F. Kocks (1981) "Kinetics of flow and strain-hardening" *Acta Metall.*, 29(11), 1865-1875.

Meyers, M.A. (1978) "A mechanism for dislocation generation in shock-wave deformation" *Scripta Metall. Mater.*, 12, 21-26.

Meyers, M.A., D.J. Benson, O. Vohringer, et al. (2002) "Constitutive description of dynamic deformation: physically-based mechanisms" *Mater. Sci. Eng. A - Struct.*, 322, 194-216.

Meyers, M.A., F. Gregori, B.K. Kad, et al. (2003) "Laser-induced shock compression of monocrystalline copper: characterization and analysis" *Acta Mater.*, 51(5), 1211-1228.

Meyers, M.A., M.S. Schneider, H. Jarmakani, et al. (2008) "Deformation substructures and their transitions in laser shock-compressed copper-aluminum alloys" *Metall. Mater. Trans. A*, 39A(2), 304-321.

Meyers, M.A., L.H. Yu and K.S. Vecchio (1994) "Shock Synthesis of Silicides - II. Thermodynamics and Kinetics" *Acta Metall. Mater.*, 42(3), 715-729.

Millett, J.C.F., N.K. Bourne and G.T. Gray (2008) "The behavior of Ni, Ni-60Co, and Ni_3Al during one-dimensional shock loading" *Metall. Mater. Trans. A*, 39A(2), 322-334.

Millett, J.C.F., N.K. Bourne and Z. Rosenberg (1997) "Shear stress measurements in copper, iron, and mild steel under shock loading conditions" *J. Appl. Phys.*, 81(6), 2579-2583.

Millett, J.C.F., Y.J.E. Meziere and N.K. Bourne (2007) "Shear stress measurement in nickel and nickel-60 wt% cobalt during one-dimensional shock loading" *J. Mater. Sci.*, 42(15), 5941-5948.

Millett, J.C.F., G. Whiteman and N.K. Bourne (2009) "Lateral stress and shear strength behind the shock front in three face centered cubic metals" *J. Appl. Phys.*, 105(3).

Molinari, A. and G. Ravichandran (2004) "Fundamental structure of steady plastic shock waves in metals" *J. Appl. Phys.*, 95(4), 1718-1732.

Mughrabi, H. (1986) "A two-parameter description of heterogeneous dislocation distributions in deformed metal crystals" *Mater. Sci. Eng.*, 85, 15-31.

Murr, L.E. (1978) "Work Hardening and the Pressure Dependence of Dislocation Density and Arrangements in Shock Loaded Nickel and Copper" *Scripta Metall. Mater.*, 12, 201-206.

Murr, L.E. (1981) "Residual Microstructure - Mechanical Property Relationships in Shock-Loaded Metals and Alloys," in Shock waves and high-strain-rate phenomena in metals (eds. M.A. Meyers and L.E. Murr), Plenum, New York: 607-673.

Murr, L.E. (1988) "Examination of microstructural development by shock waves in condensed matter: Theoretical and practical consequences" *Shock Waves in Condensed Matter - 1987* (eds. S.C. Schmidt and N.C. Holmes): 315-320.

Murr, L.E. and D. Kuhlmann-Wilsdorf (1978) "Experimental and Theoretical Observations on the Relationship between Dislocation Cell Size, Dislocation Density, Residual Hardness, Peak Pressure and Pulse Duration in Shock-Loaded Nickel" *Acta Metall.*, 26, 847-857.

Murr, L.E., M.A. Meyers, C.S. Niou, et al. (1997) "Shock-induced deformation twinning in tantalum" *Acta Mater.*, 45(1), 157-175.

Myhr, O.R., O. Grong and S.J. Andersen (2001) "Modelling of the age hardening behaviour of Al-Mg-Si alloys" *Acta Mater.*, 49(1), 65-75.

Nadgornyi, E. (1988) "Dislocation Dynamics and Mechanical Properties of Crystals" *Prog. Mater. Sci.*, 31, 1-530.

Nes, E. (1998) "Modelling of work hardening and stress saturation in fcc metals" *Prog. Mater. Sci.*, 41, 129-193.

Nesterenko, V.F., M.A. Meyers, H.C. Chen, et al. (1994) "Controlled high-rate localized shear in porous reactive media" *Appl. Phys. Lett.*, 65(24), 3069-3071.

Olivares, F.H. and J.G. Sevillano (1987) "A quantitative assessment of forest-hardening in fcc metals" *Acta Metall.*, 35(3), 631-641.

Park, H.S., K.T. Lorenz, R.M. Cavallo, et al. (2010) "Viscous Rayleigh-Taylor Instability Experiments at High Pressure and Strain Rate" *Physical Review Letters*, 104(13).

Polmear, I. (2006) Light Alloys - From Traditional Alloys to Nanocrystals, Butterworth-Heinemann, Burlington, MA.

Preston, D.L., D.L. Tonks and D.C. Wallace (2003) "Model of plastic deformation for extreme loading conditions" *J. Appl. Phys.*, 93(1), 211-220.

Regazzoni, G., U.F. Kocks and P.S. Follansbee (1987) "Dislocation kinetics at high-strain rates" *Acta Metall.*, 35(12), 2865-2875.

Remington, B.A., P. Allen, E.M. Bringa, et al. (2006) "Material dynamics under extreme conditions of pressure and strain rate" *Mater. Sci. Tech.*, 22(4), 474-488.

Roters, F., D. Raabe and G. Gottstein (2000) "Work hardening in heterogeneous alloys - A microstructural approach based on three internal state variables" *Acta Mater.*, 48(17), 4181-4189.

Seeger, A. (1954) "The temperature dependence of the critical shear stress and of work-hardening of metal crystals" *Philos. Mag.*, 45(366), 771-773.

Seeger, A. (1956) "On the theory of the low-temperature internal friction peak observed in metals" *Philos. Mag.*, 1(7), 651-662.

Shehadeh, M.A., E.M. Bringa, H.M. Zbib, et al. (2006) "Simulation of shock-induced plasticity including homogeneous and heterogeneous dislocation nucleations" *Appl. Phys. Lett.*, 89(17), 171918.

Song, I. and N.N. Thadhani (1992) "Shock-induced chemical reactions and synthesis of nickel aluminides" *Met. Trans. A*, 23(1), 41-48.

Spearot, D.E., K.I. Jacob and D.L. McDowell (2007) "Dislocation nucleation from bicrystal interfaces with dissociated structure" *Int. J. Plasticity*, 23(1), 143-160.

Steinberg, D.J., S.G. Cochran and M.W. Guinan (1980) "A constitutive model for metals applicable at high-strain rate" *J. Appl. Phys.*, 51(3), 1498-1504.

Swegle, J.W. and D.E. Grady (1985) "Shock viscosity and the prediction of shock rise times" *J. Appl. Phys.*, 58(2), 692-701.

Tamura, S. and Y. Horie (1998) "Discrete meso-dynamic simulation of thermal explosion in shear bands" *J. Appl. Phys.*, 84(7), 3574-3580.

Taylor, J.W. (1965) "Dislocation dynamics and dynamic yielding" *J. Appl. Phys.*, 36(10), 3146-3150.

Thadhani, N.N. (1990) "Shock-induced chemical synthesis of intermetallic compounds" *Shock Compression of Condensed Matter - 1989* (eds. S.C. Schmidt, J.N. Johnson and L.W. Davison): 503-510.

Thadhani, N.N. (1993) "Shock-induced chemical reactions and synthesis of materials" *Prog. Mater. Sci.*, 37, 117-226.

Thadhani, N.N. (1994) "Shock-induced and shock-assisted solid-state chemical reactions in powder mixtures " *J. Appl. Phys.*, 76(4), 2129-2138.

Thadhani, N.N. (2010), personal communication.

Thadhani, N.N., R.A. Graham, T. Royal, et al. (1997) "Shock-induced chemical reactions in titanium-silicon powder mixtures of different morphologies: Time-resolved pressure measurements and materials analysis" *J. Appl. Phys.*, 82(3), 1113-1128.

Tong, W., R.J. Clifton and S. Huang (1992) "Pressure-shear impact investigation of strain rate history effects in oxygen-free high-conductivity copper" *J. Mech. Phys. Solids*, 40(6), 1251-1294.

Torquato, S. (1991) "Random heterogeneous media: microstructure and improved bounds on effective properties" *Applied Mechanics Review*, 44, 37-76.

Tschopp, M.A. and D.L. McDowell (2008a) "Grain boundary dislocation sources in nanocrystalline copper" *Scripta Mater.*, 58(4), 299-302.

Tschopp, M.A. and D.L. McDowell (2008b) "Influence of single crystal orientation on homogeneous dislocation nucleation under uniaxial loading" *J. Mech. Phys. Solids*, 56(5), 1806-1830.

Turneaure, S.J. and Y.M. Gupta (2009) "Real time synchrotron x-ray diffraction measurements to determine material strength of shocked single crystals following compression and release" *J. Appl. Phys.*, 106(3).

Van Leer, B. (1977) "Towards the ultimate conservative difference scheme. IV. A new approach to numerical convection" *J. Comput. Phys.*, 23, 276-299.

Van Swygenhoven, H., P.M. Derlet and A.G. Froseth (2006) "Nucleation and propagation of dislocations in nanocrystalline fcc metals" *Acta Mater.*, 54(7), 1975-1983.

Vandersall, K.S. and N.N. Thadhani (2003) "Time-resolved measurements of the shock-compression response of Mo + 2 Si elemental powder mixtures" *J. Appl. Phys.*, 94(3), 1575-1583.

Varin, R.A., K.J. Kurzydlowski and K. Tangri (1987) "Analytical treatment of grain-boundary sources for dislocations" *Mater. Sci. Eng.*, 85(1-2), 115-126.

Vecchio, K.S. and G.T. Gray (1994) "Shock-loading response of 6061-T6 aluminum alumina metal-matrix composites" *Journal De Physique IV*, 4(C8), 231-236.

Vogler, T.J. and L.C. Chhabildas (2006) "Strength behavior of materials at high pressures" *Int. J. Impact Eng.*, 33, 812-825.

Wallace, D.C. (1980a) "Flow Process of Weak Shock Waves" *Phys. Rev. B*, 22(4), 1487-1494.

Wallace, D.C. (1980b) "Irreversible Thermodynamics of Flow in Solids" *Phys. Rev. B*, 22(4), 1477-1486.

Wallace, D.C. (1981) "Irreversible Thermodynamics of Overdriven Shocks in Solids" *Phys. Rev. B*, 24(10), 5597-5606.

Wang, Y.M., E.M. Bringa, J.M. McNaney, et al. (2006) "Deforming nanocrystalline nickel at ultrahigh strain rates" *Appl. Phys. Lett.*, 88(6).

Wang, Z.Q., I.J. Beyerlein and R. Lesar (2009) "Plastic anisotropy in fcc single crystals in high rate deformation" *Int. J. Plasticity*, 25(1), 26-48.

Warnes, R.H. and D.L. Tonks (1989) "Measurement and analysis of 3-GPa shock wave profiles in annealed OFE copper" *Shock Compression of Condensed Matter* (eds. S.C. Schmidt, J.N. Johnson and L.W. Davison), Elsevier: 329-332.

Williamson, R.L. (1990) "Parametric studies of dynamic powder consolidation using a particle-level numerical model" *J. Appl. Phys.*, 68, 1287-1296.

Winter, R.E. and E.J. Harris (2008) "Simulations of embedded lateral stress gauge profiles in shocked targets" *J. Phys. D Appl. Phys.*, 41(3).

Wolfer, W.G. (1999) "Phonon Drag on Dislocations at High Pressures," Lawrence Livermore National Laboratory (Report # UCRL-ID-136221).

Xu, G.S. and A.S. Argon (2000) "Homogeneous nucleation of dislocation loops under stress in perfect crystals" *Philos. Mag. Lett.*, 80(9), 605-611.

Yang, Y., R.D. Gould, Y. Horie, et al. (1997) "Shock-induced chemical reactions in Ni/Al powder mixture" *Appl. Phys. Lett.*, 70(25), 3365-3367.

Yano, K. and Y. Horie (1998) "A numerical study of shock-induced particle velocity dispersion in solid mixtures" *J. Appl. Phys.*, 84(3), 1292-1298.

Youngs, D.L. (1982) "Time dependent multi-material flow with large fluid distortion" *Numerical Methods for Fluid Dynamics* (eds. K.W. Morton and M.J. Blaines), Reading, PA, Academic: 273-285.

Zander, J. and R. Sandstrom (2008) "One parameter model for strength properties of hardenable aluminium alloys" *Mater. Design*, 29(8), 1540-1548.

Zerilli, F.J. and R.W. Armstrong (1987) "Dislocation-mechanics-based constitutive relations for material dynamics calculations" *J. Appl. Phys.*, 61(5), 1816-1825.

Zhu, T., J. Li, A. Samanta, et al. (2008) "Temperature and strain-rate dependence of surface dislocation nucleation" *Phys. Rev. Lett.*, 100(2), 025502.

Zhu, Z. and M.J. Starink (2008) "Solution strengthening and age hardening capability of Al-Mg-Mn alloys with small additions of Cu" *Mater. Sci. Eng. A - Struct.*, 488(1-2), 125-133.